

Double Pendulums for Terrestrial Interferometric Gravitational Wave Detectors

Stuart Duncan Killbourn, B.Sc.,

Department of Physics and Astronomy,
University of Glasgow.

Presented as a thesis for the degree of Ph.D.,
Department of Physics and Astronomy,
University of Glasgow, University Avenue, G12 8QQ.

© S. D. Killbourn, 1997.

October 24, 1997

ProQuest Number: 11007765

All rights reserved

INFORMATION TO ALL USERS

The quality of this reproduction is dependent upon the quality of the copy submitted.

In the unlikely event that the author did not send a complete manuscript and there are missing pages, these will be noted. Also, if material had to be removed, a note will indicate the deletion.



ProQuest 11007765

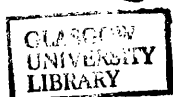
Published by ProQuest LLC (2018). Copyright of the Dissertation is held by the Author.

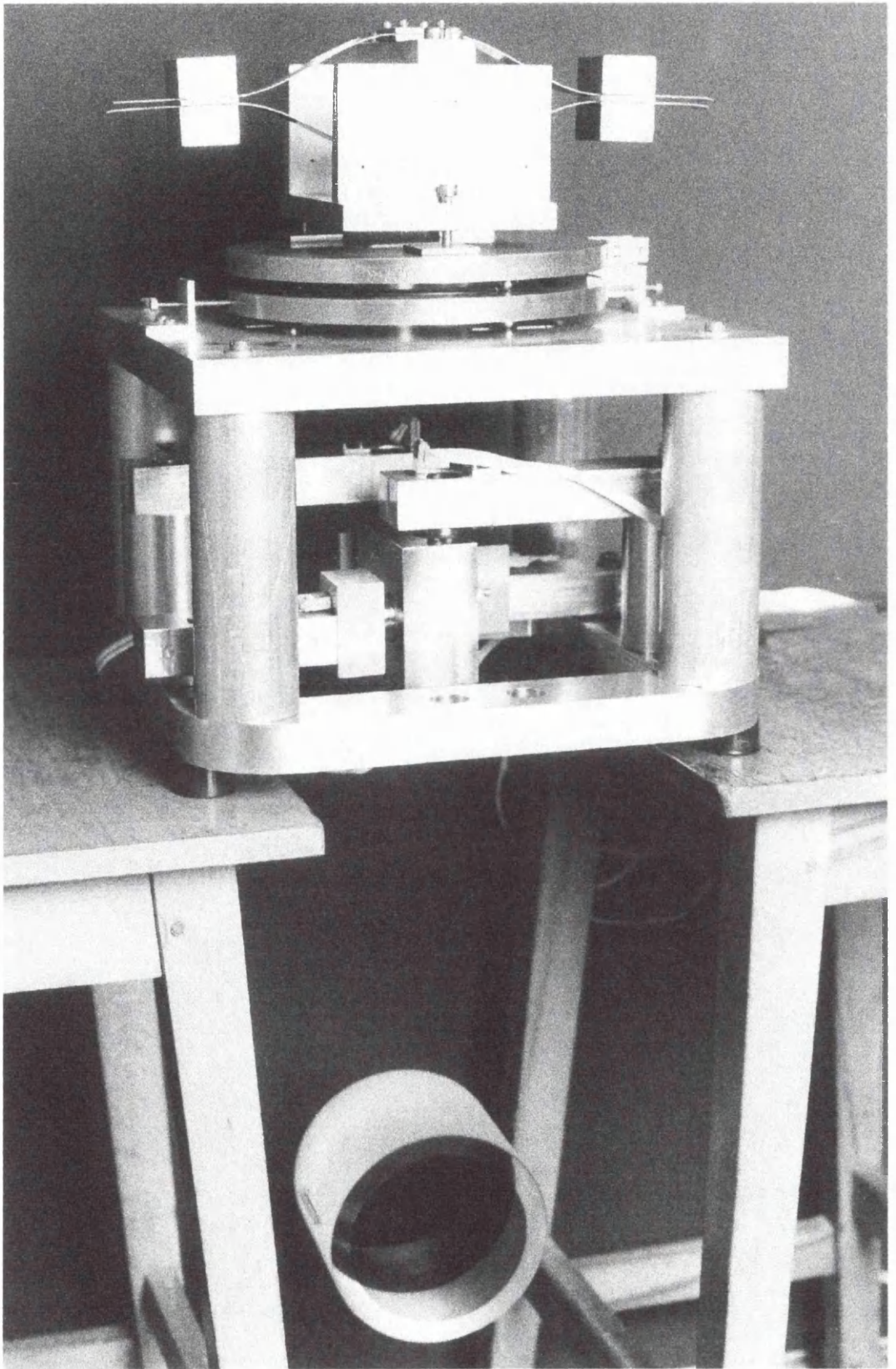
All rights reserved.

This work is protected against unauthorized copying under Title 17, United States Code
Microform Edition © ProQuest LLC.

ProQuest LLC.
789 East Eisenhower Parkway
P.O. Box 1346
Ann Arbor, MI 48106 – 1346

Thesis 10966
Copy 1





Acknowledgements

I acknowledge first the LORD whom I recognise as my creator, my saviour and the principal inspiration in all aspects of my life.

‘Lift your eyes and look to the heavens:
Who created all these?
He who brings out the starry host one by one,
And calls them each by name.
Because of his great power and mighty strength,
Not one of them is missing.’

Isaiah xxxix.26.

I am grateful to my supervisor Harry Ward who has adequately instilled in me a demand for rigorous argument and thoughtful expression. I am indebted to other members of the Gravitational Waves Group here in Glasgow. In particular, James Hough (group leader), Gavin Newton and Norna Robertson. I have found all to be both approachable and helpful during my research. On a day to day basis, I have been the recipient of the invaluable assistance of Kenneth Strain, David Robertson and Jennifer Logan (for thermal noise issues). Latterly, I have had helpful discussions with Michael Plissi and Sheila Rowan.

I wish to express my gratitude to those who have been partisans through the trials and tribulations, and who have shared the moments of glory; their names are: Kenneth Skeldon, Alison M^cLaren, Sharon Twyford, Paul M^cNamara, Morag Casey, Calum Torrie, William Hamish Bell and Janet Milne.

Technical support has been supplied by Colin Craig, Angus M^cKellar, Allan Latta and David Edwards as well as the staff of the Mechanical Workshop and the Electronic Workshop. Contributions, both technical and humorous, have been made

by Alistair Grant and Raymond Hutchins. Thanks go also to our photographer Ian M^cVicar.

I wish to acknowledge the help and encouragement given to me by members of the Gravitational Waves Groups at the Max-Planck-Institute in Garching and at Hannover Universität – hertzlichen danke!

A special distinction has been earned by David Robertson's maternal grandmother, Mrs Matheson, who has kept us all energised with the provision of home baking.

During my research I was in receipt of a SERC/PPARC studentship.

Personal thanks go to those who, although they shall probably never understand the import of this volume, have in their own way kept my life moderately sane and interesting over the past three years. I have appreciation for my long-standing friend Gordon; the co-accused: Alistair, Rachel and Catherine, and for Jason and Sheila. Love and fellowship go to the folks at Partick Baptist Church; Robbie Muir and family; Roselin, Ailsa and Shona; everyone at the YMCA Glasgow Gospel Choir; Genevieve; Eddie Whyte; my parents and the 146 (T/L) "family"; Richard; Pauline; Neil and the Last Resort, and finally to the Active Allstars from Gosport.

Many thanks are given to:

Mrs E. E. Killbourn
(1903 – 1995).

For my little sister.

Contents

Preface	xii
Summary	xv
Notation	xviii
1 Sources of Gravitational Waves	1
1.1 Introduction	1
1.2 Sources of Gravitational Waves	3
1.2.1 Burst Sources	3
1.2.2 Monochromatic Sources	7
1.2.3 Stochastic Sources	8
1.3 Conclusion	9
2 Gravitational Wave Detectors	10
2.1 Introduction	10
2.1.1 Resonant Mass Detectors	11
2.1.2 Interferometric Gravitational Wave Detectors	12
2.1.3 Spaceborne Detectors	16
2.2 Noise Sources in Terrestrial Interferometric Gravitational Wave Detectors	17
2.2.1 Acoustic and Seismic Noise	17
2.2.2 Thermal Noise	19
2.2.3 Laser Noise	20

2.2.4	Shot Noise	23
2.3	Conclusion	25
3	Noise Sources in the Glasgow Prototype Detector	29
3.1	Introduction	29
3.2	The Noise Floor of the Glasgow Prototype	30
3.2.1	Fundamental Noise Limits	32
3.2.2	Seismic Noise	32
3.2.3	Seismic Coupling <i>via</i> the Actuator Coils	36
3.2.4	Other Noise Sources	37
3.3	Conclusion	37
4	Model of Test Mass Suspension	39
4.1	Introduction	39
4.2	Choice of Coordinates	40
4.3	Restoring Forces	41
4.3.1	Extension of a Wire	41
4.3.2	Torsion of a Wire	42
4.3.3	Bending of a Wire	42
4.3.4	Example of Model	43
4.4	Normal Modes of the Test Mass Suspension	45
4.4.1	Eigenvalue and Eigenvector Extraction	46
4.5	State-space Modelling	46
4.6	Frictional Losses in the Suspension Wires	48
4.6.1	Viscous Damping	48
4.6.2	Complex Spring Damping	49
4.6.3	Damping of Normal Modes	50
4.6.4	Damping in State-space	50
4.7	Transverse Modes of the Suspension Wires	51
4.8	Internal Modes of the Test Mass	53
4.9	Conclusion	55

5	Local Control of Test Mass Suspension	56
5.1	Introduction	56
5.2	Active Damping of Normal Modes	57
5.3	Prototype Design of Double Pendulum Test Mass Suspension	59
5.4	Sensors and Actuators	64
5.4.1	Control Noise	64
5.4.2	Shadow Sensors	66
5.4.3	Coil-Magnet Actuators	68
5.4.4	Seismic Motion of the Coils	72
5.5	Longitudinal Modes of the Double Pendulum	73
5.5.1	Damping and Control Noise	74
5.5.2	Damping as a Function of Gain	77
5.6	Step Response of Damped Pendulum	82
5.7	Conclusion	82
6	Global Control of an Interferometer	85
6.1	Introduction	85
6.2	Seismic Excitation	87
6.3	Feedback to the Test Mass	89
6.3.1	Response of the Test Mass	90
6.3.2	Actuators	94
6.4	Acquisition of Lock	96
6.5	Feedback to the Intermediate Mass	100
6.6	Conclusion	108
7	Thermal Noise	109
7.1	Introduction	109
7.2	Internal Friction	110
7.2.1	Thermoelastic Damping	113
7.3	Thermal Noise in a Pendulum	114
7.3.1	Analysis of a Single Pendulum	116
7.3.2	Suspension Topology of a Double Pendulum	118

7.3.3	Conclusion	122
7.4	Transverse Modes of the Suspension Wire	123
7.4.1	Loss Associated with Transverse Modes	124
7.4.2	Measurements of Q factor of Transverse Modes	125
7.4.3	Conclusion	127
7.5	Internal Modes of the Test Mass	127
7.5.1	Elastic Equations	129
7.5.2	Finite Element Analysis	130
7.5.3	Thermal Noise Estimate of Prototype	133
7.5.4	Discussion of Internal Loss in the Test Masses	134
7.5.5	Conclusion	138
8	GEO 600	140
8.1	Overview of the GEO 600 Project	140
8.2	GEO 600 Modecleaner Mirror Suspension	144
8.3	GEO 600 Test Mass Suspension	149
8.3.1	Preliminary Design of Test Mass Suspension	149
8.3.2	Local Control	152
8.4	Conclusion	156
9	Conclusion	158
9.1	Review	158
9.2	A Final Question...	159
A	MATLAB Toolbox	161
A.1	dp2ss.m	161
A.2	assign.m	173
A.3	constant.m	175
A.4	props.m	176
A.5	dp_new.m	179
A.6	dp_prot.m	182
A.7	dp_g6_mc.m	185

A.8	fb_x1.m	188
A.9	fb_x2.m	192
B	Derivation of Equation 4.8	197

List of Figures

1.1	The Effect of a Gravitational Wave on a Ring of Test Masses.	2
2.1	A Michelson Interferometer.	13
2.2	Advanced Interferometer Designs.	14
2.3	A Dual Recycled Interferometer.	15
2.4	Example Single and Double Pendulums.	17
2.5	Estimated Strain Sensitivity of GEO 600.	26
2.6	Estimated Signal Strengths and the Sensitivity of GEO 600.	27
3.1	The Displacement Noise of the Glasgow Prototype Interferometer. . .	31
3.2	The Displacement Noise Floor of the Glasgow Prototype (Low Frequency).	33
4.1	Bending and Flexing of a Stiff Beam under Tension.	44
4.2	Longitudinal and Tilt Degrees of Freedom for Single Pendulum. . . .	45
5.1	The Differential Tilt Mode of a Double Pendulum.	61
5.2	Redesigned Double Pendulum Suspension for Prototype Detector. . .	62
5.3	Shadow Sensor and Coil-Magnet Actuator.	65
5.4	Noise Inputs to the Local Control of a Double Pendulum.	65
5.5	LED Intensity Profile.	66
5.6	LED Current Stabiliser.	67
5.7	Ideal Current and Voltage Controlled Coil Drivers.	68
5.8	A Practical Voltage-Controlled Coil Driver.	69
5.9	Effective Input Noise in Coil Driver Circuit.	70

5.10	Variation of Force with Separation of Coil and Magnet.	71
5.11	Longitudinal Modes of a Double Pendulum.	74
5.12	Filter Schemes for Damping a Double Pendulum.	76
5.13	Damped Q factor as a Function of Imposed Control Noise.	77
5.14	Circuit Diagram of Damping Servo.	78
5.15	Q Factor of Pendulum against Servo Gain.	80
5.16	Local Control Servo: Open Loop Gain.	81
5.17	Local Control Servo: Closed Loop Gain.	81
5.18	Inputs to the Local Control Servo.	82
5.19	Step Response of Double Pendulum (Longitudinal).	83
5.20	Step Response of Double Pendulum (Rotation).	83
5.21	Step Response of Double Pendulum (Tilt).	84
6.1	Displacement Transfer Function of a Single and Double Pendulum.	88
6.2	Generic Servo Control Loop.	90
6.3	Response of the Test Mass to an Applied Force.	91
6.4	Transfer Function of Internal Modes of Test Mass.	93
6.5	Servo Control Loop with Variable Actuator.	96
6.6	CMOS Logic to Generate Fringe Damping Signal for Fabry-Perot Cavity.	98
6.7	Interlaced Electrodes of a Possible Electrostatic Drive.	101
6.8	Global Control: Split Feedback Topology	101
6.9	Transfer Function of Force at Intermediate Mass to Test Mass Dis- placement.	102
6.10	Transfer Function of a Scultéy Filter.	104
6.11	Global Control: Open Loop Gain for a Split Feedback Topology.	105
6.12	Feedback Force Required to Accommodate Seismic Vibrations.	107
7.1	Ideal Spring Damped by Viscous Dash Pot.	110
7.2	Thermal Noise of a Damped Resonance.	111
7.3	An Ideal Spring Damped by a Relaxation Process.	112
7.4	Relaxation Processes of an Ideal Spring.	113

7.5	Thermal Noise Inputs for each Suspension Wire (extension and torsion).	115
7.6	Thermal Noise Inputs for each Suspension Wire (Bending).	116
7.7	Q factor of Pendulum Modes.	117
7.8	Thermal Noise for Single Pendulum.	119
7.9	Configurations for Suspending a Test Mass.	120
7.10	Thermal Noise in Double Pendulum Suspensions.	121
7.11	Thermal Noise from Transverse Modes in the Glasgow Prototype.	125
7.12	Measurements of Material Q Factor of Suspension Wires.	126
7.13	Internal Mode Shapes of the Test Masses.	132
7.14	Resonant Coupling of Magnet to an Internal Mode of the Test Mass.	137
7.15	Attachment of Magnets to the Test Mass.	138
8.1	GEO 600 Optical Scheme.	141
8.2	GEO 600 Modecleaners Layout.	143
8.3	GEO 600 Modecleaner Suspension Design.	146
8.4	GEO 600 Modecleaner Mirror and Reaction Mass.	148
8.5	GEO 600 Test Mass Suspension Design.	150
8.6	GEO 600 Test Mass Damping versus Control Noise.	154
8.7	Contributions to Local Control Noise.	155

List of Tables

5.1	Normal Mode Frequencies of Prototype Suspension.	63
6.1	Acquisition Times of a Fabry-Perot Cavity.	99
6.2	Global Control: Feedback Range Requirements.	107
7.1	Calculation of Coupling Factors for Internal Modes.	131
7.2	Resonant Frequencies of Internal Modes.	133
7.3	Measured Q factors of Internal Modes.	135
8.1	Normal Mode Frequencies of Modecleaner Suspension.	147
8.2	Normal Mode Frequencies of Test Mass Suspension.	152
8.3	Scultéty Filters for Attenuation of Control Noise.	153

Preface

Chapter 1 contains an introduction to gravitational waves. The astrophysical sources of gravitational waves are briefly considered in order to define the threshold sensitivity required for the detection gravitational of waves. The subject matter is derived from current literature.

In Chapter 2 an overview of gravitational wave detectors is given. In particular, various types of laser interferometric detector are described in conjunction with the noise sources that limit their sensitivity. This work is partly obtained from current literature and is partly composed by the author as an introduction to work that is presented in subsequent chapters.

Chapter 3 is a presentation of the sensitivity obtained by the Glasgow prototype detector. All work on the Glasgow prototype detector has been conducted with other members of the Gravitational Waves Group. The data recording described in this chapter was conducted with H. Ward, D. Robertson, K. Skeldon and M. Casey.

In Chapter 4 a dynamic model of a double pendulum and resonances of the suspension wires is formulated. This is the work of the author. A model is also described for the internal modes of a cylindrical test mass. This is the result of analysis by J. R. Hutchinson with revision by A. Gillespie and K. Blackburn (Caltech).

In Chapter 5 a double pendulum design is presented that should allow improved sensitivity when used to suspend the test masses of the Glasgow prototype. Active damping of the normal modes of the pendulum is considered. This is the application of the work presented in Chapter 4.

Chapter 6 contains a discussion of the control of a test mass by signals obtained from the interferometer output. This is applied to the operation of the Glasgow pro-

prototype detector. This is the further application of the work presented in Chapter 4.

In Chapter 7 the Brownian motion of the suspension components is evaluated. This is a significant limitation to the sensitivity of interferometric gravitational wave detectors. The work is reliant on the model formulated in Chapter 4 and was carried out with discussion with other members of the Gravitational Waves Group, particularly J. E. Logan and J. Hough.

In Chapter 8 the techniques discussed in the preceding chapters are applied to the GEO 600 project. This is a large scale interferometer with a significant chance of detecting gravitational radiation. The project is the partnership of research groups from the University of Glasgow; the University of Wales (College of Cardiff); the Albert Einstein Institute in Potsdam; Hannover Universität, and the Max-Planck-Institute für Quantenoptik in Garching. The interferometer is being constructed near Hanover. The material presented is a review of the project followed by the design work carried out by the author in conjunction with the GEO 600 Suspension Group (which is led by N. Robertson).

Chapter 9 is a conclusion of the work presented.

Appendix A is a source listing of the 'MATLAB' routines developed to model the dynamics of the double pendulum.

Appendix B is a detailed derivation of Equation 4.8.

Summary

This thesis is written for the threefold purpose of:-

1. Advocating the use of double pendulums, in preference to single stage pendulums, to suspend the test masses used in terrestrial interferometric gravitational wave detectors.
2. Justifying the necessity of developing a comprehensive dynamic model of a double pendulum suspension. This requires consideration of all six degrees of freedom (per mass) of the coupled system.
3. Demonstrating that there is sufficient confidence in the modelling techniques to proceed to the design and construction of a double pendulum suspension for use in a full scale gravitational wave detector.

The author believes that the use of double pendulums to suspend the test masses of a terrestrial interferometric gravitational wave detectors offers an accessible means of obtaining the high sensitivity required to record gravitational waves using such a detector. The following is a summary of how this assertion is justified in the course of this thesis.

Chapter 1 is an introduction to gravitation and the postulation of the existence of gravitational waves. Potential sources and the expected signal strengths are discussed. This forms a guide to the sensitivity that is required by a gravitational wave detector.

An overview of the subject of gravitational wave detectors is found in Chapter 2. Various types of detector are described; these include: resonant mass detectors, laser interferometers and also the proposed ESA space mission LISA. Noise sources that

limit the sensitivity to gravitational waves of interferometric detectors are introduced in this chapter and many are discussed later in this thesis.

Chapter 3 is a brief presentation of the noise floor of the Glasgow prototype interferometric gravitational wave detector (measured on 6th March 96). The origin of the detector noise in different frequency regions is discussed. It is shown that the the sensitivity of the detector could be improved at frequencies below 200 Hz by a more careful design of pendulum.

The formulation of a dynamic model of the pendulum suspension is presented in Chapter 4. This describes how the normal mode frequencies and Q factors of the pendulum suspension can be obtained from the equations of motion. It also describes how a state-space model of the suspension can be formulated. State-space modelling techniques are used through out this thesis for assessing the transfer functions and servo control of the double pendulums considered. It is noted that a single stage pendulum is a special case of a double pendulum. Thus, the performance of a single stage pendulum can be analysed for comparison. This chapter also contains the formulation of models for the resonant modes of the suspension wires and the vibrational modes of the test mass itself.

In Chapter 5 the state-space model of the double pendulum is used to analyse damping of the normal modes by an electronic servo. (Such control suppresses the resonant enhancement of noise sources.) This must be accomplished without introducing excess noise to the system. It is shown that the frequency of the normal modes of the pendulum determine whether this is possible. The need to achieve good damping puts constraints on the design of the pendulum. This necessitates a comprehensive model of a double pendulum. The results presented in this chapter are a validation of the design techniques employed.

The servo control required to obtain the output signal from the interferometer is discussed in Chapter 6. The requirements placed on feedback elements are analysed in conjunction with the level of seismic noise that they require to accommodate. A split feedback topology is considered to assess the feasibility of using electrostatic actuation on the test mass instead of magnetic. The issues detailed in this chapter also place constraints on the pendulum design.

A critical limit to the sensitivity of an interferometric gravitational wave detectors is the Brownian motion of the test mass and suspension. Chapter 7 is a comprehensive treatment of this noise source as it arises in a double pendulum. Concluding remarks are made at the end of Sections 7.3, 7.4 and 7.5 instead of a general conclusion at the end of the chapter.

In Chapter 8 double pendulums are considered for the GEO 600 project.

Chapter 9 forms a conclusion to the research presented in this thesis.

The numerical code used to generate the dynamic model of a double pendulum is listed in Appendix A. This has been written for the 'MATLAB' environment. To do the full state-space modelling of the pendulum and servo electronics requires the 'Control Systems Toolbox'.

Appendix B is a detailed derivation of Equation 4.8.

Notation

The following convention has been adopted in this work:-

- | | |
|------------------------|---|
| a, Z, α, Ω | Mathematical variables are in italic typeface. |
| M | Matrices are bold, upper-case letters. |
| u | Vectors are bold, lower-case letters. |
| \hat{x} | Spectral noise amplitudes (in units/ $\sqrt{\text{Hz}}$) have a <i>hat</i> . |
| \hat{x}^2 | Spectral power densities (in units/Hz) are noise amplitudes squared. |
| f | denotes a frequency measured in cycles per second (Hz). |
| ω | denotes an angular frequency (in units rad s^{-1}). |

Chapter 1

Sources of Gravitational Waves

‘I seem to be having tremendous difficulty with my lifestyle.’

Arthur Dent.

1.1 Introduction

It has long been recognised that gravitation is the weakest of the forces known to exist in the Universe. However, it is remarkable that its influence is often the strongest felt in everyday life. The influence of gravitational waves, on the other hand, could *not* be said to be readily felt. Although envisaged as *ripples on the fabric of spacetime*, they are very small ripples. As will be seen, the most cataclysmic astrophysical events produce strains at the Earth that are of order a millionth of an atom nucleus over one metre. This seems impossibly small to measure yet many experimenters believe that the detection of gravitational waves is both possible and will yield useful information on the nature and scale of the Universe.

The existence of gravitational waves was first postulated in the wake of Einstein’s formulation of General Relativity [1]. Further, they are predicted to have similar properties by other modern theories of gravitation. In fact, the differences in the predictions of rival theories of gravitation will only be apparent in the signals produced in the strong fields associated with black holes. For the purpose of this discussion General Relativity will be assumed to be accurate.

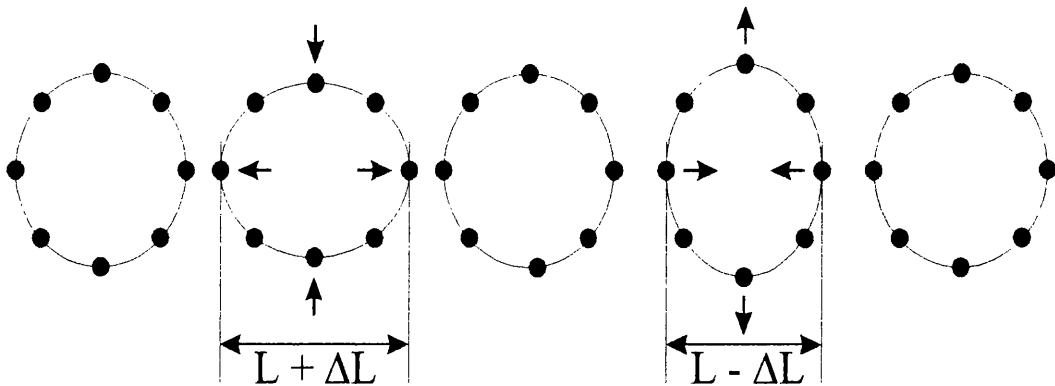


Figure 1.1: *The Effect of a Gravitational Wave on a Ring of Test Masses.*

It is observed that there is only one sign of mass. This, together with the conservation of momentum, restricts the emission of gravitational waves to time variation of the quadrupole moment of a massive body. Thus, gravitational waves are quadrupole waves and have spin equal to 2. Similar to electromagnetic waves, they are transverse and propagate at the speed of light. The effect of such a wave on a ring of test particles is shown in Figure 1.1. One period of the disturbance is shown at intervals of one quarter of the period; the wave is propagating in a direction normal to the plane defined by the ring. The ring of test particles is essentially stretched along one axis while it is squashed in the orthogonal axis. The amplitude of the gravitational wave is characterised by the strain of space it produces. This is defined to be

$$h = \frac{\Delta L}{2L} \quad (1.1)$$

where ΔL and L are as shown in Figure 1.1. A second polarisation is possible where the axes are rotated through 45° . The amplitudes of these polarisations are denoted h_+ and h_\times respectively. Circular and elliptic polarisations of gravitational waves are also possible. They are superpositions of h_+ and h_\times with an appropriate phase relation between them. This is analogous to electromagnetic waves.

Attempts to produce gravitational waves in the laboratory yield only insignificant strain amplitudes. The detection of gravitational waves will rely on astrophysical sources where the amount of mass and its velocity by far compensates for the extra distance to the source.

1.2 Sources of Gravitational Waves

In this section a summary of various expected sources will be given. This will be restricted to sources that could potentially be detected using terrestrial gravitational wave detectors. The Earth provides an unstable environment for detecting small displacements at frequencies below ~ 1 Hz. This is due to seismic disturbances and also perturbations of the gravitational field caused by density fluctuations in the Earth's atmosphere. Such effects mask the detection of gravitational waves. The maximum frequency anticipated from sources is $\sim 10^4$ Hz [2]. The upper limit arises because in order for a source to strongly emit gravitational waves it must be a collapsed object (*e.g.* a neutron star). A lower limit exists on the mass of such objects of about $1 M_{\odot}$ and hence there is an upper limit to the frequency of gravitational wave emission. Thus, the criterion for detectable sources using terrestrial detectors is that the frequency of the emitted gravitational waves lies between 1 Hz and 10^4 Hz.

1.2.1 Burst Sources

Supernovae

Supernovae events have, historically, been considered an important source of gravitational waves that are accessible to terrestrial detectors. The strain amplitude, as measured on the Earth, that is produced by such an event is given by [3]

$$h = 5 \times 10^{-22} \left(\frac{\Delta E / M_{\odot} c^2}{10^{-3}} \right)^{\frac{1}{2}} \left(\frac{15 \text{ Mpc}}{r} \right) \left(\frac{1 \text{ kHz}}{f} \right) \left(\frac{1 \text{ ms}}{\tau} \right)^{\frac{1}{2}} \quad (1.2)$$

where $\Delta E / M_{\odot} c^2$ is the fraction of the stellar rest mass radiated as gravitational waves; r is the distance from the Earth; f is the dominant frequency of the radiation and τ is the duration of the burst. The values of these quantities vary depending on the exact conditions of the collapse. The emission of gravitational waves is dependent on asymmetries in the core collapse. Supernovae events can be classified as Type I or Type II.

In a Type I supernova the progenitor is a white dwarf star that accretes matter – possibly from a binary companion – causing nuclear detonation. This may produce a neutron star as a remnant. Since the process of accretion will impart angular

momentum to the white dwarf, it is likely that the collapse to a neutron star will be highly non-axisymmetric. It is possible that the core will deform into a bar shape and, therefore, strongly emit gravitational radiation.

Type II supernovae occur when a sufficiently massive star ($> 8M_{\odot}$ when initially formed) reaches the end of its life. At this point the nuclear fusion processes in the core fail to produce sufficient radiation pressure to balance the star's self-gravity. Gravitational collapse of the stellar core becomes inevitable and a neutron star (or *pulsar*) is produced. If the initial stellar mass is large enough ($\sim 20M_{\odot}$) the formation of a black hole is possible.

It is not known how asymmetric Type II collapses are. So far, only those which are almost spherically symmetric can be modelled in simulations. These, of course, do not produce as much gravitational radiation. However, measurements by Lyne and Lorimer [4] conclude that the mean pulsar velocity is about an order of magnitude greater than the mean velocity of their progenitors, the OB stars. This strongly suggests that the collapse of the stellar core is highly non-axisymmetric and the pulsar receives a *kick* (possibly from neutrino emission in a preferred direction [5]). Clearly, such a supernovae event should be a more significant source of gravitational waves.

The complementary detection of a supernova by gravitational waves, optical and neutrino emission would be very interesting. The speed of gravitational waves could be confirmed to be the same as the speed of light to within 1 part in 10^{12} if both signals occurred within a day. Some alternatives to General Relativity predict that gravitational waves are not propagated at the speed of light.

The rate of supernovae events is approximately one per hundred years per galaxy. The experimental aim is, therefore, to observe many galaxies. If the observation range can be extended to the Virgo Cluster ($r \approx 15$ Mpc) then the event rate could be several per year. Each factor of 2 increase in detector sensitivity increases the event rate by a factor of 8. This is because the detectors are able to measure the amplitude of the gravitational wave which varies as $1/r$ from the source.

Neutron Star Coalescence

Several neutron star binary systems are currently known to exist. Such systems emit gravitational energy causing their orbit to decay and, finally, the coalescence of the two objects. The lifetimes of the observed systems are, however, $\sim 10^8$ years to $\sim 10^{10}$ years. This means that the expected event rate is low (perhaps 3 per year out to 100 Mpc). It has been suggested that neutron star binaries can be formed with much shorter lifetimes (perhaps $\sim 10^7$ years – see Thorne [2] and references therein) but these are obviously less likely to be observed. If these do in fact exist then the expected event rate is increased. The maximum rate is probably around 100 per year out to 100 Mpc.

Gravitational waves are emitted at twice the orbital frequency of the system. As the orbit decays, the orbital frequency increases resulting in a *chirp* signal. In fact, only in the final stages does the frequency of the gravitational wave lie in the sensitivity band of terrestrial detectors. It is estimated to take approximately 1000 s for the frequency to sweep from 10 Hz up to ~ 1 kHz. During this time the gravitational wave signal would have a very well determined waveform. This will aid the identification of such signals in the presence of detector noise.

The gravitational waves emitted from a binary source are determined by its chirp mass, \mathcal{M} . For two stars of masses M_1 and M_2 , the chirp mass is

$$\mathcal{M} = \frac{(M_1 M_2)^{\frac{3}{5}}}{(M_1 + M_2)^{\frac{1}{5}}} \quad (1.3)$$

and the strain amplitude is given by [3] (this is as modelled by the Newtonian point mass approximation)

$$h \approx 2.6 \times 10^{-23} \left(\frac{\mathcal{M}}{M_{\odot}} \right)^{\frac{5}{3}} \left(\frac{f}{100 \text{ Hz}} \right)^{\frac{2}{3}} \left(\frac{100 \text{ Mpc}}{r} \right) \quad (1.4)$$

where f is the frequency of gravitational waves emitted and r is the distance from the Earth. As the signal sweeps up in frequency the time, τ , spent near a particular frequency is (also given in [3])

$$\tau = \frac{f}{\dot{f}} = 7.8 \left(\frac{M_{\odot}}{\mathcal{M}} \right)^{\frac{5}{3}} \left(\frac{100 \text{ Hz}}{f} \right)^{\frac{8}{3}} \text{ s} . \quad (1.5)$$

Using matched filters to search the detector output for a chirp signal from a coalescing binary system the detector noise can effectively be suppressed by a factor of $\sqrt{\tau}$. Although the amplitude of the signal increases with frequency, it dwells longer at lower frequencies permitting greater sensitivity to be obtained. For this reason it is desirable to obtain appropriate sensitivity of a gravitational wave detector down to frequencies ~ 10 Hz. This greatly increases the detection rate of coalescing systems.

Analysis of the waveform predicted in Equations 1.4 and 1.5 allows the distance to the source to be unambiguously determined. Thus, coalescing neutron star binary systems have the potential to determine accurately the distance scale of the universe. If such an event is recorded by several detectors sufficient information should be available to locate the source within a particular galaxy. Since the red shift of the galaxy can be measured, then Hubble's constant can be determined. This method should yield Hubble's constant to an accuracy of better than 1% [6].

The final stage of the coalescence is of particular interest. At some separation, the neutron stars will deform and begin to combine. The separation at which this occurs is dependent on the equation of state of neutron star material. The gravitational wave signal is the only means of obtaining information about this stage of neutron star binary evolution.

Recent results by Wilson and Mathews [7] suggest that some coalescence events may induce instability in the individual neutron stars while they are still significantly separated. The neutron stars could then collapse forming black holes prior to coalescence. This ought to increase the amplitude of the signal emitted. This is especially true of the final stage. There are concerns, however, that higher order corrections are, in fact, more significant and the well defined chirp signal does not simply depend upon the chirp mass but also upon the individual masses and their spins. More analysis of such systems is required to determine how accurate the Newtonian approximation is. If the discrepancy is large then the event rate of detectable binary coalescences will be decreased (because the chirp signal is not as precisely known as was thought).

Black Hole Coalescence

Binary star systems may include a black hole as one or both members. These are like neutron star systems in that they decay *via* the emission of gravitational waves resulting in a signal which is qualitatively similar. However, due to the increased gravitational field involved, the precise form of the chirp signal is difficult to simulate numerically. Analysis of such signals would provide tests of General Relativity under strong field conditions. At this level, alternative theories of gravitation could be discriminated between.

1.2.2 Monochromatic Sources

Monochromatic sources emit a single frequency which is stable with time. This allows a detector to integrate the signal over a long period. The detector strain sensitivity (expressed in $1/\sqrt{\text{Hz}}$) can then be improved by a factor of $\sqrt{\tau_{\text{int}}}$ where τ_{int} is the integration time. This assumes that the detector noise is stochastic and stationary. Furthermore, searching for a known signal frequency allows a suitable detector to operate in a narrow band mode centred on the signal; such operation may be able to obtain better sensitivity. It is also possible to verify the detection of such a source using a single detector. This is because the received signal will vary as the orientation of the detector varies relative to the source. In essence, the signal is modulated, both in amplitude and in frequency, by the rotation of the Earth and the orbit of the Earth round the Sun.

Neutron Stars

A rotating neutron star will emit gravitational waves if it is not precisely axisymmetric. This, in principle, will cause the rotational rate to decrease with time. This is observed, however the energy loss is thought to be dominated by electromagnetic interactions rather than the emission of gravitational waves. The spin down rate can be used to put an upper limit to the level of gravitational wave emission.

The ellipticity of a neutron star, ϵ , can be defined as: one minus the ratio of the equatorial semi-minor and semi-major axes. The strain amplitude of gravitational

waves observed at the Earth from an elliptical neutron star is given by [8]

$$h \approx 6 \times 10^{-21} \epsilon \left(\frac{f}{100 \text{ Hz}} \right)^2 \left(\frac{1 \text{ kpc}}{r} \right) \quad (1.6)$$

where f is the gravitational wave frequency and r is the distance from the Earth. Current theories suggest that $\epsilon \leq 10^{-3}$.

Of particular interest is the Crab pulsar. This is a particularly close object ($r \sim 2 \text{ kpc}$) and so may be detectable. The gravitational waves should have a frequency of about 60 Hz. The observed spin down rate places an upper limit on the ellipticity of 6×10^{-4} . Zimmermann suggests a value between 3×10^{-6} and 3×10^{-5} [9]. This leads to a expected strain amplitude of

$$h \approx 1 \times 10^{-26} \left(\frac{\epsilon}{1 \times 10^{-5}} \right). \quad (1.7)$$

If the signal were integrated over 10^7 s (4 months) a detector would require a strain sensitivity at 60 Hz of $\hat{h} \approx 3 \times 10^{-23} / \sqrt{\text{Hz}}$ in order to achieve a signal to noise ratio of unity (given $\epsilon = 1 \times 10^{-5}$).

1.2.3 Stochastic Sources

The possibility of a cosmic background of gravitational waves exists. It is conventional to express the strength of this source in terms of the energy of gravitational waves in a frequency band $\Delta f = f$ about a frequency f normalised to the energy density required to close the universe. This fraction is denoted by Ω_{gw} . The mean strain amplitude is then [3]

$$\hat{h} \approx 2 \times 10^{-24} \left(\frac{\Omega_{gw}}{10^{-7}} \right)^{\frac{1}{2}} \left(\frac{100 \text{ Hz}}{f} \right) / \sqrt{\text{Hz}}. \quad (1.8)$$

At frequencies of about 1 cycle per 10 years an upper limit of $\Omega_{gw} \sim 10^{-7}$ has been established by observations of millisecond pulsars [10]. It would be of interest to place a similar constraint at frequencies accessible by terrestrial detectors. This would be difficult for one detector alone. A coincidence experiment between two independent detectors is much more sensitive if long integration times are used. The gravitational wave signal is correlated between the detectors (assuming they are not separated significantly compared to the wavelength of the radiation); the

noise inherent in the detectors would not be correlated. Thus, cross-correlation over a period of time should suppress the detector noise.

1.3 Conclusion

The strain sensitivity of a viable detector should be at least $\sim 10^{-22}/\sqrt{\text{Hz}}$ for some of the frequency band 1 Hz to 10^4 Hz. For detecting neutron star coalescences, frequencies below 100 Hz are the most critical.

Information from a single gravitational wave detector is of limited use. It is impossible to distinguish impulse events in the detector environment from burst sources of gravitational waves. Neither is it possible to measure both possible polarisations of the gravitational waves. Long term recording of monochromatic sources (*e.g.* pulsars) may be possible and is probably the only reasonable mode of operation. Although the chirp signal from a coalescing binary system is very characteristic, a high signal to noise ratio would be required to make a detection credible. The event rate for these sources is very uncertain.

It is far better to utilise an array of three or four detectors: position information of a source can be obtained by comparing the arrival times at each detector; there is far less ambiguity over the validity of a result if it is recorded by two or more detectors in a consistent manner, and (assuming the detectors are sensibly aligned) both polarisations of the gravitational wave can be measured simultaneously.

Chapter 2

Gravitational Wave Detectors

2.1 Introduction

In this chapter an overview of gravitational wave detectors will be presented. A brief description of two types will be given: resonant mass detectors and laser interferometers. Resonant mass detectors couple the energy carried by a gravitational wave into their acoustic resonances. Laser interferometers measure the strain of two orthogonal arms.

This thesis is concerned with the development of low noise suspensions of the test masses in terrestrial laser interferometers. The principal sources of noise that limit the sensitivity of such detectors are introduced and quantitatively assessed. This discussion is applied to a detector with arm length ~ 1 km. In Chapter 1 it was noted that a viable detector requires a strain sensitivity of $\sim 10^{-22} / \sqrt{\text{Hz}}$. This corresponds to a displacement sensitivity of $\sim 10^{-19} \text{ m} / \sqrt{\text{Hz}}$. Since there are several noise sources, the contribution from any given source should be at least a factor of ~ 10 smaller than this. Thus, the approximate specifications for a detector will be discussed with the aim of achieving a displacement noise of $\sim 10^{-20} \text{ m} / \sqrt{\text{Hz}}$ (or less) from any one noise source. This will give a good indication of the technological challenge involved.

There are currently four projects that aim to construct large scale interferometric gravitational wave detectors of approximately this sensitivity goal. They are:

GEO 600 [11] (British-German); LIGO [12] (USA); VIRGO [13] (French-Italian) and TAMA (Japan). These are due for completion from around 2001 onwards. A discussion of some aspects of the GEO 600 project is given in Chapter 8 and, at the end of this chapter, there is a comparison of the expected sensitivity to estimates for signal strengths of gravitational waves from a variety of sources.

2.1.1 Resonant Mass Detectors

Resonant mass detectors were the first gravitational wave detectors developed (by Weber [14]). In their simplest form they are composed of a massive right circular cylinder. The longitudinal resonance of the cylinder can be thought of as two masses connected by a spring. The strain produced by a gravitational wave modulates the proper length of the mass and excites this mode. This means that the detector is most sensitive at frequencies about the resonance. Thus, such detectors are generally unsuited to detecting continuous monochromatic sources unless the resonant mode is deliberately chosen to be at the same frequency as the gravitational wave. This approach has, in fact, been used by the Tokyo group where the resonant frequency of the mass is ~ 60 Hz to match the expected emission from the Crab pulsar (see [15]).

The mass must be isolated from external sources of noise. Isolation from seismic motion and acoustic pick-up is achieved by suspending the mass in a vacuum. The main limit to sensitivity is then the Brownian motion of the atoms in the mass. Thermal excitation of the longitudinal mode generates a larger amplitude than that produced by a gravitational wave. However, it is only necessary to measure changes in the mode amplitude. The exchange of energy from atomic thermal motion to a resonant mode of the mass occurs on a time scale of order the relaxation time for that mode. Thus, to detect burst sources, a short integration time for a measurement is preferred. However, there is also noise associated with the sensing of the mode amplitude. A longer integration time would reduce the level of this noise. The optimal integration time is such that the contributions from thermal noise and sensor noise are equal. It is possible to reduce the thermal motion by reducing the temperature of the mass – to liquid helium temperatures or below.

In the absence of sensor noise, the sensitivity of a resonant mass detector to

burst sources is shown in [8] to be

$$h_b = \frac{1}{L} \left(\frac{k_B T \tau_b}{2\pi f_0 m Q} \right)^{\frac{1}{2}} \quad (2.1)$$

where τ_b is the duration of the burst; f_0 , m and Q are the resonant frequency, effective mass and Q factor of the longitudinal mode of the cylinder, and L is the length of the cylinder. For a bar of $L = 3$ m, $f_0 = 1$ kHz, $m = 1$ tonne, $Q = 10^7$ and $T = 4.2$ K the expected strain sensitivity for millisecond bursts ($\tau_b \sim 0.001$ s) is 1×10^{-20} . However, current sensors are not able to perform this well. The EXPLORER experiment reports long-term sensitivity of $\sim 8 \times 10^{-19}$ to such pulses in [16].

Recent work has tended towards a spherical mass [17] instead of a cylinder. It is then possible to obtain resonant modes at about 1 kHz but with a total mass many times that of the cylinder. This increases the coupling to the gravitational wave. In fact, there are five resonant modes of a sphere with quadrupole moments. Each mode forms an independent detector. The combined output of all modes produces information about the polarisation and orientation of the incident gravitational waves. (This assumes that a sufficient number of transducers are attached to the mass to measure their vibrations.) Spherical masses offers an interesting continuation of the development of resonant mass detectors.

2.1.2 Interferometric Gravitational Wave Detectors

In Figure 1.1 the effect of a gravitational wave on the shape of a ring of test particles is shown. The differential change of length in orthogonal directions means that a Michelson interferometer is naturally suited to the detection of gravitational waves. A Michelson interferometer is formed by a beamsplitter and two mirrors. The mirrors are attached (or coated) on to test masses. A coherent source of light is split into two beams such that each is reflected off a test masses. The beams are then recombined to form a pattern of interference fringes. A schematic diagram is shown in Figure 2.1. Differential motion of the test masses changes the interference pattern. The sensed differential displacement of the masses due to a suitably polarised gravitational wave incident normal to the plane defined by the interferometer arms

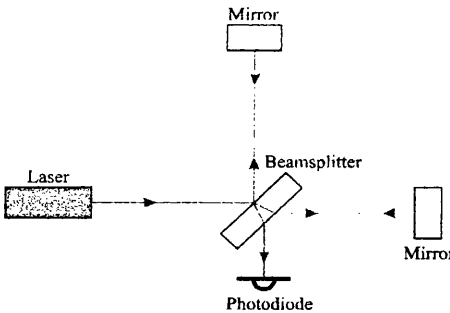


Figure 2.1: A Michelson Interferometer.

is

$$\hat{x} = L\hat{h} \left[\frac{\sin(\pi f \tau_t)}{\pi f \tau_t} \right] \quad (2.2)$$

where L is the length of each arm (defined as the distance from the beamsplitter to the test mass), τ_t is the transit time for the light to return to the beamsplitter (*i.e.* $\tau_t = 2L/c$), and f is the frequency of the gravitational wave. For waves of random polarisation and incidence the average sensitivity is reduced by a factor of $\sqrt{5}$.

The *sinc* factor in Equation 2.2 arises because the effect of the gravitational wave upon the light must be averaged over the transit time of the arms. Clearly, if the period of the gravitational wave is equal to the transit time, there is no net effect. It is also apparent from Equation 2.2 that the sensitivity of a detector increases with the length of the interferometer arms. The maximum sensitivity corresponds to an arm length of $L = \lambda_{\text{gw}}/4$ (where λ_{gw} is the wavelength of the gravitational wave). For a gravitational wave frequency of 1 kHz the detector arm length is optimised at 75 km. However, it is not practical to build an interferometer that has arms of greater than a few kilometres (except in space). Alternatively, it is possible to make the interferometer more sensitive to displacement of the test masses by making the light traverse the arm length several times before the beams are recombined. This can be achieved, for example, with delay lines or Fabry-Perot cavities in the arms. Each case requires an extra mirror in each arm located near the beamsplitter. Both of these schemes are shown in Figure 2.2.

In a delay line the laser beam is reflected several times between mirrors located at either end of the interferometer arm. The displacement sensitivity of an interfer-

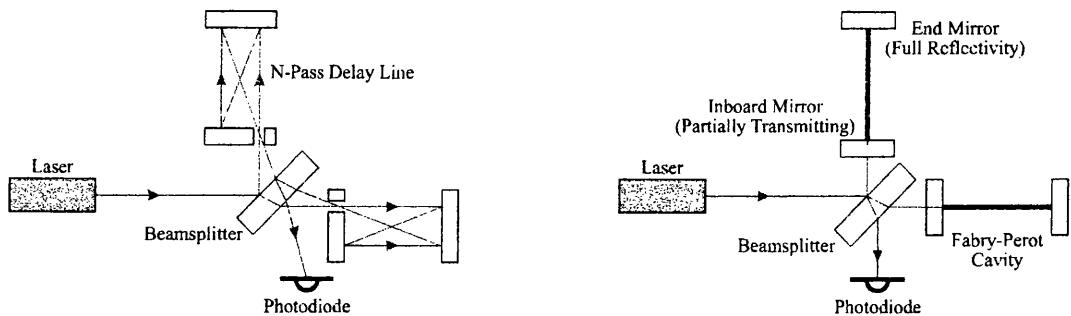


Figure 2.2: *Examples of Delay Line and Fabry-Perot Interferometers.*

ometer incorporating delay lines is increased by a factor N . (N is the number of double passes of the arm length; thus the transit time is also increased by a factor N .)

A Fabry-Perot interferometer has an optical cavity in each arm. Servo control is used to maintain the cavities on resonance with the input light. In this state the displacement sensitivity is increased by

$$N(\omega) = \frac{\mathcal{F}}{\pi} \left(\frac{1}{1 + i\omega\tau_s} \right) \quad (2.3)$$

where \mathcal{F} is the finesse and τ_s is the storage time of the Fabry-Perot cavities. The frequency dependence arises because a Fabry-Perot cavity integrates the signal over its storage time.

Displacement of a test mass produces a phase change

$$\phi = \frac{4\pi}{\lambda} N(\omega) x \quad (2.4)$$

of the interference fringe where ϕ is the phase change and λ is the wavelength of light used to illuminate the interferometer. The interference fringe is examined by a photodiode located at the output of the interferometer. It is advantageous to use servo control of one test mass to maintain a dark fringe condition at the output. This makes the interferometer less sensitive to fluctuations of the light intensity and optimises the signal-to-noise ratio when considering the shot noise on the detected light. Sensing of the interference fringe is achieved using *rf* modulation techniques at frequencies of several MHz (at these frequencies the intensity fluctuations of the laser power are shot noise limited).

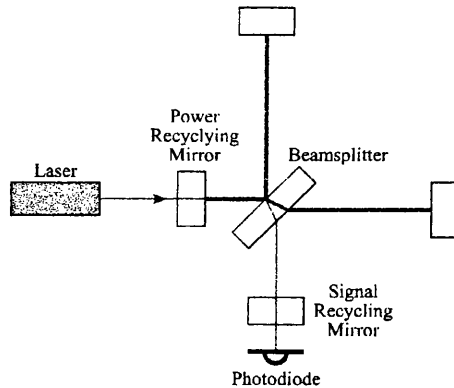


Figure 2.3: A *Dual Recycled Interferometer*.

A significant limitation to the sensitivity of an interferometric detector is the shot noise on the laser light (see Section 2.2.4). To improve the shot noise limit to sensitivity of an interferometer more complex optical configurations are possible. The addition of a mirror between the laser source and the beamsplitter is known as *power recycling* [18]. A mirror placed between the beamsplitter and the output photodetector produces *signal recycling*. When both of these are implemented together this is known as *dual recycling* [19]. Figure 2.3 shows the layout of a dual recycled Michelson interferometer. Both the power and signal recycling mirrors are partially transmitting.

Displacement of a test mass, in effect, frequency modulates the light in the interferometer arm. This imposes modulation sidebands on the carrier frequency (*i.e.* the laser frequency). When the output of the interferometer is locked to a dark fringe, light at the carrier frequency returns towards the laser. The power recycling mirror reflects this light back into the interferometer. The coupled optical system formed by the power recycling mirror and the two arms of the interferometer is analogous to a Fabry-Perot cavity (and is known as the *power recycling cavity*). Thus, resonant build up of light power is achieved in the power recycling cavity if it is maintained on resonance with the input laser light. Because more light power is stored in the interferometer, the shot noise limit to sensitivity is reduced.

If the interferometer is locked to a dark fringe for the carrier frequency this means that the signal sidebands are emitted at the output. The presence of the

signal recycling mirror makes a particular frequency of sideband resonant in the coupled cavity formed by the signal recycling mirror and the two arms (known as the *signal recycling cavity*). This gives resonant enhancement of the signal and allows the shot noise limit to displacement sensitivity to be improved at the expense of a reduction in the detector bandwidth. The quality factor of the tuned response and the frequency at which the signal is resonantly enhanced are determined by the reflectivity and the position of the signal recycling mirror respectively. The position of the signal recycling mirror must, therefore, be controlled to ensure that the centre frequency of the tuned response does not vary with time.

The interferometer is sensitive to differential displacement of the test masses along the optical beam. A random displacement of one test mass constitutes a noise source that could mask the sensitivity of the interferometer to a signal produced by gravitational waves. It is therefore necessary that the test masses have sufficiently low displacement noise. For example, they must be isolated from seismic and acoustic excitation. Section 2.2 contains a summary of the most important sources of displacement noise of the test masses. Significantly, the Earth is not a sufficiently stable environment to achieve the required displacement noise at frequencies below ~ 1 Hz. This is due to spurious changes in the local gravitational field.

2.1.3 Spaceborne Detectors

To make measurements at frequencies below ~ 1 Hz, it is necessary to locate the interferometer in space. This eliminates the problems of seismic noise and gravitational field perturbations inherent to terrestrial detectors. It also permits substantially longer arms to be used. There are, of course, significant technical difficulties involved in any space project.

LISA (Laser Interferometer Space Antenna) is such a project. It proposes the location of three spacecraft in a helio-centric orbit at a distance of 1 AU from the sun (but lagging the Earth by 20°). The spacecraft would form an equilateral triangle where the length of each side would be 5×10^9 m. The frequencies of interest to LISA are much lower than those of terrestrial detectors. They range from 10^{-4} Hz up to 10^{-1} Hz. The expected strain sensitivity of LISA should be $\sim 10^{-21} / \sqrt{\text{Hz}}$ from

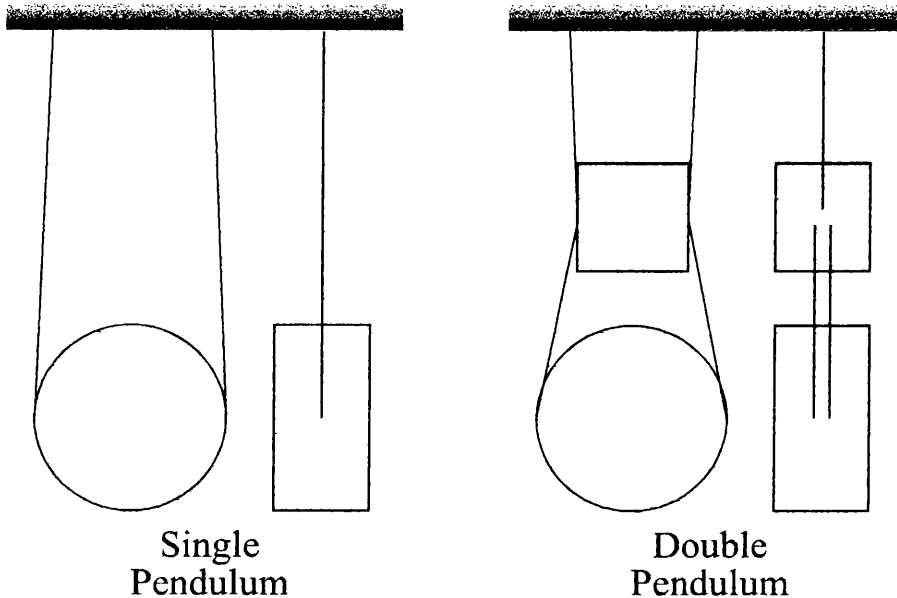


Figure 2.4: *Example Single and Double Pendulums.*

10^{-3} Hz to 10^{-2} Hz.

LISA is currently being considered by ESA and NASA. However, there is no guarantee that it will be launched. For further details of the LISA mission see [20].

2.2 Noise Sources in Terrestrial Interferometric Gravitational Wave Detectors

As is shown in Section 2.1.2, the test masses of an interferometric gravitational wave detector require to have low displacement noise. To this end they are suspended as pendulums. This affords attenuation of both seismic noise and thermal noise. In much of this thesis, a comparison is made between the properties of a single stage pendulum and a double pendulum. Examples of these are illustrated in Figure 2.4. A summary of noise sources in an interferometric detector is now given.

2.2.1 Acoustic and Seismic Noise

Acoustic pick-up by the test masses is eliminated by housing the entire test mass suspension in a moderate vacuum. A higher vacuum is, in fact, required to reduce

fluctuations of the refractive index in the residual gas in the interferometer arms. This limits the sensitivity according to [3]

$$\hat{x} = 4\beta \left(\frac{2k_B T P L}{\pi c w} \right)^{\frac{1}{2}} \quad (2.5)$$

where P is the partial pressure of the residual gas, c is the mean molecular velocity (*i.e.* $c = \sqrt{8k_B T / \pi m}$ and m is the molecular mass), w is the beam radius and β is the proportionality constant between refractive index and partial pressure of the gas. For Hydrogen, $\beta \sim 1.4 \times 10^{-9}$ but is a factor of ~ 10 greater for heavier molecules. A pressure of $\sim 10^{-8}$ mbar for H_2 and a partial pressure for all other gases a factor of 10 better is specified for the GEO 600 project.

The level of seismic motion is approximately $(10^{-7}/f^2) \text{ m}/\sqrt{\text{Hz}}$ from 1 Hz up to ~ 100 Hz in all three directions. This obviously depends on the location of the detector. Seismic motion of the ground requires to be filtered at measurement frequencies. The resonant behaviour of a pendulum system gives attenuation of ground motion above its resonant frequencies. For a single pendulum with resonant frequency f_0 the attenuation is by a factor of (f_0^2/f^2) . The transfer function for a double pendulum (above both resonances of the coupled system) was shown by Morrison [21] to be

$$\frac{x_2}{x_0} = \left(1 + \frac{m_2}{m_1} \right) \frac{f_1^2 f_2^2}{f^4} \quad (2.6)$$

where f_1 and f_2 are resonant frequencies of the individual stages considered by themselves and m_1 and m_2 are the masses of the intermediate mass and test mass respectively. This is clearly better than a single stage pendulum.

Typically, a double pendulum may have $\sqrt{f_1 f_2} \approx 1$ Hz and $m_1 \approx m_2$. This gives attenuation of seismic motion by a factor of 1.2×10^7 at 50 Hz. Further stages of filtering are required in addition to the action of the pendulum. Layers of rubber and metal can be used: these are known as *vibration isolation stacks*. They provide resonant filtering of high frequency motion in the same way as the pendulum.

The use of resonant mechanical systems to attenuate high frequency motion leads to the enhancement of seismic motion at the resonant frequencies. For this reason the modes of the systems require to have low Q factors. For stacks this can

be achieved by using lossy rubber elements; for the pendulum the modes can be damped by an electronic control servo.

2.2.2 Thermal Noise

Thermal motion of a test mass and its suspension is a limit to the displacement sensitivity of an interferometer. There are three main sources of this form of excitation:

1. pendulum modes of the suspension;
2. transverse modes of the suspension wires, and
3. internal (acoustic) modes of the test mass itself.

The power spectral density for the thermally excited displacement noise of a simple 1-degree of freedom pendulum is given by (adapted from [22])

$$\hat{x}_{\text{pend}}^2 = \frac{4k_B T \omega_0^2}{m} \frac{\phi(\omega)}{\omega^5} \quad (2.7)$$

where ω_0 is the resonant frequency of the pendulum (typically ~ 1 Hz), m is the mass of the test mass and $\phi(\omega)$ is the loss tangent of the mode (at the resonant frequency this is $(1/Q)$ but see Section 4.6.2 for a full description of $\phi(\omega)$). The loss tangent of the pendulum mode is typically 100 times less than the intrinsic loss tangent of the material used for the suspension wires. This is because most of the potential energy in the system is stored by the gravitational field and not by bending the suspension wires.

For a test mass of 10 kg and a pendulum resonance of 0.6 Hz, a loss tangent of $\sim 10^{-8}$ (at 50 Hz) is required to achieve a displacement sensitivity of 10^{-20} m/ $\sqrt{\text{Hz}}$ at 50 Hz. (If the loss tangent is assumed to be independent of frequency the pendulum mode would have a Q factor of 10^8).

Equation 2.7 also provides an estimation of thermal noise arising from a double pendulum. The dominant source of the thermal excitation comes from the lower stage pendulum itself (*i.e.* from the suspension wires) and is applied directly to the test mass. This means that the thermal noise is effectively filtered by only one resonance of the double pendulum response. Seismic noise, in contrast, is filtered

by both resonances. This is also true of thermal noise introduced at the upper pendulum stage. It is therefore critical that the final stage of the pendulum exhibits good thermal noise properties; the specification can be relaxed for the upper stage. Good thermal noise properties can be achieved by using materials which have a very small loss tangent. It follows that the pendulum resonances have a high Q factor. This would resonantly enhance, for example, seismic noise and place unnecessary demands on the dynamic range required by the output sensor. The pendulum modes, therefore, require to be actively damped.

Since the suspension wires are made from low loss materials, their transverse modes also have a high Q factor (for steel wires this is $\sim 10^5$). Thermal excitation of these modes produces peaks in the detector noise spectrum. It would therefore be impossible to make observations at a frequency close to a wire resonance. However, since the Q factor is very high, the peak is very narrow and so only affects a small frequency band.

The displacement noise caused by thermally driven vibrations of the internal modes of one test mass is approximately given by

$$\hat{x}_{\text{int}}^2 = \frac{4k_B T}{\pi^{\frac{5}{3}} \rho c^2} \frac{\phi(\omega)}{\alpha w \omega} \quad (2.8)$$

where ρ , c and $\phi(\omega)$ are the density, speed of sound and internal loss tangent of the test mass material; w is the radius of the Gaussian spot on the test mass and α represents the coupling of the internal modes to the Gaussian mode of the laser beam. A typical value of α is 0.4. The strong dependence of the level of thermal noise on the beam size was first noted by Gillespie [23].

All thermal noise issues are discussed in greater detail in Chapter 7.

2.2.3 Laser Noise

Laser light is used to perform the interferometry between the test masses of the gravitational wave detector. There are various routes by which noise can be introduced *via* the laser light. These include:

1. frequency noise on the input light;

2. intensity noise on the input light;
3. scattered light within the interferometer, and
4. laser beam geometry fluctuations.

Since the two arms of the interferometer are not precisely matched in length, frequency perturbations of the input light can limit the displacement sensitivity. This is described by

$$\hat{x} = \Delta L \frac{\hat{\nu}}{\nu} \quad (2.9)$$

where ΔL is the difference in length of the interferometer arms and ν is the frequency of the laser. Where $\nu = 2.8 \times 10^{14}$ Hz ($\lambda = 1064$ nm) and $\Delta L = 0.1$ m then the laser must be stable to $\hat{\nu} = 3 \times 10^{-5}$ Hz/ $\sqrt{\text{Hz}}$ in order to reach a displacement sensitivity of $\hat{x} = 10^{-20}$ m/ $\sqrt{\text{Hz}}$.

All currently proposed large scale detectors will use Nd:YAG solid-state lasers emitting at a wavelength of 1064 nm. The inherent frequency noise of the light emitted from a Nd:YAG laser (of a non-planar ring oscillator design) is $\sim 2 \times 10^2$ Hz/ $\sqrt{\text{Hz}}$ (between 100 Hz and 1 kHz) [24]. A loop gain of $\sim 10^7$ is required in the frequency stabilisation servo. A two stage loop is normally required. In the first loop the laser is locked to resonate in a short Fabry-Perot cavity. This stabilises the frequency enough to permit the laser to then be locked to a higher finesse reference cavity (the second loop). Usually this comprises part of the interferometer itself (*e.g.* one arm of the interferometer or the power recycling cavity).

If the output of an interferometer is at a dark fringe the interferometer is insensitive to intensity fluctuations of the light. A control servo is used to suppress motion away from the dark fringe, however, there will always be some offset, Δx , from the locking point. Intensity noise couples *via* this offset from the dark fringe position according to

$$\hat{x} = \Delta x \frac{\hat{I}}{I} \quad (2.10)$$

where I is the light intensity. A fraction of the laser power can be used as a reference for the light intensity. This allows the intensity to be stabilised to, at best, the shot noise in the reference. For a reference beam of ~ 3 mW, the intensity of the laser light

can be stabilised to 1 part in $\sim 10^7$. A discussion of how intensity stabilisation can be implemented and other sources of noise that may limit the achievable stabilisation is found in [25]. To achieve a displacement sensitivity of $\hat{x} = 10^{-20} \text{ m}/\sqrt{\text{Hz}}$ with this level of intensity stabilisation requires the *rms* displacement offset from the dark fringe to be less than $\sim 10^{-13} \text{ m}$. The displacement noise of the test masses is $\sim 10^{-6} \text{ m}$ at 1 Hz (from seismic excitation) so the control servo requires a loop gain of at least 10^7 . To achieve this loop gain with a fairly robust servo requires a unity gain bandwidth of $\sim 1 \text{ kHz}$. Chapter 6 is a discussion of this locking servo.

Light scattered within the interferometer will limit the sensitivity of a detector if such light reaches the output photodetector. A small amount of contamination by scattered light (which has an arbitrary phase) will corrupt the interference pattern at the output of the interferometer. This may mask the displacement signal of the test masses if the scattered light is modulated. Such modulation can arise *via* frequency noise on the input light (but the stability requirement above is usually good enough to prevent this) or if light is scattered from the inside of the vacuum system (this is almost certainly vibrating at acoustic frequencies). Baffles that absorb light can be placed inside the pipes housing the arms of the interferometer. This helps prevent scattered light from reaching the output photodetector.

Scattered light is a particular problem in an interferometer that uses delay lines in its arms. The two mirrors that comprise the delay line effectively form an optical cavity. Light scattered from the mirrors can then build up in high-order resonant modes of this cavity. The build up of scattered light in this manner is fatal to obtaining good sensitivity. This problem gets worse as the number of passes of the arms is increased. If only one double-pass of the arms is implemented then this problem can be avoided (as in the GEO 600 project), however, the displacement sensitivity is only increased by, at best, a factor of 2.

Changes in the pointing of the laser beam (*beam jitter*) and changes in its diameter (*beam pumping*) can limit the displacement sensitivity of an interferometer [26]. For example, angular misalignment of the beamsplitter will cause beam jitter to

mask displacement of the test masses according to [26]

$$\hat{x} = 4\alpha \hat{y} \quad (2.11)$$

where y is the lateral displacement of the laser beam at the beamsplitter and α is the angular misalignment of the beamsplitter. Servo control of the beamsplitter can reduce α to around 10^{-7} rad. This means that in order to achieve a displacement sensitivity of $\hat{x} = 10^{-20}$ m/ $\sqrt{\text{Hz}}$ the lateral beam position fluctuations must be less than $\hat{y} = 2.5 \times 10^{-14}$ m/ $\sqrt{\text{Hz}}$ at the beamsplitter. For a Nd:YAG laser the beam position fluctuations have been measured to be 2×10^{-8} m/ $\sqrt{\text{Hz}}$ (for a beam radius of 10 mm) [27]. Thus, suppression of position fluctuations by six orders of magnitude are required. The use of single mode optical fibres or resonant optical cavities (known as *modecleaners*) should provide such suppression (see Rüdiger *et al* [28] and Skeldon *et al* [26]).

2.2.4 Shot Noise

A fundamental limit to the sensitivity of an interferometer is the shot noise in the photocurrent produced at the output. The photocurrent detected at the output of the interferometer is

$$I = \frac{I_0}{2} [1 + \cos(\phi)] \quad (2.12)$$

where I_0 is the maximum photocurrent (for a bright fringe condition) and ϕ is the relative phase of the two beams on recombination. The dark fringe condition corresponds to $\phi = \pi$. It was noted above that a servo locking the interferometer to the dark fringe still permits a small offset $\Delta\phi : 2\pi \gg \Delta\phi \gg \phi_{\text{gw}}$ where ϕ_{gw} is a typical signal amplitude. The offset from the dark fringe produces residual light power on the photodiode. The shot noise in this light is given by (noting that $\cos(\pi + \Delta\phi) \approx \Delta\phi^2/2 - 1$ for small $\Delta\phi$)

$$\hat{I}_{\text{noise}} = \sqrt{2eI} = \Delta\phi \sqrt{\frac{eI_0}{2}} \quad (2.13)$$

where e is the electronic charge. The differential of Equation 2.12 gives the response at the output to a phase change between the recombined beams

$$\hat{I}_{\text{signal}} = -\frac{I_0}{2} \Delta\phi \hat{\phi} . \quad (2.14)$$

By equating the noise given in Equation 2.13 with the signal given in Equation 2.14 the shot noise limit to displacement sensitivity is (also using Equation 2.4)

$$\hat{x} = \frac{1}{N(\omega)} \frac{\lambda}{4\pi} \sqrt{\frac{2e}{I_0}}. \quad (2.15)$$

The typical conversion factor of light power to photocurrent is ≈ 0.4 A/W for a wavelength of 1064 nm. At this wavelength current technology has realised laser powers of ~ 10 W. This allows the displacement sensitivity of a simple Michelson interferometer to be

$$\hat{x} = 2.5 \times 10^{-17} \left(\frac{\lambda}{1064 \text{ nm}} \right) \left(\frac{10 \text{ W}}{P} \right)^{\frac{1}{2}} \left(\frac{0.4 \text{ A/W}}{\eta} \right)^{\frac{1}{2}} \text{ m}/\sqrt{\text{Hz}} \quad (2.16)$$

where P is the laser power and η is the conversion efficiency of the photodiode. To achieve a displacement sensitivity of $\hat{x} \sim 10^{-20}$ m/ $\sqrt{\text{Hz}}$ advanced interferometric techniques are required. These include: Fabry-Perot interferometers, power recycling and signal recycling.

The light power stored in a power recycled interferometer is increased by a factor ($\mathcal{F}_{\text{PR}}/\pi$) where \mathcal{F}_{PR} is the finesse of the power recycling cavity. The displacement sensitivity is, therefore, improved by the square root of the power enhancement. If the finesse of the power recycling cavity is $\sim 10^4$, the shot noise limit to displacement sensitivity is improved by a factor of ~ 60 . The finesse of the power recycling cavity is limited by absorption losses when the beam is transmitted through the beamsplitter (or compensation plate). In fact, absorption in the beamsplitter causes local heating and forms a thermal lens. The strength of the thermal lens increases in proportion to the incident light. This effect limits the light that can be stored in the power recycling cavity because the thermal lens becomes sufficiently strong to make the cavity non-resonant for the fundamental Gaussian mode.

Signal recycling also gives an improvement of the shot noise limit to displacement sensitivity. For a Michelson interferometer (possibly including delay lines) the signal is resonantly enhanced by a factor (adapted from [29])

$$|G_{\text{SR}}| = \frac{r_a t_s}{1 - r_a r_s} \left[1 + r_a r_s [\tau_{\text{SR}}(\omega - \omega_{\text{SR}})]^2 \right]^{-\frac{1}{2}} \quad (2.17)$$

where r_a and r_s are the amplitude reflectivities of the interferometer arm and the signal recycling mirror respectively; τ_{SR} is the storage time of the signal recycling

cavity; t_s is the amplitude transmission of the signal recycling mirror, and ω_{SR} is the frequency to which the signal recycling is tuned. (To include beamsplitter losses in Equation 2.17 see [29].) As the transmission of the signal recycling mirror is decreased the resonant enhancement of the signal sidebands is increased but the bandwidth is reduced. This allows a signal recycled interferometer to operate in broadband or narrow band modes. For mirror losses of 20 ppm, signal recycling factors of ~ 150 are possible. The reduction in the shot noise limit to sensitivity is by the signal recycling factor.

2.3 Conclusion

The detection of gravitational waves would appear possible using large scale interferometric detectors. These will require advanced interferometer configurations. GEO 600 is such an interferometer. Its estimated strain sensitivity is shown in Figure 2.5. This shows the contributions from a variety of noise sources discussed above. Shot noise and thermal noise represent fundamental limits to the performance of the instrument. It is anticipated that other noise sources can be reduced well below the total noise floor as shown (*i.e.* by at least a factor of 10). Seismic noise will, of course, dominate at low frequencies.

Figure 2.6 shows how this strain sensitivity compares with the expected signal strengths as discussed in Chapter 1. As a stand alone instrument GEO 600 may be able to detect signals from pulsars if it is possible to suppress detector noise by using a long integration time. The upper limit for the Crab pulsar is certainly within the scope of GEO 600, however, the signal is likely to be much weaker than this.

Since the signal from a supernova is by nature a burst, it will require simultaneous detection by at least two detectors to conclude that the signal is genuine. Alternatively, simultaneous optical verification may lend some support. Initial stages of other interferometers (*e.g.* LIGO and VIRGO) should reach a similar strain sensitivity to GEO 600 but with interferometer arms that are more than five times longer. GEO 600 is able to compete because it will implement a dual recycled interferometer. A network of up to four detectors should be available to do coincidence experiments.

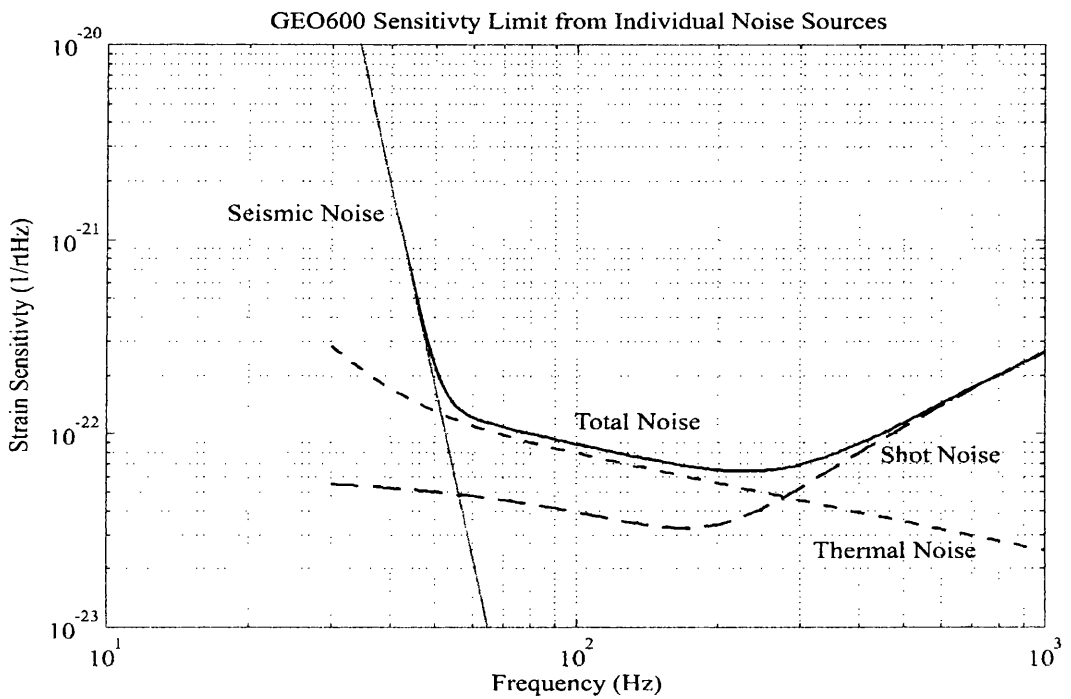


Figure 2.5: *The estimated strain sensitivity of GEO 600 is shown for broadband signal recycling (the transmission of the signal recycling mirror is taken as 0.1 giving a signal enhancement of 20). The input power was taken as 5 W and a power recycling factor of 2000 is assumed possible. The thermal noise from the internal modes is calculated assuming $\phi(\omega) = 2 \times 10^{-7}$ and structural damping.*

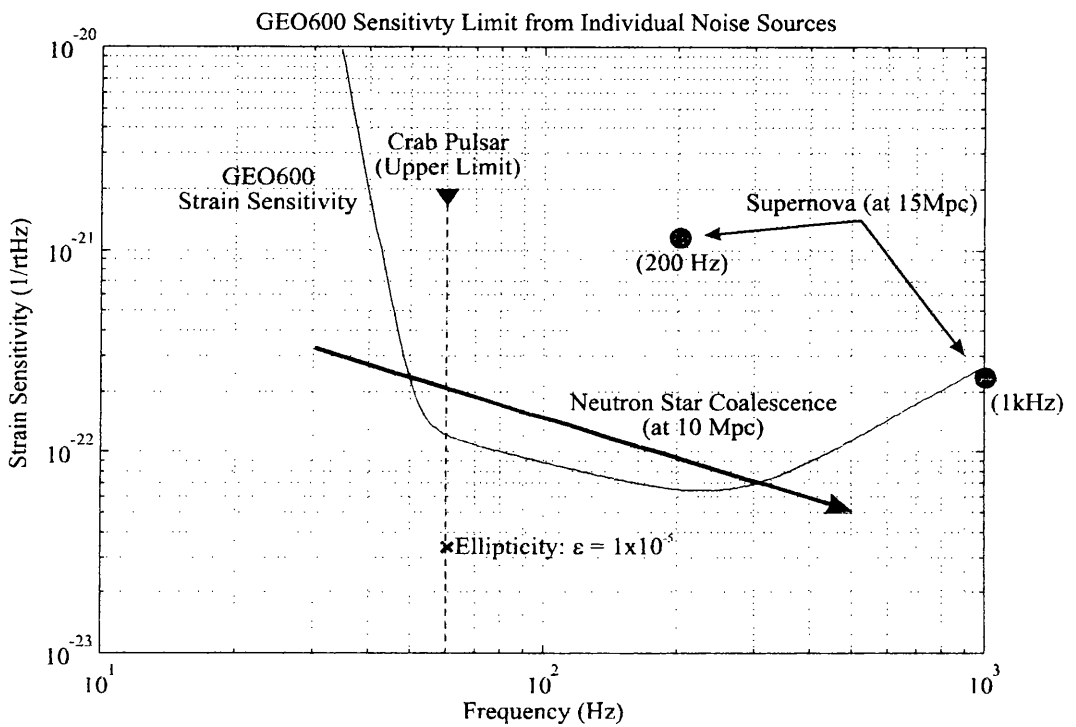


Figure 2.6: The estimates for source strengths are shown multiplied by a factor of $1/\sqrt{5}$. This accounts for the degraded signal because the alignment of the interferometer is not optimal for waves incident from all positions in the sky. The pulsar signal has been multiplied by 3×10^3 to account for an integration time of 10^7 s. The strain sensitivity of GEO 600 is shown as in Figure 2.5.

This offers a good chance of detecting gravitational waves.

The event rate for neutron star coalescence out to 10 Mpc is likely to be too low to make them a worthwhile source. Advanced designs for both LIGO and VIRGO feature even higher strain sensitivity (by a factor of ~ 10) over a larger frequency range. It is likely that this will be achieved using the advanced techniques that will be pioneered by the GEO 600 project. Advanced detectors should be able to detect coalescing binaries at a sufficient rate to record useful astrophysical information.

Chapter 3

Noise Sources in the Glasgow Prototype Detector

A Fundamental Law of Asymmetry exists and states:

‘Nothing is ever precisely symmetrical, therefore, the cross-coupling coefficients are always non-zero.’

(They are, however, permitted to be very close to zero.)

This Author.

3.1 Introduction

On the 6th March 1996, the Glasgow prototype detector [30] was run for over an hour. During this time the interferometer signal was sampled and stored on computer. In this chapter, the displacement sensitivity obtained in this experiment will be presented. From analysis of the noise floor some limiting sources of noise will be identified and this will form the justification of work to improve the sensitivity of the detector.

The Glasgow prototype uses laser interferometry in the measurement of the differential length changes of two orthogonal Fabry-Perot cavities. The Fabry-Perot cavities are formed between mirrors coated on to the surfaces of four test masses each of which is suspended as a double pendulum. The effect of a gravitational

wave is to modulate the proper distance between the test masses in the two arms. Displacement, real or apparent, of any of the test masses constitutes a noise source that limits the sensitivity of the detector to gravitational waves.

3.2 The Noise Floor of the Glasgow Prototype

The data taken during the hour-long experiment are a time record of the apparent differential arm length fluctuations. It is more instructive to view this in the frequency domain. This is achieved by a Fourier transform. Figure 3.1 shows the Fourier transform of a short stretch of the recorded data. On the assumption that the measured displacement was not caused by gravitational radiation this is the noise floor of the Glasgow prototype. The estimated levels of some individual noise sources are shown for comparison. The features marked with an ‘M’ occur at harmonics of the mains supply frequency. These are caused by pick-up in the electronics and produce either real or apparent motion of the test masses. Careful wiring can minimise these features. The single feature marked with a ‘T’ occurs at the rotational frequency of the turbo molecular pump used to keep the interferometer under vacuum. The spike is probably due to acoustic coupling through the vacuum system.

The entire recorded data were Fourier analysed by Jones [31] to produce a very detailed spectrum of the noise. This showed that below ~ 200 Hz the noise contains considerable structure; this is suggestive of mechanically generated noise (*e.g.* seismic noise or geometry fluctuations of the laser beam). At frequencies above ~ 200 Hz the noise is smooth. This may arise from either a single, dominant seismic coupling or by a combination of, for example, shot noise or thermal noise. Some features present in this range are noted in Section 3.2.4.

It was also noted by Jones [31] that the noise tended to increase during periods of lock. This is most readily explained by noise coupling through a time varying offset in the interferometer. The most obvious candidate is the *dc* offset required to lock a Fabry-Perot cavity on resonance to the input light. Thermal expansion would tend to increase the offset required with locking time. The offset is, of course, reset when the interferometer is relocked and the sensitivity should be restored. This is

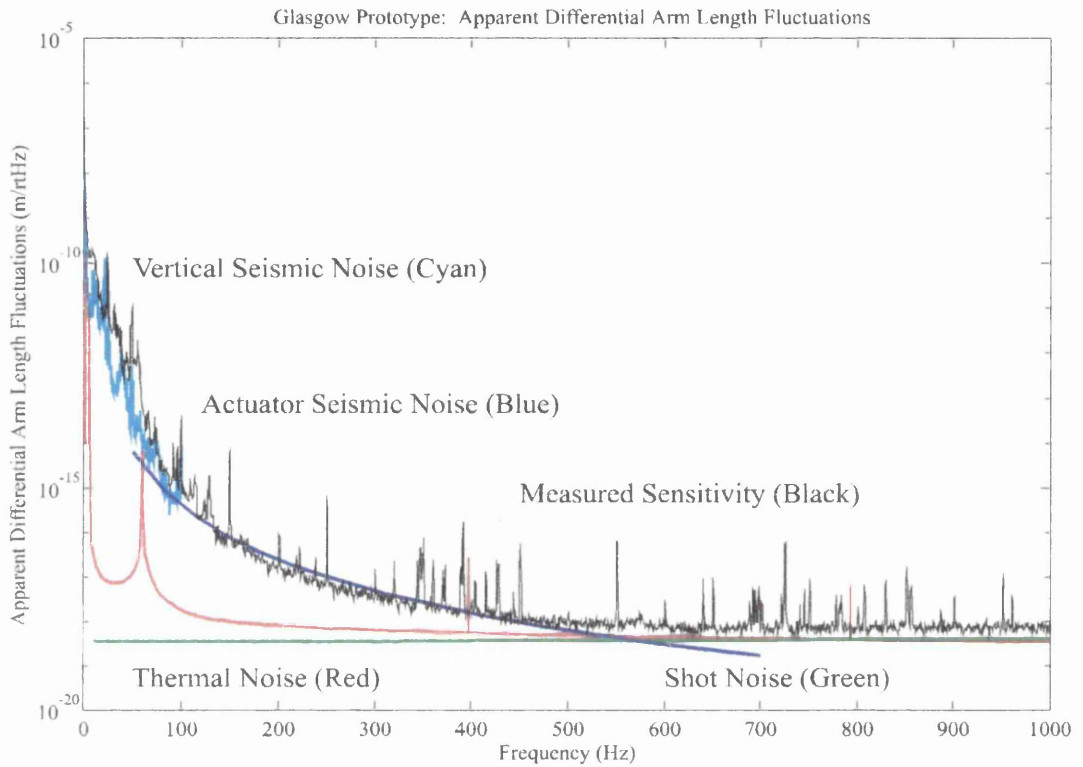


Figure 3.1: The spectral density of the displacement noise of the Glasgow prototype interferometer is shown. ‘M’ are harmonics of the mains supply. ‘T’ is the rotation frequency of the turbo molecular vacuum pump. A total of 32 peaks (16 fundamental and 16 second harmonic peaks) are present in the spectrum that are produced by the thermal motion of the transverse modes of the suspension wires. The fundamental frequencies are distributed around 400 Hz (within ± 40 Hz). A typical thermal noise peak is shown at 400 Hz and 800 Hz. The peak height is corrected because the bin-width is larger than the peak-width.

observed.

3.2.1 Fundamental Noise Limits

The shot noise limit to the displacement sensitivity of the Glasgow prototype (or similar detectors) is well understood. (For a discussion see [32] and references therein – particularly [33].) For values of cavity storage time and fringe visibility measured at the time of the data recording the shot noise limit was estimated to be $4.2 \times 10^{-19} \text{ m}/\sqrt{\text{Hz}}$ at 1 kHz. Above the Fabry-Perot cavity linewidths the shot noise increases by one power of frequency. The linewidths of the cavities were approximately 2 kHz, thus the frequency dependence is not obvious from Figure 3.1.

At frequencies above ~ 500 Hz the measured displacement sensitivity is very close to the shot noise limit but distinctly higher. For example, at 1 kHz the displacement sensitivity is $5.8 \times 10^{-19} \text{ m}/\sqrt{\text{Hz}}$; the excess noise is therefore $4.0 \times 10^{-19} \text{ m}/\sqrt{\text{Hz}}$. This could arise from thermal motion of the internal modes of the test masses. Assuming that the form of internal friction is structural damping (*i.e.* $\phi(\omega)$ is constant with frequency), the excess noise corresponds to a loss tangent of $\phi(\omega) \approx 3 \times 10^{-6}$ (see the discussion concerning Equation 2.8). Measurements of the relaxation times of the longitudinal modes of the test masses (presented in Chapter 7) indicate that the intrinsic loss tangent of these test masses is $\leq 2 \times 10^{-6}$. To conclude that the excess noise is due to thermal motion would be premature. It would be instructive to examine this noise source at frequencies below 500 Hz. This may help verify if the frequency dependence is proportional to $1/\sqrt{f}$.

3.2.2 Seismic Noise

Figure 3.2 shows the displacement noise between 50 Hz and 250 Hz. This has been reproduced from the analysis carried out by Jones in [31]. (The y -axis has been scaled to show the displacement sensitivity of the interferometer.) There are features in this frequency range that can be attributed to resonances of the double pendulum suspension. A total of eight peaks are marked for the vertical and roll modes. These are the modes in which the intermediate mass and test mass react against each

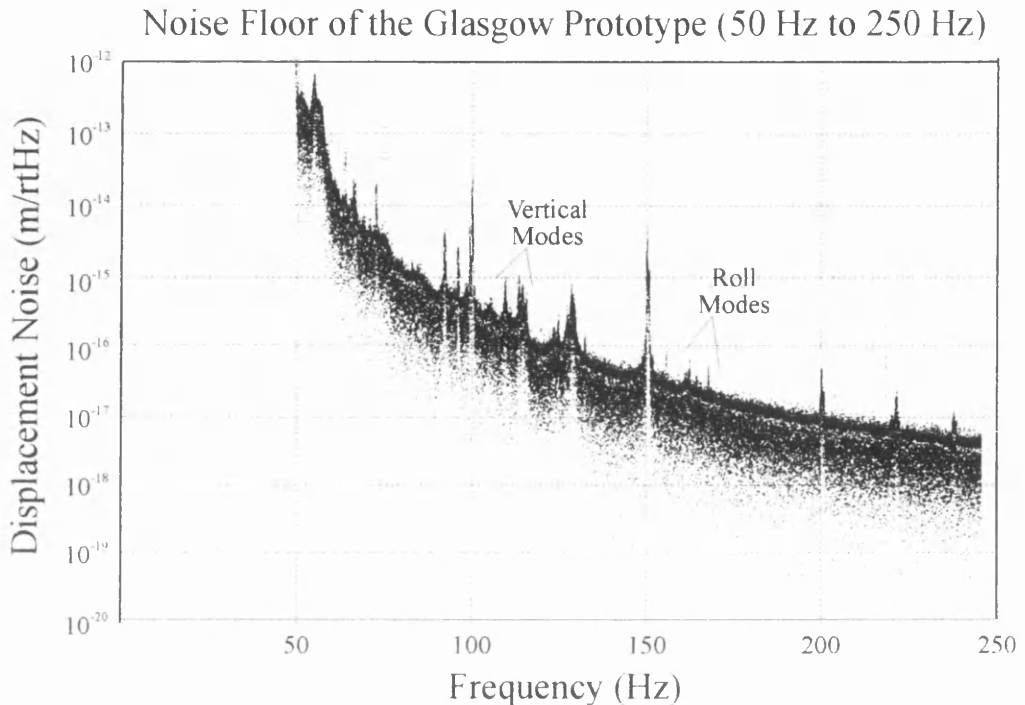


Figure 3.2: *Displacement Noise of the Glasgow Prototype (Low Frequency).*

other. It is apparent that any of the pendulum modes – not just the longitudinal modes – can couple to the sensed displacement of the test mass. Other features are present in the spectrum. It is probable that these arise from mechanical resonances in the vacuum system that houses the interferometer.

Longitudinal motion of the test mass is, of course, directly sensed by the interferometer. Motion in other degrees of freedom is also sensed but less directly. Sideways motion of the test mass is roughly the same as longitudinal motion but, because it does not couple directly, it cannot be the dominant noise source.

Tilt and rotation of the test mass couple if the laser spot is offset from the centre of the test mass face. Rotational motion is not strongly coupled to any other degree of freedom so the spot is optimally positioned with no lateral offset. Tilt motion, on the other hand, is strongly coupled to the longitudinal degree of freedom. The optimal position of the spot is not necessarily at the face centre. It will vary in height depending on the strength of coupling. This varies for different designs of

pendulum.

Vertical motion of the suspension point can couple to sensed displacement in several ways. A cross-coupling factor, C_V , can be used to describe the fraction of vertical motion of the test mass that also appears as longitudinal motion (real or apparent).

If, when the side projection of the test mass suspension is considered, there are two wires visible (one to the front of the mass and one to the back), a difference in the spring constants of these wires couples vertical motion of the test mass to tilt. Thus, an offset in the spot height on the mirror face allows the cross-coupling of vertical seismic noise. This was analysed by M^cLaren [34] who gave the cross-coupling factor as

$$C_V = \frac{mVd}{I_y} \frac{\delta k}{k} \quad (3.1)$$

where m and I_y are the mass and tilt moment of inertia of the test mass; V is the spot height with respect to the centre of mass; d is the separation of the wires, and $(\delta k/k)$ is the fractional difference of the wire spring constants. For the pendulums used in the Glasgow prototype the suspension wires are equal in length to within a few millimetres. This matches the wire spring constants to $\sim 1\%$. Taking V as 1 mm gives $C_V = 3 \times 10^{-4}$.

Coupling of vertical seismic noise is also possible if the optical beam is not perpendicular to the gravitational field. This arises when the absolute heights of the masses are different at either end of the cavity. To align the cavity the masses must be tilted with respect to the gravitational field. A static tilt of the test mass gives a cross-coupling factor of

$$C_V = \frac{\Delta z}{L} \quad (3.2)$$

where Δz is the height separation and L the length of the cavity. For the prototype the vertical height difference may be up to 5 mm. This gives a cross-coupling factor of $C_V \leq 5 \times 10^{-4}$.

A similar effect occurs because the gravitational field is not parallel at both ends of the cavity. This is unavoidable because the Earth is round and the gravitational

field spreads in a radial direction. This gives a cross-coupling factor of

$$C_V = \frac{L}{2R_E} \quad (3.3)$$

where R_E is the radius of the Earth and L the length of the cavity. Over the 10 m arms of the Glasgow prototype this effect is small, however, it becomes significant for gravitational wave detectors with longer arms (*e.g.* a few kilometres).

If a static force is applied to the test mass it will be offset from its equilibrium position. In this case, vertical motion of the suspension point produces real longitudinal displacement of the test mass attenuated by the passive filtering afforded by the vertical resonances of the pendulum. The cross-coupling factor is

$$C_V = \frac{\Delta x}{l} \quad (3.4)$$

where l is the length of the pendulum (for a double pendulum this is approximately the length of the second stage) and Δx is the offset from equilibrium. An offset from equilibrium position is required to lock the Fabry-Perot cavity on resonance to the input light. A typical offset will be a few cavity fringes. However, thermal expansion of the arms will give a time dependent offset up to the maximum range of the feedback actuator. If this is exceeded the servo will lose lock. The importance of this coupling mechanism can be reduced by applying *dc* feedback to the cavity length at the intermediate mass of the pendulum. The Glasgow prototype has an actuator range of 20 μm ; this gives a maximum coupling factor of $C_V = 1 \times 10^{-4}$.

In order to measure the level of cross-coupling for the pendulums in the Glasgow prototype, the level of seismic motion of the top plate at the upper vertical resonance of the double pendulum (at 110 Hz) was estimated by extrapolation from measurements made up to 100 Hz. The vertical motion of the test mass was inferred from this estimate by a knowledge of the transfer function of the double pendulum. The cross-coupling factor was then deduced from the observed displacement noise at the resonant frequency. The value obtained for C_V was between 3×10^{-4} and 1.5×10^{-3} . This value is consistent with the estimates given by the cross-coupling mechanisms described above. The vertical seismic noise shown in Figure 3.1 was calculated using $C_V = 1 \times 10^{-3}$.

Roll about the optic axis can cross-couple to the sensed displacement of the test mass because there are asymmetries in the pendulum construction. It is difficult to estimate the level of this coupling but it is not thought to be strong. However, roll motion is readily excited by tilting of the top plate.

3.2.3 Seismic Coupling *via* the Actuator Coils

When the expected levels of shot noise and thermal noise are subtracted from the spectrum the excess noise between 200 Hz and 500 Hz is $3.6 \times 10^{-18} \text{ m}/\sqrt{\text{Hz}}$ at 300 Hz with a frequency dependence roughly proportional to $1/f^4$ (the power may vary by ± 0.5).

In Section 6.3.2 the coupling of vertical motion of the feedback coils used to control the position of the test mass is shown to be

$$\hat{x} \approx 50 \times \Delta x \hat{z}_c \quad (3.5)$$

where Δx is the *dc* offset of the test mass from the equilibrium point of the pendulum and z_c is the vertical displacement of the feedback coils. A conservative estimate for z_c is possible assuming that seismic motion of the ground obeys $(10^{-7}/f^2) \text{ m}/\sqrt{\text{Hz}}$. The block in which the feedback coils were mounted was isolated from the ground by four pieces of rubber. This gives attenuation of ground motion above its vertical resonance (at ≈ 20 Hz) with an ideal frequency dependence of f^2 . When this attenuation is combined with the natural $1/f^2$ dependence of seismic motion, the frequency dependence of vertical seismic motion of the feedback coils can be $1/f^4$. Using these assumptions gives $z_c \sim 5 \times 10^{-15} \text{ m}/\sqrt{\text{Hz}}$ at 300 Hz. The estimated displacement noise due to coupling of vertical seismic motion of the feedback coils is shown in Figure 3.1 for a value of $\Delta x = 20 \mu\text{m}$.

The value of Δx typically varies with the locking time from $\sim 2 \mu\text{m}$ to $20 \mu\text{m}$. This provides an explanation of why the noise floor of the detector changes over the locking time. However, the level of coupled seismic noise would be less than is shown in Figure 3.1. There are two reasons why the coupled noise may be under-estimated:-

1. The isolation of the feedback coils' mounting block is not ideal. The isolation afforded by the rubber pieces will be short-circuited *via* the electrical connec-

tions to the feedback coils. The attenuation could be proportional to $1/f^{\frac{3}{2}}$ and the frequency dependence of the excess noise would still be compatible with observation. Such non-ideal performance would increase the apparent noise by a factor of 4.

2. The seismic motion of the detector environment may be greater than that assumed. This may arise either because the absolute level is higher or the frequency dependence generally observed below 100 Hz does not continue to higher frequency.

3.2.4 Other Noise Sources

There are a number of narrow band features in the spectrum. In addition to harmonics of the mains frequency and a single feature due to the turbo pump, there are peaks that correspond to the transverse modes of the suspension wires. 16 of these occur at the fundamental frequency and 16 at the second harmonic. In all cases the second harmonic is a factor of 2 higher in frequency than the fundamental.

A broad bulge (~ 20 Hz wide) is observed around 575 Hz. The origin of this is unknown.

Three very narrow peaks are observed in the displacement sensitivity. These occur at frequencies of approximately 480 Hz, 660 Hz and 675 Hz. It is unlikely that these are monochromatic gravitational wave signals but are instead probably due to pick-up that is synchronous to the data sampling clock.

3.3 Conclusion

At frequencies between 500 Hz and 1 kHz (and possibly above) estimated levels of shot noise and thermal noise are sufficient to explain the background noise floor of the detector.

The cross-coupling factor of vertical motion of the test mass to sensed displacement is approximately 0.001. At this level of cross-coupling, vertical seismic noise limits the displacement sensitivity of the Glasgow prototype at frequencies around 100 Hz.

The problem of cross-coupling leads to the following criteria on normal mode frequencies for a pendulum suspension. They are:-

1. At normal mode frequencies, seismic motion is enhanced by the Q factor of the mode. The Q factors of the pendulum modes should be high and cross-coupled seismic motion will almost certainly dominate the displacement noise spectrum and thus prevent sensitivity to gravitational waves at these frequencies. The normal mode frequencies of the suspension should therefore be chosen, where possible, to lie outside the desired detection band of gravitational waves.
2. It is desirable to specify that cross-coupled seismic noise does not exceed the longitudinal motion - at least at frequencies other than normal modes of the suspension. The most significant cross-coupling arises from vertical motion of the suspension point. If the seismic excitation of the suspension point of a pendulum is equal for longitudinal and vertical degrees of freedom then the following constraint applies

$$\prod_{n=1}^N f_{Vn} < \frac{1}{\sqrt{C_V}} \prod_{n=1}^N f_{Ln} \quad (3.6)$$

where N is the number of pendulum stages; f_{Vn} and f_{Ln} are the normal mode frequencies of the pendulum for the vertical and horizontal degrees of freedom respectively, and C_V is the cross-coupling factor. (This result comes directly from the transfer function of a resonant system and assumes that the ground motion imposes a fixed displacement disturbance at the suspension point of the pendulum.)

It is the assertion of this author that a pendulum design should be avoided that has normal mode frequencies within the detection band of interest to gravitational waves. Further, all normal mode frequencies are preferred as low as possible. This ensures that seismic motion is attenuated by the passive response of the pendulum by the maximum possible factor. To implement such a design strategy necessitates a complete model of the double pendulum in all degrees of freedom.

Chapter 4

Model of Test Mass Suspension

‘Every body continues in its state of rest, or of uniform motion in a straight line, unless it is acted upon by a force.’

Isaac Newton, *Philosophiæ Naturalis Principia Mathematica*.

4.1 Introduction

The suspensions used in terrestrial interferometric gravitational wave detectors require to be carefully designed. Regard must be made to:

1. the isolation of seismic noise;
2. the level of thermal noise present;
3. active damping of the normal modes, and
4. active control of the test mass position.

To facilitate the design of a pendulum, its performance should be modelled. Because cross-coupling effects cannot be ignored, the pendulum model must consider all degrees of freedom. In particular, the model should allow the normal mode frequencies and the dynamic response of the system to be calculated. Therefore, the equations of motion

$$\mathbf{M}\ddot{\mathbf{X}} = \mathbf{K}\mathbf{X} \tag{4.1}$$

must be obtained and solved. (\mathbf{M} is the mass-inertia tensor and \mathbf{K} is the spring matrix.)

4.2 Choice of Coordinates

The simplest choice of coordinates is to use three orthogonal translation coordinates and three rotation coordinates denoting rotation about the centre of mass associated with each translation axis. This choice of coordinates diagonalises the mass-inertia tensor. The matrix elements are simply the suspended mass for the translation coordinates and the moments of inertia for the rotational coordinates.

The coordinates are defined as

- x_μ longitudinal translation along the optic axis,
- y_μ sideways translation transverse to the optic axis,
- z_μ vertical translation,
- θ_μ tilt about the y -axis,
- ϕ_μ rotation about the vertical axis,
- ψ_μ roll about the optic axis.

Notation:

$$x \in \{x_\mu, y_\mu, z_\mu, \theta_\mu, \phi_\mu, \psi_\mu\}$$

Note that it is the vertical direction that defines the orientation of the coordinate axes and *not* the alignment of the laser beam. Thus, it may be the case that there is a (small) elevation angle between the x -axis and the optic axis. In Section 3.2.2 this is shown to give rise to cross-coupling of vertical motion into sensed displacement of the test mass.

The lower index, μ , refers to the pendulum stage. It shall be numbered from the top downwards. Thus $\mu = 0$ is the top plate from which the pendulum is suspended and $\mu = 1$ is the first pendulum mass and so on. The static equilibrium position is taken to be the origin so that each coordinate represents a small displacement.

Normally, a subset of the coordinates can be considered independently. For example, vertical motion can be considered independently but longitudinal and tilt

motion are strongly coupled. Using this strategy the complete description of the test mass suspension is greatly simplified.

4.3 Restoring Forces

The pendulum suspension has been modelled by considering only the restoring forces that are produced by distortions in the suspension wires and by gravity. The mass at each stage is assumed to be rigid with the connecting wires acting as linear springs. The linear approximation is valid when the coordinate displacements are much less than the lengths of the suspension wires. This is always the case in subsequent analysis. The top plate from which the suspension is hung is assumed to have a much greater mass than the pendulum masses. This means that it does not couple significantly to the pendulum dynamics and is not considered.

The spring matrix, \mathbf{K} , is obtained by considering how a small change in one coordinate perturbs each spring with respect to extension, torsion, bending and with respect to the gravitational potential. The action of the restoring force upon all the coordinates is then calculated. In the following sections, the magnitude of each spring mechanism is discussed and then an example of the method is given for longitudinal and tilt coordinates of a single pendulum.

4.3.1 Extension of a Wire

When the tension of the suspension wire is significantly less than the breaking load then the wire obeys Hooke's law and acts as a linear spring

$$T = -k \Delta l \tag{4.2}$$

where Δl is the extension of the wire and T is the wire tension. The value of the spring constant k can be deduced from the material properties of the wire. For a wire of circular cross-section the spring constant is

$$k = \frac{Y \pi r^2}{l} \tag{4.3}$$

where Y is the Young's modulus; r is the radius of the wire, and l the total length.

The tension in the wire is deduced by equating its vertical component with the weight of all masses suspended by it. If there is more than one wire suspending a mass then the load is assumed to be equally distributed between the wires.

The maximum allowed load on a wire can be determined from the breaking stress of the wire material. Stress in the wire is defined as

$$\text{Stress} = \frac{\text{Tension}}{\text{Area of Cross-Section}} \quad (4.4)$$

and so has units of pressure. The breaking stress is a material property and represents the maximum extension possible before the wire breaks. For practical reasons the stress in the suspension wire should be significantly less than the breaking stress: a safety factor of three is considered to be adequate. This maintains the wire in the linear regime where Hooke's law applies.

4.3.2 Torsion of a Wire

The model will assume that the suspension wires are rigidly fixed at each end and are not free to twist at their attachment point. A differential rotation can be produced in the wire by rotating the stages of the pendulum with respect to each other. The restoring torque for a differential rotation, $\Delta\gamma$, is given by

$$\Gamma = -\kappa \Delta\gamma . \quad (4.5)$$

The torsional spring constant for a circular wire is dependent on the material properties

$$\kappa = \frac{\pi r^4 Y}{4l(\nu + 1)} \quad (4.6)$$

where ν is Poisson's ratio; Y , r and l are as previously defined.

4.3.3 Bending of a Wire

A wire can be considered as a stiff beam under tension such that it satisfies the 4th order differential equation [35]

$$T \frac{\partial^2 x}{\partial z^2} - YI \frac{\partial^4 x}{\partial z^4} = \rho S \frac{\partial^2 x}{\partial t^2} \quad (4.7)$$

where T is the the wire tension; I is the cross-sectional moment; ρ is the density; S is the cross-sectional area; x is the transverse displacement, and z is the position along the wire. (For a wire with circular cross-section $I = \pi r^4/4$.)

It is shown in Appendix B that the energy stored in deforming the wire is given by

$$E = \frac{b}{4} \left[2X^2 + (\alpha^2 + \beta^2) (2\lambda^2 - 2\lambda l + l^2) - 2lX(\alpha + \beta) + 4\alpha\beta\lambda(l - \lambda) \right] \quad (4.8)$$

where the values X , α and β are defined in Figure 4.1. X is the produced when the ends of the wire are displaced horizontally with respect to each other. α and β are produced when the clamping points are tilted. When the upper stage of a double pendulum (or a single pendulum) is considered, α is taken to be zero since the top plate is not allowed to tilt. The constants λ and b are defined to be

$$\lambda = \sqrt{\frac{YI}{T}} \quad (4.9)$$

$$b = \frac{\sqrt{YIT}}{l^2} . \quad (4.10)$$

The generalised restoring force on each coordinate is given by

$$F_x = -\frac{\partial E}{\partial x} . \quad (4.11)$$

4.3.4 Example of Model

The equations of motion for the longitudinal and tilt degrees of freedom (*i.e.* x_1 and θ_1) are obtained for a single pendulum. Figure 4.2 shows this pendulum.

The wire tension produces a force which acts along the length of the wire. When the mass is displaced horizontally the wire is no longer absolutely vertical so there is a component of the tension which acts horizontally as a restoring force. Thus,

$$F_{x_1} = -T \sin(\epsilon) \quad (4.12)$$

and to first order approximation

$$F_{x_1} \approx -\left[\frac{T}{l_1}\right] x_1 + \left[\frac{Tt}{l_1}\right] \theta_1 . \quad (4.13)$$

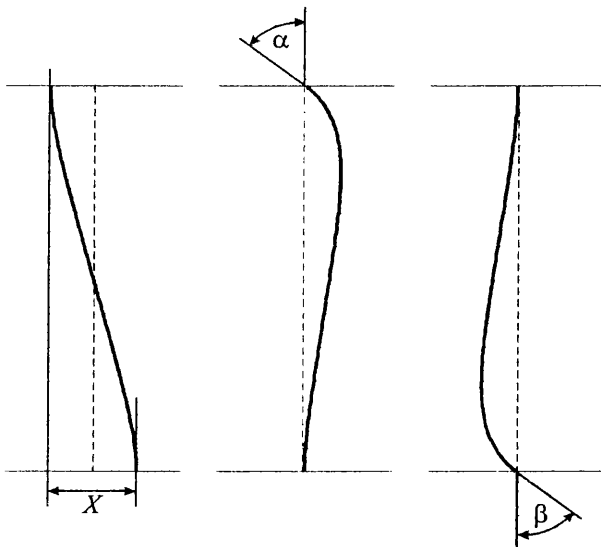


Figure 4.1: *Bending and Flexing of a Stiff Beam under Tension.*

Because the mass is suspended a distance t above the centre of mass, there is a couple into the tilt of the mass

$$\Gamma_{\theta_1} = Tt \sin(\epsilon - \theta_1) \quad (4.14)$$

and again to first order

$$\Gamma_{\theta_1} \approx \left[\frac{Tt}{l_1} \right] x_1 - \left[Tt \left(1 + \frac{t}{l_1} \right) \right] \theta_1 . \quad (4.15)$$

It is apparent that the suspension wire bends as the mass is displaced from its equilibrium position. From the definitions given in Figure 4.1 we can identify the bending parameters as

$$X = x_1 - t\theta_1 \quad (4.16)$$

$$\alpha = 0 \quad (4.17)$$

$$\beta = \theta_1 . \quad (4.18)$$

Thus the restoring force and torque from bending the wire is given by

$$F_{x_1} = -b_1 x_1 + b_1 \left[t + \frac{l_1}{2} \right] \theta_1 \quad (4.19)$$

$$\Gamma_{\theta_1} = b_1 \left[t + \frac{l_1}{2} \right] x_1 - b_1 \left[\frac{l_1^2}{2} + tl_1 + t^2 - \lambda_1 l_1 + \lambda_1^2 \right] \theta_1 . \quad (4.20)$$

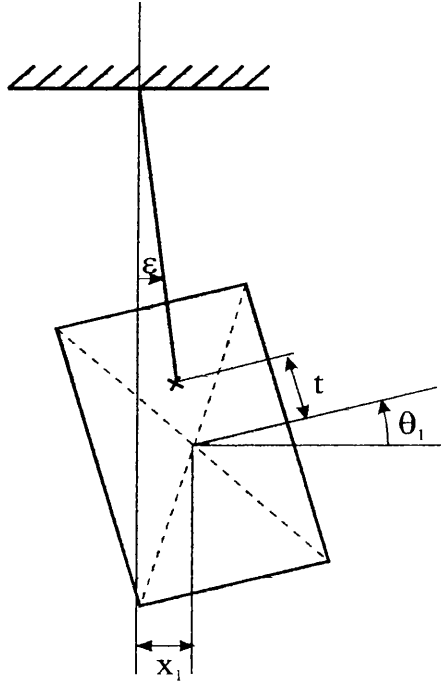


Figure 4.2: *Longitudinal and Tilt Degrees of Freedom for Single Pendulum.*

The restoring forces have been deduced as a function of the coordinates of the suspended mass. Thus, the equations of motion are now determined for the two degrees of freedom considered. In matrix notation this can be written

$$\underbrace{\begin{bmatrix} m_1 & 0 \\ 0 & I_{1y} \end{bmatrix}}_{\mathbf{M}} \underbrace{\begin{bmatrix} \ddot{x}_1 \\ \ddot{\theta}_1 \end{bmatrix}}_{\ddot{\mathbf{X}}} = \underbrace{\begin{bmatrix} k_{x_1 x_1} & k_{x_1 \theta_1} \\ k_{\theta_1 x_1} & k_{\theta_1 \theta_1} \end{bmatrix}}_{\mathbf{K}} \underbrace{\begin{bmatrix} x_1 \\ \theta_1 \end{bmatrix}}_{\mathbf{X}}. \quad (4.21)$$

The entries in the spring matrix, \mathbf{K} , are the coefficients of the coordinates in the expressions for restoring force. For example: $F_{x_1} = k_{x_1 x_1} x_1 + k_{x_1 \theta_1} \theta_1$. Because all the restoring forces are independent of each other, these factors are all summed.

4.4 Normal Modes of the Test Mass Suspension

Because there are six degrees of freedom per suspended mass, there will be six normal modes per mass. For example, a double pendulum will have precisely twelve normal modes. It is desirable to calculate the frequency of each normal mode of the test

mass suspension.

4.4.1 Eigenvalue and Eigenvector Extraction

A linear system is assumed. It follows that the system executes simple harmonic motion, *i.e.*

$$\mathbf{X}(t) = \mathbf{X}_0 e^{-i\omega t} \quad (4.22)$$

and, by differentiating,

$$\ddot{\mathbf{X}} = -\omega^2 \mathbf{X} \quad (4.23)$$

such that the equations of motion can be simplified to

$$\mathbf{KX} = -\omega^2 \mathbf{MX} \quad (4.24)$$

which is the generalised eigenvalue problem. Modified versions (to handle complex matrices) of the EISPACK routines for the QZ algorithm [36] were used to extract numerically the generalised eigenvalues and generalised right eigenvectors. The eigenvalues yield the normal mode frequencies; the eigenvectors yield the relative translation or rotation of each degree of freedom associated with the mode. The routine `dp2ss.m` in Appendix A performs this analysis.

4.5 State-space Modelling

When considering the dynamic response of multiple input and output systems the most appropriate method to use is state-space modelling. This technique uses four matrices labelled **A**, **B**, **C** and **D** to describe a linear time invariant system. These are defined by the following system of equations

$$\dot{\mathbf{x}} = \mathbf{Ax} + \mathbf{Bu} \quad (4.25)$$

$$\mathbf{y} = \mathbf{Cx} + \mathbf{Du} \quad (4.26)$$

where \mathbf{x} is a column vector of the system *states* and \mathbf{y} is a column vector containing the outputs of the system.

Let s be the number of states of the system: m the number of inputs, and n the number of outputs. Then **A** is an $s \times s$ matrix; **B** is an $s \times m$ matrix with each

column representing a different input to the system; \mathbf{C} is an $n \times s$ matrix with each row representing an output, and \mathbf{D} is an $m \times n$ matrix. \mathbf{u} is a column vector and has n elements all equal to one.

It is convenient to use the coordinates and their derivatives with time as the states of the system. Thus, the example of the single pendulum can be expressed

$$\begin{array}{c} \dot{\mathbf{x}} \\ \left[\begin{array}{c} \dot{x}_1 \\ \dot{\theta}_1 \\ \ddot{x}_1 \\ \ddot{\theta}_1 \end{array} \right] \end{array} = \begin{array}{c} \mathbf{A} \\ \left[\begin{array}{cccc} 0 & 0 & 1 & 0 \\ 0 & 0 & 0 & 1 \\ \mathbf{M}^{-1}\mathbf{K} & & 0 & 0 \\ & & 0 & 0 \end{array} \right] \end{array} \begin{array}{c} \mathbf{x} \\ \left[\begin{array}{c} x_1 \\ \theta_1 \\ \dot{x}_1 \\ \dot{\theta}_1 \end{array} \right] \end{array} . \quad (4.27)$$

Since the \mathbf{M} matrix is diagonal then its inverse exists and has elements equal to the reciprocal of mass and of the moments of inertia.

Normally, the inputs to the system are forces such as those produced by the action of a current carrying coil upon a magnet attached to the mass. A force input produces a change in $\ddot{q} = F_q/m_q$. So in the single pendulum example the \mathbf{B} matrix for a force applied along the x -axis would be

$$\begin{array}{c} \dot{\mathbf{x}} \\ \left[\begin{array}{c} \dot{x}_1 \\ \dot{\theta}_1 \\ \ddot{x}_1 \\ \ddot{\theta}_1 \end{array} \right] \end{array} = \begin{array}{c} \mathbf{B} \\ \left[\begin{array}{c} 0 \\ 0 \\ \frac{F_{x1}}{m_1} \\ 0 \end{array} \right] \end{array} \begin{array}{c} \mathbf{u} \\ [1] \end{array} . \quad (4.28)$$

The outputs are usually displacements as measured by a shadow sensor or by the interferometry used to detect motion of the test mass. The \mathbf{C} matrix is, therefore, simple. For a sensor detecting motion along the x -axis of the single pendulum the \mathbf{C} matrix is

$$\begin{array}{c} \mathbf{y} \\ [y] \end{array} = \begin{array}{c} \mathbf{C} \\ \left[\begin{array}{cccc} 1 & 0 & 0 & 0 \end{array} \right] \end{array} \begin{array}{c} \mathbf{x} \\ \left[\begin{array}{c} x_1 \\ \theta_1 \\ \dot{x}_1 \\ \dot{\theta}_1 \end{array} \right] \end{array} . \quad (4.29)$$

The \mathbf{D} matrix allows straight through connection of an input to the output. For the pendulum this is not required. Therefore, the \mathbf{D} matrix has all elements equal to zero.

It is possible to calculate numerically transfer functions between inputs and outputs of the state-space system. To reduce the computational load, the Hessenberg algorithm [37] was used. This involves identically transforming the state-space matrices such that \mathbf{A} is transformed to upper Hessenberg form. The frequency response is then obtained by solving the system

$$G(\omega) = \mathbf{C}(i\omega\mathbf{I} - \mathbf{A})^{-1}\mathbf{B} + \mathbf{D} \quad (4.30)$$

at a range of frequency points where the state-space matrices are, in fact, the transformed matrices. The frequency response is useful for evaluating how well, for example, the system isolates seismic noise.

4.6 Frictional Losses in the Suspension Wires

Clearly, there are frictional losses in distorting the suspension wires. This damps the motion of the pendulum and a Q factor for the mechanical resonances can be defined. In Chapter 7, the implications for thermal noise arising from the frictional losses will be discussed. A resonance peak could also affect the stability of servo systems involving the pendulum. The system would then oscillate which would be most undesirable. Servo systems involving the pendulums are considered in Chapters 5 and 6. It is, therefore, important to know how damped all the normal modes are.

4.6.1 Viscous Damping

When the frictional losses in the system are proportional to velocity this is known as *viscous damping*. Such a resonant mechanical system can be described by the equation

$$F_q = m\ddot{q} + c\dot{q} + kq \quad (4.31)$$

where F_q is the input driving force and c is the coefficient of friction. If F_q varies harmonically (*i.e.* $F_q = F_0 e^{-i\omega t}$) then q also varies harmonically. This can be written

$$q = q_0 e^{-i\omega t} \quad (4.32)$$

$$\dot{q} = -i\omega q_0 e^{-i\omega t} \quad (4.33)$$

$$\ddot{q} = -\omega^2 q_0 e^{-i\omega t} \quad (4.34)$$

The response to the input force is given by

$$\frac{q_0}{F_0} = \frac{1}{k - m\omega^2 + ic\omega} . \quad (4.35)$$

It is apparent that on resonance (when $\omega^2 = k/m$) the peak response is limited by the friction. In fact, the Q factor of the resonance is

$$Q = \frac{\omega_0 m}{c} \quad (4.36)$$

where ω_0 is the resonant frequency.

4.6.2 Complex Spring Damping

The friction produced in a spring can be characterised by adding a small complex part to the Young's Modulus: $Y_{\text{complex}} = Y[1 + i\phi(\omega)]$. The equation for such a damped resonator is

$$F_q = m\ddot{q} + k[1 + i\phi(\omega)]q . \quad (4.37)$$

The loss tangent, $\phi(\omega)$, can be any odd function of frequency. It represents a phase lag between the applied force and the response of the spring. The response is given by

$$\frac{q_0}{F_0} = \frac{1}{k - m\omega^2 + ik\phi(\omega)} . \quad (4.38)$$

This can be compared to the case for viscous damping – noting that for $\phi(\omega) \propto \omega$ they are identical.

$\phi(\omega)$ may be constant over a range of frequencies (but not all the way to zero frequency); this is known as *structural damping*. The Q factor for this model is given by

$$Q = \frac{1}{\phi(\omega_0)} . \quad (4.39)$$

4.6.3 Damping of Normal Modes

Structural damping is easily applied to the spring matrix, \mathbf{K} , by adding a complex term to k , κ , and b . The eigenvalue extraction is still possible, however, the eigenvalues will now be complex. The harmonic motion of a coordinate is then

$$q(t) = q_0 e^{-i(\omega+i\sigma)t} \quad (4.40)$$

$$= q_0 e^{-i\omega t} e^{\sigma t} . \quad (4.41)$$

The $e^{\sigma t}$ term denotes a time dependence on the amplitude of the oscillation. Since friction dissipates energy in the pendulum mode, the amplitude should decay with time. In this case σ must be negative.

The Q factor of the mode can then be deduced

$$Q = -\frac{\omega_0}{2\sigma} . \quad (4.42)$$

These differ from the intrinsic Q of the material because energy is stored in the gravitational field which can be considered as conservative. Different modes store different fractions of their energy in the gravitational field so each mode has a particular Q factor.

It should be emphasised that the Q factor of a mode only gives information about the loss at the normal mode frequency and by itself does not convey any information about the system losses away from the resonance.

4.6.4 Damping in State-space

The complex \mathbf{K} matrix can be used in the state-space model to include the damping due to the losses in the suspension wires. This allows the correct calculation of transfer functions and is used to evaluate the level of thermal noise in the suspension (see Chapter 7).

However, for computational reasons, a complex \mathbf{K} matrix cannot be used when the system is used to analyse the effect of control servos upon the pendulum. In this case, if damping is desired, then it is possible to include viscous damping (*i.e.* the

loss is proportional to velocity). This can be seen in the system

$$\overbrace{\begin{bmatrix} \dot{x}_1 \\ \dot{\theta}_1 \\ \ddot{x}_1 \\ \ddot{\theta}_1 \end{bmatrix}}^{\dot{\mathbf{x}}} = \overbrace{\begin{bmatrix} 0 & 0 & 1 & 0 \\ 0 & 0 & 0 & 1 \\ \mathbf{M}^{-1} \Re[\mathbf{K}] & \frac{\mathbf{M}^{-1}}{\omega_D} \Im[\mathbf{K}] \end{bmatrix}}^{\mathbf{A}} \overbrace{\begin{bmatrix} x_1 \\ \theta_1 \\ \dot{x}_1 \\ \dot{\theta}_1 \end{bmatrix}}^{\mathbf{x}} \quad (4.43)$$

where ω_D is the frequency at which viscous damping and structural damping are equivalent. Normally, this would correspond to the frequency of a normal mode liable to affect the stability of a control servo. Thus, it is possible to check if the resonance peak gives rise to unstable unity gain points.

4.7 Transverse Modes of the Suspension Wires

A wire under tension has a series of modes associated with its transverse vibrations. These are often referred to as *violin modes* since they are analogous to the origin of sound produced by many stringed musical instruments (*e.g.* a violin). These modes are present in the wires suspending the pendulum masses. This section contains a derivation of their eigenmodes and the formulation of a state-space model to describe them. In order to maintain good thermal noise properties (see Section 7.4), these modes will have high Q factors. (For steel wires the Q factor are expected to be $\sim 10^5$.) This has implications to the global control of the interferometer (which is discussed in Chapter 6).

The case of a vibrating wire has been well studied in the history of Physics. Here, a simple model is presented to describe a wire whose ends are fixed securely to the intermediate mass and test mass. Since the pendulum masses are very much greater than the mass of the wire their amplitude is small compared to that of the wire. The stiffness of the wire will be ignored. In this case, the transverse mode frequencies are given by

$$\omega_n = \frac{n\pi}{l} \sqrt{\frac{T}{\lambda}} \quad (4.44)$$

and the amplitude profile is described by

$$x_n(z) = A_n \sin\left(\frac{n\pi z}{l}\right) \quad (4.45)$$

where n is the mode number; l is the length of the wire; T is the wire tension; λ is the linear density; A_n is the amplitude and z is the position along the wire such that $0 \leq z \leq l$ ($z = 0$ corresponds to the intermediate mass). The wire tension acts along the length of the wire so the transverse force applied to the masses can be calculated from the amplitude profile. This is expressed in the equation

$$m\ddot{x}_m = T \left. \frac{\partial x}{\partial z} \right|_{z=0,l} \quad (4.46)$$

where m is either of the pendulum masses and x_m is its displacement. Considering harmonic motion of the system leads to $\ddot{x}_m = -\omega^2 x_m$. The frequency of the normal mode can be substituted here for ω to give (after cancellation) the coupling

$$\frac{x_m}{A} = -\frac{m_{\text{wire}}}{n\pi m} \quad (4.47)$$

where m_{wire} is the mass of the wire ($m_{\text{wire}} = \lambda l$). Typically, this coupling is $\sim 10^{-5}$. Because the amplitude of the pendulum masses is small, most of the energy in the mode is associated with motion of the wire. Hence, the effective mass of the mode is given by $0.5 \times m_{\text{wire}}$. The factor of 0.5 arises because the square of the amplitude profile must be averaged over the length of the wire.

The eigenvector of n^{th} transverse mode of the wire is

$$\mathbf{e}^n = \begin{bmatrix} -\frac{m_{\text{wire}}}{n\pi m_1} \\ \sin\left(\frac{n\pi z}{l}\right) \\ (-1)^n \frac{m_{\text{wire}}}{n\pi m_2} \end{bmatrix}. \quad (4.48)$$

This is not an exact description of the wire profile; it clearly breaks down at the ends of the wire. This, however, should not introduce any significant error. Transfer functions involving the transverse modes of the suspension wires can be calculated from the state-space matrices

$$\mathbf{A} = \begin{bmatrix} 0 & 1 \\ \frac{2k_n}{m_{\text{wire}}} & \frac{2k_n}{m_{\text{wire}} Q_n \omega_n} \end{bmatrix} \quad (4.49)$$

$$\mathbf{B} = \frac{2}{m_{\text{wire}}} \begin{bmatrix} 0 \\ \mathbf{e}_{\text{input}}^n \end{bmatrix} \quad (4.50)$$

$$\mathbf{C} = \begin{bmatrix} \mathbf{e}_{\text{output}}^n & 0 \end{bmatrix} \quad (4.51)$$

$$\mathbf{D} = [0] . \quad (4.52)$$

where Q_n is the Q factor of the mode (see Section 7.4 for estimations of this) and k_n is the effective spring constant of the mode ($k_n = 0.5 \times m_{\text{wire}} \omega_n^2$). The entries in the \mathbf{B} and \mathbf{C} matrices depend upon where the input force is applied and where the displacement is sensed. In fact, $\mathbf{e}_{\text{input}}^n$ and $\mathbf{e}_{\text{output}}^n$ are the corresponding elements of the eigenvector of the mode that determine how coupled the input and output are to the mode. In Section 6.5, the transfer function of force applied at the intermediate mass to displacement of the test mass is shown. In this case

$$\mathbf{e}_{\text{input}}^n = -\frac{m_{\text{wire}}}{n\pi m_1} \quad (4.53)$$

and

$$\mathbf{e}_{\text{output}}^n = (-1)^n \frac{m_{\text{wire}}}{n\pi m_2} . \quad (4.54)$$

Strictly, the pendulum resonances and the transverse modes are in series. This means that the phase lags by 180° above each resonance. The model, as presented, is actually a parallel model for simplicity. However, this is of no consequence because, in all the servos considered, it is the height of each resonant peak that determines the stability of the servo. This model of the transverse modes is included in the routine `fb_x1.m` in Appendix A to calculate the response of a double pendulum to a force applied at the intermediate mass.

4.8 Internal Modes of the Test Mass

A model of the internal modes of the test mass is also required. This has two points of application:-

1. The thermal noise associated with these modes is a fundamental limit to the sensitivity of an interferometric gravitational wave detector. This is fully discussed in Chapter 7.

2. They are excited by actuation to the test mass. This is discussed in Section 6.3.

Typically the test masses are solid right cylinders. A numerical technique to calculate the normal modes of such a cylinder was originally described by Hutchinson [38]. It was later developed by Gillespie and Rabb [23] to the application of test masses in gravitational wave detectors. The numerical code employed by the author to obtain the results presented in this thesis is a further refinement of this written by Blackburn (currently at Caltech). The author is indebted to these people and the LIGO project for making this code available to model the test masses used in the Glasgow prototype and proposed for the GEO 600 project.

A state-space model of the internal modes can be formulated in complete analogy to the model of the transverse modes of the suspension wires. A mode is completely specified if the resonant frequency, Q factor, effective mass and eigenfunction are known. The eigenfunction is merely the 3-dimensional vector field which describes the position perturbations of each point in the test mass. All these, except the Q factor, are calculated by the numerical model as described above. (The Q factors of the modes have been measured – see Section 7.5).

The entries in the **B** and **C** matrices are now the values of the eigenfunction (of the n^{th} mode) at the point where the input force is applied and where the displacement is sensed. In all cases the displacement of the test mass is sensed by the optical mode of the interferometer. Thus, the coupling factor to the sensed displacement is the integral of the eigenfunction with the Gaussian profile of the optical mode. It is clear that modes that have a node at the centre of the end faces do not couple to the sensed displacement. Therefore, the internal modes considered have been restricted to the axisymmetric modes. Some of these modes (for the test masses used in the Glasgow prototype) have been included in the routine **fb_x2.m** in Appendix A to calculate the response of a pendulum to a force applied at the test mass.

As will be seen in Chapter 7, the internal modes of the test mass are required to have a high Q factor to avoid excess thermal noise. The Q factor should be determined by the intrinsic material loss. For fused silica masses the internal modes

are expected to have Q factors of between 5×10^5 and 5×10^6 . However, this can be reduced by the attachment of magnets or wires to the test mass. Measurements of the Q factors for the test masses used in the Glasgow prototype are presented in Table 7.3.

4.9 Conclusion

A procedure for deriving the equations of motion of a test mass suspension has been described. Once the equations of motion have been obtained, the normal mode frequencies can be calculated. The Q factors of the modes follow by including the friction inherent in the distortions of the suspension wires. The equations of motion also allow the dynamic response of the system to be modelled using state-space techniques. This is required so that servo control of the pendulum can be modelled.

These tools will be the basis for results obtained in the following chapters.

Chapter 5

Local Control of Test Mass Suspension

5.1 Introduction

The pendulum suspension of the test mass is an intrinsically resonant system. It, therefore, resonantly enhances seismic noise. This places unnecessary demands on the dynamic range required by the interferometric sensing between the test masses. Damping of the pendulum modes will reduce the *rms* motion by a factor proportional to \sqrt{Q} – typically, this is by at least two orders of magnitude. This is a substantial reduction of the dynamic range requirements for the displacement sensing. Suppression of the resonant motion also makes the initial locking of the interferometer much easier. This is discussed in Chapter 6. Damping of the tilt and rotation modes of the suspension reduce excursions from the correct orientation of the test mass. Control of the test mass orientation and damping of mechanical resonances is known as *local control* (*i.e.* local to the test mass as opposed to the interferometer as a whole).

If several stages are used in the pendulum (*e.g.* a double pendulum) then it is sufficient to control the motion of an intermediate mass; the test mass is controlled as a result. However, to achieve good damping performance requires careful design of the pendulum.

The treatment of local control presented in this chapter is different from previous

discussions of local control applied to double pendulums (*e.g.* in [39]) because all six degrees of freedom have been considered. This has allowed a pendulum design which realises lower frequency modes than before. This provides improved isolation of control noise (as well as other noise sources – most notably seismic noise).

Each stage of the pendulum suspension has six degrees of freedom. Strictly, it is only required to damp the longitudinal, tilt and rotational modes. However, it is desirable to suppress *any* motion of the test mass when feasible. In particular, sideways and, in some cases, vertical motion can also be damped. To this end several control channels are used. Each senses the displacement of a point and feeds back a suitable force to the same point in order to damp the pendulum modes. Careful choice of sensor position is required to adequately sense each normal mode. This is considered to be a more robust approach than techniques that perform algebraic operations on sensor readings and feedback signals. Given the importance of local control as a foundation for all other interferometer control servos, it is strongly desired to make it as reliable as possible.

Significant effort has also been made to further reduce the noise imposed on the test mass by the local control servos. It is desired that control noise should not compromise detector sensitivity above 100 Hz. This has resulted in assessing the performance of various servo filters in terms of the damping that can be achieved versus the noise imposed on the test mass. The results of this analysis are presented in Section 5.5.1.

5.2 Active Damping of Normal Modes

In this section an analytical description of a damping servo is presented. It is assumed that a sensor detects the displacement of the pendulum and an actuator applies a feedback force.

If the frictional damping intrinsic to the pendulum is ignored then the equation of motion of a mechanical mode can be written as

$$\mathcal{F}_m = m\ddot{q} + kq + |G(w)| e^{i\Phi(\omega)} q \quad (5.1)$$

where m and k are the generalised mass and generalised spring constant of the mode;

$|G(\omega)|$ is the magnitude of the feedback gain (in units of Force/Displacement) at a phase of $\Phi(\omega)$ with respect to the generalised amplitude, q . The response of the system is

$$\frac{q_0}{\mathcal{F}_0} = \frac{1}{[k + |G| \cos \Phi] - m\omega^2 + i |G| \sin \Phi} \quad (5.2)$$

and the Q factor of the resonance given by

$$Q = \frac{m\omega_0^2}{|G| \sin \Phi} \quad (5.3)$$

where ω_0 is the resonant frequency. It is clear that damping is optimised for

$$\sin \Phi = 1 \quad (5.4)$$

$$\Phi = +90^\circ. \quad (5.5)$$

This condition is equivalent to feeding back a force proportional to the velocity of the pendulum mass. Thus, the servo filtering should differentiate the sensed displacement.

The resonant frequency of the damped system is given by

$$\omega_0^2 = \frac{k + |G| \cos \Phi}{m} \quad (5.6)$$

so when the phase is not equal to $+90^\circ$ the action of the feedback causes a change in the resonant frequency.

The gain of the servo, G , is the electronic gain multiplied by the coupling of the sensor and actuator to the normal mode. The sensor measures displacement, (*e.g.* the displacement x_1) but this is *not* a measurement of q . In fact,

$$x_n = X_n^m q_m \quad (5.7)$$

where X_n^m is a transformation matrix formed from the eigenvectors of the system.

Similarly, the force applied by the actuator, F_n , is not the generalised force, \mathcal{F}_m , but is shown in [40] to be related according to

$$\mathcal{F}_m = \frac{\partial x_n}{\partial q_m} F_n \quad (5.8)$$

Following from Equation 5.7 the actuator is coupled to the normal mode by the same coupling strength as the displacement sensor.

This analysis gives a theoretical calculation of the damping that is possible by an electronic servo. It shows that the Q factor is inversely proportional to servo gain and that the coupling of the sensors and actuators to the normal modes is an important consideration.

5.3 Prototype Design of Double Pendulum Test Mass Suspension

In this section, a redesigned double pendulum suspension for the test masses currently used in the Glasgow prototype is presented. The test masses have cylindrical geometry with diameter 127 mm and thickness 102 mm. Being composed of fused silica, they have a mass of 2.82 kg. The aim of redesigning the double pendulum suspension is to improve upon the existing design by Morrison (see [39] for a mechanical description of this). In particular, the following points are addressed:

1. The existing pendulum has mechanical resonances at 110 Hz and 165 Hz. The redesign should not include resonant frequencies in the nominal frequency range of interest (*i.e.* above 100 Hz). Furthermore, the frequencies should be reduced as much as possible.
2. The pendulum should have improved isolation of seismic noise in the vertical direction.
3. Where possible, the normal modes should lie within the bandwidth of an active damping servo (*i.e.* less than 5 Hz). This enables the resonance to be suppressed. This condition should definitely be applied to the longitudinal, tilt and rotation modes of the suspension. The existing pendulum has a tilt mode at 54 Hz.
4. The intermediate mass should be approximately equal to the test mass. This leads to better isolation of seismic noise (as shown by Equation 2.6). Previously, the intermediate mass was lighter by more than a factor of 5.

5. A point-to-point damping servo will be implemented as this is considered to be more robust. The existing servo performs algebraic operations on two sensors to generate an error signal. This is more prone to instability caused by cross-coupling.
6. There should be no mechanical resonances in the pendulum where they may cause the damping servo to be unstable. This occurs if the resonance peak produces extra unity gain points where the phase of the damping servo is less than -180° .

The most serious limitation to the existing pendulum is the tilt mode at 54 Hz. In this mode both masses tilt out of phase. The most significant restoring force is the extension and compression of the wires. The mode is illustrated in Figure 5.1. It can be shown that this system has a natural frequency given by (assuming that other effects can be ignored: *e.g.* bending of the wire)

$$\omega_0^2 = 2k \left(\frac{\delta_1^2}{I_{1y}} + \frac{\delta_2^2}{I_{2y}} \right) \quad (5.9)$$

where k is the spring constant of the wire; δ is half the separation of the wires on the intermediate mass and test mass (denoted by the subscripts '1' and '2' respectively), and I is the moment of inertia of the intermediate mass and the test mass. The natural frequency of this system can be lowered by reducing the separation of the wires. For the test masses used in Glasgow prototype, a separation of 10 mm allows the upper tilt mode to be servo controlled. This must be in conjunction with an intermediate mass approximately equal to the test mass whose dimensions are chosen to give preferentially high moments of inertia to the tilt degree of freedom.

It is a design philosophy to damp electronically as many normal modes as possible. Since the sideways modes are approximately equal in frequency to the longitudinal modes these would also be servo controlled.

It has been shown that seismic isolation is critically required in the vertical direction (see Chapter 3). This problem is best resolved by lowering the frequencies of the vertical modes of the double pendulum. This can be partly achieved by reducing the cross-sectional area of the wires. A comprehensive solution is the

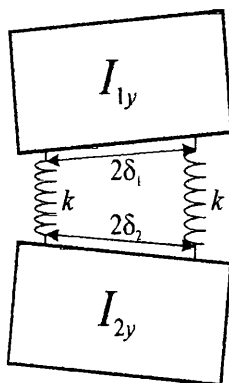


Figure 5.1: *Differential Tilt Mode.*

location of a soft vertical spring at the suspension point. It is then possible to reduce the frequency of the fundamental vertical mode so that it can be servo controlled. This is not considered here though such a spring is installed in the Glasgow prototype with the pendulum now presented.

Use of the model described in Chapter 4 and consideration of the points above has led to the double pendulum design shown in Figure 5.2. The intermediate mass is $100 \text{ mm} \times 40 \text{ mm} \times 76 \text{ mm}$ in the x , y and z -axes respectively. This gives greater moments of inertia to the tilt and rotational degrees of freedom. The lower stage wires have a radius of $62 \mu\text{m}$; this corresponds to a tension of approximately one third of the breaking stress when the test mass is suspended.

A double pendulum to this design was constructed and the frequencies of the normal modes were measured. The predictions of the model together with the measurements are recorded in Table 5.1. Some discrepancies are to be expected because there are inevitable errors in the mechanical construction. In particular, the frequencies of the tilt modes are very sensitive to the accuracy of the mechanical construction. The lower frequency mode is sensitive to the height of the suspension point above the centre of mass on the intermediate mass; the upper mode is sensitive to the separation of the wires (as is shown by Equation 5.9). Other mode frequencies are affected by the wire lengths and their spring constants; the clamps used to hold the wires also contribute some extra mass.

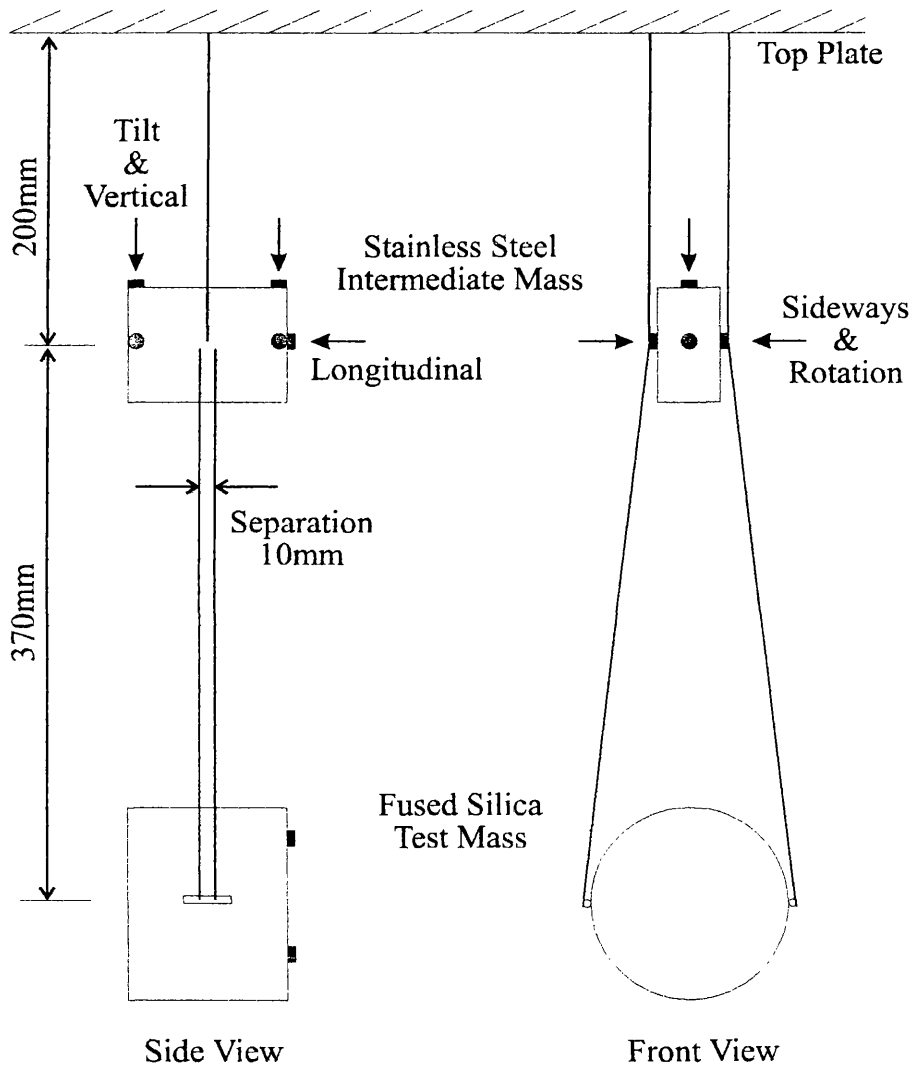


Figure 5.2: *Redesigned Double Pendulum Suspension for Prototype Detector.*

Normal Mode	Model Prediction (Hz)	Experimental Result (Hz)
Longitudinal	0.709	0.700
Longitudinal	1.92	1.86
Tilt	0.856	0.82
Tilt	3.15	3.24
Sideways	0.724	0.718
Sideways	1.91	1.88
Rotation	0.553	0.556
Rotation	1.86	1.86
Roll	14.3	13.08
Roll	31.4	31.6
Vertical	10.8	10.2
Vertical	29.3	28.2

Table 5.1: *The frequencies of the normal modes of the pendulum were measured by timing a given number of oscillations of each mode. For modes with frequencies above a few Hertz spectral analysis was performed on the output of a shadow sensor (as described in Section 5.4.2). The experimental error is indicated by the number of significant figures quoted.*

The predictions for the normal mode frequencies are, however, sufficiently good to design double pendulums that conform to the philosophy detailed previously in this section. It should also be noted that the author has also measured the mode frequencies of the existing pendulum and compared these to the model predictions. Agreement is also found to an equivalent standard. Because the two pendulums are fundamentally different in design (most notably the mass of the intermediate mass), this is indicative of the validity of the model used to describe double pendulums suitable for the suspension of test masses.

5.4 Sensors and Actuators

The sensors and actuators used to achieve local control for the pendulum described in Section 5.3 are now considered. Shadow sensors are used to measure the displacement of the pendulum. The control forces are applied by current carrying coils acting upon magnets attached to the intermediate mass. Figure 5.3 shows the component parts of the sensor-actuator unit. The photodiode and LED fit inside the coil windings with electrical connections wired through the back of the coil former. This is a very compact assembly and ensures that the feedback force is applied to the sensing point. The original design of the units is from the prototype gravitational wave detector in Garching [41].

5.4.1 Control Noise

The term *control noise* refers to displacement of the test mass produced by the combination of sensor noise and actuator noise. The actuator noise should arise only from the final coil driver and will be independent of the electronic gain. Shadow sensor noise, on the other hand, will depend upon the electronic gain. As the electronic gain is increased, control noise will remain constant until shadow sensor noise dominates. Thereafter, control noise increases with gain. The noise inputs are shown in relation to the servo in Figure 5.4. The damping filters allow for adjustment of the electronic gain.

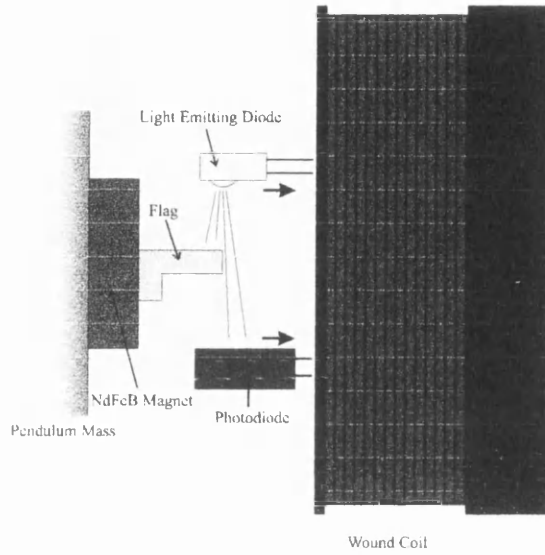


Figure 5.3: *Shadow Sensor and Coil-Magnet Actuator.*

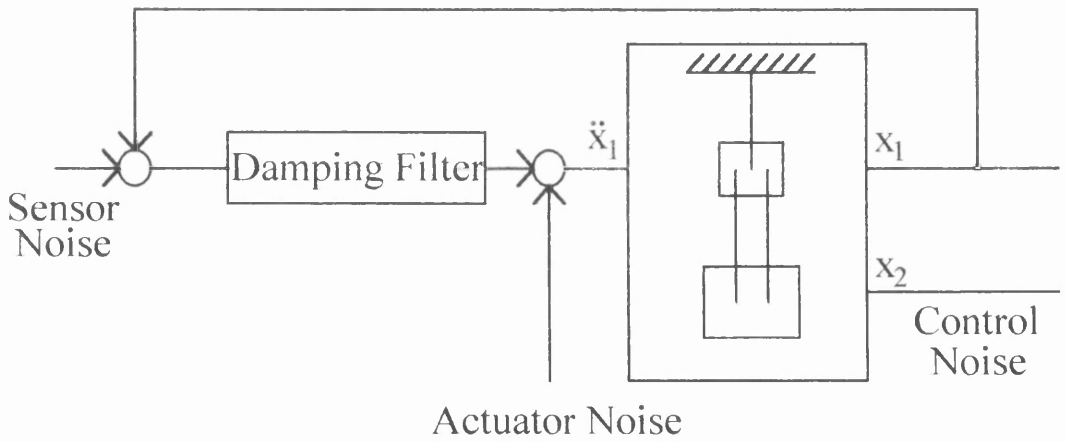


Figure 5.4: *Noise Inputs to the Local Control of a Double Pendulum.*

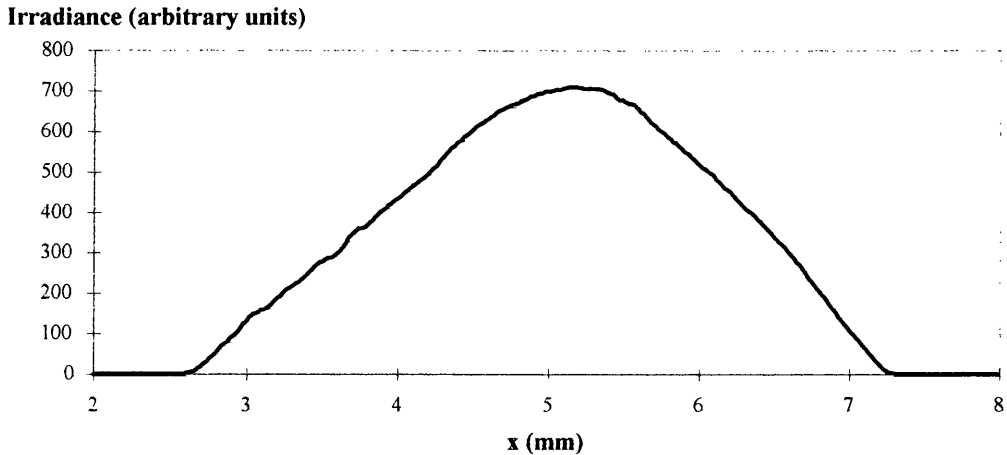


Figure 5.5: *LED Intensity Profile.*

5.4.2 Shadow Sensors

A shadow sensor consists of an LED illuminating a photodiode. An opaque flag attached to the mass partially obscures the light beam. Thus, the photocurrent produced varies with the displacement of the pendulum.

GaAlAs Infrared Emitting Diodes (OP240SLB) were used in the shadow sensors. Their peak emission is at 875nm. The photodiodes were silicon planar (SFH 206) diodes. These have an infra-red filter that admits only a band of wavelengths centred at 950 nm – this is adequately matched to the LED emission. The photosensitive area is 2.71 mm in length. For a flag half way between the LED and photodiode the sensor range is half this dimension.

Figure 5.5 shows the intensity profile of the LED illumination. The response of the sensor is given by this intensity profile. It is, therefore, a function of the flag position. Over the range of the sensor (≈ 1.35 mm), there is a 20% variation in the sensor response if the photodiode is centred at the brightest part.

Variation of the LED illumination is indistinguishable from displacement of the pendulum mass and, hence, represents a noise source to the sensor. It is, therefore, essential to stabilise the intensity of the LED. This can be achieved by stabilising the current passed through the LED. This does not fix the absolute intensity (which can vary if the LED efficiency is effected by temperature changes or ageing), however, at frequencies of interest to gravitational wave detection the intensity is expected

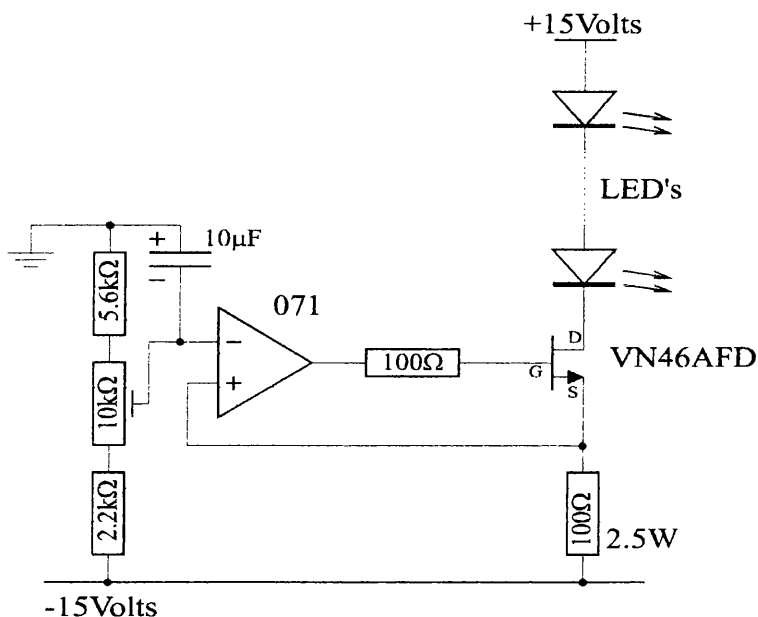


Figure 5.6: *LED Current Stabiliser.*

to be stable. Figure 5.6 shows the circuit used to do this. The LED's for several sensors were wired in series for convenience. Essentially, the current through the $100\ \Omega$ resistor is stabilised by the op-amp. This is the current drawn through the LED's (except for a small leakage current through the FET gate).

The preset resistor is adjusted to give approximately 20 mA current in the LED's. From manufacturer's data this current should result in a decrease in brightness of 12% over 100,000 hours of operation.

The intensity noise produced by the LED cannot be reduced below the shot noise in the detected photocurrent. For an LED current of 20 mA the maximum photocurrent was about $25\ \mu\text{A}$. If the flag obscures half the light produced by the LED then the sensor noise due to shot noise in the light is given by

$$\hat{x} = 1 \times 10^{-10} \left(\frac{R}{1.35\ \text{mm}} \right) \left(\frac{25\ \mu\text{A}}{I_{\text{max}}} \right)^{\frac{1}{2}}\ \text{m}/\sqrt{\text{Hz}} \quad (5.10)$$

where \hat{x} is the sensor noise; R is the sensor range, and I_{max} is the maximum photocurrent detected. Shot noise has a white spectral distribution but is filtered by the damping servo. The differentiation required to generate a damping signal increases the noise at higher frequency. However, the damping signal is only required at the

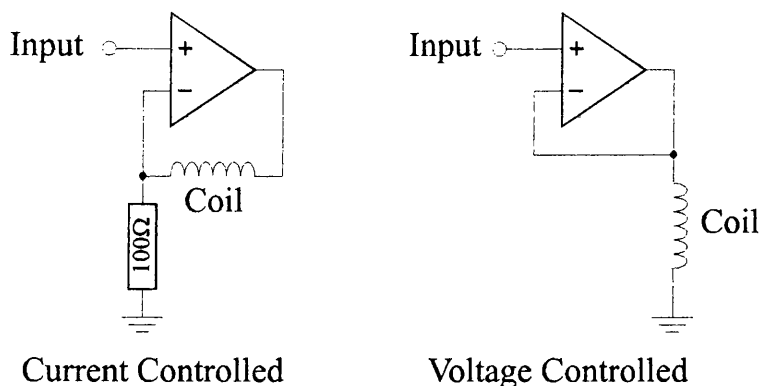


Figure 5.7: *Ideal Current and Voltage Controlled Coil Drivers.*

pendulum resonances. At a higher frequency the differentiation can be ended and low-pass filters added. The response of the pendulum also attenuates noise above its normal mode frequencies.

5.4.3 Coil-Magnet Actuators

The feedback force is produced by passing a current through a coil of wire to act on a magnet attached to the pendulum mass. Two possible configurations of drive to the coils are now considered: either by controlling the current passed through the coil, or by controlling the voltage across the coil. Figure 5.7 shows idealised versions of the two possibilities.

In selecting between these possibilities the following points are critical:

1. the current noise in the coil should not cause excessive control noise at frequencies of interest;
2. the power dissipated in the coil must not cause heating, and
3. coupling of seismic motion of the coil should not compromise the isolation of the pendulum.

In practice, the coils are located inside the vacuum system at some distance from the drive amplifier. This introduces stray capacitance in the connecting cables and, of course, the coil has its own self capacitance. These practicalities make it very difficult to stabilise the circuit where the coil is in the feedback path of the drive

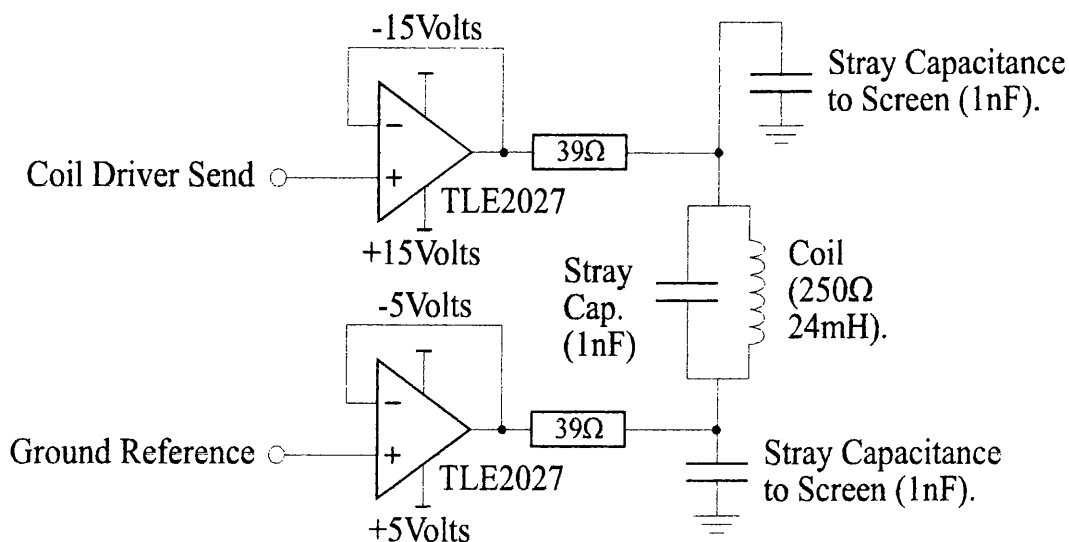


Figure 5.8: A Practical Voltage-Controlled Coil Driver.

amplifier. One solution is to put resistance in series with the coil at the output and inverting input of the op-amp to isolate stray capacitance. However, this reduces the dynamic range of the driver.

It is more robust to drive the coil with a voltage source. In this case the current is determined by the coil's own resistance. The circuit for a practical coil driver is shown in Figure 5.8. Driving both ends of the coil has the advantage that the ends are impedance matched so common mode pick up should not drive current through the coil. It also forms a differential receiver for the drive signal. This permits the coil drivers to be situated externally from the filter electronics. This has two advantages: the coil driver dissipates significant power and therefore requires heat sinking; the coil driver can be located close to the vacuum tank which will reduce stray capacitance effects. (If the signal were not differentially received the circuit would be susceptible to substantial ground current flowing in the connecting cable. Since a long cable would have appreciable impedance this would produce coupling between channels.)

The $39\ \Omega$ resistors prevent the output of the op-amp being short-circuited at high frequency by the cable capacity. The effective input noise of this circuit is estimated to be $4.2\ \text{nV}/\sqrt{\text{Hz}}$. The voltage noise across the coil was measured and the noise associated with the measurement subtracted. This was then referred back to the

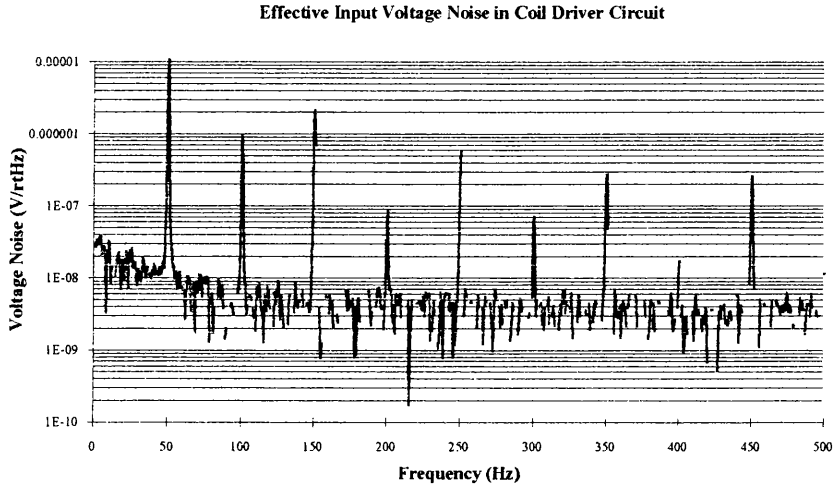


Figure 5.9: *Effective Input Noise in Coil Driver Circuit.*

input of the circuit. The spectrum of input voltage noise is shown in Figure 5.9. The voltage noise was very close to the measurement noise and this has resulted in gaps in the spectrum caused by the subtraction. The measurement demonstrates that the effective input noise is in accordance with the noise estimate.

The source impedance of this circuit is the series resistance of the coil and $2 \times 39\Omega$ giving a total of 330Ω .

The coil used to apply the feedback was wound from 0.1 mm diameter enamelled copper wire. The coil has an inner radius of 10 mm and an outer radius of 14 mm. The length of the coil was 6 mm. This amounts to 1600 turns of wire. Such a coil will be considered as N current loops at the midpoint of radius and length. It is anticipated that this approximation should not greatly affect the estimations of coil performance. (More detailed work has been done by Mackenzie [42] which considers the finite size of the coil. The results obtained are not significantly different from the simpler analysis presented.)

Sintered NdFeB magnets with dimensions 10 mm diameter by 3 mm thick were used. They can be considered as a magnetic dipole, p , which experiences a force

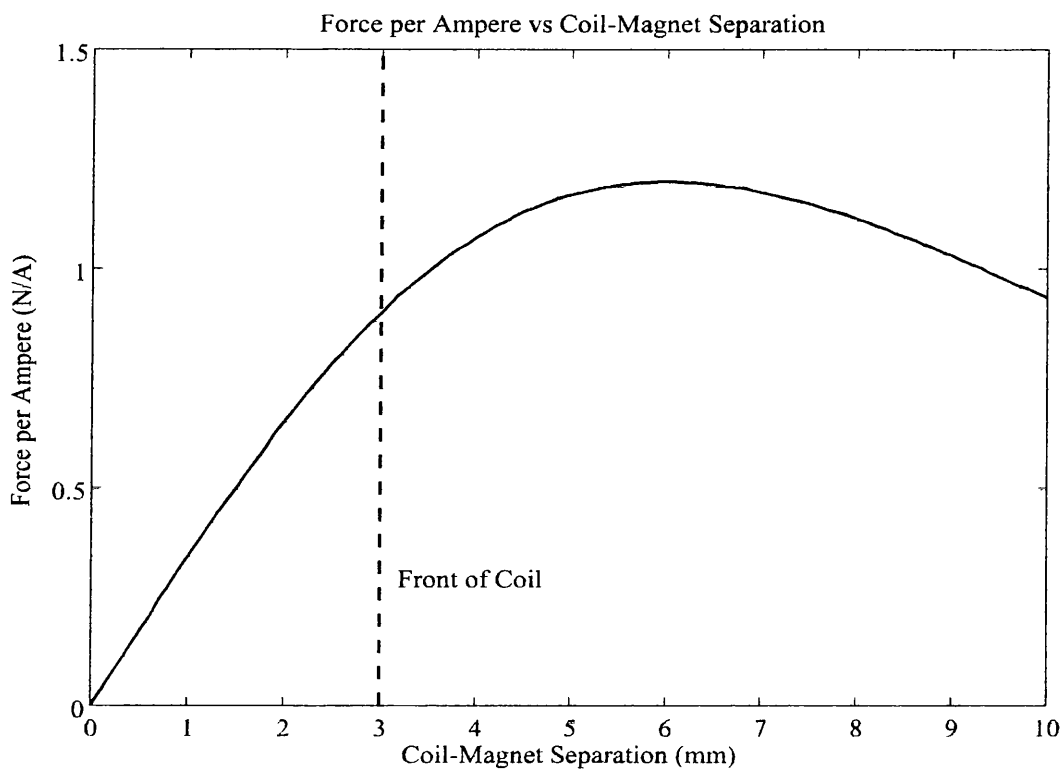


Figure 5.10: *Variation of Force with Separation of Coil and Magnet.*

along the axis of the coil. This is given by

$$F_x = p \frac{dB_x}{dx} \quad (5.11)$$

where B_x is the axial magnetic field produced by the coil and x is the distance along the axis from the coil. For a coil with N turns, and radius a the magnetic field is given by

$$B_x = \frac{\mu_0 I N a^2}{2(a^2 + x^2)^{\frac{3}{2}}} \quad (5.12)$$

where μ_0 is the permeability of space and I is the current in the coil. The applied force is, therefore, proportional to the current and is a function of the coil-magnet separation. Figure 5.10 shows this variation; the optimal separation is where the response is maximised. This occurs when $x = a/2$.

5.4.4 Seismic Motion of the Coils

Using a current carrying coil to act on a magnet allows (seismic) motion of the coils to be coupled to the pendulum mass. The electromagnetic coupling of coil motion should not exceed the mechanical coupling of motion of the suspension point. This assumes that since the suspension point and coil holders are rigidly connected, the same seismic motion is present at both. For a double pendulum the mechanical coupling of motion of the suspension point to force at the intermediate mass is given by

$$F_{x1} = \left(\frac{mg}{l_1} \right) x_0 \quad (5.13)$$

where m is the total suspended mass and l_1 is the length of the upper stage. There are two mechanisms by which coil motion can couple to the pendulum; these are now discussed.

When a static force is applied to the pendulum non-linearity of the force with coil-magnet separation couples motion of the coil. This can be seen by taking the differential of Equation 5.11

$$\hat{F}_x = p \left(\frac{d^2 B_x}{dx^2} \right) \hat{x}_{\text{coil}} \quad (5.14)$$

where \hat{F}_x is the effective force noise applied to the pendulum and \hat{x}_{coil} is the seismic motion of the coil. B_x should be calculated for the maximum current flowing in the coil. For the coil-magnet separation that gives peak response this coupling is precisely zero. Operating close to this point ensures that coupling of motion of the coils is much less than the mechanical coupling.

Relative motion of the coil and magnet induces a current in the coil. This, in turn, applies a force to the magnet. (This is similar to damping of the pendulum caused by current induced in a nearby coil. This has been discussed by Logan in [43] from which Equation 5.16 was obtained.) According to Faraday's Law, the induced *emf* is

$$\epsilon = -\frac{d\phi}{dt} = -\frac{d\phi}{dx} \frac{dx}{dt} \quad (5.15)$$

where ϕ is the magnetic flux cutting the coil due to the magnet; this is given by

$$\phi = \frac{\mu_0 N a^2 p}{2(x^2 + a^2)^{\frac{3}{2}}} \quad (5.16)$$

The induced current depends upon the source impedance, R , of the circuit used to drive the coil. Expressing this in terms of Fourier noise components (so that $\hat{x}_{\text{coil}} = \omega \hat{x}_{\text{coil}}$) then

$$\hat{I} = \frac{\hat{\epsilon}}{R} = -\frac{d\phi}{dx} \frac{\omega}{R} \hat{x}_{\text{coil}} . \quad (5.17)$$

The force applied to the magnet is then calculated as in Equation 5.11. This coupling is frequency dependent and will exceed the mechanical coupling above frequencies given by

$$\omega = \frac{mgR}{l_1} \left[\frac{2(a^2 + x^2)^{\frac{5}{2}}}{3\mu_0 N a^2 p x} \right]^2 . \quad (5.18)$$

For the coils considered this frequency is 10 kHz (when $x = a/2$). Thus, this coupling should not compromise the mechanical isolation at frequencies of interest.

In this discussion it has been assumed that the seismically induced motion of the coils is the same as that of the suspension point. This may not be the case if the mounts for the coils have mechanical resonances. The structure holding the coils was, therefore, made very stiff so that mechanical resonances would occur at high frequencies where the filtering action of the pendulum is greater.

5.5 Longitudinal Modes of the Double Pendulum

A double pendulum will have two modes associated with the longitudinal axis (*i.e.* along the optical axis). These are the most critical modes of the suspension because they couple directly to the output of the detector. Figure 5.11 shows what these modes typically look like. For the lower frequency mode both masses move in phase with the ratio of amplitudes given approximately by the ratio of distances from the suspension point. The higher frequency mode has both masses moving out of phase. Typically, the ratio of amplitudes is inversely proportional to the ratio of masses. This means that the intermediate mass exhibits equal or greater motion. Tilting of the masses is ignored in this discussion.

From Equation 5.3 it is clear that the damping gets better as the servo gain is increased. Eventually, the system goes unstable when the phase at the upper unity gain point is less than -180° .

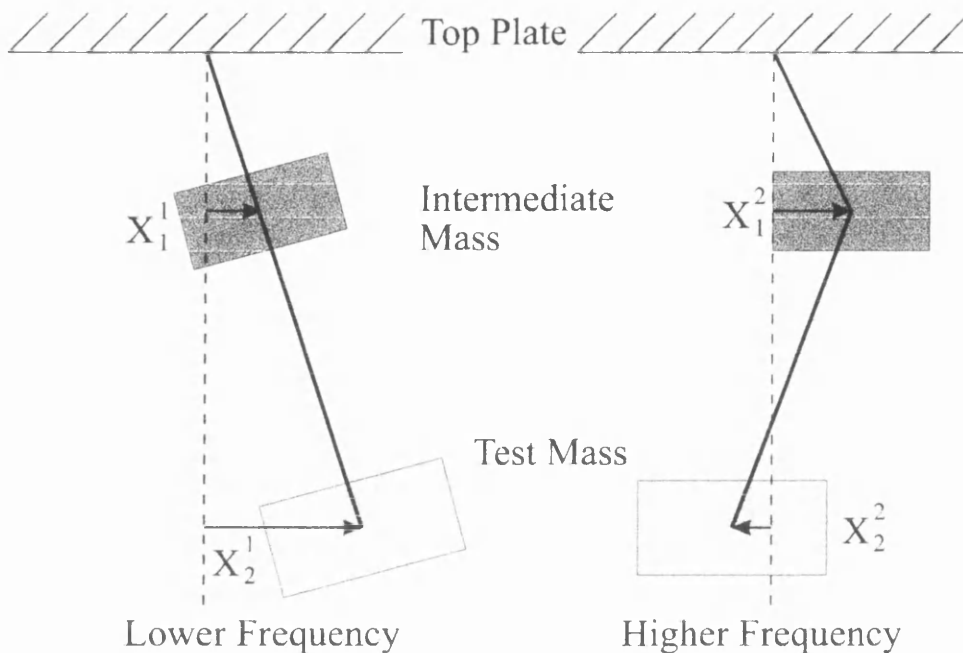


Figure 5.11: *Longitudinal Modes of a Double Pendulum.*

It is difficult to effect adequate damping of both mechanical resonances with feedback to the intermediate mass only. The principal problem is to achieve sufficient gain at the lower resonance. The gain is intrinsically greater for the higher frequency mode because:

1. generation of the damping signal requires a high-pass filter (*i.e.* to differentiate the displacement measurement), and
2. sensing and feeding back at the intermediate mass gives more efficient coupling between x and q for the higher frequency mode.

5.5.1 Damping and Control Noise

It is desirable to find a servo scheme which produces good damping of the modes without adding excessive control noise. It should be observed that while the servo gain is unimportant in itself the control noise imposed on the test mass is crucial. As discussed in Section 5.4.1, control noise is a function of electronic gain. The performance of damping servos on the double pendulum detailed in Section 5.3 were analysed using state-space techniques. The damping achieved by the servo can be

calculated from the poles of the closed loop state-space system. Control noise was also calculated using the pendulum model. The following paragraphs refer to parts of Figure 5.12.

The simplest servo filter is differentiation to a frequency well above the highest normal mode as is shown in (i) in which the differentiation is stopped at 12 Hz. In all schemes there must be low-pass filters to reduce shadow sensor noise at high frequencies. These will to some extent reduce the phase margin of the servo. However, if resonant pole filters are used, the phase lag occurs in a narrow region near the resonance. These are represented in (iv) which comprises a single-pole, low-pass filter at 12 Hz; a resonant filter is at 15 Hz with a Q factor of 3, and a second resonant filter is at 18 Hz with a Q factor of 4. These frequencies are chosen to give adequate phase margin for damping pendulum modes up to 3 Hz (*e.g.* the upper tilt mode of the pendulum considered).

A transitional filter can be used to produce a flat response between the lower and upper longitudinal modes. This is shown in (ii); the flat region extends from 0.7 Hz to 2 Hz. The ratio of the gain at the upper normal mode to the lower normal mode is then reduced. A greater degree of damping should be possible for the lower mode while the upper mode remains stable. This is partially true, however, the phase of the damping signal at the lower normal mode is not at its optimal value of $+90^\circ$. This can be restored by additional differentiation below the lower resonance (as shown in (iii)). The steepened region extends from 0.1 Hz up to 0.7 Hz – both filters stopping together give $+90^\circ$ phase lead at the breakpoint.

For the three different filter schemes discussed the damped normal mode Q factors are plotted against the level of control noise imposed on the test mass at 100 Hz. This is shown in Figure 5.13. Only the Q factor of the lower longitudinal mode is plotted for simplicity. The upper mode is always better damped except close to the end of the curves (the points labelled ‘x’) where the servo becomes unstable. It is clear from these graphs that the scheme shown in (iii) is far superior to the others because it achieves very good damping with minimal increase in control noise over the coil driver noise. The control noise, as estimated, is more than two orders of magnitude less than that implemented by Morrison [39]. It is not thought that this

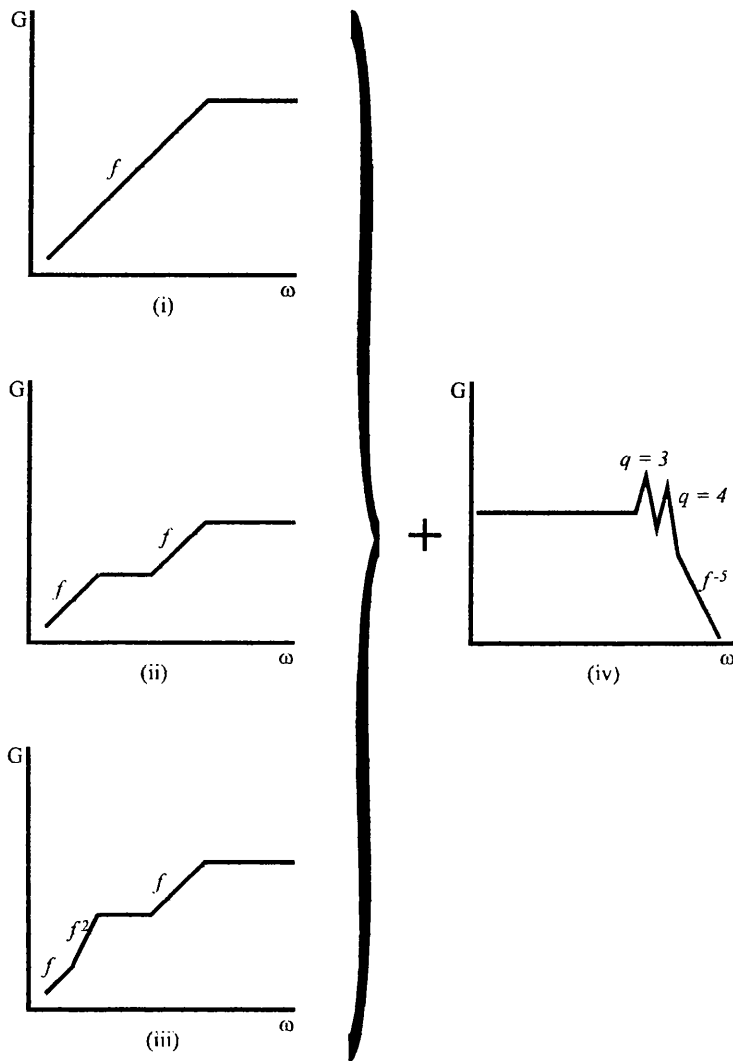


Figure 5.12: Part (i) shows simple differentiation of the displacement signal (up to 12 Hz): a flat region is introduced in part (ii) between the lower and upper longitudinal modes, and in part (iii) an additional transitional differentiator gives optimal phase at the lower mode. The low-pass filters shown in part (iv) are used with all the differentiation schemes to attenuate high frequency noise introduced by the sensor.

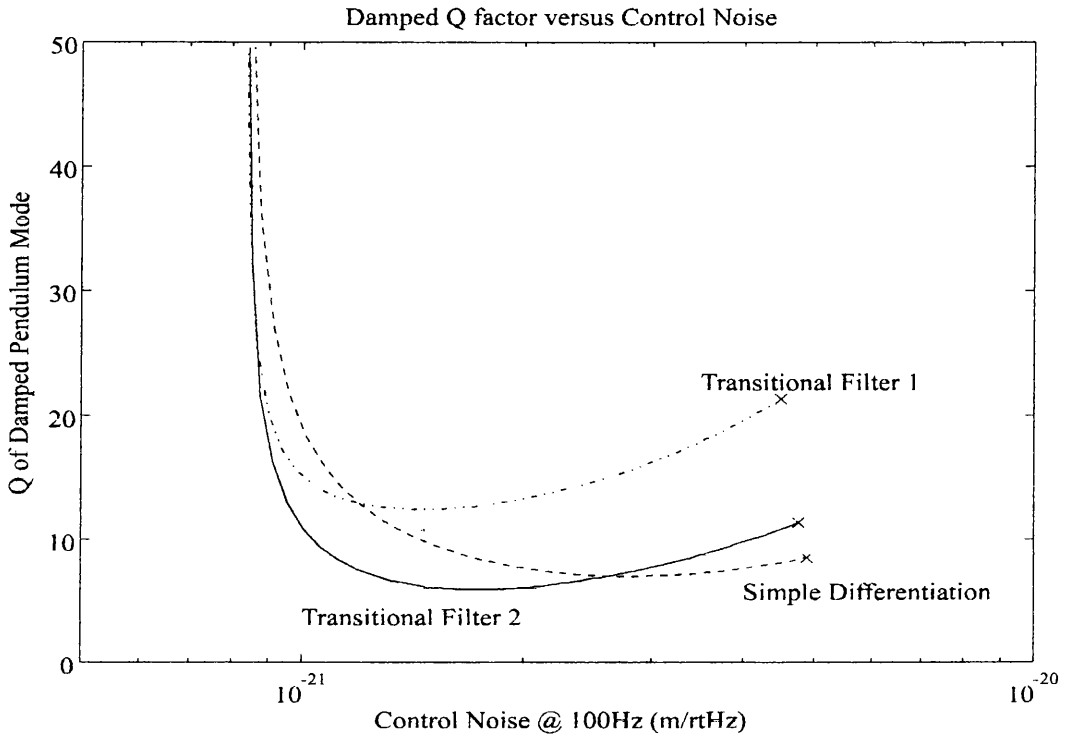


Figure 5.13: *Damped Q factor as a Function of Imposed Control Noise.*

development will improve the sensitivity of the Glasgow prototype detector since other noise sources dominate above this level (as is noted in Chapter 3).

5.5.2 Damping as a Function of Gain

It is useful to profile the Q factor of the mode as a function of the servo gain. This ensures that the required damping can be obtained over a sufficient range of gain to make the servo practical. It is anticipated that the servo gain may change significantly over long periods of operation. For example, the LED's will burn-out producing progressively less illumination with time. The gain is also dependent on the position of the pendulum mass because the response of the sensor is not uniform and the actuation strength varies with the coil-magnet separation.

Figure 5.14 shows the electronic circuit used for the damping servo. The design is the realisation of Figure 5.12 parts (iii) and (iv). The circuit has three monitor points labelled DC, AC and MON. The SEND and RET terminals make allowance for interfacing with an automated gain control. In fact, a manual potentiometer was

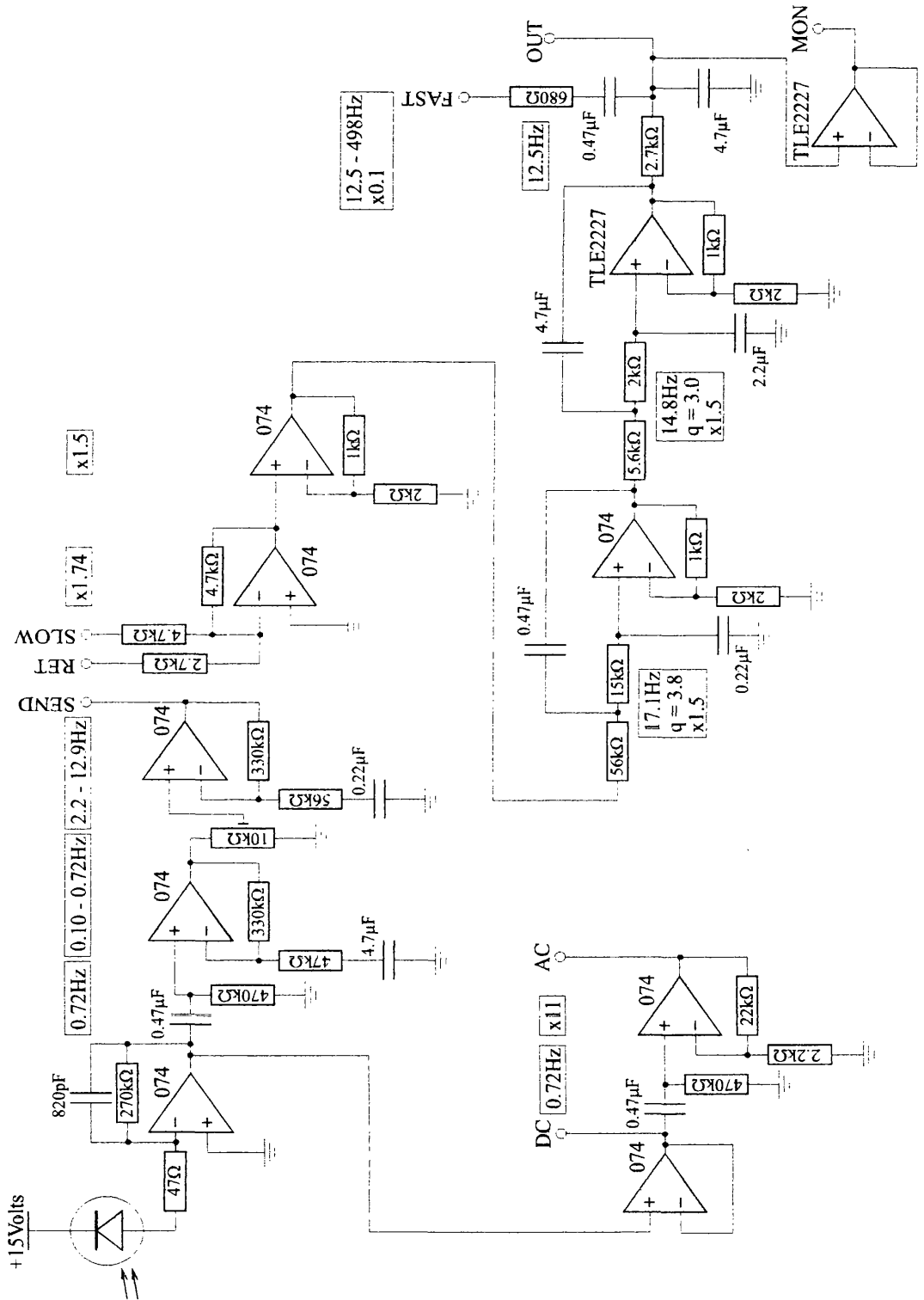


Figure 5.14: Circuit Diagram of Damping Servo.

used. The SLOW and FAST inputs allow *dc* and *ac* signals to be added to the coils. These could control the orientation of the mass or provide feedback to the position of the test mass. The SLOW input is added before the noise attenuation filters and is strongly attenuated above 12 Hz. The FAST input is added afterwards but is attenuated by a factor of 10 to preserve the low noise properties of the output. The output, OUT, goes to the input of the coil driver circuit shown in Figure 5.8.

The pendulum was damped by all control channels except the longitudinal servo. The Q factor of the resonance was then measured by applying an impulse to the test mass and the recording the ringdown of the pendulum (as measured by the shadow sensor on the intermediate mass). The ringdown was then fitted to an exponentially decaying sinusoidal wave to extract the Q factor and the frequency of the pendulum mode.

With the longitudinal servo gain set to zero the Q factor of the pendulum is determined by the damping due to coupling to other degrees of freedom (mainly to tilt). As the servo gain is increased the ringdown becomes shorter until the servo becomes unstable. For several values of servo gain the Q factor was measured. Corrections were made for the damping observed for zero gain. The results are shown in Figure 5.15 and are compared to the damping predicted by the state-space model of the system. The *x*-axis is normalised to the maximum gain of the circuit shown in Figure 5.14. The error in the fitted Q factors is $\approx 6\%$ (this is obtained from analysis of the fit). However, the data does not contain a pure ringdown of the longitudinal mode but has some coupling of other modes. This means that the fitting function does not accurately describe the data so the results are further prone to error. In some cases two ringdowns were fitted to the same data which produced better results. By fitting the data over different intervals and noting the spread in results the error in Q factor is estimated to be about 10%.

From this graph it is evident that there is a factor of four over which the gain can vary without a serious degradation in performance. For a normalised gain of $\times 0.5$ the open loop gain is shown in Figure 5.16 and the closed loop gain shown in Figure 5.17. At this gain setting the Q factor of the lower longitudinal mode is about 6. From Equation 5.3 the Q factor is estimated to be 4.6.

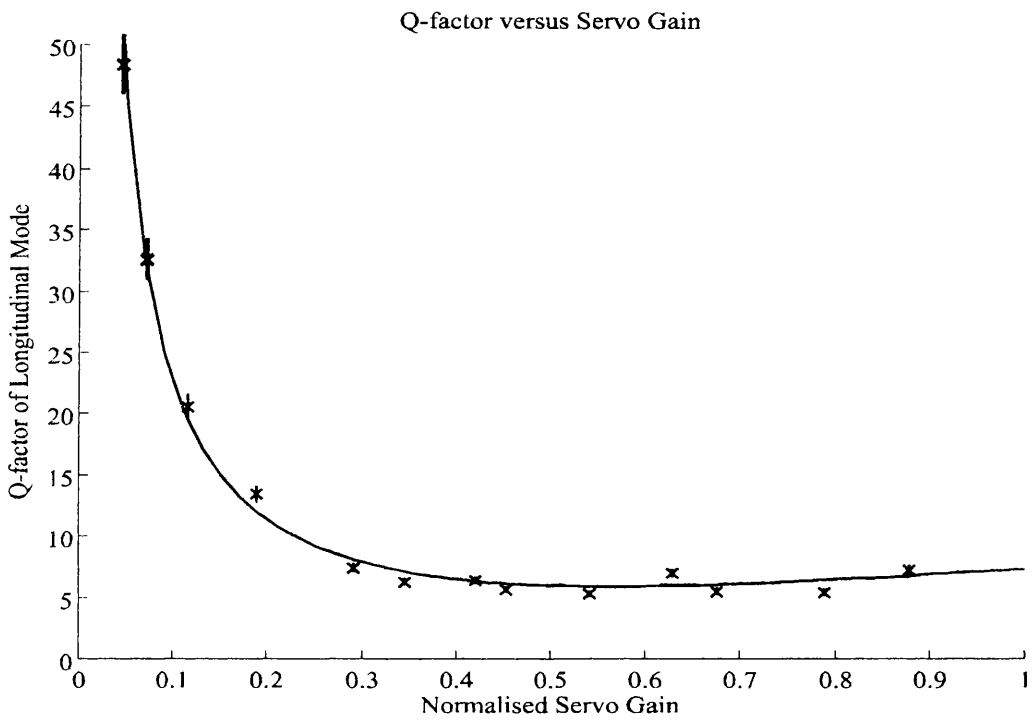


Figure 5.15: The Q factor predicted by the state-space modelling is indicated by the solid line and is compared to measurements of the Q factor of the damped pendulum which are plotted as \times 's. The gain axis is normalised to the maximum gain of the circuit.

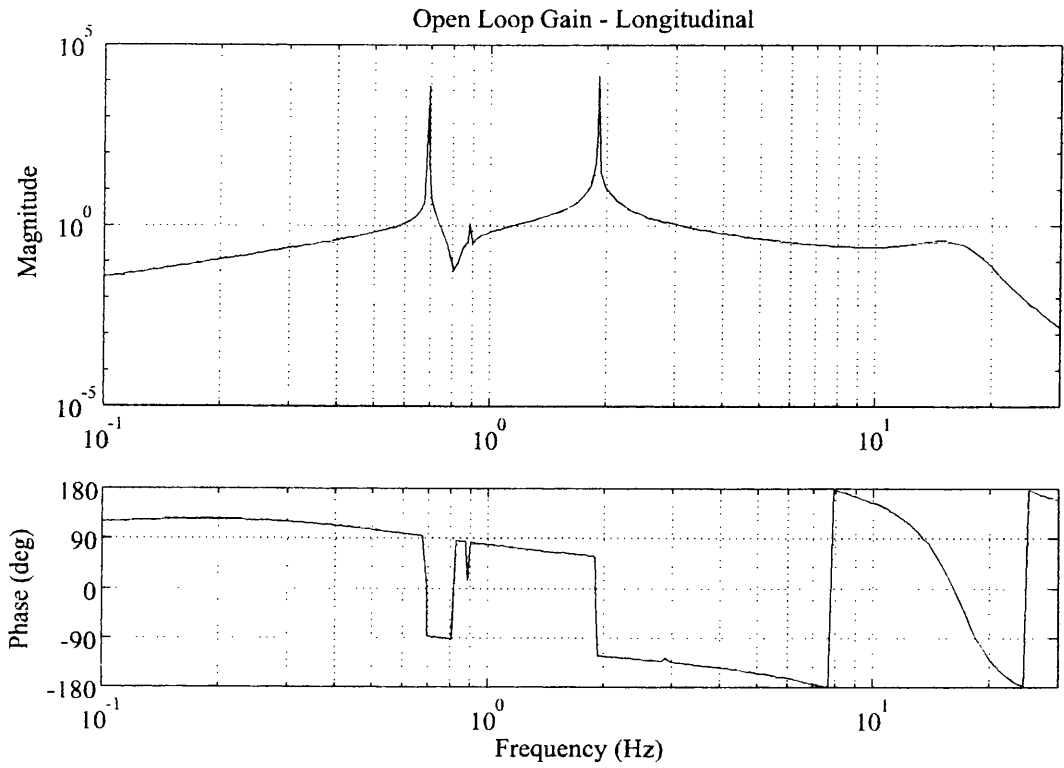


Figure 5.16: *Open Loop Gain.*

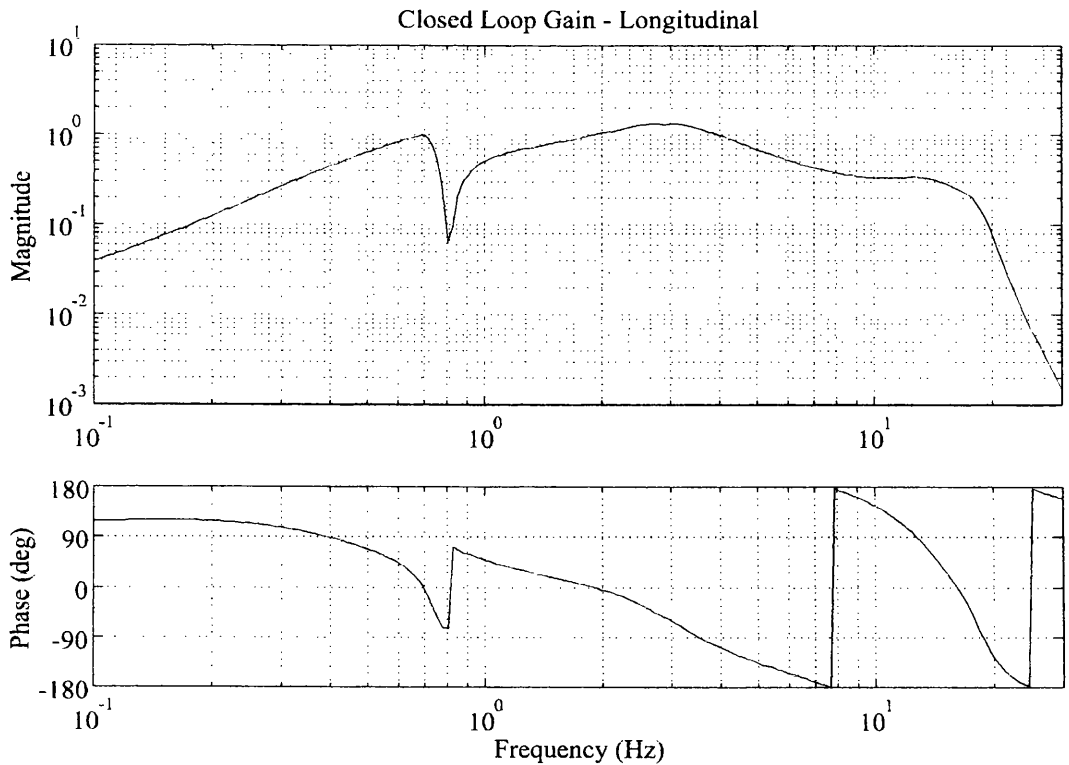


Figure 5.17: *Closed Loop Gain.*

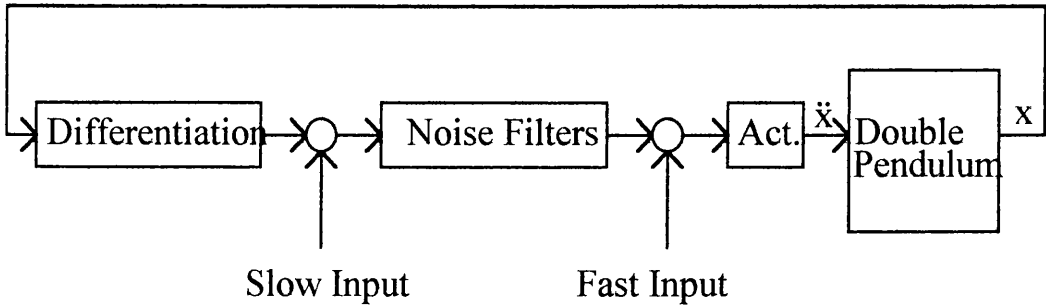


Figure 5.18: *Inputs to the Local Control Servo.*

5.6 Step Response of Damped Pendulum

A standard method of assessing the performance of a servo system is to look at the response to a *dc* step. The step was applied to the *slow input* of the local controls (see Figure 5.18). This is a *dc* coupled input which is strongly filtered at high frequencies (starting at 12 Hz). This diagnostic reflects the real operation of aligning the test mass to the rest of the interferometer.

Figures 5.19, 5.20 and 5.21 show the calculated step responses for longitudinal, rotation and tilt degrees of freedom of the double pendulum described in Section 5.3. Also shown are the residuals, *i.e.* the error between the measured response and the calculated response. These are small compared with the *dc* step size. The tilt response exhibits the largest residual. This is because the tilt modes are very sensitive to the attachment heights of wires with respect to the centre of mass. However, the difference does not indicate a poorly damped system.

5.7 Conclusion

A double pendulum has been designed to suspend the test masses currently used on the Glasgow prototype. The normal mode frequencies predicted by the dynamic model have been compared to those measured on a real set up. The agreement is found to be good. This gives confidence that the dynamic model is accurate.

State-space modelling of the test mass suspensions has allowed the performance of damping servos to be analysed. Model predictions and experimental results are in good agreement. This gives confidence that the design of test mass suspensions

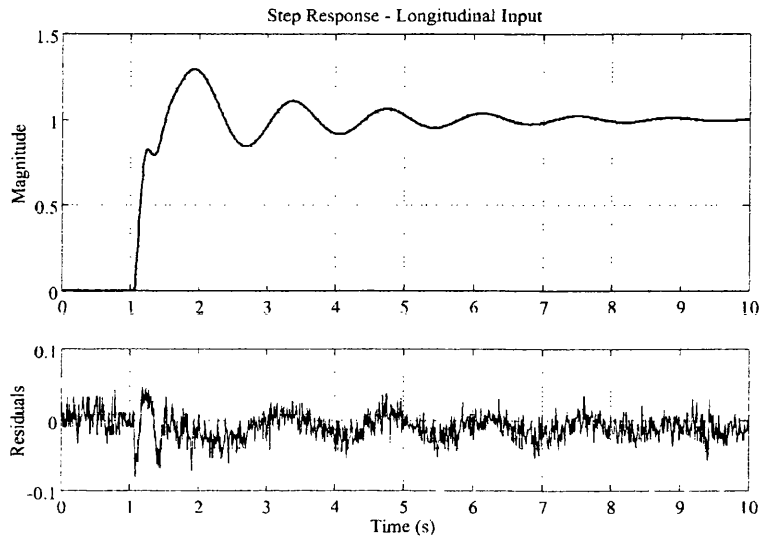


Figure 5.19: *Step Response of Double Pendulum (Longitudinal).*

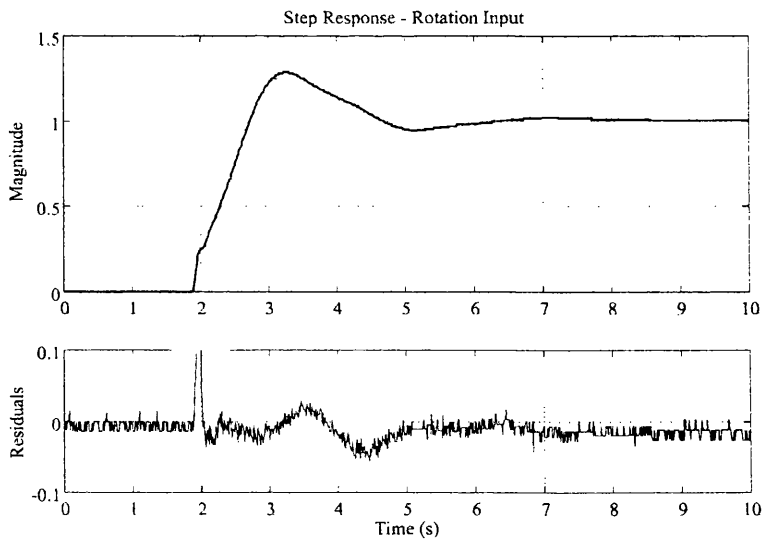


Figure 5.20: *Step Response of Double Pendulum (Rotation).*

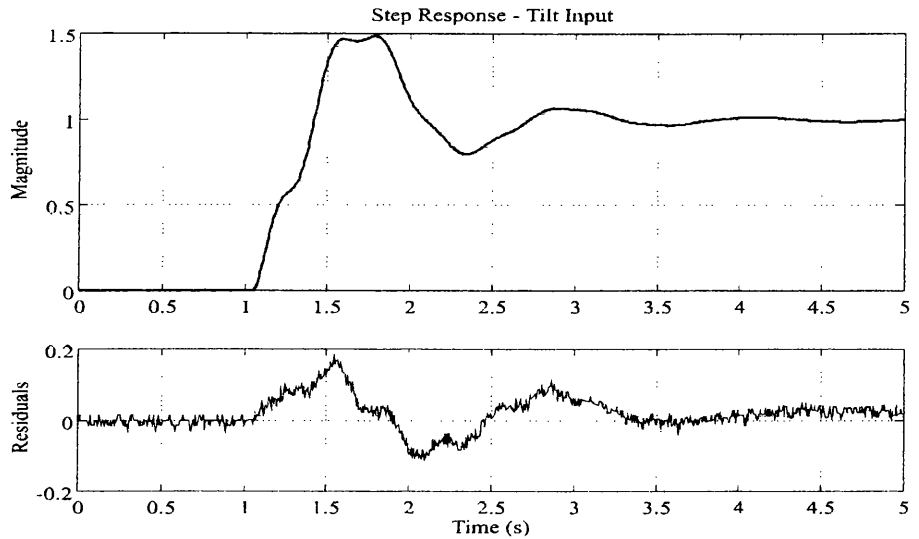


Figure 5.21: *Step Response of Double Pendulum (Tilt)*.

is aided by use of these techniques.

The practical considerations of local control have been addressed and solutions demonstrated by their implementation on a real double pendulum suspension.

The advantages of using a double pendulum suspension over a single stage pendulum are partially evident from this chapter. A double pendulum allows control forces to be applied at the intermediate mass and thus control noise is filtered by the additional pendulum stage. The disadvantage of a double pendulum is the complexity of an additional six mechanical modes which require consideration in the design.

Chapter 6

Global Control of an Interferometer

‘...due to a terrible miscalculation of scale the entire battle fleet was accidentally swallowed by a small dog.’

The Hitch-Hiker’s Guide to the Galaxy.

6.1 Introduction

It is advantageous to operate highly sensitive interferometers at a dark fringe at the output port. (This means that the interferometer is less sensitive to fluctuations of the input light intensity.) In this case, a differential change in the arm lengths shifts the interference fringe and light is emitted at the output. Thus, servo control of the position of at least one test mass is required to maintain the dark fringe condition.

In this chapter, the feedback used to servo the position of a test mass will be discussed. The discussion will refer to the Glasgow prototype detector but the issues are similar for all interferometric gravitational wave detectors irrespective of how the output signal is obtained. The Glasgow prototype detector is comprised of two orthogonal Fabry-Perot cavities. A Fabry-Perot cavity is a basic form of interferometer in that it interferes the input light with light that has been stored in the cavity for many successive bounces. The Glasgow prototype uses one cavity

as the frequency reference for the input light. Feedback is, therefore, applied to the laser frequency in order to lock the light to the cavity. The second cavity is servoed to follow the input light. Thus, the feedback applied to the second cavity is proportional to the differential arm length change.

The outputs from the cavities are *not* optically recombined (as they would be in a Michelson interferometer) but are, instead, electronically recombined. Recombination of the signal from both arms gives cancellation of frequency noise on the input light.

Locking a Fabry-Perot cavity to a dark fringe on the reflected light (the reflected light constitutes the output) is equivalent to maintaining the resonance condition for a standing wave between the two mirrors. Thus, the laser frequency is held at a free spectral range of the cavity or *vice versa*. The locking signal is obtained for both cavities using *rf* reflection fringe locking [44]. It should be noted that the response of a Fabry-Perot cavity to frequency excursions from its free spectral range introduces a single pole low-pass filter at a frequency corresponding to its linewidth. For the Glasgow prototype this is ≈ 2 kHz.

The largest changes to the arm lengths are caused by thermal expansion. However, thermal expansion of the interferometer arms occurs only on time scales which are much longer than the period of the pendulum suspensions of the test masses. As such, the effects of thermal expansion are independent of the pendulum dynamics and, in this chapter, will not be discussed.

The range required by feedback actuators is therefore determined by the level of seismic noise. It is assumed that cross-coupling from other degrees of freedom does not exceed longitudinal motion of the test mass. This assumption follows from the design criteria stated in Chapter 3. The pendulum on which the actuation will be considered is that described in Section 5.3. In Section 6.5 an estimation is made of the actuation range required to lock an optical cavity where the mirrors are suspended as double pendulums. A comparison is made for feedback applied to the test mass only and for feedback applied to both the intermediate mass and the test mass.

The control servo will reduce the offset from the locking point by its loop gain.

The *rms* offset from the locking point must be kept small. This is because:

1. an offset from the dark fringe allows intensity noise on the laser light to couple to the output signal, and
2. the fringe detection is non-linear; large excursions from the locking point may allow non-linear mixing of signals into the detection band.

In Section 2.2.3 it is shown that a loop gain of at least $\sim 10^7$ (at ~ 1 Hz) is required to prevent intensity noise coupling to the output.

6.2 Seismic Excitation

Seismic motion of the ground is often approximately described by (from 1 Hz to 100 Hz) [3]

$$\hat{x}_G = \frac{10^{-7}}{f^2} \text{ m}/\sqrt{\text{Hz}} . \quad (6.1)$$

Obviously, this depends on the proximity of sources of ground disturbance (*e.g.* roads and motors). The Glasgow prototype is located within a building where there is a high level of activity. Because the interferometer does not sit directly on the foundations, the resonant structure of the building causes large bulges in the seismic noise spectrum. In particular, the floor is observed to resonate at around 70 Hz. Thus, the seismic environment is far from optimal.

Ground vibrations must be filtered in order to measure the very small displacements caused by gravitational waves. This is part of the reason why the test mass is suspended as a pendulum. The transfer function of displacement of the suspension point to that of the test mass is shown in Figure 6.1 for a single pendulum of length 0.5 m. This is compared to the transfer function for a double pendulum with a mass equal to the test mass inserted at the midpoint of the suspension wire. Using such a two stage pendulum gives much greater isolation from ground vibrations at frequencies above the resonant modes. It is partly for this reason that double pendulums have been developed and installed in the Glasgow prototype and are proposed for the GEO 600 project (see Chapter 8).

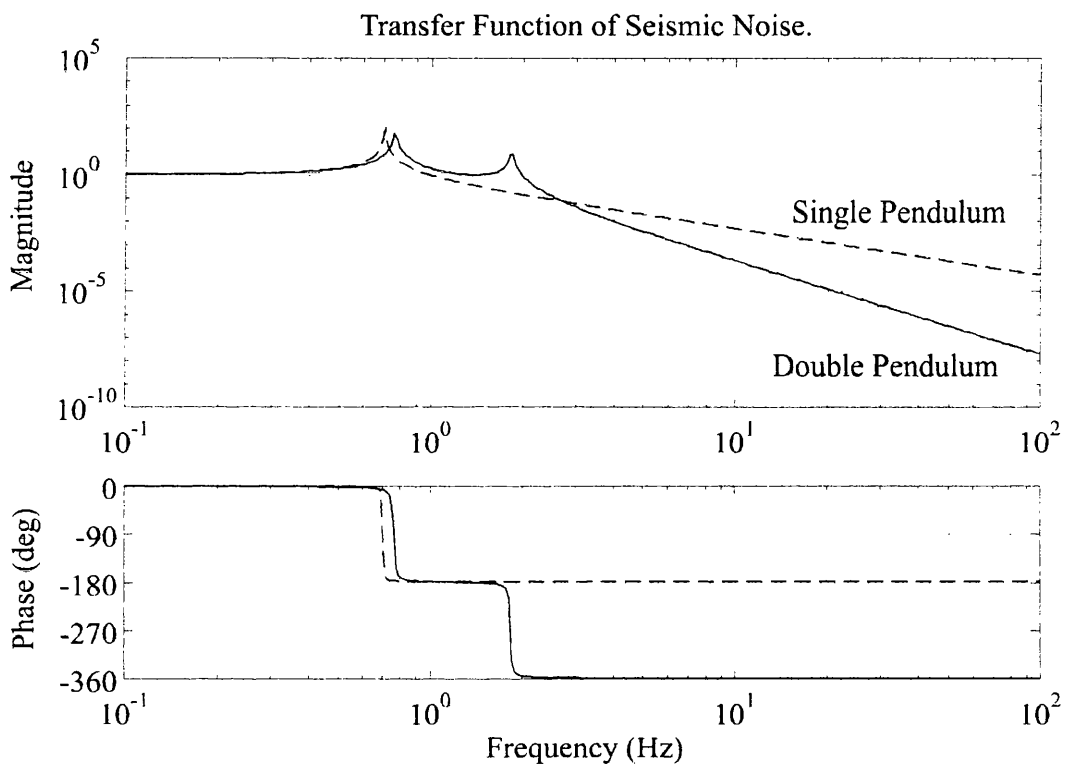


Figure 6.1: *Transfer Function of Displacement of the Suspension Point to Displacement of the Test Mass for a Single and Double Pendulum.*

Additional filtering of seismic motion is achieved by using *vibration isolation stacks*. These are blocks of metal separated by pieces of soft rubber. They provide resonant passive isolation of ground vibrations in a similar manner to the pendulum. The isolation stacks used in the Glasgow prototype are described by M^cLaren in [45].

6.3 Feedback to the Test Mass

In this section, the means of maintaining the dark fringe condition of an interferometer is discussed in terms of applying a corrective force directly to the test mass. It is critical that the implementation of feedback does not impose noise on to the test mass that would limit the detector's sensitivity to gravitational waves. Thus, the feedback force must be applied with a sufficiently low-noise drive. When the feedback signal is measured after control noise has been added, there is some suppression of the noise by the loop gain. This can be seen by considering the schematic control loop in Figure 6.2. The feedback applied is given by

$$\hat{x}_{\text{fb}} = \hat{\epsilon} \mathbf{GH} + \hat{n} \mathbf{H} \quad (6.2)$$

where ϵ is the error point; n is the noise added by the servo; \mathbf{G} and \mathbf{H} are the transfer functions of the servo: \mathbf{G} before the noise is added and \mathbf{H} after the noise is added. The error point is given by

$$\hat{\epsilon} = \hat{x} - \hat{\epsilon} \mathbf{GH} - \hat{n} \mathbf{H} \quad (6.3)$$

$$\hat{\epsilon} = \frac{\hat{x} - \hat{n} \mathbf{H}}{1 + \mathbf{GH}} \quad (6.4)$$

where x is the displacement of the test mass from other noise sources. When Equations 6.2 and 6.4 are combined this gives the feedback signal to be

$$\hat{x}_{\text{fb}} = \hat{x} \frac{\mathbf{GH}}{1 + \mathbf{GH}} - \hat{n} \frac{\mathbf{H}}{1 + \mathbf{GH}} . \quad (6.5)$$

This shows that the noise introduced by the servo is suppressed by the loop gain. It is also seen that, assuming $\mathbf{GH} \gg 1$, the feedback signal is an accurate representation of the disturbance of the test mass. It is important that there are no noise sources after the feedback signal has been measured as these are unaffected by the servo.

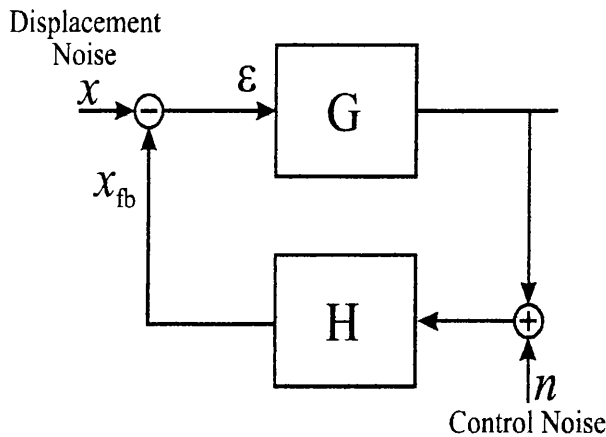


Figure 6.2: *Generic Servo Control Loop.*

6.3.1 Response of the Test Mass

The test mass is suspended as the second stage of a double pendulum. The response of the test mass to a force applied directly to it can be calculated using the state-space model of the suspension described in Chapter 4. Essentially, the resultant displacement is filtered by the lower longitudinal mode of the suspension. This gives two poles of filtering on the feedback signal. Thus, some differentiation of the error signal will be required to make a stable servo control loop.

In any mechanical system it is desirable to collocate the feedback actuation and the sensing point. It is difficult to apply this principle to the control of the test masses because optical sensing is used. The reflective face of the test mass cannot be obscured by mechanical components of the actuator. For this reason the test mass in the Glasgow prototype is controlled by feedback forces applied to the back face of the test mass. Because the actuation and sensing are not collocated, the elastic properties of the intervening material are much more important in the response of the test mass. The elastic properties of the test mass are characterised by its internal modes of vibration (a discussion of internal modes is given in Section 4.8). In particular, the eigenfunction of the *longitudinal* mode (which has a frequency of 25.5 kHz) is symmetrical around the centre of the test mass (*i.e.* the centre cross-section of the cylinder is a node). Thus, opposite faces move in anti-phase giving a phase lag of -180° between the applied force and the response of the reflective

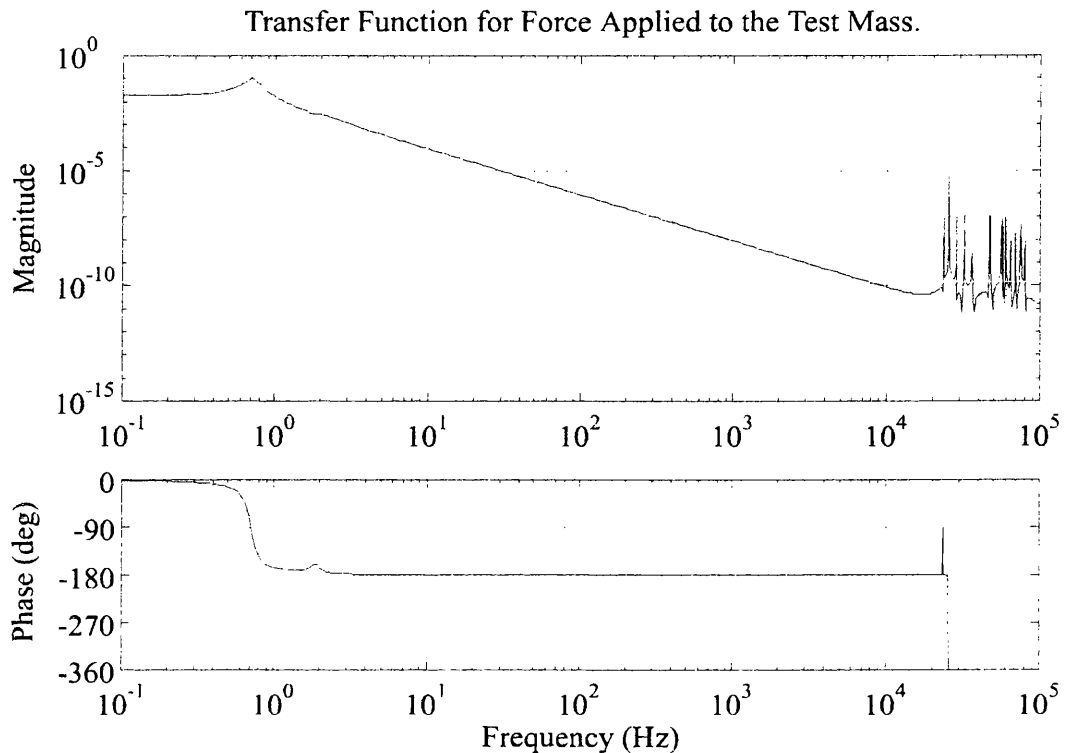


Figure 6.3: *Transfer Function Showing the Effect of the Internal Modes of the Test Mass.*

face. This corresponds to the phase lag introduced by the propagation time of a compression wave through the test mass. The modes of the pendulum and the internal modes have been modelled as parallel paths. In this model the peak height is correct although the phase at the resonance may not be. This is acceptable since the only important information is the phase at the unity gain point. The internal modes limit the unity gain point of the control servo to well below the first mode of the test mass. At this frequency the response is dominated by the pendulum modes.

In fact, there are many internal modes of the test mass. The numerical modelling of the test masses noted in Section 4.8 enables the eigenfunctions of the internal modes to be calculated. This permits the internal modes to be included in the transfer function of force applied at the back face of the test mass to the sensed displacement. Such a state-space model is generated by the routine `fb_x2.m` in Appendix A. Figure 6.3 shows the modelled transfer function.

Figure 6.4 shows a comparison of the measured and modelled transfer functions of the test mass at frequencies of the first few internal modes. The measurement was made by correlating the interferometer error point with a sine wave added to the feedback signal. The sine wave was swept in frequency over the range shown. The modelled transfer function uses measurements for Q factors of the internal modes (see Table 7.3), all other data is the result of numerical analysis.

The filtering electronics of the locking servo includes two transitional differentiators. One counters the roll-off of the Fabry-Perot cavity to make the response flat up to 10 kHz. A second acts between 700 Hz and 10 kHz to provide phase margin at the unity gain point which occurs at ≈ 2 kHz. The low frequency gain is increased by a transitional integrator from ~ 28 Hz to 280 Hz. This achieves a loop gain of $\sim 10^7$ at 1 Hz.

Precautions must be taken to ensure that the resonant peaks do not cause the loop gain to return above unity gain. (This would cause the servo to be unstable since the phase cannot be greater than -180° at both unity gain points on either side of the resonance.) Because the internal modes have a Q factor of up to 5×10^5 , the most appropriate method of suppressing the gain is to use notch filters tuned to their resonant frequencies.

The height of a resonant peak is determined by the Q factor and the coupling of the actuator to the mode. It is possible to minimise the coupling strength by applying the feedback at a node, however this is difficult to realise for all modes simultaneously. In principle, feedback could be applied at the outer edge of the front face of the test mass but this provides no advantage with respect to coupling to the internal modes of the test mass. A family of modes known as *drum* modes have circular nodes at some radius on the face of a cylinder; these reflect the propagation time of a shear wave across the face of the test mass.

In the absence of more direct feedback, the bandwidth of the servo is limited to a few kHz. This makes the acquisition of lock difficult; this is discussed in Section 6.4. It also means that the loop gain of the servo is still relatively small at frequencies of interest to gravitational wave detection. Thus, the feedback signal is not a true representation of the displacement of the test masses. Measurements of

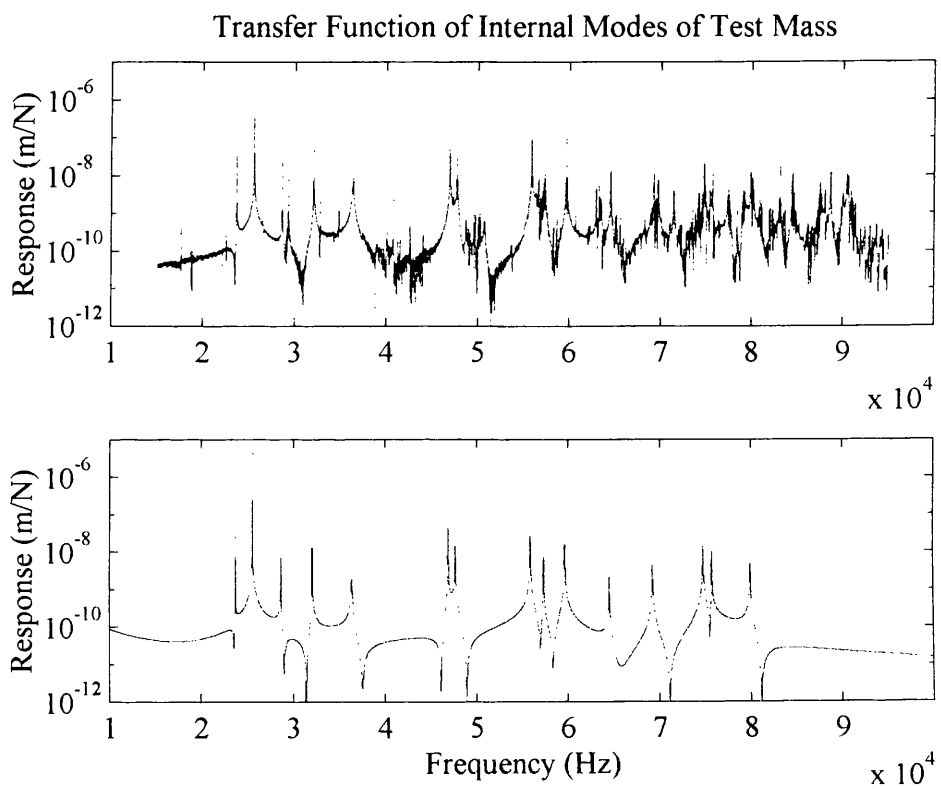


Figure 6.4: *The top graph shows the experimentally obtained transfer function of the internal modes of a test mass used in the Glasgow prototype detector. This can be compared with the bottom graph which is the response predicted by the model described in Section 4.8. The modelled response is valid up to ≈ 80 kHz.*

the feedback signal must be calibrated to deduce the displacement measured by the interferometer. This is discussed by Morrison in [46].

6.3.2 Actuators

Three coil-magnet actuators are used to control the longitudinal position of the test mass. These are wired in series and therefore the same current is passed through each coil. The coils have 500 turns of 0.2 mm diameter enamelled copper wire giving a total series resistance of all three coils is 68.5Ω . The windings are 6 mm long and have an average diameter of 12 mm. The coils were mounted on a plate which was isolated from ground motion by four pieces of rubber. The vertical resonance of the coil mounting-block on these rubber pieces was about 20 Hz.

Motion of the test mass (and hence the magnets attached to the test mass) induces Eddy currents in the actuator coils. This is a loss to the pendulum and will produce thermal noise in the same manner as friction in the suspension wires. The loss tangent for this form of damping is

$$\phi(\omega) = \frac{\omega}{m\omega_0^2 R} \left(\frac{d\phi}{dx} \right)^2 \quad (6.6)$$

where m is the test mass, ω_0 is the pendulum frequency, R is the source impedance of the coil driver and ϕ is the magnetic flux through the coil ($(d\phi/dx)$ is identical to the force per unit current between the coil and magnet). The resultant displacement noise can be estimated from Equation 2.7. To achieve a sensitivity of $\sim 10^{-19} \text{ m}/\sqrt{\text{Hz}}$ (at 100 Hz) requires a source impedance of $\geq 1 \text{ M}\Omega$. Of the coil driver circuits considered in Section 5.4.3 only the current controlled configuration can present a high source impedance and drive sufficient current through the coils. The coil driver is of this type.

The coupling of coil motion to the measured displacement of the test mass is different from that described in Section 5.4.4. This is because the servo bandwidth extends over the measurement bandwidth and therefore the action of the servo loop must be considered. The displacement of the test masses is obtained by measuring the feedback signal applied to lock the Fabry-Perot cavity. However, it is the voltage at the output of the coil driver that is, in fact, recorded. Therefore, a change in the

separation of the coils and magnets (*i.e.* seismic motion of the coils) changes the actuation strength at a point in the control loop after the feedback signal has been measured. This is shown in Figure 6.5. At frequencies where the servo loop gain is high, the measured feedback signal, x_m , is given by

$$x_m = \frac{x}{\mathbf{H}} \quad (6.7)$$

where x is the differential displacement of the test masses and \mathbf{H} is the actuation strength. The effect of varying the actuation strength is shown by taking the differential of Equation 6.7

$$\delta x_m = -\frac{x}{\mathbf{H}^2} \delta \mathbf{H} \quad (6.8)$$

The *rms* displacement of the test mass is likely to be dominated by the *dc* component required to lock cavity away from the equilibrium point of the pendulum; this is denoted by Δx . Substituting Equation 6.7 into Equation 6.8 leads to

$$\bar{x} = \frac{\Delta x}{\mathbf{H}} \left(\frac{d\mathbf{H}}{dr_c} \right) \hat{\mathbf{r}}_c \quad (6.9)$$

where \mathbf{H} is the actuation strength and \mathbf{r}_c is the displacement of the actuation coils. $(\partial \mathbf{H} / \partial x_c)$ can be evaluated from the coil-magnet interaction described in Sections 5.4.3 and 5.4.4. However, it is inevitable that vertical motion of the coils will exceed their longitudinal motion. Using Maxwell's Equation, $\text{div} \mathbf{B} = 0$, and a simplified coil-magnet geometry the variation of the actuation strength along the z -axis is estimated to be

$$\frac{\partial \mathbf{H}}{\partial z_c} \approx \frac{\partial \mathbf{H}}{\partial x_c} \quad (6.10)$$

For the feedback coils considered $(\partial \mathbf{H} / \partial x_c) / \mathbf{H}$ has a value of up to $\pm 50 \text{ m}^{-1}$ for an offset of up to 1 mm from the optimal separation of the coil and magnet.

The Fabry-Perot cavity will virtually always be locked with an offset from the equilibrium point of the pendulum. This is because the distance between the two test masses must be an integer number of half-wavelengths of the laser light. Furthermore, the cavity is more likely to acquire lock when the velocity of the test mass is a minimum; this occurs at the extrema of any pendulum motion. Once lock has been acquired, the cavity may drift further due to thermal expansion. The maximum value of Δx is equal to the *dc* range of the actuators: *i.e.* $20 \mu\text{m}$. The allowed

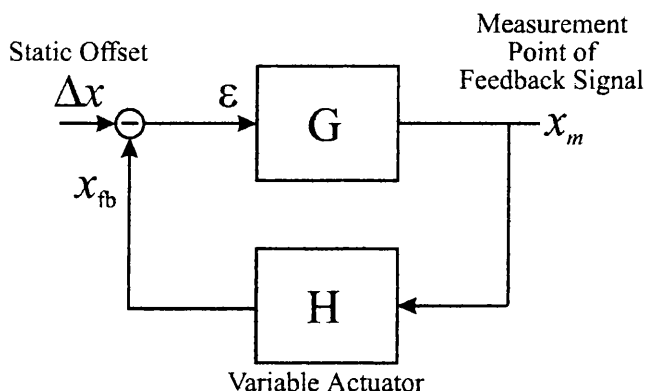


Figure 6.5: *Servo Control Loop with Variable Actuator.*

displacement of the reaction coils is, therefore, only 1000 times larger than that of the test masses themselves.

If the displacement sensitivity required by proposed large scale gravitational wave detectors ($\hat{x} \sim 10^{-19} \text{ m}/\sqrt{\text{Hz}}$ – see Chapter 2) is to be achieved, the feedback actuators will need to be isolated from seismic motion. In particular, isolation of vertical seismic motion is required. In Section 3.2.2 it is observed that cross-coupling of vertical motion of the test masses is by a factor of order 1×10^{-3} . The allowed vertical motion of the test masses and actuator coils are therefore approximately equal. The coils could be mounted on a reaction mass and suspended in a similar manner to the test masses.

6.4 Acquisition of Lock

An interferometric gravitational wave detector can only make high sensitivity measurements of changes in the differential arm length when it is in a locked state. This locked state can be lost on account of one of a number of events. For example:

1. thermal expansion exceeds the *dc* range of the servo actuators;
2. seismic disturbances, and
3. mode-hopping of the laser.

It is critical that the time taken to re-acquire lock is not a significant fraction of the typical length of time during which data can be taken.

The most problematic step is the acquisition of lock of the second Fabry-Perot cavity to laser light which has already been stabilised to the orthogonal cavity. The test masses which form the ends of the optical cavity are seismically excited and are observed to swing through the resonance condition about 5 times every second. The difficulty arises because the locking signal is only meaningful when the cavity is close to resonance. It is more often the case that the test masses swing through resonance without lock being acquired. The time taken to lock the cavity could be reduced if the relative velocity of the test masses could be reduced.

By observing the fringes produced as the cavity moves through the resonance condition, it is possible to deduce the velocity and direction of the motion. The light intensity reflected from the input mirror initially drops because light is admitted to the cavity. When the cavity moves away from resonance, the stored light leaks out and interferes with the input light to give a train of fringes that decay to the static level. The rate of decay of the fringe amplitude is a measure of the losses in the cavity; the frequency of the ringing is proportional to the relative velocity of the test masses. An analogous fringe is also observed on the demodulated signal used in the *rf* reflection fringe locking technique except that this signal allows the direction of the cavity length change to be determined from the polarity of the fringe.

Using CMOS logic, the *dc* and *rf* fringes are analysed to yield a pulse which is applied to one test mass to reduce its velocity relative to the other mass. The logic circuit which does this is shown in Figure 6.6. The fringe damping signal is added into the error point of the *rf* reflection locking servo. Once lock has been acquired the fringe damping servo is disconnected to avoid adding any noise to the feedback. Use of these fringes to aid acquisition of a suspended mass, Fabry-Perot cavity has also been made by Camp *et al* [47] on the Caltech prototype detector.

Operation of the circuit shown in Figure 6.6 is now discussed. The light intensity is *ac* coupled and a comparator used to detect the zero-crossings caused by the ringing after the cavity has moved through the resonance condition. The ringing of the intensity signal is used to generate monostable pulses. The number of pulses

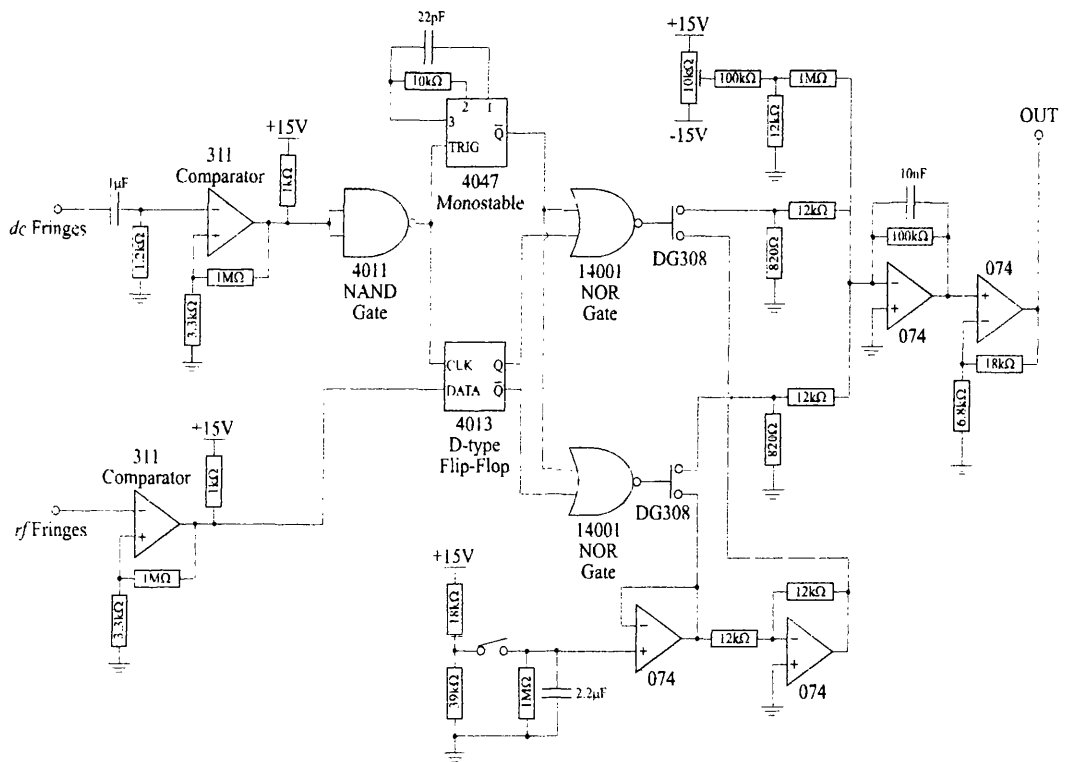


Figure 6.6: *The CMOS logic that Generates Fringe Damping Signal for Fabry-Perot Cavity.*

	Fringe Damping ON (s)	Fringe Damping OFF (s)
Average Time	12.5	> 64
Shortest Time	1.8	15.1
Longest Time	40.9	> 121

Table 6.1: *Acquisition Times.*

in the duration of a fringe is proportional to the velocity of the mass. The zero-crossings of the light intensity correspond with extreme values of the rf fringes the sign of which determines the direction of the cavity length change. A D-type flip-flop samples the rf fringe at positive to negative crossings on the dc fringe. This signal is then correlated with the monostable pulses (using the NOR gates) to control the analogue switches. The analogue switches give either positive or negative pulses to the final output buffer. The impulse applied to the test mass is proportional to the number of monostable pulses and, hence, it is also proportional to the test mass velocity. This ensures that the relative motion of the test masses is damped.

The times taken for the Fabry-Perot cavity to lock to the stabilised input light was recorded with and without the fringe damping. A summary of the locking times is presented in Table 6.1. As can be seen, this method of reducing the velocity of the test mass allows the Fabry-Perot cavity to be locked in a significantly shorter time.

The action of the fringe damping servo can be assessed by observing the number of impulses applied in each direction to the test mass. The servo is observed to be very effective at reducing the length excursions of the cavity to of order one fringe but the acquisition of lock by the analogue servo is still problematic. As the length of the cavity approaches the dark fringe condition the analogue servo acts to pull one test mass towards the locking point. This increases the rate of change of the cavity length. Thus, the test mass overshoots the locking point and it is only then that the servo acts to slow the test mass down. However, the impulse imparted by the servo approximately cancels yielding no net result. Acquisition of lock must rely upon the

cavity naturally coming close to the locking point irrespective of the servo action. The author proposes that better performance may be possible if the analogue servo is triggered to switch ‘on’ when the cavity length is precisely at the dark fringe. If the lock is not acquired, the servo can be re-primed for the next fringe. In this approach the servo only ever acts to reduce the rate of change of cavity length.

6.5 Feedback to the Intermediate Mass

The application of feedback has been considered in terms of the action of current carrying coils upon magnets attached to the test mass. It is undesirable to attach magnets to the test mass since they are observed to introduce significant mechanical loss and are a potential source of thermal noise (see Chapter 7). An alternative possibility is to use the dielectric property of the test mass material. A dielectric material is polarised and attracted by an electric field. Therefore, a fluctuating electric field generated near the test mass can be used to apply a feedback force. This is the principle of the *electrostatic* drive. Such drives are discussed in [48]. One possible type of electrostatic drive comprises two interlaced ‘combs’ – see Figure 6.7. These could be deposited on a glass plate and positioned ~ 1 mm behind the test mass. As one electrode is charged with respect to the other, the fringe field produces a force on the test mass.

This electrostatic drive is limited in one respect: it has a significantly reduced range compared to a coil-magnet actuator. (The range is limited by the maximum voltage that is practical to use.) It is possible to reduce the actuation range required by the test mass drive if the larger, low-frequency length changes of the cavity are corrected by feedback actuation to the intermediate mass of the double pendulum. The feasibility of such a feedback topology is now discussed. It is assumed that the feedback to the test mass is by some electrostatic drive while feedback can be applied to the intermediate mass by a coil-magnet actuator. The range of the coil-magnet actuator will be assumed to be adequate. The schematic control servo is shown in Figure 6.8.

Feedback to the intermediate mass suffers from similar problems as feedback

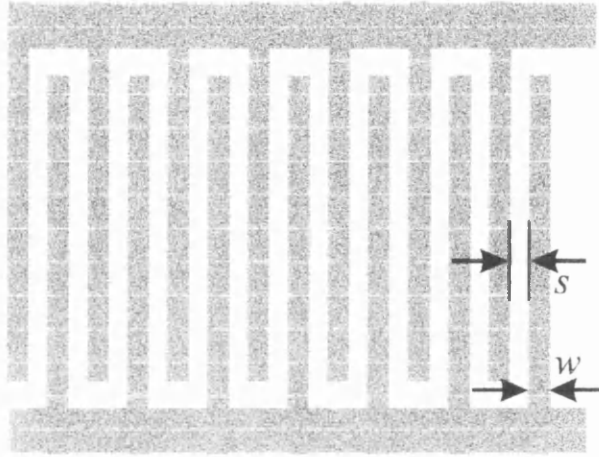


Figure 6.7: The electrodes of a possible electrostatic drive are shown. The width of the strips is 'w' and they are separated by 's'. It is anticipated that 's' will be approximately equal to the separation of the electrodes and the test mass.

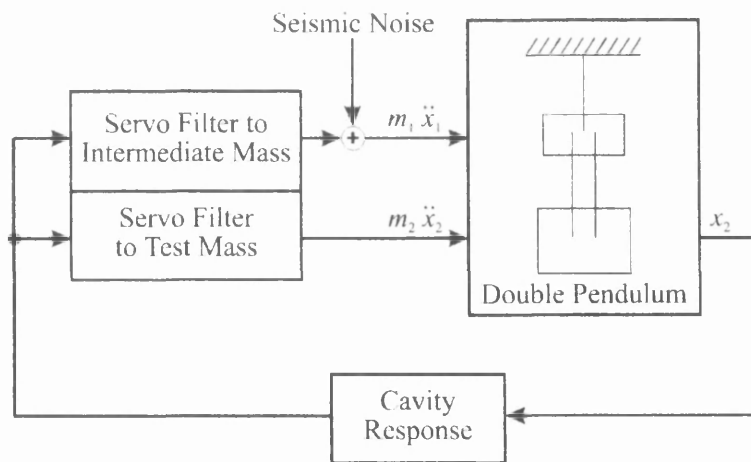


Figure 6.8: Servo with Split Feedback Topology.

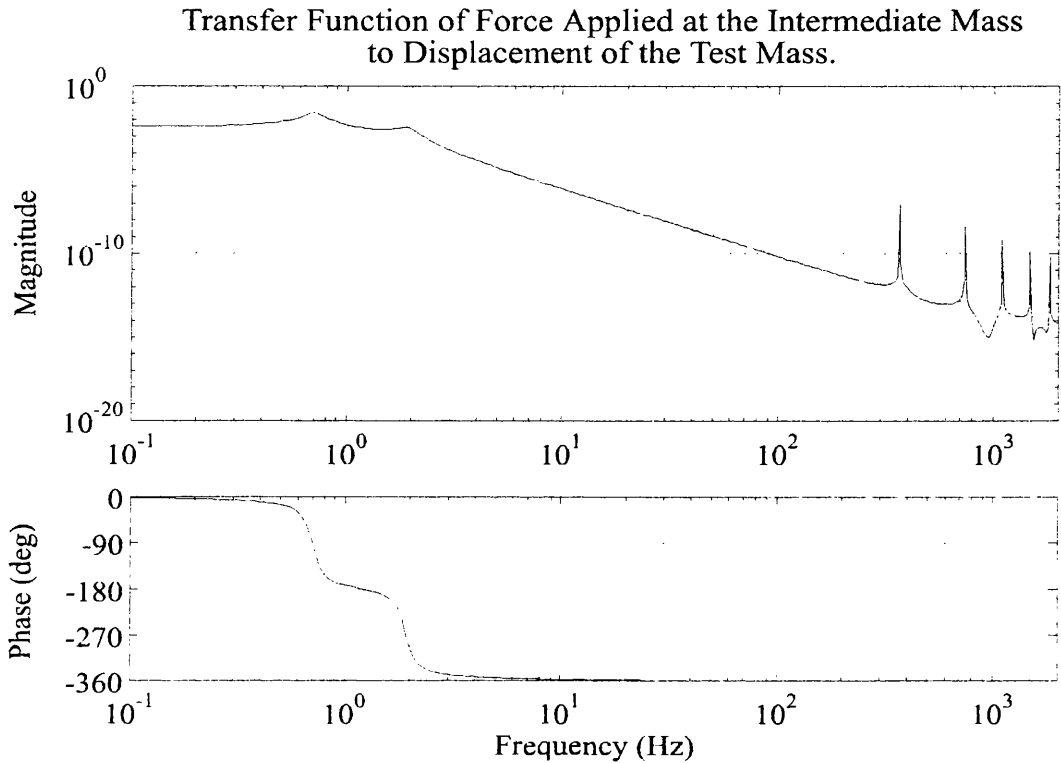


Figure 6.9: *Transfer Function of Force at Intermediate Mass to Test Mass Displacement.*

applied to the back face of the test mass: namely that the elastic properties of the intervening material limit the bandwidth that can be achieved. The actuation applied at the intermediate mass must propagate down the suspension wires to the test mass. Thus, the transfer function has resonant peaks associated with the transverse modes of the suspension wires (these are discussed in Section 4.7). The transfer function for force applied at the intermediate mass to test mass displacement is shown in Figure 6.9. (This is the result of the state-space model produced by `fb_x1.m` in Appendix A.) The Q factors of the transverse modes are calculated assuming the internal friction of the wire is described by a structural damping term and thermoelastic damping (see Section 7.4.1).

To reduce the range required by the test mass actuator, the open loop servo gain of the path to the intermediate mass must be greater where the displacement noise is largest. The response of the test mass to a force applied at the intermediate mass

falls off at the rate of $1/f^4$ above both pendulum normal modes. This compares to a fall-off of $1/f^2$ for feedback applied to the test mass. Thus, the cross-over from feedback dominated by actuation at the intermediate mass to feedback dominated by actuation at the test mass should naturally occur above the upper longitudinal mode of the double pendulum. The higher this frequency can be pushed, the greater the reduction in range required by the actuator to the test mass.

The frequency of the cross-over is limited by the transverse resonances of the suspension wires. (This is completely analogous to the internal modes limiting the bandwidth of feedback to the test mass.) It is not possible to damp these resonances since this would inevitably increase their thermal noise contribution (see Section 7.4). Electronic filters can be used to suppress the peaks in the transfer function caused by these modes. Using such an approach, a cross-over at 30 Hz is considered possible where the fundamental transverse modes occur at ~ 400 Hz and the suspension wires are made from steel and consequently have Q factors $\sim 2 \times 10^5$). The open loop gain for both feedback paths is shown in Figure 6.11. The unity gain point is nominally 2 kHz.

The filtering considered in the servo model was as follows: a transitional differentiator was used to *flatten* the response of the optical cavity up to 10 kHz. To make the unity gain point stable requires a further transitional differentiator acting between 700 Hz and 5 kHz.

This, in itself, is stable and sufficient to lock the cavity with the *proviso* that the actuator has a large enough range. When the feedback to the intermediate mass is implemented it is not necessary to *dc* couple the feedback to the test mass. Clearly, it is very desirable to *ac* couple this at as high a frequency as possible in order to minimise the feedback signal produced in response to seismic noise. To achieve good attenuation at ~ 1 Hz while maximising the phase margin at the cross-over, a resonant high-pass filter peaking at 5 Hz with a Q factor of 3 was considered.

In the feedback path to the intermediate mass, a transitional differentiator is required to give phase margin at the cross-over frequency. This acts between 10 Hz and 80 Hz. Attenuation must be included at the transverse mode frequencies. This can be efficiently achieved by using Scult ty filters. These have a transfer func-

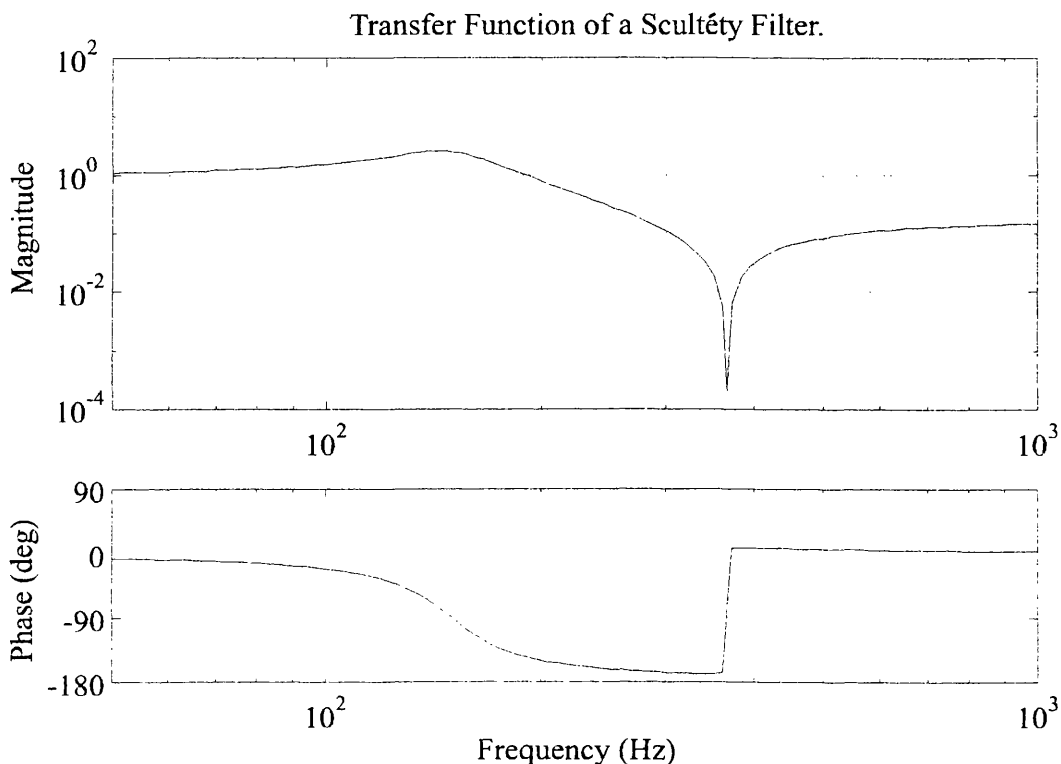


Figure 6.10: *Transfer Function of a Scultéty Filter: Resonant Peak at 150 Hz, Q factor of 3; Notch Tuned to Transverse Mode Frequency 366 Hz.*

tion as shown in Figure 6.10. The resonant peak is placed at a frequency between the cross-over and the transverse mode frequency. The Q factor of the peak is chosen so that it does not return above the feedback gain to the test mass. The notch associated with the filter should be tuned to the transverse mode frequencies. The filters considered had peaks at 150 Hz and 200 Hz with Q factors of 3 and 4 respectively. They also give high frequency suppression by a factor of $(f_{\text{notch}}/f_{\text{peak}})^2$. An additional passive filter acts from 200 Hz. A total attenuation of greater than 3600 is required at the first resonance and 530 at the second. This is mostly achieved using the notch of the Scultéty filter. Here an attenuation of 2000 is assumed from the notch alone. In practice, this may require more filtering.

It is assumed that the dominant source of displacement of the test masses is seismic motion of the suspension point in the horizontal direction. Vibrations of the ground are assumed to be flat with frequency below 1 Hz and to vary as $1/f^2$

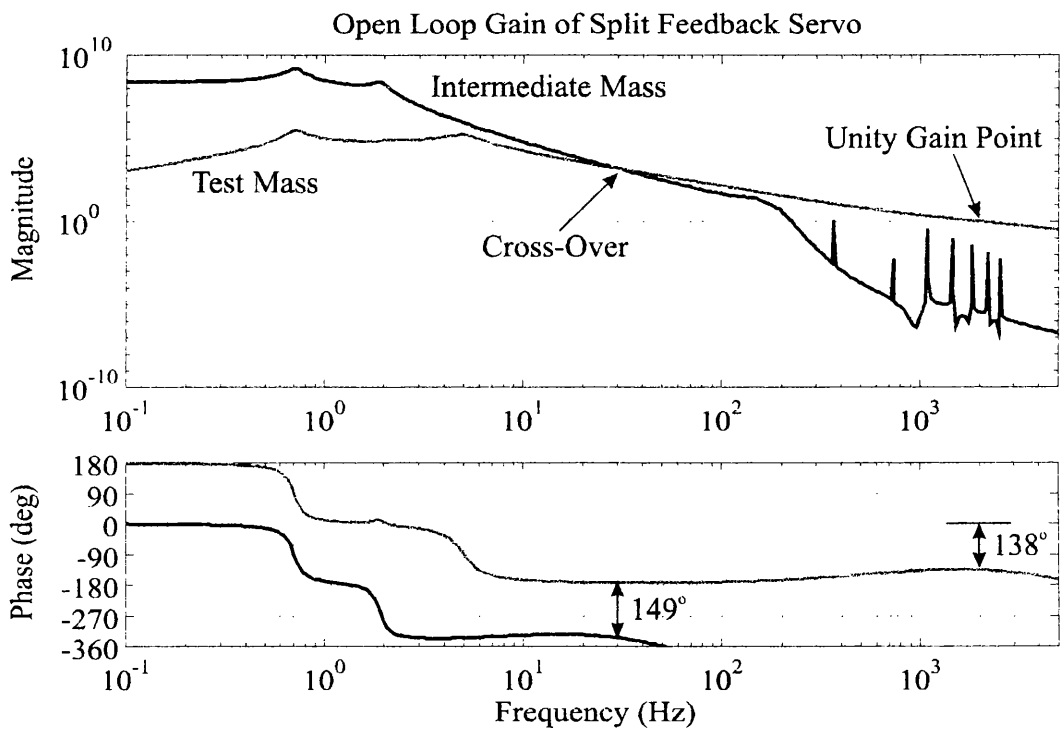


Figure 6.11: *Open Loop Gain for a Split Feedback Topology.*

above 1 Hz. (Only frequencies up to 100 Hz will be considered.) Seismic motion of the ground is filtered by the seismic isolation stacks. For the four layer stacks used in the Glasgow prototype the horizontal frequencies are 2.0 Hz, 9.0 Hz, 16.5 Hz and 20.5 Hz. These frequencies and the transmissibility of the stacks were predicted and verified by M^cLaren [45].

The double pendulum is also considered to be damped by the local control servos as described in Chapter 5. The longitudinal modes have Q factors of 6 and 2 for the lower and upper frequency modes respectively.

The servo was modelled using state-space techniques. This allowed the calculation of the closed loop response of the servo to a force input at the intermediate mass. Displacement of the suspension point produces a force at the intermediate mass given by

$$F_{x_1} = \frac{T_1}{l_1} x_0 \quad (6.11)$$

where T_1 is the tension in the upper wire and l_1 is its length. The relevant transfer functions are the ratios of feedback force at each actuator to input force. These can be multiplied by an estimate of the input force from seismic motion of the suspension point to give the spectral density of feedback force required. When only horizontal seismic motion is considered the frequency spectrum of feedback required is shown in Figure 6.12. Results for a split feedback topology are compared to the actuation required for a simple servo acting on the test mass only.

The *rms* value can be calculated by integrating the power spectral density over frequency axis and taking the square root of the answer. The integration is limited from 0.1 Hz up to 100 Hz since the contribution outside this band was negligible. The *rms* values of feedback force required are presented in Table 6.2. The results include a factor of 2 to account for all four suspended test masses of the Glasgow prototype and a safety factor of 10 to give headroom for statistically large excursions or impulse events. The value shown for feedback solely to the test mass can be compared to the maximum force available using the present system of three coils and magnets; this is $\sim 1.6 \times 10^{-3}$ N.

As can be seen from the results, application of feedback to the intermediate mass

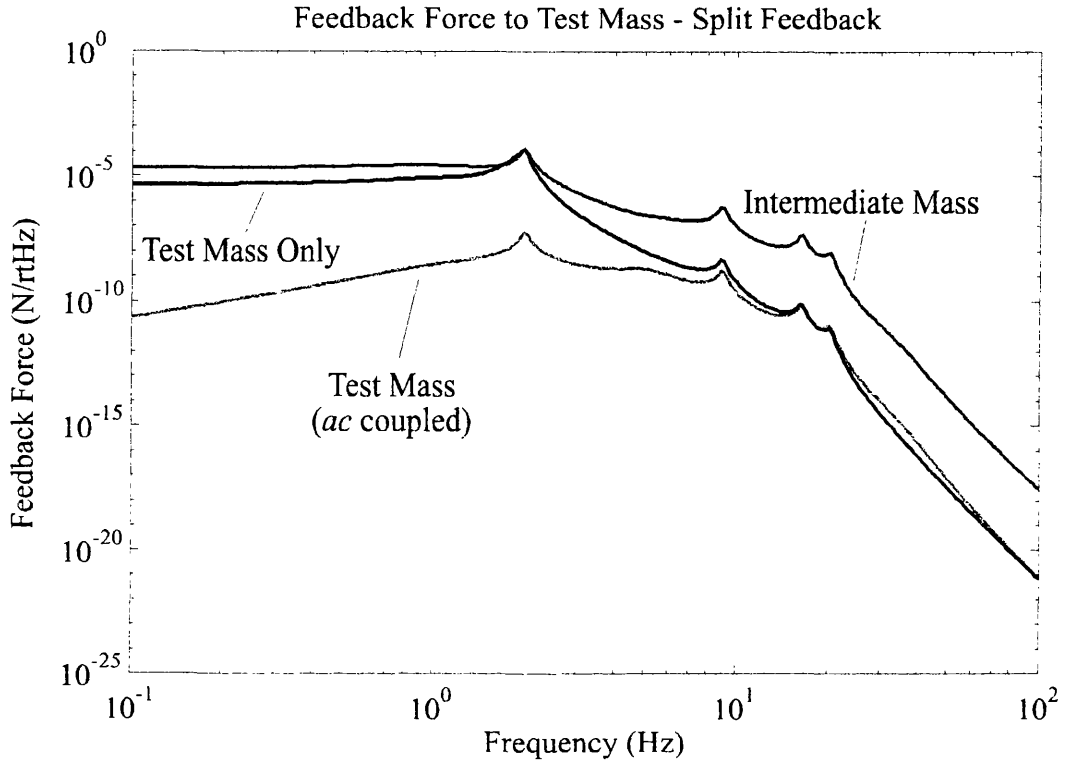


Figure 6.12: *Feedback Force Required to Accommodate Seismic Vibrations.*

Feedback Actuator	<i>rms</i> Force (N)
Intermediate Mass and Test Mass	1.1×10^{-3}
Test Mass only	4.6×10^{-7}
	1.0×10^{-3}

Table 6.2: *Feedback Range Requirements.*

reduces the range required by a factor of about 2000 for the conditions stated above. In practice, cross-coupling of vertical motion is significant in the displacement noise of the test masses. It is estimated that vertical cross-coupling exceeds the horizontal motion at frequencies above ~ 7 Hz (given that the levels of ground motion in the horizontal and vertical degrees of freedom are equal). However, at 7 Hz the seismic excitation is an order of magnitude below the peak value at 2 Hz (corresponding to the first horizontal resonance of the isolation stack). Furthermore, ground motion is expected to be less at higher frequencies. The author suggests that cross-coupling effects would, at worst, increase the range requirements by a factor of ~ 2 . This contribution would mainly arise from resonant enhancement of ground motion by the first vertical resonance of the isolation stack.

6.6 Conclusion

The range required by feedback elements to lock a suspended mass, Fabry-Perot cavity is determined by the level of seismic excitation of the suspension point. Passive seismic isolation stacks can resonantly enhance this level at low frequency and increase the range requirements: they should therefore be well damped. Active suppression of seismic motion could also be used to reduce the actuator range.

Vertical motion of a coil-magnet feedback actuator is shown to give a significant coupling of seismic noise to the test mass. The feedback actuator should be isolated in a similar manner to the test masses, for example: a suspension incorporating a low frequency vertical spring.

It has been shown that a split feedback topology can substantially reduce the range requirement of the actuation direct to the test mass. This implements low frequency feedback to the intermediate mass. The double pendulum suspension is ideally suited to this feedback topology. This is a considerable advantage of a double pendulum compared to an equivalent single stage pendulum.

Chapter 7

Thermal Noise

7.1 Introduction

In [49] Callen and Welton obtain a relationship, “between the generalized resistance and the fluctuations of the generalized forces in linear dissipative systems.” This relationship is known as the *fluctuation-dissipation* theorem. The test mass suspension is, ideally, a linear system. This is true when sufficiently small perturbations are considered so that the suspension materials do not exceed their yield stress. In this case, the suspension wires can be considered as linear springs and provide restoring forces proportional to the displacement of the test mass or intermediate mass. Dissipation is present in the system because friction is associated with perturbations of the linear springs (*i.e.* the suspension wires). The suspension is, therefore, subject to fluctuations in the generalised forces associated with the linear springs (*e.g.* fluctuations in the wire tension). Fluctuations in the generalised forces, \hat{F}_{th} , are described by

$$\hat{F}_{th} = \sqrt{4k_B T R(\omega)} \quad (7.1)$$

where k_B is Boltzmann’s constant and T is the absolute temperature. The dependence on temperature leads to this form of noise being termed *thermal noise*. It can be interpreted as a manifestation of the thermal motion of the constituent atoms of the suspension. $R(\omega)$ is the generalised resistance of the linear spring and is the real

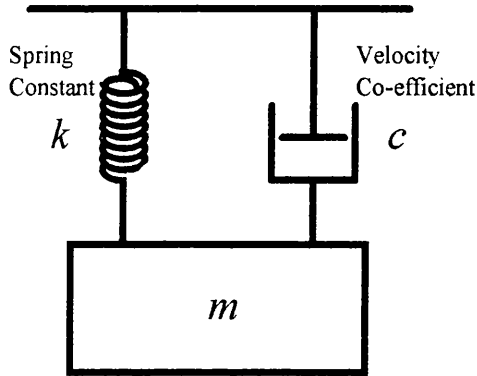


Figure 7.1: *Ideal Spring Damped by Viscous Dash Pot.*

part of its impedance. For a mechanical system the impedance is defined as

$$Z(\omega)_{\text{mech}} = \frac{\text{Applied Force}}{\text{Resultant Velocity}} . \quad (7.2)$$

There are three sources of thermally driven fluctuations that are relevant to the suspension of a test mass:

1. the modes of the pendulum;
2. the transverse modes of the suspension wires, and
3. the internal modes of the test mass.

Each of these can produce sufficient motion of the test mass to limit the sensitivity of an interferometric gravitational wave detector at frequencies of interest. Therefore, it is desirable to estimate the level of thermal noise produced in each case. This allows the optimisation of the suspension in terms of configuration and choice of materials.

7.2 Internal Friction

A dissipative linear spring (such as the wires of the test mass suspension) can be represented by an ideal spring in parallel with a dash pot (see Figure 7.1). The mass, m , moves only up or down without tilting. The dash pot produces a viscous

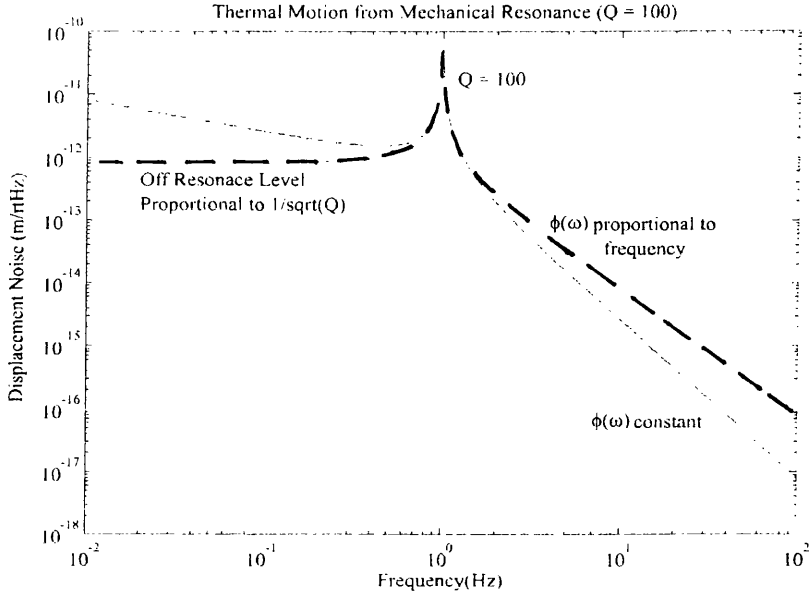


Figure 7.2: *Thermal Noise of a Damped Resonance.*

force proportional to the velocity of the mass. Thus, the equation of motion is

$$F_z = m\ddot{z} + c\dot{z} + kz . \quad (7.3)$$

When harmonic motion is assumed the mechanical impedance is

$$Z_{\text{mech}} = \frac{F_z}{\dot{z}} = \frac{-m\omega^2 z + i\omega cz + kz}{i\omega z} \quad (7.4)$$

and hence the mechanical resistance is

$$R_{\text{mech}} = \Re\{Z_{\text{mech}}\} = c . \quad (7.5)$$

This determines the magnitude of the force fluctuations in the spring, as given by Equation 7.1. The spectral form of the displacement noise of the mass can be obtained from the frequency response of the system (given in Equation 4.35).

For many materials the internal friction is not viscous in form. It is a useful generalisation to describe damping in terms of a loss tangent, $\phi(\omega)$, such that Hooke's law becomes $F_x = -k[1 + i\phi(\omega)]x$. Section 4.6.2 contains a discussion on this characterisation. The mechanical resistance of such a spring is then expressed by

$$R(\omega) = \frac{k\phi(\omega)}{\omega} . \quad (7.6)$$

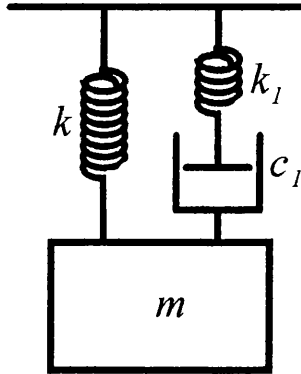


Figure 7.3: *An Ideal Spring Damped by a Relaxation Process.*

For the case where $\phi(\omega) \propto \omega$ this is equivalent to viscous damping.

In many materials the loss tangent is observed to be constant over a wide range of frequencies relevant to the detection of gravitational waves [50]. This is known as *structural damping*. When the loss tangent is constant with frequency the fluctuations in the generalised forces have a $1/\sqrt{\omega}$ dependence. The spectral forms of the displacement noise for viscous and structural damping of identical resonant systems are shown in Figure 7.2. Clearly, when the resonant frequency is above the frequency band of interest the noise due to structural damping is greater than that due to viscous damping. Conversely, when the resonance is below the frequency band of interest the noise is reduced. An estimation of the thermal noise in a system requires a knowledge of the frequency dependence of $\phi(\omega)$.

The characterisation of internal friction by $\phi(\omega)$ becomes more important when considering losses that arise from relaxation processes. The damping of an ideal spring by a relaxation process is represented in Figure 7.3. (The system of a spring and dash pot in series is called a Maxwell unit.) The relaxation process has a corresponding characteristic time $\tau = c_1/k_1$. Essentially, on a time scale shorter than τ the dash pot does not respond, however, on a time scale longer than τ the dash pot is able to respond and *relaxes* the series spring. The loss tangent produced by such a damping mechanism is

$$\phi(\omega) = \Delta \frac{\omega\tau}{1 + \omega^2\tau^2} \quad (7.7)$$

where Δ is the *relaxation strength* (with $\Delta = k_1/k$). This has the form of a Debye

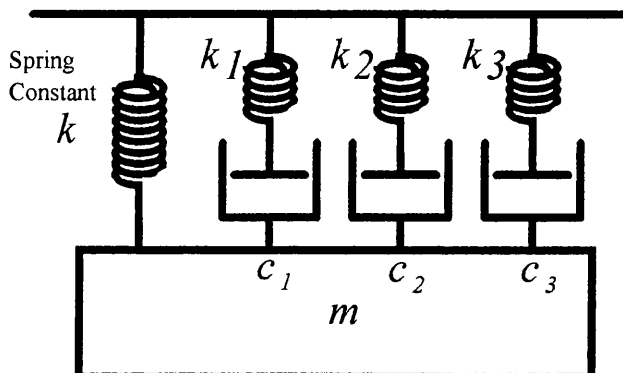


Figure 7.4: *Relaxation Processes of an Ideal Spring.*

peak with characteristic frequency $1/2\pi\tau$ (Hz).

One way in which the loss tangent can be constant with frequency is that several relaxation processes with different relaxation times are present. Such a system is shown in Figure 7.4. Considering an arbitrary number of Maxwell units allows the loss tangent to become arbitrarily uniform over a selected frequency band.

7.2.1 Thermoelastic Damping

An example of a relaxation process is heat flow. In a thin wire this produces *thermoelastic damping*. When a wire is bent one side is in compression and a rise in temperature is produced. The other side is extended and, consequently, the temperature is decreased. Therefore, a temperature gradient exists across the wire. On long time scales heat flows to equalise the temperature. This is an irreversible process which produces a loss to the system since the thermal energy is no longer available to drive the restoring force. The characteristic time scale of this relaxation process was shown by Zener [51] to be

$$\tau = 7.37 \times 10^{-2} \frac{d^2 \rho c_{\text{heat}}}{\kappa} \quad (7.8)$$

where d is the diameter of the wire; ρ is the density; c_{heat} is the specific heat capacity, and κ is the thermal conductivity of the material. The factor of 7.37×10^{-2} arises from considering a wire of circular geometry. Zener also showed that the relaxation

strength is

$$\Delta = \frac{Y\alpha^2T}{c_{\text{heat}}} \quad (7.9)$$

where Y is the Young's Modulus; α is the coefficient of thermal expansion, and T is the absolute temperature. In the case of steel suspension wires the loss tangent can be modelled as the sum of a structural damping term and the thermoelastic damping term obtained from Equation 7.7 [52]. The magnitude of the structural damping term has been measured to be approximately 5×10^{-4} (by the author: see Figure 7.12 and also by Kovalik [52]).

The thermoelastic damping mechanism applies to deformations of the suspension wires where compression and expansion occur simultaneously. This is produced when the wire is bent. For extension and torsion of the wire, no temperature gradient is generated so no heat is able to flow.

The model of thermoelastic damping, as proposed, is unlikely to hold for wires under very high tension. In this case, the bending length is very short. This allows significant heat to flow along the wire into the clamp holding the end. Results from Saulson *et al* [53] suggest that this is indeed the case. Preliminary modelling suggests that the thermoelastic damping peak is broadened to higher frequency but the maximum loss is reduced. This is because heat flow into the clamp occurs on a shorter time scale than across the wire but with a comparable relaxation strength.

7.3 Thermal Noise in a Pendulum

In Section 4.3 the restoring forces due to deformations of the suspension wires are discussed. Each of these is subject to internal friction and, therefore, results in fluctuations of the restoring force. To estimate the thermal noise due to the modes of the test mass suspension these fluctuations are propagated through the suspension to the sensed displacement of the test mass. This is possible using the state-space model of the pendulum described in Section 4.5.

It is easy to see that dissipation in a wire has associated fluctuations in tension. This is the most straight forward realisation of the fluctuation-dissipation theorem applied to mechanical systems. There are also torques applied to the pendulum

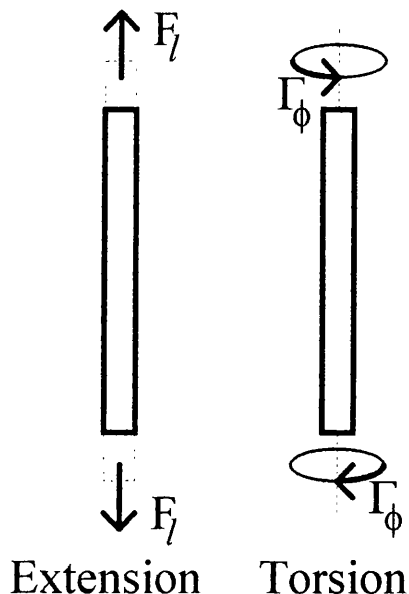


Figure 7.5: *Thermal Noise Inputs for each Suspension Wire (extension and torsion).*

masses associated with loss produced by torsion of the suspension wires. Both of these mechanisms are illustrated in Figure 7.5.

Much harder to obtain (but extremely important) are the forces applied to the pendulum that arise from losses associated with bending the wires. The energy stored in bending the wire is described by the bend at the top, the bend at the bottom and the horizontal displacement of the ends of the wire. These are the bending parameters X , α and β defined in Section 4.3.3. Equation 4.8 expresses the energy in terms of these coordinates. The existence of cross-terms in this expression shows that the coordinates X , α and β are not orthogonal. The change of variables

$$\alpha = \eta - \zeta \quad (7.10)$$

$$\beta = \eta + \zeta \quad (7.11)$$

$$X = \xi + l\eta \quad (7.12)$$

allows the elastic energy to be expressed as

$$E(\xi, \zeta) = b \left[\frac{\xi^2}{2} + \frac{L^2 \zeta^2}{2} \right] \quad (7.13)$$

where $L^2 = l^2 - 4\lambda l + 4\lambda^2 \approx l^2$. It is clear that ξ and ζ are orthogonal. This allows the thermal fluctuations of their generalised forces to be applied as uncorrelated

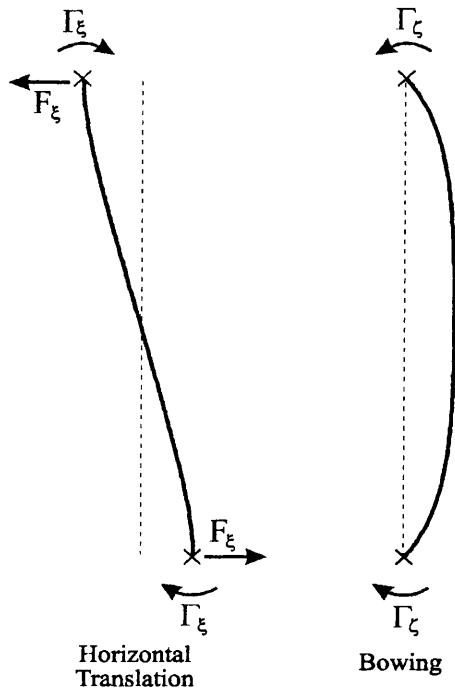


Figure 7.6: *Thermal Noise Inputs for each Suspension Wire (bending).*

noise sources. Figure 7.6 shows the generalised forces associated with ξ and ζ . The transfer functions of the applied forces to sensed displacement noise are calculated using the state-space model of the pendulum. This allows the thermal noise to be estimated given a knowledge of the loss tangent, $\phi(\omega)$. Because bending of the wires occurs, the thermoelastic effect should be included when calculating $\phi(\omega)$.

7.3.1 Analysis of a Single Pendulum

In this section the dependence of thermal noise on the dynamics of a single pendulum will be investigated. There are two main parameters that can vary in such a system: the height above the centre of mass at which the suspension wires are attached, and the height at which the displacement of the test mass is measured by the interferometer.

A fused silica cube of dimensions $100\text{ mm} \times 100\text{ mm} \times 100\text{ mm}$ was used to represent a suspended test mass. This can be suspended by two wires attached to the sides of the mass. The height at which the wires are attached can be varied.

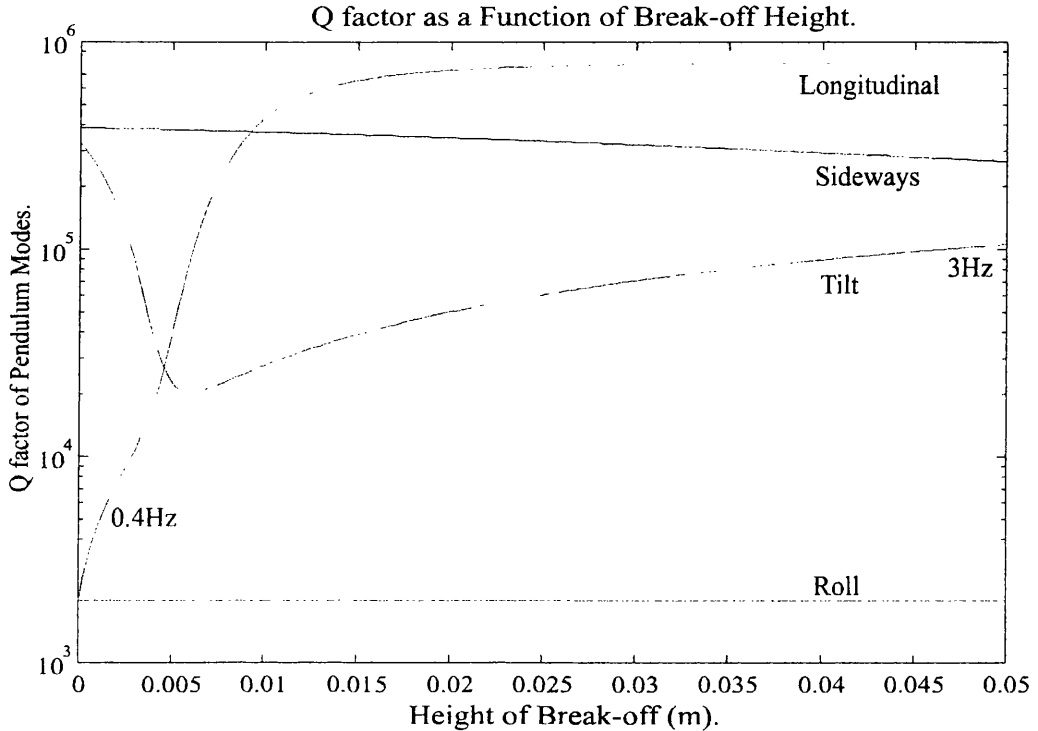


Figure 7.7: *Q factor of Pendulum Modes Against the Height of the Break-off Point.*

The length of the suspension wires is also varied so that the distance between the suspension point and the centre of mass is kept constant. Longitudinal motion and tilt of the mass are strongly coupled in this configuration. Since there are two degrees of freedom, the coupled system has two normal modes. The restoring force for the longitudinal degree of freedom is mainly due to the gravitational field. Thus, the loss associated with longitudinal motion is small. In contrast, tilting the mass is a lossy motion because much of the restoring force is produced by bending the suspension wires. The dynamics of this system can be solved and the Q factors of the normal modes calculated for a variety of attachment heights. It is also useful to compare this to the two coupled modes associated with sideways motion and roll. The Q factors for all these modes are plotted in Figure 7.7.

The frequency of the tilt mode increases as the point of attachment is raised. This is because the gravitational restoring force increases in strength. For an attachment height of about 5 mm above the centre of mass, the frequencies of the longitudinal and tilt modes are almost identical. At this point the coupling between the degrees

of freedom is strongest. In fact, the phase of tilt motion to longitudinal motion is reversed above and below this point. The highest Q factor is always associated with the greatest longitudinal motion.

For sideways motion, the mass is constrained by the wires to move purely in translation without coupling to roll motion. Thus, bending must occur at the top and bottom of the wire. Longitudinal motion is not subject to this constraint since the mass is essentially free to tilt. Thus, bending is only produced at the top of the wire. It is reasonable to expect that this should incur only half the loss compared to sideways motion. The longitudinal mode, therefore, has an inherently higher Q factor than the sideways mode. The graph shows that the longitudinal mode (when the tilt coupling is strong - *i.e.* at an attachment height of 0.05 m) has a Q factor precisely double that of the sideways mode (when the wires are attached at the centre of mass).

The pendulum thermal noise was calculated for different attachment heights and for different spot heights on the mirror. The results are shown in Figure 7.8. The height of attachment has a small effect: the thermal noise gets marginally worse at higher attachment points. The spot height on the mirror produces the greatest effect. It is evident that there is a minimum in the sensed displacement for a spot height ≈ 5 mm below the centre of mass. If thermal noise from the pendulum were the dominant limiting noise source in the detector then positioning the spot at this minimum would be advantageous. However, the advantage is typically small and an offset in spot height can couple seismic noise (see Section 3.2.2). Further, it should be noted that the spot cannot be located close to the edge of the mirror because a significant fraction of the spot intensity would then miss the mirror. A safety margin of at least 3 beam radii should be allowed.

7.3.2 Suspension Topology of a Double Pendulum

There are several possible topologies for suspending a test mass as a double pendulum. It is important to permit the orientation (both tilt and rotation) of the test mass to be controlled by forces applied at the intermediate stage. Figure 7.9 shows two possibilities which allow this. The essential difference is that if four wires are

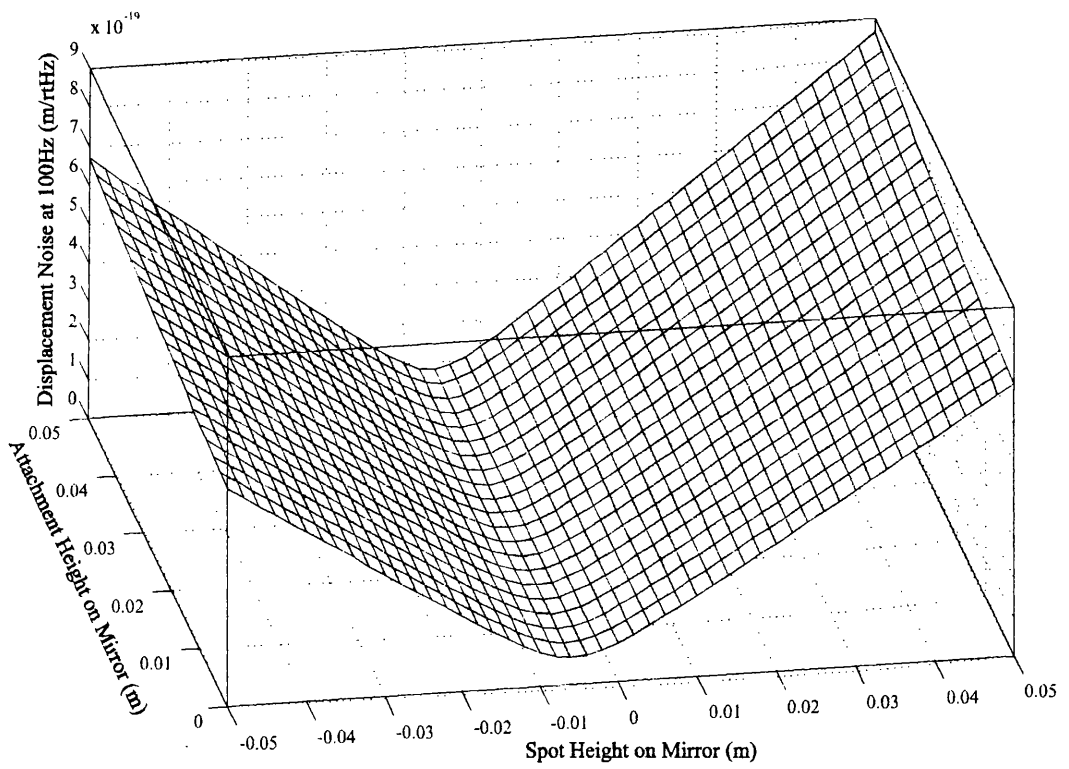


Figure 7.8: *Thermal Noise for Single Pendulum as a function of Attachment Height of Wires and Spot Height on the Mirror.*

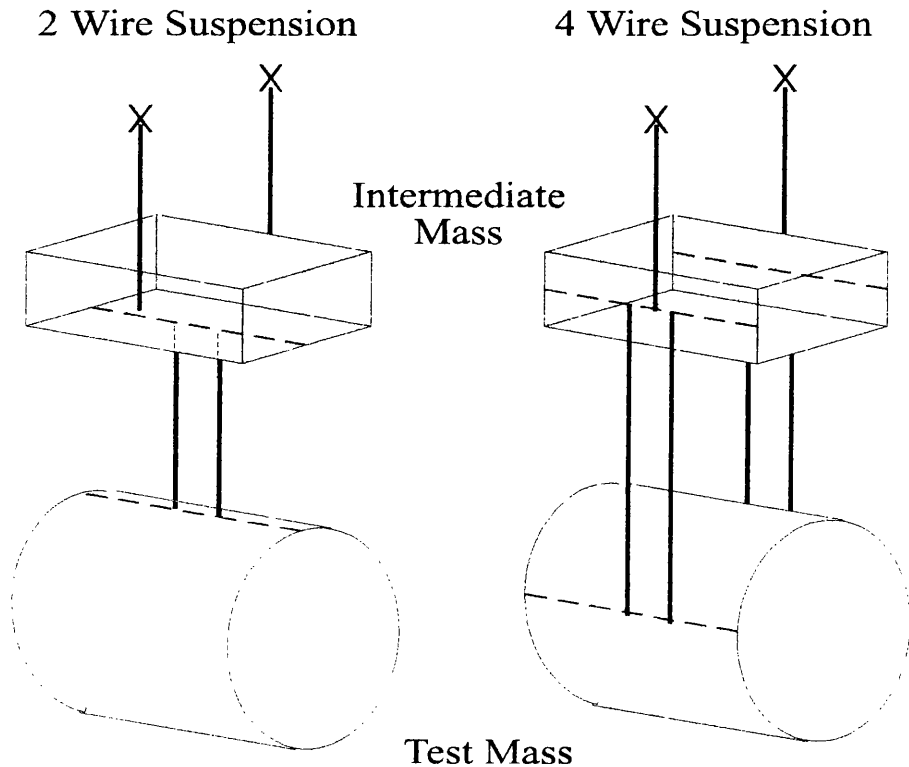


Figure 7.9: *Configurations for Suspending a Test Mass.*

used on the lower stage, the attachment points can be close to the level of the centre of mass; if two wires are used then it is only possible to attach them to the top of the mass. It is an important issue to resolve the advantages and disadvantages of both these techniques. For a gravitational wave detector where sensitivity at low frequencies (down to ~ 10 Hz - see Chapter 1) is desired the thermal noise arising from the pendulum modes of the test mass suspension is a critical noise source.

The pendulum thermal noise is now considered for possible test mass suspensions for the GEO 600 project. This requires the construction of a test mass suspension that allows good sensitivity above 50 Hz. Four possibilities are compared: the suspension with two or four wires (as illustrated in Figure 7.9) using in each case either steel wires or fused silica fibres. The thermal noise is calculated for each of these cases as a function of the spot height on the test mass. The results are shown in Figure 7.10.

The cross sectional area was chosen so that the test mass loaded the wires to

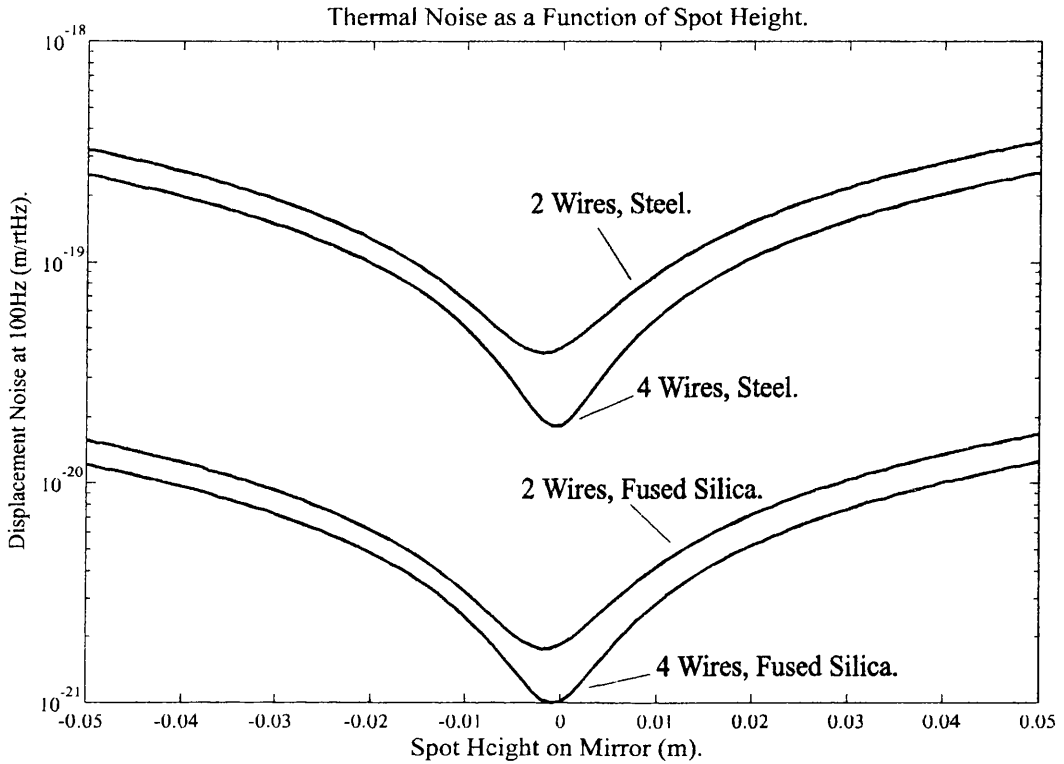


Figure 7.10: *Thermal Noise in Double Pendulum Suspensions.*

approximately one third of their breaking stress. For steel this was 7.5×10^8 Pa; for fused silica fibres a stress of 2.7×10^8 Pa was assumed. The loss tangent for fused silica fibres was assumed to be 2×10^{-7} – certainly a Q factor of 3.5×10^6 has been measured for fused silica ribbons by Rowan, Twyford and Hough, here at Glasgow. The loss tangent for steel was taken to be 5×10^{-4} (from measurements presented in Section 7.4.2).

The intrinsic loss of fused silica is smaller than that of steel by approximately three orders of magnitude. This means that the thermal noise should be about 30 times less for fused silica suspensions. This is, to some extent, offset by the need to use fused silica fibres of greater diameter. However, the predicted level of thermal noise for fused silica is substantially less than that for steel.

The difference between a two wire and four wire topology is more subtle. By analysing the energy stored in bending a stiff wire (see Equation 4.8) the loss is introduced by the parameter

$$b = \frac{\sqrt{YIT}}{l^2} \quad (7.14)$$

where Y is the Young's Modulus, I is the moment of cross-section of the wire, T is the applied tension and l is the wire length. If the wires are to be maintained at the same fraction of their breaking stress then the total cross sectional area should remain constant. Taking into account the dependence of I upon the radius and T upon the number of wires, the loss for all wires varies as $1/\sqrt[4]{N}$ where N is the number of wires. Thus, the thermal noise should be factor of $\sqrt[4]{2}$ greater for the two wire case compared to that for four wires. Further, the total length of the pendulums is fixed. This means that the wire length is shorter when two wires are used because they must be attached to the top of the test mass. For the pendulums considered this further increases the thermal noise for the two wire suspension by factor of $\sqrt{2}$ compared with using four wires. (This point is significant because the test mass radius is comparable to the length of the suspension wires. This is the case in all reasonable suspensions.)

It is evident that the topology of the test mass suspension affects the level of thermal noise expected from the pendulum modes. A four wire suspension is seen to be better than a two wire suspension. However, technical issues are more likely to dominate the decision. For example, optical contacting of fused silica fibres to the test mass is more reliable when the joint is subject to tension rather than shear [54]. A joint in tension requires the attachment to be to the top of the test mass, thus, favouring a two wire suspension.

One advantage of a two wire suspension is that there are half the number of transverse modes of the suspension wires. The transverse modes of the suspension wires are discussed in Section 4.7.

7.3.3 Conclusion

The thermal noise associated with the pendulum modes has been modelled using thermally driven fluctuations of the wire stress. These are then propagated through the test mass suspension using the state-space model. The resultant displacement noise has been calculated for single and double pendulums for different wire topologies in order to optimise the pendulum design for low thermal noise. The most significant factor is the height on the test mass at which the interferometry is con-

ducted. Calculations indicate the existence of a minimum of thermal noise; typically this is just below the centre of mass.

7.4 Transverse Modes of the Suspension Wire

The thermal motion of the transverse modes of the suspensions wires is now considered. An estimate of the resulting displacement noise is made. This is required to specify the minimum Q factor that must be attained so that the off-resonance thermal noise does not limit the sensitivity of a gravitational wave detector.

A model describing these modes is presented in Section 4.7. Although vibrations of the wires couple weakly to the test masses it is still a significant source of displacement noise. To calculate the displacement noise produced by thermal vibrations of the suspension wires fluctuations in the generalised force (as in Equation 7.1) are applied to the system. Then the generalised amplitude, \hat{A}_n , is (adapted from [22])

$$\hat{A}_n^2 = \frac{4k_B T}{\omega m_n} \left[\frac{\omega_n^2 \phi_n(\omega)}{(\omega_n^2 - \omega^2)^2 + \omega_n^4 \phi_n^2(\omega)} \right] \quad (7.15)$$

where ω_n is the resonant frequency, $\phi_n(\omega)$ is the loss tangent and m_n is the effective mass – all refer to the n^{th} mode. The effective mass of all the transverse modes is $0.5 \times m_{\text{wire}}$ (this was noted in Section 4.7). The displacement of the test mass is related to the generalised amplitude by Equation 4.47. This enables the sensitivity limit of the interferometer to be estimated: this should be summed for all modes though only the first few have a significant contribution [55]. The thermal noise power due to the transverse modes is thus given by

$$\dot{x}_{\text{tm}}^2 = \sum_n \frac{8k_B T m_{\text{wire}}}{\omega n^2 \pi^2 m_2^2} \left[\frac{\omega_n^2 \phi_n(\omega)}{(\omega_n^2 - \omega^2)^2 + \omega_n^4 \phi_n^2(\omega)} \right] \quad (7.16)$$

where m_2 is the test mass. This reflects the total from one suspension wire. Typically, there are two or four wires per test mass and two or four test masses in the interferometer. The frequency of the fundamental transverse mode varies for each suspension wire resulting in a number of peaks in the displacement noise spectrum. The off-resonance level should be added for all the wires present in the interferometer.

This analysis considers the thermal noise from each transverse mode to be uncorrelated. This is equivalent to saying that the loss is distributed uniformly in the wire and is not localised to a particular defect in the suspension (*e.g.* friction in the clamps holding the wire ends).

7.4.1 Loss Associated with Transverse Modes

When a wire is tensioned by the loading of a pendulum mass, the loss of the transverse modes are less than the intrinsic loss of the material. Effectively, most of the energy is again stored in the gravitational field and only a small amount is stored in the deformation of the wire. It has been shown by Gonzalez and Saulson [56] that the loss tangent of the n^{th} mode is given by

$$\phi_n(\omega) = \frac{2}{al} \left(1 + \frac{(n\pi)^2}{2al} \right) \phi(\omega)_{\text{mat}} \quad (7.17)$$

where a is defined in Section 4.3.3 and l is the length of the wire. $\phi(\omega)_{\text{mat}}$ is the intrinsic loss of the material. Because a transverse mode involves bending of the wire, thermoelastic damping will contribute to this loss tangent. For a steel wire tensioned at a third of its breaking stress the enhancement of the mode Q factor over the intrinsic material Q is

$$\text{Enhancement} = 2 \times 10^2 \left(\frac{l}{0.37 \text{ m}} \right) \left(\frac{89 \mu\text{m}}{r} \right) \quad (7.18)$$

where r is the wire radius. The enhancement is also a function of the mode number, n , but the effect is small for the first few modes and has been omitted for clarity. The mode frequency is given by

$$f_n = 480 \times n \left(\frac{0.37 \text{ m}}{l} \right) \text{ (Hz)} . \quad (7.19)$$

These are normalised to the dimensions of the wires used to suspend the test masses of the Glasgow prototype. Although the wires in the Glasgow suspension are not quite at this tension it is evident that the transverse modes occur within the frequency band of interest to gravitational wave detection. This causes peaks in the displacement noise spectrum (as shown in Figure 7.11). This is unavoidable. However, if the modes have high Q factors then each resonance will effect only a very narrow frequency band.

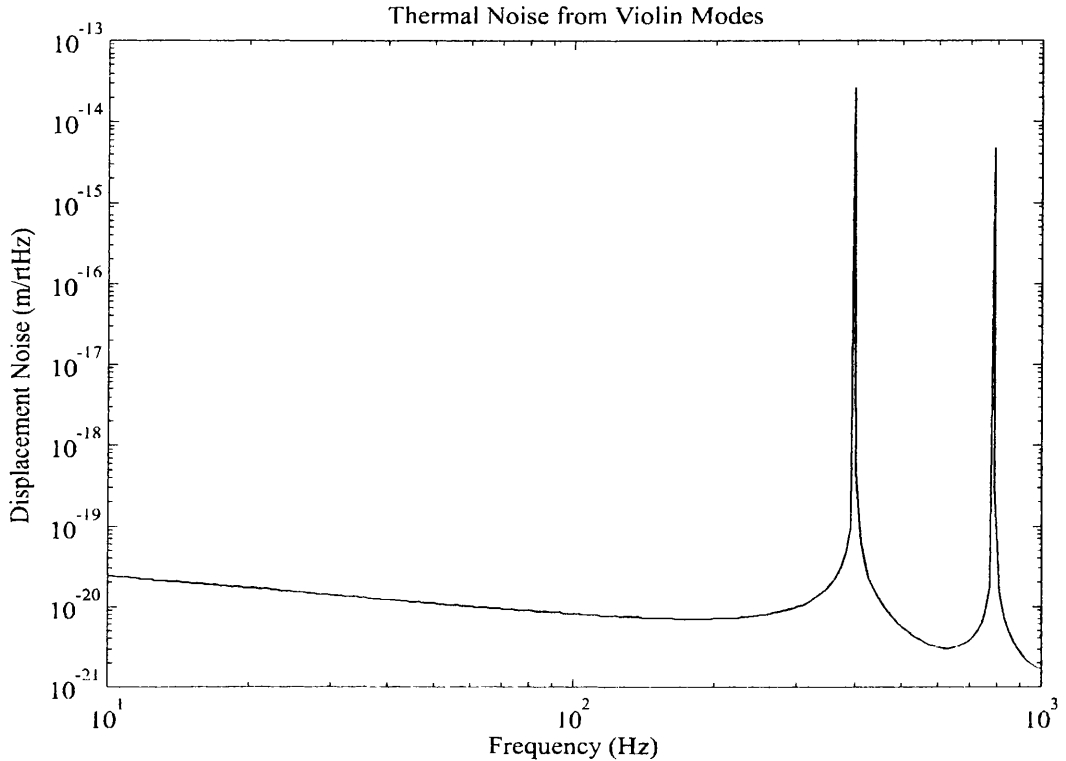


Figure 7.11: *Thermal Noise from Transverse Modes in the Glasgow Prototype.*

7.4.2 Measurements of Q factor of Transverse Modes

The Q factors of the wires used in the Glasgow prototype have been measured *in situ*. They can be easily excited by applying a sinusoidal force at the intermediate mass of the suspension and observing the displacement of the test mass interferometrically. The Q factor can be measured by switching off the excitation drive and recording the ringdown of the mode.

The wires used in the test mass suspensions are steel and have a radius of $89 \mu\text{m}$. At the intermediate mass the ends were clamped between two pieces of Aluminium. The wires run under the test mass and bars made from fused silica are used to define a break-off point. Small grooves were filed in the break-off bars to prevent the wires moving freely. The tension in the wire can be deduced (from Equation 4.44) by a measurement of the transverse mode frequency. Since all the properties of the wires are known, the expected enhancement of the Q factor can be estimated.

The results from the suspensions used in the Glasgow prototype are shown in

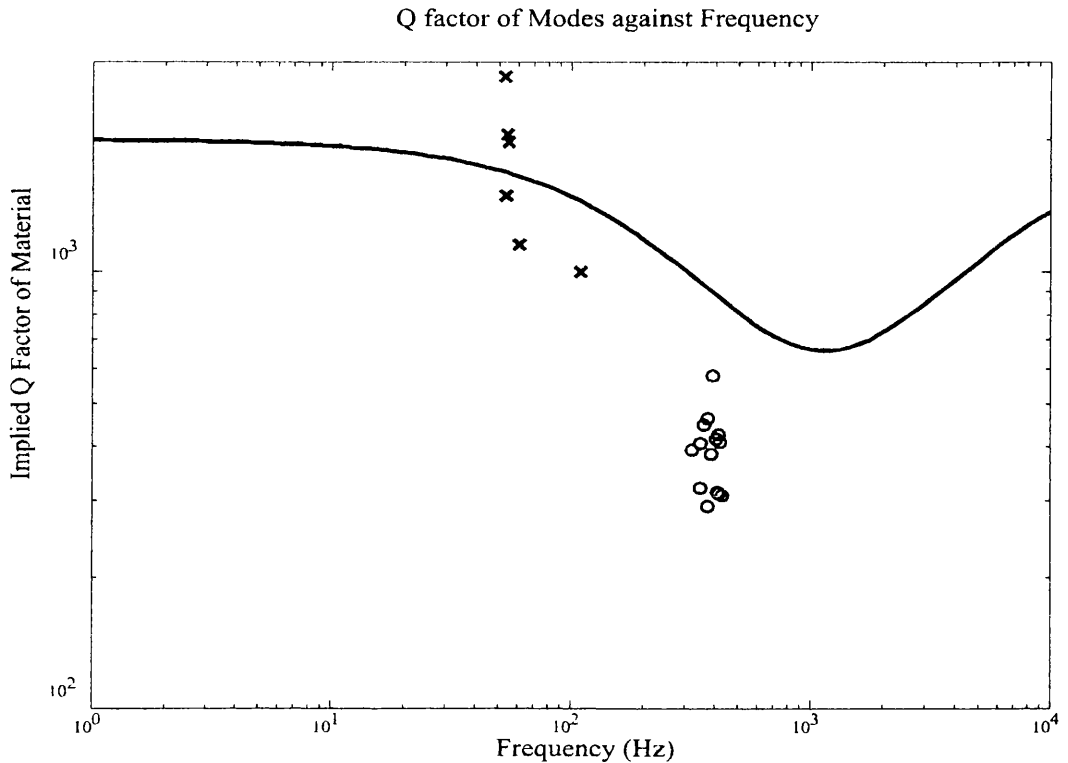


Figure 7.12: The \times 's indicate pendulum modes involving extension of the suspension wires. These are not subject to thermoelastic damping and, thus, are a measure of the structural damping term. The solid line shows the expected Q factor that would be measured for a mode subject to structural damping and thermoelastic damping. This assumes a structural damping term that limits the Q factor to 2000. The \circ 's are results for the transverse modes. These have been divided by the expected enhancement factor to obtain the intrinsic material loss.

Figure 7.12. The points marked with \times 's are for pendulum modes. These produce almost pure extension of the wire and are not subject to thermoelastic damping. Thus, they are a measurement of the structural damping term of the wire material. The solid line marks the Q factors expected when the loss in steel consists of a structural damping term and the thermoelastic damping. Points marked with \circ 's are the fundamental transverse modes. The measured Q factors have been divided by the expected enhancement due to tension to estimate the material loss. The transverse modes are subject to thermoelastic damping.

7.4.3 Conclusion

The results for the transverse modes are a factor of ≈ 2 less than is predicted by the model of loss in steel. This indicates that additional losses are present in the system. Mostly likely, friction associated with the break-off of the wires from the test mass is contributing to the loss.

From measurements on the Glasgow prototype detector, it has been shown that the Q factor of a wire is significantly increased when the gravitational field stores most of the energy.

7.5 Internal Modes of the Test Mass

The interferometer is sensitive to phase shift in the light reflected from the test mass. The phase shift is a measure of the integrated displacement of the test mass face weighted by the Gaussian profile of the optical mode. Apparent displacement (*i.e.* without translation of the centre of mass) can arise if the test mass face distorts in such a way to produce net motion of the area sensed by the optical mode. Such distortion is characterised by a set of normal modes – known as *internal modes*. The internal modes are excited by the Brownian motion of the atoms in the test mass to produce a limitation to the sensitivity of an interferometric gravitational wave detector.

In this section the thermal noise from internal modes in the test masses used in the Glasgow prototype detector will be estimated. These test masses are made from fused silica and have cylindrical geometry with a super-mirror coated on one of the end faces. The dimensions are 63.5 mm in radius by 101.6 mm thick. A total of four mirrors form two orthogonal Fabry-Perot cavities. Two of the mirrors are flat and two have a 15 m radius of curvature. The radius of the optical mode is 1.08 mm on the flat mirror and 1.87 mm on the curved mirror. Both curved mirrors have magnets attached to the rear face: one is required so that feedback can be applied to the test mass (as is discussed in Chapter 6); the other is used to calibrate the detector output. An estimate for the thermal noise sensed by the interferometer should include contributions from all masses. These are added in quadrature.

To make the interferometer less sensitive to tilt or rotation of the test mass the optical mode is centred on the mirror face. Obviously, some of the internal modes have a node at this point and, therefore, do not couple strongly to the interferometer signal. (Any coupling relies on asymmetries in the test mass or misalignment from the face centre.) Thus, to estimate the thermal noise only the axisymmetric modes need to be included. It is assumed that coupling of other modes will be offset by reduced coupling of axisymmetric modes.

It is sufficient to describe an internal mode by its resonant frequency, effective mass and profile of face distortion. The effective mass is best normalised to the actual mass. For a given spot size, the coupling factor between the optical mode and the internal mode can be calculated from the profile of face distortion. This can be incorporated with the effective mass to give an empirical factor, α_n , that characterises the coupling of the internal mode to the optical mode. Modes for which this factor is smaller contribute more to the thermal noise. In principle, each mode will also have a unique loss tangent, $\phi_n(\omega)$; however, this will be assumed to be universal for the test mass material in the frequency range of interest for the detection of gravitational waves. The loss associated with each mode will be further discussed in Section 7.5.4.

The equipartition theorem states that each normal mode has an energy of $\frac{1}{2}k_B T$ associated with its thermal motion. This allows the displacement noise from each mode to be calculated. The thermal noise power is then given by [23]

$$\hat{x}_{\text{int}}^2 = \sum_n \frac{4k_B T}{\alpha_n \omega m} \left[\frac{\omega_n^2 \phi_n(\omega)}{(\omega_n^2 - \omega^2)^2 + \omega_n^4 \phi_n^2(\omega)} \right] \quad (7.20)$$

where ω_n are the internal mode frequencies and $\phi_n(\omega)$ are the frequency dependent loss tangents associated with each mode. The resonant frequencies of the internal modes are, by design, above the frequency band of interest for detecting gravitational waves. Equation 7.20 can then be simplified for $\omega \ll \omega_n$ to give (also from [23])

$$\hat{x}_{\text{int}}^2 = \sum_n \frac{4k_B T}{\alpha_n m \omega_n^2} \frac{\phi_n(\omega)}{\omega}. \quad (7.21)$$

7.5.1 Elastic Equations

The internal modes of a cylindrical mass have been analysed by Hutchinson [38]. He describes how to solve the elastic equations of a cylinder in free space. These boundary conditions are almost identical to those of a cylindrical test mass suspended by thin wires. Gillespie and Raab [23] have recently adapted Hutchinson's work to the study of test masses for use in gravitational wave detectors. Their conclusions are now discussed and applied to the test masses of the Glasgow prototype.

It can be seen from Equation 7.21 that the contribution to thermal noise power from a mode is inversely proportional to the square of its resonant frequency. However, Gillespie and Raab found that some higher order modes have a concentration of motion at the centre of the test mass face and, therefore, strongly couple to the optical mode. Thus, the value of α_n can be sufficiently small so that the mode is still significant. In fact, they suggest that α_n varies as $1/\omega_n$. If the optical mode is centred on the mirror face then only the axisymmetric modes need to be considered. In this case, the mode density (in frequency space) varies linearly with ω_n . When all these factors are taken into account, the modes in equal frequency intervals contribute equally to the thermal noise power. Thus, the total thermal noise power rises linearly with the maximum resonant frequency of internal mode considered.

It is only when the acoustic wavelength is of order the spot diameter that the internal modes become decoupled from the optical mode. This happens because the distortions are averaged out over the area sensed by the optical mode. The frequency, f_{\max} , up to which internal modes should be considered is given by

$$f_{\max} = \frac{c}{2w} \quad (7.22)$$

where w is the spot radius and c is the velocity of sound in the test mass material. The internal modes are, in fact, a combination of compression waves and shear waves. The two mechanisms have different propagation velocities; these are given in [57] as

$$c_{\text{comp}} = \sqrt{\frac{Y}{\rho} \frac{(1 - \nu)}{(1 + \nu)(1 - 2\nu)}} \quad (7.23)$$

$$c_{\text{shear}} = \sqrt{\frac{Y}{\rho} \frac{1}{2(1+\nu)}} \quad (7.24)$$

where Y is the Young's modulus, ρ is the density and ν is Poisson's ratio for the test mass material. For the purposes of the thermal noise estimate an average of these two numbers should suffice. For fused silica this is about $4.8 \times 10^3 \text{ ms}^{-1}$. For the test masses used in the Glasgow prototype all modes with resonant frequencies up to $\sim 3 \text{ MHz}$ contribute to the internal thermal noise.

The total thermal noise can be estimated by multiplying the thermal noise from the first mode by the ratio of the maximum frequency, f_{max} , and frequency of the lowest mode. The frequency of the lowest internal mode of the test mass is given approximately by

$$f_{\text{min}} \approx \frac{c}{2d} \quad (7.25)$$

where d is the thickness of the test mass. For a cylinder whose radius is equal to the thickness (and hence the volume, $V = \pi d^3$) the total thermal noise from all contributing modes is then, after some substitution, given by

$$\overline{\dot{x}_{\text{int}}^2} \approx \frac{4k_B T}{\pi^{\frac{5}{3}} \rho c^2} \frac{\phi(\omega)}{w\omega} \overline{\left(\frac{1}{\alpha}\right)} \quad (7.26)$$

where $\overline{\left(\frac{1}{\alpha}\right)}$ is a typical value of $1/\alpha$ for the fundamental modes. Results from numerical analysis suggest a value of ~ 2.5 . This corresponds to $\alpha = 0.4$. Table 7.1 shows calculated values of α for the first few modes of the test masses used in the Glasgow prototype detector. These are cross-checked with results from finite element analysis.

7.5.2 Finite Element Analysis

In order to verify the mode shapes produced by solutions of the elastic equations, the internal modes were calculated using finite element techniques. The test mass is divided into many elements whose coupled dynamics can be solved. The edges of these elements define a mesh with nodes located at their corners. Finite element analysis produces the amplitude of the position perturbations of the nodes and so describe the dynamics of each mode. A limitation of this method is that only those modes which are adequately sampled by the mesh can be calculated.

Mode Description	Finite Element	Elastic Equations
Asymmetric Drum	0.474	0.555
Longitudinal	0.363	0.368
Symmetric Drum	0.719	0.647
Expansion	1.755	2.85
2 nd Asymmetric Drum	0.223	0.175

Table 7.1: *Calculation of Coupling Factors for Internal Modes.*

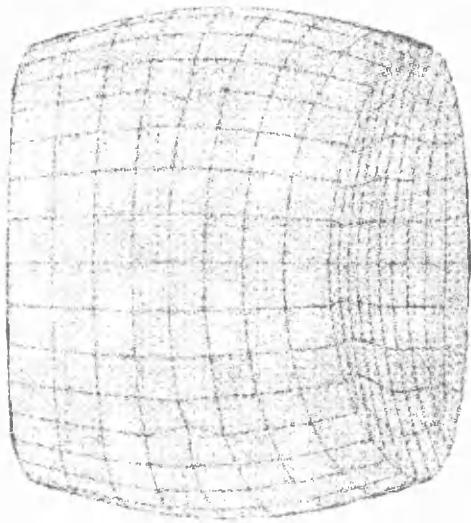
A mesh for the test masses of the Glasgow prototype was generated and then analysed using Abaqus 5.2 (courtesy of The Department of Mechanical Engineering, Glasgow University). The mesh consisted of 768 elements; each was about 1.65 cm³. This was adequate for verifying the fundamental modes and also the first high order mode which exhibited large motion at the face centre. Since the spot size was small compared to the mesh size, the coupling between the internal mode and the optical mode was taken as the amplitude of node at the centre of the test mass face.

The values of α_n calculated by both methods are compared for the first five axisymmetric modes in Table 7.1. Figure 7.13 shows some of the mode shapes obtained.

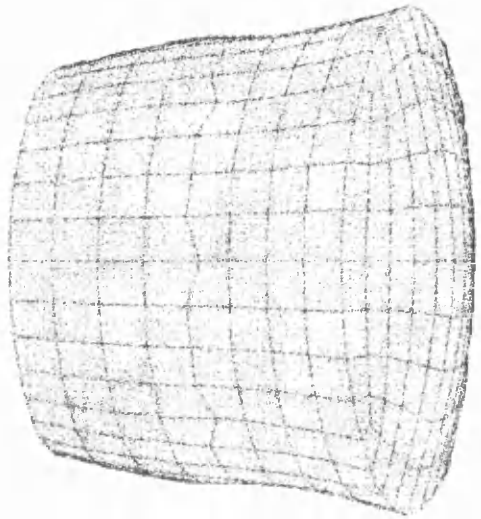
As can be seen, the values for α_n are similar for both methods. In particular, the value obtained for the 2nd Asymmetric Drum Mode indicates that this high-order mode is significant in its contribution to thermal noise. It was not possible to verify modes of higher frequency than this using the mesh described above because the element size was too large. To use a finer mesh would require increased computing capacity that was not readily available.

It is also useful to compare the resonant frequencies of the internal modes predicted by the numerical techniques with measurements of the test masses. These are shown in Table 7.2. The measured frequencies are for test masses without magnets attached. These differ by less than 0.1% between the two test masses.

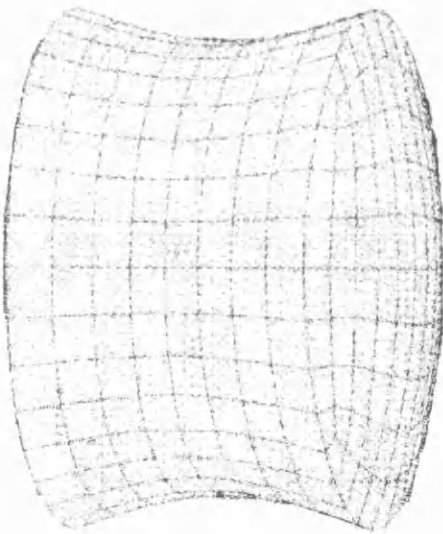
The calculated frequencies are accurate to within 2–3% of the measured values. This gives confidence that the calculation of the mode dynamics and hence the values of α_n are also sufficiently accurate to allow the thermal noise to be estimated.



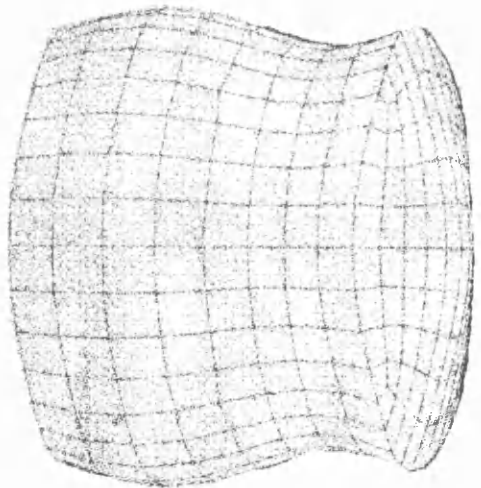
Longitudinal Mode



Asymmetric Drum Mode



Symmetric Drum Mode



2nd Asymmetric Drum Mode

Figure 7.13: *Internal Mode Shapes of the Test Masses.*

Mode Description	Measured Frequency (Hz)	Finite Element (Hz)	Elastic Equations (Hz)
Asymmetric Drum	23748	23003	23992
Longitudinal	25520	24678	25784
Symmetric Drum	28649	26597	28972
Expansion	32040	31477	32582
2 nd Asymmetric Drum	36249	34240	36640

Table 7.2: *Resonant Frequencies of Internal Modes.*

7.5.3 Thermal Noise Estimate of Prototype

The thermal noise from internal modes of the test masses is estimated for the Glasgow prototype detector. The loss tangent, $\phi_n(\omega)$, is taken to be identical for each mode and constant with frequency. The loss function cannot be greater than 2×10^{-6} since internal mode Q factors of 5×10^5 have been measured in the prototype test masses (both by the author and by Wood [58]). In fact, Wood measured a Q factor of 9.1×10^5 but with only a single wire suspension. For the purposes of this estimation, the loss tangent is assumed to be 2×10^{-6} .

Using measurements of resonant frequencies and values of α_n taken from Table 7.1 (an average of both columns was used) the thermal noise power was calculated for the first five axisymmetric modes. This is then multiplied by a factor of f_{\max}/f_5 where f_5 is the resonant frequency of the fifth axisymmetric mode. This factor takes into account the contributions from all other modes whose resonant frequencies are less than the cut-off frequency f_{\max} . This must be done separately for both mirrors comprising the Fabry-Perot cavity because the spot size is different on each mirror. Since there are two cavities, the thermal noise power should be doubled. The displacement noise measured by the interferometer is the square root of the thermal noise power.

At 1 kHz the thermal noise from the internal modes is estimated to be 4.0×10^{-19} m/ $\sqrt{\text{Hz}}$. The observed noise floor of the detector is expected to be a combination of thermal noise from internal modes and shot noise at this frequency. The

shot noise level was estimated to be $4.2 \times 10^{-19} \text{ m}/\sqrt{\text{Hz}}$ at 1 kHz. Combining these in quadrature gives an total estimation of the detector noise floor at 1 kHz to be $5.8 \times 10^{-19} \text{ m}/\sqrt{\text{Hz}}$. The noise floor is observed to be $5.8 \times 10^{-19} \text{ m}/\sqrt{\text{Hz}}$. This is consistent with the estimated thermal noise.

7.5.4 Discussion of Internal Loss in the Test Masses

On the assumption that the observed noise at around 1 kHz in the Glasgow prototype detector is a combination of shot noise and internal thermal noise, the loss tangent due to the internal friction of the test masses is approximately 2×10^{-6} . However, measurements of the Q factor of internal modes (at frequencies of $\geq 30 \text{ kHz}$) in bulk fused silica imply that the intrinsic loss is an order of magnitude less than this (see Gillespie [59]).

The restoring force is generated purely by distortion of the test mass itself and therefore the loss associated with each mode should be the intrinsic material loss. In general, the internal losses should not be assumed to be homogenous throughout the test mass. For example, there may be effects associated with the surface of the test mass. The most significant inhomogeneity is the attachment of magnets and wires. This can introduce additional losses to the test mass.

Logan [60] showed that there is coupling of the internal modes to the transverse modes of the suspension wires. The results show the variation in Q factor of an internal mode as the wire length (and hence the transverse mode frequency) is varied. The Q factor is decreased when the transverse mode frequency is matched to the internal mode. However, modelling of this coupling showed that the thermal noise was only increased at the transverse mode frequencies. (In fact, more thermal noise is associated with motion of the centre of mass than with coupling through the internal modes.) Away from the transverse mode frequencies the thermal noise from the internal modes only arises from the intrinsic loss of the test mass material.

The magnets attached to the test mass are a source of significant loss. This is readily seen by comparing the Q factors of internal modes for the masses that have magnets attached with those that do not. Table 7.3 shows experimental measurements for all the masses. Both the end masses have magnets attached.

Mode Description	Inboard Primary	Inboard Secondary	End Secondary	End Primary (1)	End Primary (2)
Asymmetric Drum	230000	62000	74000	36000	184000
Longitudinal	540000	440000	220000	38000	430000
Symmetric Drum	110000	120000	44000	15000	78000
Expansion	170000	120000	50000	2600	106000
2 nd Asymmetric Drum	35000	260000	730	2100	246000
47 kHz	100000	100000	20000	14000	48000
48 kHz	280000	340000	13000	27000	51000
56 kHz	110000	120000	9900	33000	46000
58 kHz	140000	190000	20000	9200	17500
59 kHz	540000	320000	17000	29000	275000

Table 7.3: *The measured Q factors of internal modes of the test masses used in the Glasgow prototype detector. Neither of the Inboard masses have magnets attached but both End masses do. The columns End Secondary and End Primary (1) contain measurements with magnets 3 mm thick by 10 mm diameter glued directly to the test mass face. End Primary (2) contains measurements obtained when a smaller magnet 1 mm thick by 3 mm diameter was attached via a fused silica stand-off 1 mm in diameter and 3 mm long. Repetition of the measurements indicated that the error in the Q factors is about 3%: for Q factors below ~ 2000 the error is as much as 10%.*

If the loss implied by the Q factors presented in Table 7.3 were constant with frequency this would give rise to a thermal noise limit well in excess of the current observed sensitivity. The extremely low Q factor measured for the 2nd Asymmetric Drum Mode of the secondary end mass ($Q = 730$) would be responsible alone for the observed noise floor at 1 kHz. Since other modes would also significantly contribute then the loss at the resonant frequency cannot indicate the loss at lower frequencies.

The magnets can be considered to be resonantly coupled to the test mass as is shown in Figure 7.14. The internal mode is represented by a mass on a lossless spring. The magnet is coupled to the test mass by a lossy spring. It is clear that there are two coupled modes of the system both of which are damped by the lossy spring. However, the thermal driving force should be applied as a fluctuation in the restoring force of the lossy spring. At low frequencies this results mostly in motion of the magnet. A coupling factor is required to take into account the amplitude of motion at the point where the magnet is attached. If the point of attachment is a node then neither the loss nor thermal motion associated with the magnet can couple to the internal mode. This mechanism explains how the Q factor of a resonance can be reduced without increase in the thermal noise away from the resonant frequency - specifically in the region of interest to gravitational wave detection. However, it is still possible that the attachment of magnets is responsible for the excess loss suggested by the measured noise. A method of attaching the magnets to the test mass that reduces their coupling is now considered.

Initially, the magnets used on the test masses of the Glasgow prototype were 10 mm in diameter by 3 mm thick. The whole area of one face was glued to the test mass. This means that distortion of the face couples strongly to distortion of the magnet and causes a significant loss to the internal mode. Another source of loss is the glue joint that fixes the magnet to the mass.

It is desirable to reduce the contact area between the magnet and the test mass and also the amount of glue required. This was achieved by attaching the magnets using stand-offs (as was implemented by Gillespie on the Caltech prototype [61]). Both attachment techniques are compared in Figure 7.15. The stand-off is a piece of fused silica rod 1 mm in diameter and 3 mm long. This reduces the contact area

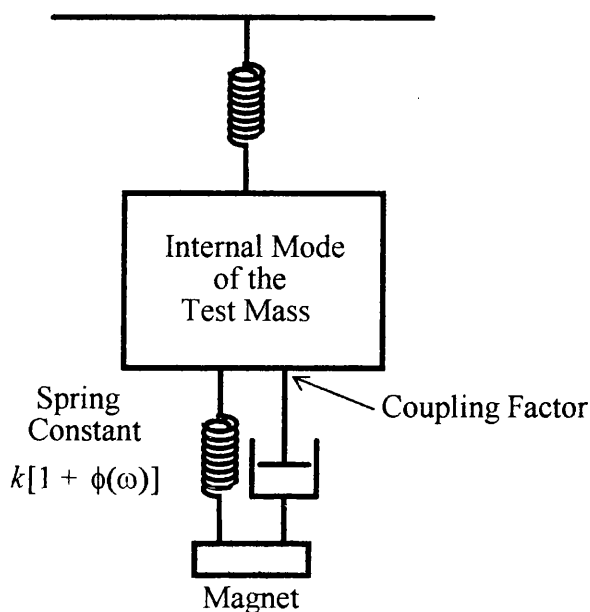


Figure 7.14: *Resonant Coupling of Magnet to an Internal Mode of the Test Mass.*

between the test mass and the magnet by a factor of 100. This should reduce the coupling of the magnet to the internal modes of the test mass and also reduce the amount of glue used in the attachment. Smaller magnets (3 mm in diameter by 1 mm thick) are now used. This further the reduces the coupling of thermal motion because there is less mass to react against – a factor of 33 less. The improvement in measured Q factor for the internal modes of this mass can be seen by comparing the last two columns in Table 7.3. For all modes measured, the Q factor was increased; for some modes the Q factor is as much as 100 times better.

Another source of friction are the wire loops that are passed underneath the test mass to hold its weight. The cylindrical surface of the test mass has a ground finish. It is thought that this could cause friction with the wire loops and thus reduce the Q factor. This could explain why internal mode Q factors are reduced even for the Inboard masses which do not have magnets attached.

The Q factors measured for the test masses of the Glasgow prototype can be compared for the case of a single loop suspension (recorded by Wood [58]) with a suspension using two wire loops (as presented in Table 7.3). The highest Q factor attained was almost a factor of 2 higher for the single loop case. (In both cases the

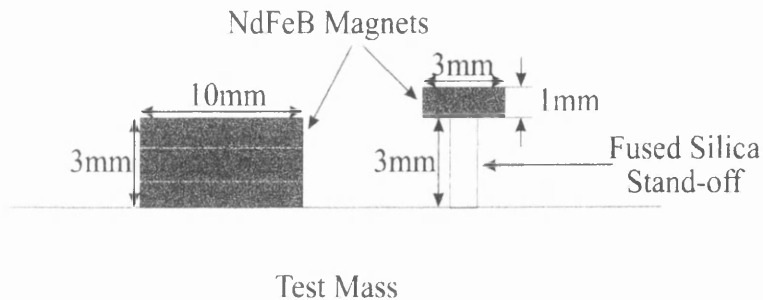


Figure 7.15: *Attachment of Magnets to the Test Mass.*

highest Q factor was measured for the longitudinal mode making this a reasonable comparison.)

It is also to be noted that the fused silica masses with which Gillespie [59] measured internal mode Q factors consistently in excess of 5×10^6 had their sides polished. This is expected to reduce the friction with the wire loops.

7.5.5 Conclusion

The Q factors have been measured for some of the internal modes that contribute significantly to the thermal noise of the detector. This cannot give a true indication of the loss at frequencies about 1 kHz since the noise floor of the detector would be much higher. Thus, the reduction in Q factor of the internal modes is explained in terms of resonant coupling of the magnets. In this model the thermal noise is not increased at lower frequencies. This, however, does not mean that the attachment of magnets does not cause an increase in the loss of the test material at lower frequencies, merely that it is not at a level to explain the low Q factors that have been measured. It is, therefore, still justified to pursue techniques of attaching the magnet that reduce the effect on the test mass. Another possibility for applying feedback to the mass is to use an electrostatic drive. This uses the dielectric properties of the test mass in an electric field. It has the advantage that it does not require any attachments to the test mass which could introduce frictional loss and cause excess thermal noise.

There is some suggestion that the internal Q factors could be limited by friction with the wire loops used to hold the masses. This seems to be reduced if the cylindrical surface of the mass is polished instead of being left with a ground finish. Elimination of the wire loops would definitely remove any frictional loss associated with them. To achieve this, attachment techniques such as optical contacting or spot welding could be used to manufacture a monolithic suspension. These are being actively researched (at time of writing) by Rowan *et al* [62] here at Glasgow and also by Traeger [63] at the Universität Hannover.

Chapter 8

GEO 600

‘The LORD said, “If as one people speaking the same language they have begun to do this, then nothing they plan to do will be impossible for them.”’

Genesis xi.6.

8.1 Overview of the GEO 600 Project

GEO 600 is a joint British-German project to build a high sensitivity interferometer for detecting and observing gravitational waves. Figure 8.1 shows a schematic diagram of the optical configuration that is currently proposed. GEO 600 will be a dual recycled Michelson-type interferometer with a double-pass folded delay line in each arm.

The source of the laser light will be a non-planar ring oscillator laser emitting at 1064 nm – the near infra-red. This will be used as the master for a more powerful, injection-locked laser that will produce between 5 and 10 Watts of single mode and single frequency light. Both these lasers will be pumped by laser diodes.

A small amount of light will be split-off from the main beam to lock the laser to a rigid reference cavity. This is done to increase the frequency stability of the laser which aids the acquisition of the interferometer locking servos when only a limited bandwidth is available. The cavity will be made from a low thermal expansion ma-

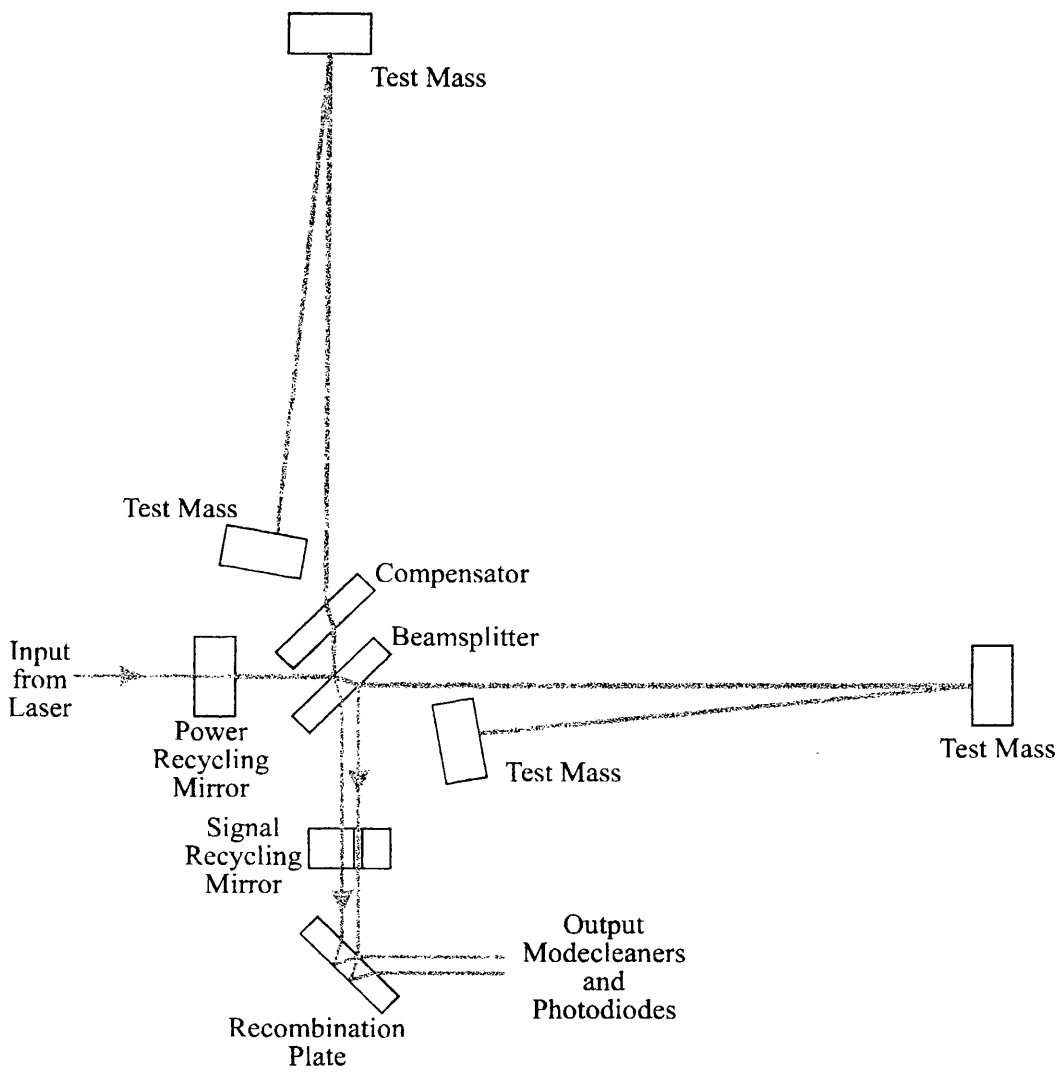


Figure 8.1: *GEO 600 Optical Scheme.*

terial thereby also providing a stable *dc* reference for the laser. The reference cavity requires to be isolated from seismic and acoustic vibrations. An optical fibre may also be placed between the laser and the cavity to reduce fluctuations in the beam pointing: in this way the fibre acts like a modecleaner. These measures will ensure that the laser light available to the interferometer will be stable to approximately $1 \times 10^{-3} \text{ Hz}/\sqrt{\text{Hz}}$ [65].

High finesse Fabry-Perot cavities will be used as modecleaners to reduce the geometry perturbations of the laser beam that illuminates the interferometer. This type of modecleaner is described by Skeldon *et al* [26]. Such a cavity will also filter intensity noise and frequency noise of the laser light [28]. Two such modecleaning cavities are required in order to achieve the sensitivity goal of GEO 600. They are located between the laser and the interferometer. Each will be a three mirror ring cavity of approximately 8 metres in length and will be *rf* reflection fringe locked to the input laser light. All mirrors in the modecleaners will be suspended so that they are isolated from ground vibrations. This is analogous to the suspension of the test masses but, as will be seen, the allowed displacement noise is four orders of magnitude higher. Section 8.2 details the suspensions that will be used.

After the light has passed through the modecleaner cavities it will be *rf* reflection fringe locked to the power recycling cavity of the interferometer: this is the master frequency reference of the interferometer at signal frequencies. At low frequencies, the seismic excitation of the pendulum modes of the mirror suspensions would impose large frequency excursions on the laser. The rigid cavity used to pre-stabilise the laser is a superior low frequency reference. Thus, at low frequencies, the power recycling cavity should be locked to the input light but with a very limited bandwidth. This requires actuation to the power recycling mirror or, alternatively, common mode to the lengths of the arms. The cross-over from one regime to the other is expected to be $<10 \text{ Hz}$.

The output of the interferometer will be maintained at a dark fringe. This will be achieved by servoing the differential length of the interferometer arms. Thus, feedback actuation is required to at least one test mass. The actuation force could be produced by current carrying coils acting on magnets or by an electrostatic drive.

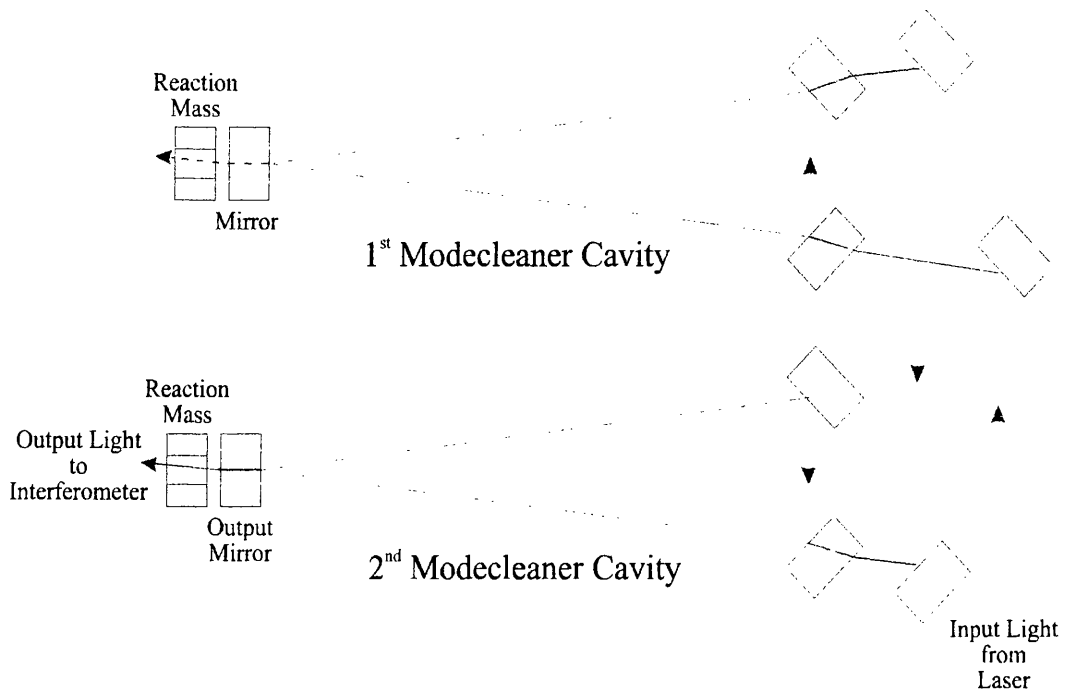


Figure 8.2: *GEO 600 Modecleaners Layout.*

An electrostatic drive is preferred because it should maintain high Q factors of the test mass internal modes (and maintain thermal noise properties). A suitable electrostatic drive is, however, still to be experimentally realised. In either eventuality, seismic motion of the actuator can couple to the test mass and could cause excess displacement noise. Thus, the actuator will be mounted on a reaction mass which will also be suspended as a pendulum thereby isolating the actuator from seismic motion.

The error signal corresponding to a differential change in length of the arms will be obtained by the technique of external modulation¹. This involves combining an auxiliary reflection from the interferometer (*e.g.* from the opposite face of the beamsplitter) with the output fringe. This is shown in Figure 8.1. This detection process will also utilise *rf* modulation techniques; see [64] for a discussion of this topic.

The position of the signal recycling mirror requires to be controlled in order to

¹The use of external modulation for GEO 600 is currently under review.

maintain the resonant tuning of the signal sideband enhancement. It is likely that Schnupp modulation [66, 67] will be used to do this. (Schnupp modulation may also be used to extract the output signal of the interferometer.)

Due to distortions of the optics used in the interferometer (particularly thermal distortion of the beamsplitter [68]), light can be scattered from the fundamental Gaussian mode into higher-order modes. These are not resonant in the system and therefore can be emitted from the output. Such light does not contain information about the displacement of the test masses but will increase the shot noise if it were detected by the output photodetectors. Thus, the output beams will be passed through a further modecleaning cavity to reject this light. A short rigid ring cavity is likely to be used for this.

8.2 GEO 600 Modecleaner Mirror Suspension

The suspensions detailed in this section have been designed to meet the requirements for the GEO 600 modecleaners and, by default, they are also good enough to be used for beam directing optics. For simplicity, the same design and specification will be used for all such mirrors.

The displacement noise specification arises because motion of the mirrors imposes frequency noise on the laser light *via* Doppler shifting. For mirrors forming a Fabry-Perot cavity (*i.e.* the modecleaner mirrors), the frequency noise imposed on the light is given by

$$\frac{\dot{\nu}}{\nu} = \frac{\mathcal{F}}{\pi} \frac{\omega \hat{x}}{c} \quad (8.1)$$

where ν is the frequency of the laser; \mathcal{F} is the modecleaner cavity finesse; \hat{x} is the displacement noise of the mirror and c is the speed of light. The factor, (\mathcal{F}/π) , is the average number of round trips of the modecleaner cavity before light is transmitted. The finesse of the modecleaner cavities will be $\sim 2 \times 10^3$.

The level of pre-stabilisation of the laser frequency should not be compromised by the motion of the mirrors. For a laser frequency stabilised to about $1 \times 10^{-3} \text{ Hz}/\sqrt{\text{Hz}}$ the displacement noise of each mirror (there are six in total) should be less than $2 \times 10^{-15} \text{ m}/\sqrt{\text{Hz}}$ which should apply at all frequencies above 50 Hz. This is much

less stringent than the requirement for the suspension of the test masses.

Because the length of the modecleaner will be servoed to the laser frequency, the displacement noise of the mirrors will be suppressed by the loop gain. It is more appropriate to view this suppression as an added safety margin rather than a necessity for operation.

Using the pendulum modelling techniques described in Chapters 4, 5 and 6 a design for the modecleaner mirror suspensions was found which adequately met the design requirements. This is now presented.

The mirrors that comprise the modecleaner have dimensions 100 mm diameter by 50 mm thick. They are manufactured from fused silica and have a mass of 0.86 kg. In order to achieve good damping of the double pendulum the intermediate mass is approximately equal to this (0.80 kg). It is necessary to make the intermediate mass from Aluminium (or other low density metal) to make it a suitable size. The dimensions are 70 mm \times 50 mm \times 85 mm. The length (70 mm) is constrained because a reaction mass will be suspended behind one mirror in each modecleaner to provide feedback to the cavity length. The separation of the mirror and the reaction mass should be sufficient (but not greatly larger than required) for a coil-magnet actuator. The separation will be approximately 25 mm. It is intended that the reaction mass will be suspended by an identical pendulum.

A diagram showing the pendulum is shown in Figure 8.3. The total height available determines the pendulum length of 800 mm from the top plate to the beam axis. Table 8.1 lists the normal mode frequencies predicted by the **dp2ss.m** routine in Appendix A.

Modelling of the local control servos indicates that the longitudinal, sideways, rotation and tilt modes can be actively damped with relative ease. The vertical and roll modes will be left undamped. These modes all have a Q factor determined by the internal friction of the wire material. It is important that the level of cross-coupling to these modes does not produce an unstable unity gain point in the local control servo. To avoid sensing vertical motion directly when damping tilt motion, sensing of tilt motion will be done on the longitudinal face of the intermediate mass. Normally, this is avoided because it adds noise directly into longitudinal motion

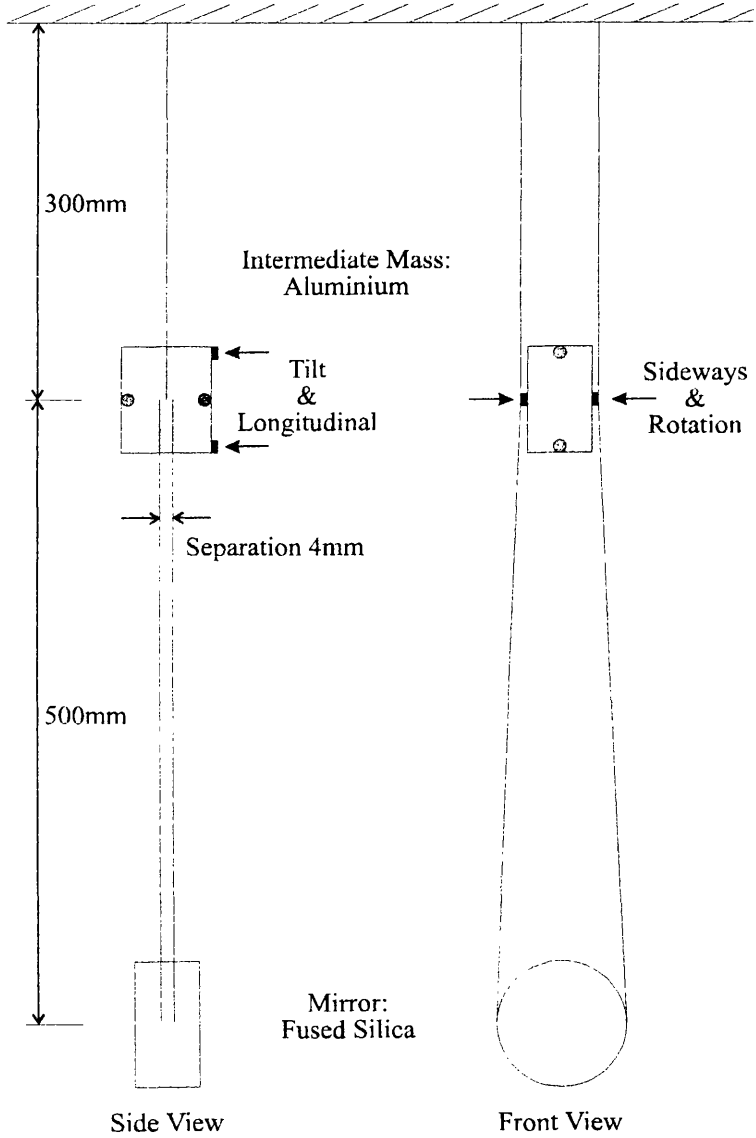


Figure 8.3: *GEO 600 Modecleaner Suspension Design.*

Normal Mode	Frequency (Hz)
Longitudinal	0.60
Longitudinal	1.54
Tilt	0.89
Tilt	2.05
Sideways	0.60
Sideways	1.54
Rotation	0.70
Rotation	1.88
Roll	17.1
Roll	38.1
Vertical	13.0
Vertical	33.1

Table 8.1: *Normal Mode Frequencies of Modecleaner Suspension.*

of the pendulum. However, it is acceptable here because the displacement noise specification for the modecleaner mirrors is greater than that required by the test masses.

The modecleaner cavity must be locked to the input laser light. This requires actuation on one of the mirrors to provide feedback to the length of the cavity. A coil-magnet actuator will be used to apply a force to one of the modecleaner mirrors. The coils will be mounted on an Aluminium mass suspended behind the selected mirror. Figure 8.4 shows this arrangement. The bandwidth of this servo will be limited by the internal acoustic modes of the modecleaner mirror. The lowest mode expected to be around 24 kHz and will have a fairly high Q factor. This is essentially the same problem as was discussed in Section 6.3.

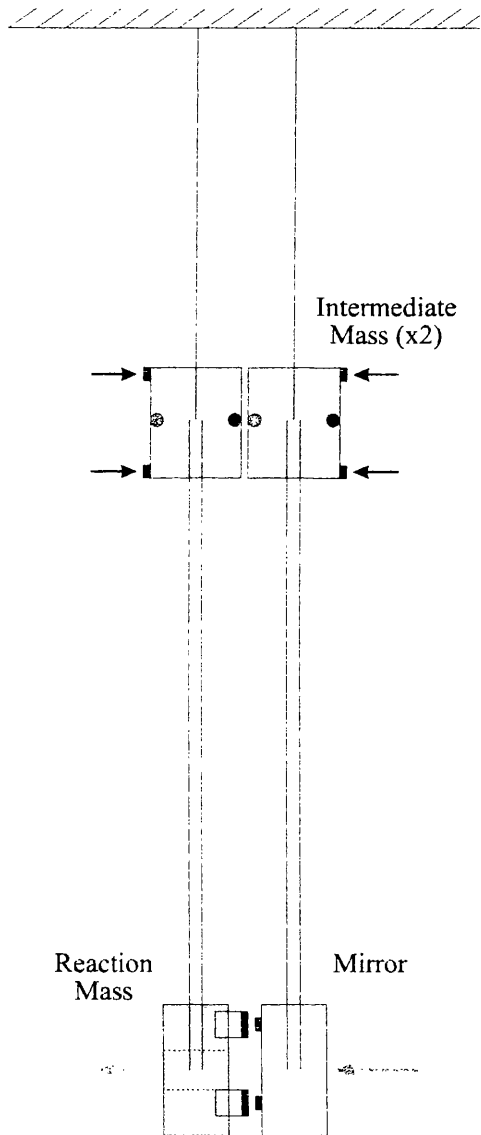


Figure 8.4: *GEO 600 Modecleaner Mirror and Reaction Mass.*

8.3 GEO 600 Test Mass Suspension

The currently proposed GEO 600 test masses will be made from fused silica, have a diameter of 240 mm and thickness of 140 mm. This gives a total mass of 13.9 kg to be suspended. In order to reduce thermal noise from the pendulum modes, the test mass could be suspended by fused silica fibres from the intermediate mass. To avoid friction occurring at joints, it is proposed to construct a monolithic suspension. The suspension fibres would probably be attached to the top of the test mass either by a welded joint or by optically contacting. A monolithic suspension could allow Q factors for the longitudinal pendulum modes to be $\sim 10^8$.

To facilitate the use of a split feedback topology (see Section 6.5), it is desirable to ensure that there are no normal modes of the suspension close to the proposed cross-over frequency between feedback applied at the intermediate stage and that applied directly to the test mass. Therefore, the frequency range from 20 Hz to 80 Hz should be clear of modes.

In the next section, a preliminary design will be presented demonstrating that a suspension topology is possible where the normal mode frequencies are all within the bandwidth of local control servos. An exception to this is the upper vertical mode.

8.3.1 Preliminary Design of Test Mass Suspension

Figure 8.5 shows the preliminary design. The intermediate mass is 14.2 kg. It has been chosen to have dimensions of 100 mm \times 120 mm \times 150 mm in the x , y and z -axes respectively. The z dimension is chosen to be greatest to give larger moments of inertia for tilt and roll degrees of freedom. These modes are typically higher in frequency than those involving rotation around the vertical axis.

The upper-stage wires are tensioned to approximately one third of their expected breaking stress. The breaking stress of steel is 2-3 GPa. With a total load of 28.1 kg the required radius for two wires is 240 μ m. The stress is 760 MPa and the frequency of the fundamental transverse mode is 518 Hz.

The lower-stage wires are also tensioned close to one third of their breaking

stress. The breaking stress for fused silica has been measured here at Glasgow [69] to be 800 MPa. A value equal to or greater than this is implied by an experiment reported by Braginski *et al* [70]. To suspend a test mass of 13.9 kg on two fibres requires the fibre radius to be at least $\sim 280 \mu\text{m}$. For this value, the stress is 270 MPa and the fundamental transverse mode is at 576 Hz.

Both suspension points of the double pendulum are independently sprung in the vertical direction. Two pre-stressed cantilever leaf-springs are proposed. The size of the leaf-springs will be chosen to make the lower vertical mode ≤ 3 Hz. Because both suspension points are sprung independently, the roll modes are also reduced in frequency. The separation of the upper wires is chosen so that the frequency of the roll mode is able to be electronically damped. This separation is 60 mm. Furthermore, by using two wires to suspend the test mass, the roll mode in which the intermediate mass and the test mass rotate in anti-phase relies on the bending of the wires as a restoring force. Thus, it is also at a low frequency.

The separation of the lower wires is 10 mm. This was chosen so that the differential tilt mode would occur at a low frequency. It is estimated by Equation 5.9 to be 1.7 Hz. In fact, because restoring forces other than extension of the wires are also significant, the frequency will be slightly higher.

For a lower stage length of about 0.5 m it is not possible to reduce the upper vertical mode to much less than about 10 Hz. This is restricted because the suspension wires must have a sufficiently large cross-sectional area to support the weight of the test mass. For a fused silica suspension the minimum possible frequency is higher than this because the breaking stress of fused silica is much less than that of steel. Concerns that the fibres may deteriorate over long periods of time (*i.e.* several years) may mean that the allowed stress should be reduced. This would have the consequence of raising frequency of the upper vertical mode.

The predicted normal mode frequencies of this suspension design are listed in Table 8.2 (these are results of the `dp2ss.m` routine in Appendix A). These meets the design requirements as described above.

Normal Mode	Frequency (Hz)
Longitudinal	0.595
Longitudinal	1.48
Tilt	3.0
Tilt	3.4
Sideways	0.607
Sideways	1.47
Rotation	0.067
Rotation	0.863
Roll	2.4
Roll	3.6
Vertical	2.74
Vertical	20.6

Table 8.2: *Normal Mode Frequencies of Test Mass Suspension.*

8.3.2 Local Control

Following the discussion and results in Section 5.5, a local control servo for damping the modes of the GEO 600 test mass suspensions has been devised. This assumes that shadow sensors and coil-magnet actuators similar to those considered previously will be used. The displacement signal would be filtered by:-

1. An RC high-pass filter; the low-cut occurs at 0.7 Hz.
2. A transitional differentiator that acts between 0.2 Hz and 0.7 Hz.
3. A second transitional differentiator that acts between 1.5 Hz and 10 Hz.
4. Low-pass filtering to attenuate control noise above 12 Hz (see below).

The noise specification for GEO 600 extends down to 50 Hz. This makes it more difficult to attenuate the noise introduced by the local control servo than the case studied in Section 5.5.1. It is possible to use add more low-pass filters to give

Peak Frequency (Hz)	Q factor	Notch Frequency (Hz)
15	3	50
18	4	70
24	5	100

Table 8.3: *Scultéty Filters for Attenuation of Control Noise.*

steeper filtering but greater attenuation can be achieved by adding notches at signal frequencies to suppress sensor noise. A series of Scultéty filters (suggested by Schilling [71]) is ideal for this. Noise attenuation filters consisting of three Scultéty filters (which are detailed in Table 8.3) and a simple RC low-pass filter were found to be adequate. The low-pass filter introduces a pole at 12 Hz. This passive filter is required as the final element of the local control channel to attenuate the electronic noise from preceding active filters. It is followed only by the current driver for the coil.

The damping predicted for the two longitudinal modes of the proposed GEO 600 test mass suspension is shown in Figure 8.6. This is plotted against the control noise (at 50 Hz) introduced by the damping servo. Damping that reduces the Q factor of the fundamental longitudinal mode to ~ 4 is predicted to give rise to control noise of $5 \times 10^{-21} \text{ m}/\sqrt{\text{Hz}}$. This assumes that the noise performances of the shadow sensors and coil-magnet actuators are the same as those described in Section 5.4. These have a sensor noise corresponding to $1 \times 10^{-10} \text{ m}/\sqrt{\text{Hz}}$ and an actuator noise of $1.5 \times 10^{-11} \text{ N}/\sqrt{\text{Hz}}$. This is for a *dc* range of $40 \mu\text{m}$ for the longitudinal actuator. In fact, the sensors being developed for GEO 600 may be quieter than this, however, the actuator noise is difficult to reduce without reducing the range. Figure 8.7 shows a comparison of the displacement noise arising from sensor noise and actuator noise as a function of frequency (with the servo gain set to give minimum Q factor for the fundamental longitudinal mode). The noise contributions are approximately equal at around 50 Hz.

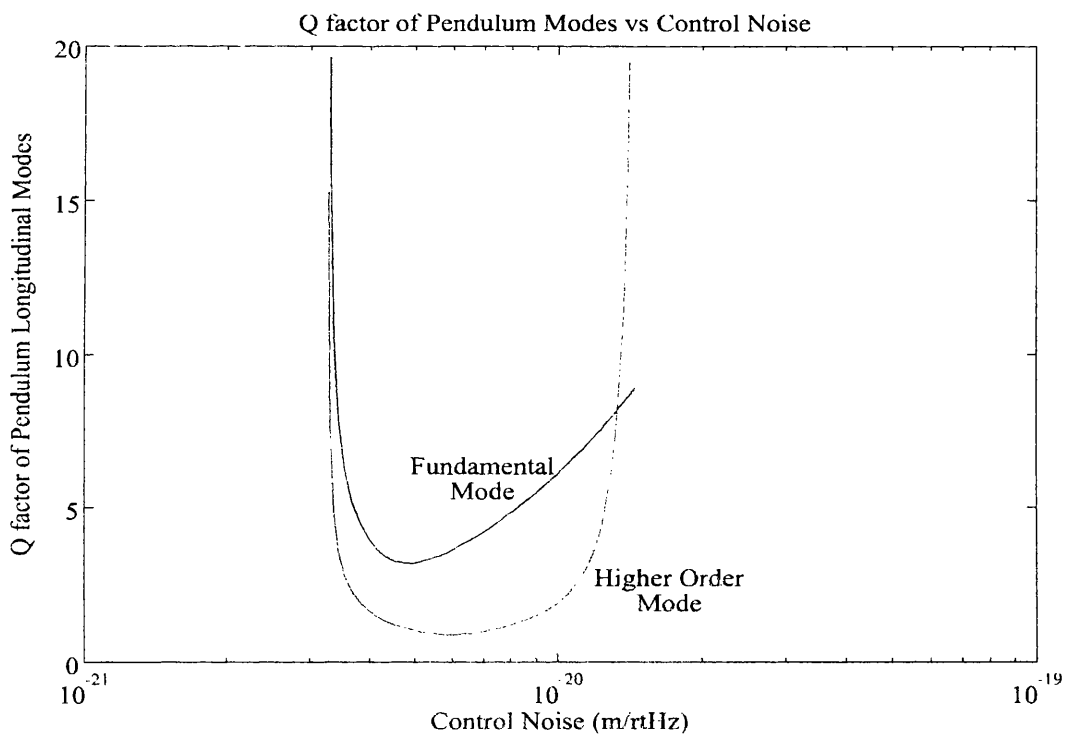


Figure 8.6: *GEO 600 Test Mass Damping versus Control Noise.*

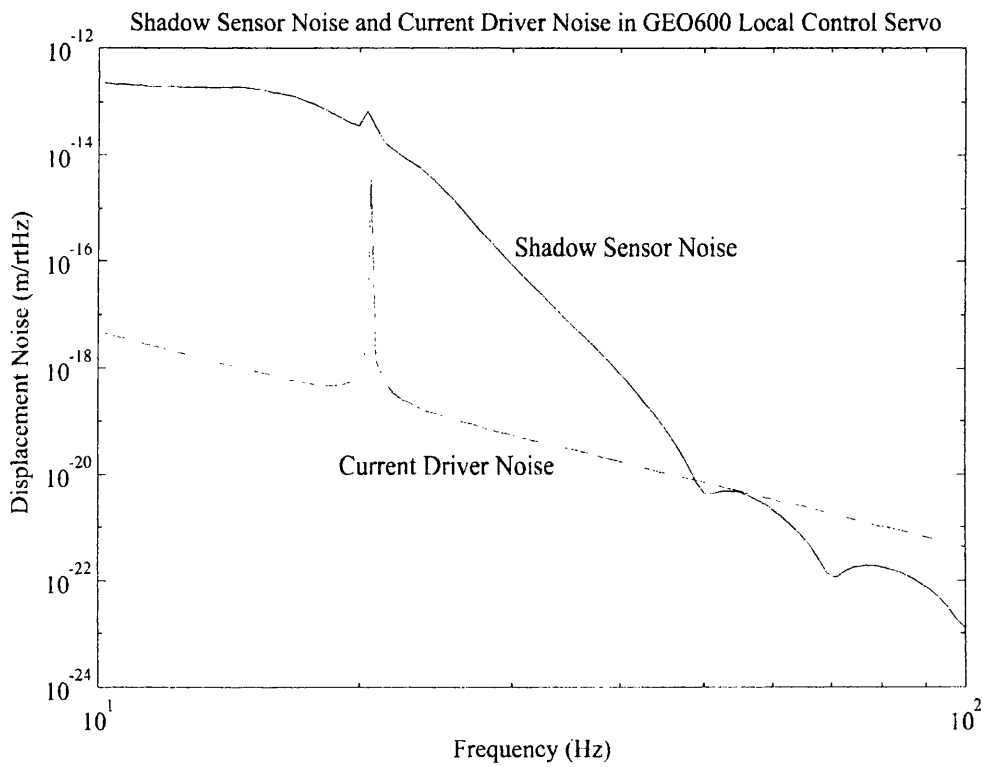


Figure 8.7: *Contributions to Local Control Noise.*

Modelling of the damping for the proposed GEO 600 test mass suspension indicates all other modes will have a sufficiently damped Q factor with the exception of the upper vertical mode. This is problematic. Its frequency is predicted to be at ~ 20 Hz, however, the servo gain is not attenuated significantly below unity gain at this frequency. It is difficult to achieve adequate damping of the tilt and vertical degrees of freedom without making the servo unstable at the upper vertical mode. There are several possible solutions to this:-

1. The frequency of the upper vertical mode can be increased. This may be required if the allowed stress in fused silica fibres is lower than 270 MPa. In this case the fibre diameters will have to be increased and this raises the frequency of the upper vertical mode. At higher frequency the servo gain is reduced.
2. The servo gain is not greatly attenuated because the noise attenuation filters have a peaked response from 15 Hz to 24 Hz. This could be lowered by changing the filters used to attenuate control noise. Since the tilt and vertical degrees of freedom do not couple directly to the sensed displacement noise, there may be some scope for this approach.
3. The mode could be passively damped by coupling vertical motion at ~ 20 Hz to a damped passive resonator mounted on the intermediate mass. The servo gain can then be increased in proportion to the reduction in Q factor of the mode. This has the advantage that it would actually damp the upper vertical mode, thus, seismic noise would not be enhanced at this frequency to the same extent as if the mode were left undamped.

The author favours Point 3 as the preferred course of action. Further development of this technique is required.

8.4 Conclusion

An overview of the GEO 600 project has been presented. The GEO 600 interferometer will incorporate the advanced interferometric techniques of power recycling and

signal recycling on a large scale detector.

The GEO 600 project requires two modecleaners to suppress beam jitter and beam pumping of the input laser light. The modecleaners will be formed from three mirror ring cavities; the mirrors will be suspended to isolate them from seismic noise. The suspension of the modecleaner optics has been discussed and a design presented. This is currently being tested here in Glasgow by Plissi and Torrie. The displacement noise specification for these optics is $\sim 2 \times 10^{-15} \text{ m}/\sqrt{\text{Hz}}$.

A preliminary design for the test mass suspensions has also been presented. The displacement noise of the test masses requires to be at most $\sim 1 \times 10^{-20} \text{ m}/\sqrt{\text{Hz}}$. Local control has been considered for this design and the estimated control noise should not compromise the sensitivity. There still remains the issue of how to handle the upper vertical mode of the suspension. Experimental tests are required to see if resonant damping can be used in this case.

Construction of the GEO 600 interferometer began in September 1995 and is due for completion around 2000.

Chapter 9

Conclusion

‘But I still haven’t found what I’m looking for...’

Bono.

9.1 Review

The design and construction of low displacement noise suspensions for the test masses of terrestrial gravitational interferometric detectors is far from a trivial task.

The suspension design must:

1. provide isolation of seismic noise (both longitudinal and cross-coupled);
2. facilitate active damping of the normal modes;
3. facilitate position control of the test mass for locking the interferometer, and
4. be compatible with the low-loss properties required to minimise thermal noise.

The advantages of a double pendulum system (compared to a single stage pendulum) have been reported: superior seismic isolation; isolation of control noise imposed by the active damping servo, and the possibility of applying positional feedback at the intermediate stage to reduce the actuator range required at the test mass. With reduced range requirements, an electrostatic actuator becomes more practical. This would remove the need for the attachment of magnets to the test masses and could

improve the thermal noise limit. (In the event that an electrostatic drive is not practical, the reduced range would allow very much smaller magnets to be used. This would also address the thermal noise issue.)

The double pendulum system is more complex than a single stage pendulum. To the author's knowledge, this is the only disadvantage of a two-stage system. This complexity required the development of a comprehensive model of the pendulum dynamics. The problem of cross-coupling between degrees of freedom necessitated this model to consider the dynamics of all six degrees of freedom per pendulum mass. Using this model, it was possible to ensure that a pendulum design was amenable to servo control (both damping and position control). Models of the internal dynamics of the suspension wires and the test mass itself have also been utilised.

The results presented in Chapter 5 demonstrate that the model predictions are in good agreement with the experimental results. This gives confidence that the modelling techniques are sufficiently accurate to permit the design work for the GEO 600 project. Indeed, in Chapter 8 designs are presented for suspending the optics of GEO 600. This interferometer, in collaboration with other detectors, could mark the birth of a new era of astronomy and astrophysics. The author recognises this volume is a mere fraction of the travail involved in verifying Einstein's work and unveiling the hidden workings of our Universe.

9.2 A Final Question...

It may be asked, "Why not use three stages – a *triple* pendulum?" Indeed, that too is possible. This approach is similar to the Virgo design of super-attenuator. The author observes the following points:-

1. Further pendulum stages do not reduce thermal noise or shot noise. These noise sources are expected to limit the sensitivity at most signal frequencies (*e.g.* above 50 Hz in GEO 600).
2. More pendulum stages *do* reduce seismic noise. Therefore, the detection band could be extended to lower frequencies. This is on the condition that the

normal mode frequencies of the suspension are below the desired sensitivity band. The coupled mode frequencies of a many-stage system must be kept low and they must be well damped.

3. Thermal noise from the pendulum modes of the suspension are likely to become the limiting noise source at these lower frequencies.

The author surmises that there is some advantage to increasing the number of pendulum stages and indeed notes that the top-plate of the GEO 600 suspensions will be suspended [72]. This reduces the attenuation required of the isolation stacks. Active suppression of seismic noise is another potential development. In this case, seismic noise would not be resonantly enhanced at low-frequency (about 1 Hz) but could, in fact, be reduced. This is highly desirable.

Appendix A

MATLAB Toolbox

A.1 dp2ss.m

Syntax

```
[freq,iMKLT,iMKSR,iMKR,iMKV] = dp2ss(dp_name,switches)
```

Inputs: **dp_name** source file for double pendulum parameters.
 switches 'e' report results of eigensystem analysis.
 'v' include vertical spring.

Outputs: **freq** normal mode frequencies (Hz).
 iMK spring matrices for state-space analysis.

Functions called by dp2ss.m:

- assign.m
- constant.m

Purpose

The function returns the normal mode frequencies of the double pendulum parameterised by the file **dp_name**. The frequencies are complex numbers. The complex part signifies the inherent damping of the mode by friction included in the suspension wires. Also returned are the spring matrices used in the eigenvalue analysis. These can be used in state-space models of the pendulum to further assess its performance.

Algorithm

The restoring forces included in this model are the gravitational field as well as the extension, torsion and bending of the suspension wires. Extension and torsion of the wires is fairly straight forward. To obtain the effects of bending, the wire is modelled as a stiff beam under tension – this is a fourth order differential equation.

The dynamics are obtained for four (reasonably) independent systems: longitudinal and tilt; sideways and roll; rotation, and vertical.

The inclusion of a vertical spring in the model effectively places two independent springs at the suspension point of the upper wires. The springs are considered to be rigid in all degrees of freedom except vertical translation. Thus, the vertical and roll modes are reduced in frequency. The internal dynamics of such a spring are not assessed – extra modes may result in practice.

Source Code

```
function [freq,iMKLT,iMKSR,iMKR,iMKV] = dp2ss(dp_name,switches)
%[freq,iMKLT,iMKSR,iMKR,iMKV] = dp2ss(dp_name,switches)
%
%freq          returns the complex frequencies of modes
%              in the order Long+Tilt; Side+Roll; Rotataion and Vertical.
%iMKLT         inv(M)*K matrix for Long+Tilt
%iMKSR         inv(M)*K matrix for Side+Roll
%iMKR          inv(M)*K matrix for Rot
%iMKV          inv(M)*K matrix for Vert
%
%dp_name       name of function whit assigns the pendulum parameters
%switches     'e' report eigenvalues and eigenvectors on screen.
%              'v' include soft vertical spring.
%
%Stuart Killbourn (March '96)

%*****
%global variables defined in 'constant.m'

global g

constant;

%*****
%global variables defined in dp_name

global modeld
global m1 I1x I1y I1z
```

```

global m2 I2x I2y I2z
global FibresU FibresL
global Qu Ql Yu Yl PRu PRl
global Ru Rl lu l2
global t s delta1 delta2 h
global eta0 eta1u eta1l eta2

%*****
%assign pendulum parameters corresponding to dp_name

if (assign(dp_name) == 1)
    error = 1;
    return
end

%*****
%default input

if (exist('switches') ~= 1)
    switches = 'es';
end

%*****
%Calculated parameters
%these are various lengths and angles that are defined by the pendulum
%wire spacing and attachment points.

N1      = (eta1u - eta0);
N2      = (eta2 - eta1l);

D2      = (delta2 - delta1);
U2      = sqrt(N2^2 + D2^2);

nu      = asin(N1/lu);
zeta    = asin(N2/l2);
omega   = asin(U2/l2);

v1      = cos(nu)*lu;
v2      = cos(omega)*l2;

J       = sqrt(v2^2 + N2^2);
L       = sqrt(v2^2 + D2^2);

D       = sqrt(delta1^2 + s^2);
H       = sqrt(delta2^2 + h^2);

epn     = asin(D2/l2);
psi     = asin(s/D);
lam     = asin(h/H);

%total vertical height of pendulum to test mass centre
Vertical = v1 + t + s + v2 + h;

```

```

%wire tension
Tu      = (m1 + m2)*g/(FibresU*cos(nu));
Tl      = m2*g/(FibresL*cos(omega));

%moment of wire cross-section
Ixu     = pi*Ru^4/4;
Ixl     = pi*Rl^4/4;

%spring constant of wire
ku      = (1 + i/Qu)*Yu*pi*Ru^2/lu;
kl      = (1 + i/ql)*Yl*pi*Rl^2/l2;

%torsional constant of wire
kappaU  = (1 + i/Qu)*pi*Ru^4*Yu/(4*(PRu+1)*lu);
kappaL  = (1 + i/ql)*pi*Rl^4*Yl/(4*(Prl+1)*l2);

%bending parameter: beta
bu      = (1 + i/Qu)*sqrt(Yu*Ixu*Tu);
bl      = (1 + i/ql)*sqrt(Yl*Ixl*Tl);

%(1/characteristic bending length)
au      = sqrt(Tu/(Yu*Ixu));
al      = sqrt(Tl/(Yl*Ixl));

if (max(switches == 'v') == 1)
%include vertical spring at upper suspension point (frequency ~2Hz)

fprintf(1,'Vertical Spring Included at Suspension Points.\n');

ks      = (m1 + m2)*(2*pi*2)^2*(1 + i/Qu);
ku      = 1/(1/ku + 1/ks);

end

%*****
%Longitudinal and Tilt Modes (x1 > x1; x2 > x2; theta1 > t1; theta2 > t2)
%static tension in upper wire

kx1x1   = -1*Tu/lu;
kx1t1   = Tu*t/lu;
kt1x1   = Tu*t/lu;
kt1t1   = -1*Tu*t*(1 + t/lu);

KTuTL   = FibresU * [  kx1x1  0      kx1t1  0
                      0      0      0      0
                      kt1x1  0      kt1t1  0
                      0      0      0      0      ];

%*****
%static tension in lower wire

```

```

kx1    = -1*v2;
kx2    = v2;
kt1    = -1*(v2*s + D2*delta1);
kt2    = -1*(v2*h - D2*delta2);

kxx1   = v2;
kxx2   = -1*v2;
kkt1   = (v2*s + D2*delta1);
kkt2   = (v2*h - D2*delta2);

k       = [ kx1 kx2 kt1 kt2 ].';
kk      = [ kxx1 kxx2 kkt1 kkt2 ];

kt1t1  = (v2*s + D2*delta1);
kt2t2  = (v2*h - D2*delta2);

kkk     = -1*(T1/l2)*diag([0,0,kt1t1,kt2t2],0);

KT1TL  = (FibresL)*((T1/(l2^3))*(k * kk) + kkk);

%*****
%extension in lower wire

kx1     = D2;
kx2     = -1*D2;
kt1     = -1*(v2*delta1 - D2*s);
kt2     = (v2*delta2 + D2*h);

kxx1    = -1*D2;
kxx2    = D2;
kkt1    = (v2*delta1 - D2*s);
kkt2    = -1*(v2*delta2 + D2*h);

k        = [ kx1 kx2 kt1 kt2 ].';
kk       = [ kxx1 kxx2 kkt1 kkt2 ];

Kk1TL   = (FibresL)*(k1/l2^2)*(k * kk);

%*****
%bending of upper wire

kx1x1   = -1;
kx1t1   = (t + lu/2);
kt1x1   = (t + lu/2);
kt1t1   = -1*(t^2 + 1/(au^2) + (lu^2)/2 - lu/au + t*lu);

KbuTL   = (bu/(lu^2))*FibresU * [  kx1x1  0      kx1t1  0
                                0      0      0      0
                                kt1x1  0      kt1t1  0
                                0      0      0      0  ];

%*****

```

```

%bending of lower wires

ce      = cos(epn);

kx1     = -1*ce;
kx2     = ce;
kt1     = -1*(D*sin(psi+epn) + l2/2);
kt2     = -1*(H*sin(lam-epn) + l2/2);

kx1     = ce;
kx2     = -1*ce;
kkt1    = (D*sin(psi+epn) + l2/2);
kkt2    = (H*sin(lam-epn) + l2/2);

k       = [ kx1 kx2 kt1 kt2 ].';
kk      = [ kx1 kx2 kt1 kt2 ];

kt1t1   = (1/al^2) + (l2^2/4) - (l2/al);
kt1t2   = (l2/al) - (1/al^2) - (l2^2/4);
kt2t1   = kt1t2;
kt2t2   = kt1t1;

kkk     = [ 0 0 0 0
            0 0 0 0
            0 0 kt1t1 kt1t2
            0 0 kt2t1 kt2t2 ];

KblTL   = (FibresL)*(bu/l2^2)*((k * kk) - kkk);

%*****
%forming the system of differential equations to be solved

MLT     = diag([m1 m2 I1y I2y ]);

KLT     = (KTuTL + KklTL + KTlTL + KbuTL + KblTL);

iMKLT   = inv(MLT) * KLT;

[VectLT, EigLT] = eig(-iMKLT,eye(4));

FreqLT  = sqrt(diag(EigLT))/(2*pi);
QmodeLT = 0.5*real(FreqLT)./imag(FreqLT);

%*****
%Sideways and Roll Modes (y1 > y1; y2 > y2; psi1 > p1; psi2 > p2)
%static tension in upper wire

ky1y1   = -v1^2;
ky1p1   = v1*(v1*t - N1*eta1u);
kp1y1   = v1*(v1*t - N1*eta1u);
kp1p1   = -1*lu^2*(v1*t - N1*eta1u) - (v1*t - N1*eta1u)^2;

```

```

KTuSR = (FibresU*Tu/lu^3) * [ ky1y1  0      ky1p1  0
                             0      0      0      0
                             kp1y1  0      kp1p1  0
                             0      0      0      0 ];

%*****
%extension of the upper wires

ky1y1 = -1*N1^2;
ky1p1 = N1*(t*N1 + etalu*v1);
kp1y1 = N1*(t*N1 + etalu*v1);
kp1p1 = -1*(t*N1 + etalu*v1)^2;

KkuSR = FibresU*(ku/lu^2) * [ ky1y1  0      ky1p1  0
                             0      0      0      0
                             kp1y1  0      kp1p1  0
                             0      0      0      0 ];

%*****
%bending of upper wires

ky1y1 = -1*cos(nu)^2;
ky1p1 = -1*(etalu*sin(nu) - t*cos(nu) - (lu/2))*cos(nu);
kp1y1 = -1*(etalu*sin(nu) - t*cos(nu) - (lu/2))*cos(nu);
kp1p1 = -1*((1/au^2) + (lu^2/2) - (lu/au) + (t*cos(nu...
) - 2*etalu*sin(nu) + lu)*t*cos(nu) + (etalu*sin(nu) - lu)*etalu*sin(nu));

KbuSR = FibresU*(bu/lu^2) * [ ky1y1  0      ky1p1  0
                             0      0      0      0
                             kp1y1  0      kp1p1  0
                             0      0      0      0 ];

%*****
%static tension in lower wire

ky1 = -1*v2;
ky2 = v2;
kp1 = -1*(v2*s + N2*eta11);
kp2 = -1*(v2*h - N2*eta2);

kky1 = v2;
kky2 = -1*v2;
kkp1 = (v2*s + N2*eta11);
kkp2 = (v2*h - N2*eta2);

k = [ ky1 ky2 kp1 kp2 ].';
kk = [ kky1 kky2 kkp1 kkp2 ];

kp1p1 = (v2*s + N2*eta11);
kp2p2 = (v2*h - N2*eta2);

kkk = -1*(T1/l2)*diag([0,0,kp1p1,kp2p2],0);

```

```

KT1SR = (FibresL)*((T1/l2^3)*(k * kk) + kkk);

%*****
%extension of lower wire

ky1 = N2;
ky2 = -1*N2;
kp1 = -1*(v2*eta11 - N2*s);
kp2 = (v2*eta2 + N2*h);

kky1 = -1*N2;
kky2 = N2;
kkp1 = (v2*eta11 - N2*s);
kkp2 = -1*(v2*eta2 + N2*h);

k = [ ky1 ky2 kp1 kp2 ].';
kk = [ kky1 kky2 kkp1 kkp2 ];

Kk1SR = (FibresL)*(k1/l2^2)*(k * kk);

%*****
%bending of lower wires

cz = cos(zeta);
sz = sin(zeta);

ky1 = -1*cz;
ky2 = cz;
kp1 = -1*(s*cz + eta11*sz + (l2/2));
kp2 = -1*(h*cz - eta2*sz + (l2/2));

kky1 = cz;
kky2 = -1*cz;
kkp1 = (s*cz + eta11*sz + (l2/2));
kkp2 = (h*cz - eta2*sz + (l2/2));

k = [ ky1 ky2 kp1 kp2 ].';
kk = [ kky1 kky2 kkp1 kkp2 ];

kp1p1 = (1/a1^2) + (l2^2/4) - (l2/a1);
kp1p2 = (l2/a1) - (1/a1^2) - (l2^2/4);
kp2p1 = kp1p2;
kp2p2 = kp1p1;

kkk = [ 0 0 0 0
        0 0 0 0
        0 0 kp1p1 kp1p2
        0 0 kp2p1 kp2p2 ];

Kb1SR = (FibresL)*(bu/l2^2)*((k * kk) - kkk);

```

```

%*****
%forming the system of differential equations to be solved

MSR      = diag([m1 m2 I1x I2x]);

KSR      = (KTuSR + KkuSR + KbuSR + KTlSR + KklSR + KblSR);

iMKSR    = inv(MSR) * KSR;

[VectSR, EigSR] = eig(-iMKSR,eye(4));

FreqSR   = sqrt(diag(EigSR))/(2*pi);
QmodeSR  = 0.5*real(FreqSR)./imag(FreqSR);

%*****
%Rotational Modes (phi1 > f1; phi2 > f2)
%reaction against upper wires

KTuR     = -1*(FibresU*Tu*eta0*eta1u/lu) * [ 1      0
                                             0      0  ];

%*****
%torsion of upper wires

KRuR     = -1*FibresU*kappaU * [ 1      0
                                0      0  ];

%*****
%bending of the upper wires

KXuR     = -1*FibresU*(bu/lu^2)*eta1u^2 * [ 1      0
                                             0      0  ];

%*****
%reaction against lower wires

kf1f1    = -1*(Tl/l2)*(eta1l*eta2 + delta1*delta2 - delta1^2*...
(1-(L/l2)^2)- eta1l*(1-(J/l2)^2));
kf1f2    = (Tl/l2^3)*(J^2*eta2*eta1l + L^2*delta1*delta2);
kf2f1    = (Tl/l2^3)*(J^2*eta2*eta1l + L^2*delta1*delta2);
kf2f2    = -1*(Tl/l2)*(eta2*eta1l + delta1*delta2 - delta2^2*...
(1-(L/l2)^2) - eta2*(1-(J/l2)^2));

KTlR     = FibresL * [  kf1f1  kf1f2
                       kf2f1  kf2f2  ];

%*****
%extension of lower wires

kf1f1    = -1*(kl/l2^2)*(D2^2*eta1l^2 + N2^2*delta1^2);
kf1f2    = (kl/l2^2)*(D2^2*eta2*eta1l + N2^2*delta1*delta2);
kf2f1    = (kl/l2^2)*(D2^2*eta2*eta1l + N2^2*delta1*delta2);

```

```

kf2f2 = -1*(kl/l2^2)*(D2^2*eta2^2 + N2^2*delta2^2);

Kk1R = FibresL * [ kf1f1 kf1f2
                   kf2f1 kf2f2 ];

%*****
%bending of the lower wires

kf1f1 = -1*(delta1^2 + eta1l^2);
kf1f2 = eta1l*eta2 + delta1*delta2;
kf2f1 = eta1l*eta2 + delta1*delta2;
kf2f2 = -1*(delta2^2 + eta2^2);

KX1R = FibresL*(bl/l2^2) * [ kf1f1 kf1f2
                             kf2f1 kf2f2 ];

%*****
%torsion of the lower wires

KR1R = -1*FibresL*kappaL * [ 1 -1
                             -1 1 ];

%*****
%solving the eigenvalue problem to extract the mode frequencies

MR = diag([I1z I2z]);

KR = KTuR + KTlR + Kk1R + KRuR + KR1R + KXuR + KX1R;

iMKR = inv(MR) * KR;

[VectR, EigR] = eig(-iMKR,eye(2));

FreqR = sqrt(diag(EigR))/(2*pi);
Qmoder = 0.5*real(FreqR)./imag(FreqR);

%*****
%Vertical Modes (z1 > 1; z2 > 2)
%extension of upper wire

KkuV = -1*FibresU*ku*cos(nu)^2 * [ 1 0
                                   0 0 ];

%*****
%extension of lower wires

KklV = -1*FibresL*kl*cos(omega)^2 * [ 1 -1
                                       -1 1 ];

%*****

```

```

%solving the eigenvalue problem to extract the mode frequencies

MV      = diag([m1 m2]);

KV      = KkuV + KklV;

iMKV    = inv(MV) * KV;

[VectV,EigV] = eig(-iMKV,eye(2));

FreqV   = sqrt(diag(EigV))/(2*pi);
QmodeV  = 0.5*real(FreqV)./imag(FreqV);

%*****
%output vector

freq    = [   FreqLT
            FreqSR
            FreqR
            FreqV ];

%*****
%print results on screen - eigenvalues and eigenvectors

if (max(switches == 'e') == 1)

fprintf(1,'\n');
fprintf(1,'Modes of Double Pendulum\n');
fprintf(1,modeld);
fprintf(1,'\n');
fprintf(1,'Vertical Height of Pendulum (to mirror centre) %6.3f m.\n'...
,Vertical);

X1      = real(VectLT(1,1:4));
X2      = real(VectLT(2,1:4));
T1      = real(VectLT(3,1:4));
T2      = real(VectLT(4,1:4));

fprintf(1,'\n');
fprintf(1,'Longitudinal and Tilt\n');
fprintf(1,'Freq \t\t %7.3f \t %7.3f \t %7.3f \t %7.3f \t (Hz) \n'...
,FreqLT);
fprintf(1,'Q \t\t %7.1f \t %7.1f \t %7.1f \t %7.1f \t (x1000) \n'...
,QmodeLT/1000);
fprintf(1,'X1 \t\t %7.4f \t %7.4f \t %7.4f \t %7.4f \t (m) \n',X1);
fprintf(1,'X2 \t\t %7.4f \t %7.4f \t %7.4f \t %7.4f \t (m) \n',X2);
fprintf(1,'T1 \t\t %7.4f \t %7.4f \t %7.4f \t %7.4f \t (rad) \n',T1);
fprintf(1,'T2 \t\t %7.4f \t %7.4f \t %7.4f \t %7.4f \t (rad) \n',T2);

Y1      = real(VectSR(1,1:4));
Y2      = real(VectSR(2,1:4));
P1      = real(VectSR(3,1:4));

```

```

P2      = real(VectSR(4,1:4));

fprintf(1,'\n');
fprintf(1,'Sideways and Roll\n');
fprintf(1,'Freq \t\t %-7.3f \t %-7.3f \t %-7.3f \t %-7.3f \t (Hz) \n'...
,FreqSR);
fprintf(1,'Q \t\t %7.1f \t %7.1f \t %7.1f \t %7.1f \t (x1000) \n'...
,QmodeSR/1000);
fprintf(1,'Y1 \t\t %7.4f \t %7.4f \t %7.4f \t %7.4f \t (m) \n',Y1);
fprintf(1,'Y2 \t\t %7.4f \t %7.4f \t %7.4f \t %7.4f \t (m) \n',Y2);
fprintf(1,'P1 \t\t %7.4f \t %7.4f \t %7.4f \t %7.4f \t (rad) \n',P1);
fprintf(1,'P2 \t\t %7.4f \t %7.4f \t %7.4f \t %7.4f \t (rad) \n\n',P2);

F1      = real(VectR(1,1:2));
F2      = real(VectR(2,1:2));

fprintf(1,'Rotational Modes\n');
fprintf(1,'Freq \t\t %-7.3f \t %-7.3f \t (Hz) \n',FreqR);
fprintf(1,'Q \t\t %7.1f \t %7.1f \t (x1000) \n',QmodeR/1000);
fprintf(1,'F1 \t\t %7.4f \t %7.4f \t (rad) \n',F1);
fprintf(1,'F2 \t\t %7.4f \t %7.4f \t (rad) \n\n',F2);

Z1      = real(VectV(1,1:2));
Z2      = real(VectV(2,1:2));

fprintf(1,'Vertical Modes\n');
fprintf(1,'Freq \t\t %-7.3f \t %-7.3f \t (Hz) \n',FreqV);
fprintf(1,'Q \t\t %7.1f \t %7.1f \t (x1000) \n',QmodeV/1000);
fprintf(1,'Z1 \t\t %7.4f \t %7.4f \t (m) \n',Z1);
fprintf(1,'Z2 \t\t %7.4f \t %7.4f \t (m) \n\n',Z2);

end

return

```

A.2 assign.m

Syntax

[error] = assign(name)

Inputs: **name** source file for pendulum parameters.

Outputs: **error** Error flag.

Functions called by assign.m:

- dp_g6_mc.m
- dp_new.m
- dp_prot.m

Purpose

This program simply calls the file in which the parameters defining the pendulum are defined (*i.e.* **dp_?????.m** or **sp_?????**). These are set as global variables.

If the global variable **assigned** is set to a value of '1' then the parameter file is not called - this prevents the parameters being reset each time certain functions are called.

Source Code

```
function [error] = assign(name)
%[error] = assign(name)
%
%error           error flag
%name           name of pendulum file
%
%Stuart Killbourn (June '96)

global assigned

if (assigned == 1)
    return
end

error = 0;

len = length(name);
```

```

if (len > 8)
    fprintf(1,'name too long\n');
    error = 1;
    return
end

while (length(name) < 8)
    name = [name, ' '];
end

%*****
%This is the list of all pendulum filenames (8 characters long)

if (name == 'dp_new ')
    dp_new;
elseif (name == 'dp_prot ')
    dp_prot;
elseif (name == 'dp_g6_mc')
    dp_g6_mc;
else
    fprintf(1,'No pendulum file found\n')
    error = 1;
end

return

```

A.3 constant.m

Syntax

[] = constant()

There are no inputs or outputs to this function.

No functions are called by **constant.m**.

Purpose

This program defines some physical constants used by many functions. These are set as global variables.

If the global variable **assigned** is set to a value of '1' then the constants are not redefined - this prevents the values being reset each time certain functions are called.

Source Code

```
function constant
%Universal constants - all programs should reference this.
%
%Stuart Killbourn (June 96)

global assigned

if (assigned == 1)
    return
end

fprintf(1,'Universal Constants Assigned\n');

global g kB T

%*****
%Universal Constants

g      = 9.81;           %gravitational field strength (N/kg)
kB     = 1.381e-23;    %Boltzmann's constant (J/K)
T      = 300;          %ambient temperature (K)

return
```

A.4 props.m

Syntax

```
[rho,Y,Q,PR,th_exp,th_cond,cp,BS] = props(material)
```

Inputs:	material	name of material.
Outputs:	rho	density (kg m^{-3}).
	Y	Young's Modulus (N m^{-2}).
	Q	structural damping Q factor.
	PR	Possion's ratio.
	th_exp	coefficient of thermal expansion (K^{-1}).
	th_cond	thermal conductivity ($\text{W m}^{-1} \text{K}^{-1}$).
	cp	specific heat capacity ($\text{J kg}^{-1} \text{K}^{-1}$).
	BS	breaking stress (Pa).

No functions are called by **props.m**.

Purpose

This file returns the mechanical properties of various materials suitable for a test mass suspension. More can be added by following the pattern of the variables **materials** and **prop_vals**.

Source Code

```
function [rho,Y,Q,PR,th_exp,th_cond,cp,BS] = props(material)
%material      name of material
%rho           density                (kg/m^3)
%Y             Young's Modulus       (N/m^2)
%Q             Structural Damping Q
%PR            Possion's Ratio
%th_exp        Co-efficient of thermal expansion (1/K)
%th_cond       Thermal conductivity  (W/m.K)
%cp            Specific Heat Capacity (J/kg.K)
%BS            Breaking Stress        (Pa)
%
%Stuart Killbourn (October '96)

%allowed names of materials - pad out with spaces to make as long as the
%longest these are in the same order in which they appear in the definition
%of 'prop_vals' below.
```

```

materials = [ 'steel      '
              '5thou     '
              '7thou     '
              'aluminium  '
              'fused_silica'
              'sapphire   '
              'silicon    '
              'BK7       ' ];

```

%list of properties for materials - '1' is a dummy for unknown info

```
prop_vals = [
```

%rho	Y	Q	PR	th_exp	th_cond	cp	BS
7870	2.00e11	2000	0.29	11.8e-6	80.2	449	3e9 %steel
7900	1.65e11	2000	0.29	11.8e-6	60	449	2e9 %5thou
7900	1.72e11	2000	0.29	11.8e-6	60	449	2e9 %7thou
2700	1	2e5	1	1	1	1	1 %aluminium
2202	7e10	1e6	0.16	5.1e-7	1.38	772	8e8 %fused silica
3980	3.4e11	1.8e8	1	8.4e-6	25	418.4	2e9 %sapphire
2320	1e11	3e7	1	2.33e-6	148	715.46	8e8 %silicon
2510	1	3000	1	1	1	1	1 %BK7

```
];
```

```

%steel      the big rubber bible
%5thou      as steel and experiment
%7thou      as steel and experiment
%aluminium  Q from Jenny's thesis
%fused silica sheila's GEO600 report
%sapphire   sheila's GEO600 report
%silicon    sheila's GEO600 report
%BK7        Q from Saulson (private communication)

```

```

while (length(material) < size(materials)*[0 1]')
    material = [material, ' '];
end

```

```

for j = 1:(size(materials)*[1 0]')
    if (min(materials(j,:) == material) == 1)
        rho = prop_vals(j,1);
        Y = prop_vals(j,2);
        Q = prop_vals(j,3);
        PR = prop_vals(j,4);
    end
end

```

```
        th_exp = prop_vals(j,5);
        th_cond = prop_vals(j,6);
        cp = prop_vals(j,7);
        BS = prop_vals(j,8);
    end
end

if (exist('rho') ~= 1)
    fprintf(1,['(props.m) Material name not recognised: ',material,'\n']);
end

return
```

A.5 dp_new.m

Syntax

[] = dp_new()

There are no inputs or outputs to this function.

Functions called by dp_new.m:

- props.m

Purpose

This file sets parameters that describe the design of pendulum detailed in Section 5.3.

These are set as global variables.

Source Code

```
function dp_new
%list of parameter assignments for low frequency double pendulum
%
%Stuart Killbourn (June 96)

fprintf(1,'Parameters for New Prototype Pendulum Assigned\n');

%*****
%global variables defined in this program

global modeld
global m1 I1x I1y I1z
global m2 I2x I2y I2z
global ix iy iz
global tx tr
global FibresU FibresL
global matU matL matI matT
global Qu Ql Yu Yl PRu PRl
global Ru Rl lu l2
global t s delta1 delta2 h
global eta0 eta1u eta1l eta2
global offV offH z2dn
global lc lc_name lc_gain

%*****
%Glasgow Prototype Pendulum
%With low frequency modes

modeld = 'Glasgow Prototype - 1996';

ix      = 0.100;           %dimensions of intermediate mass
```

```

iy      = 0.041;
iz      = 0.076;

matI    = 'steel';

rhoI    = props(matI);

m1      = rhoI*ix*iy*iz;           %intermediate mass

I1x     = m1*(iy^2+iz^2)/12;      %moment of inertia (sideways tilt)
I1y     = m1*(iz^2+ix^2)/12;      %moment of inertia (longitudinal tilt)
I1z     = m1*(iy^2+ix^2)/12;      %moment of inertia (rotation)

tx      = 0.1016;                 %dimensions of test mass
tr      = 0.0635;

matT    = 'fused_silica';

rhoT    = props(matT);

m2      = rhoT*pi*tr^2*tx;        %calculation of mass and moment of inertia

I2x     = m2*(tr^2/2);            %moment of inertia (sideways tilt)
I2y     = m2*(tr^2/4+tx^2/12);    %moment of inertia (longitudinal tilt)
I2z     = m2*(tr^2/4+tx^2/12);    %moment of inertia (rotation)

FibresU = 2;                      %number of upper wires
FibresL = 4;                      %number of lower wires

matU    = '7thou';
matL    = '5thou';

[rho,Yu,Qu,PRu] = props(matU);
[rho,Yl,QL,PRl] = props(matL);

Ru      = 89e-6;                   %wire radii
Rl      = 62e-6;

lu      = 0.1995;                 %upper wire length
l2      = 0.3700;                 %lower wire lengths

%parameters in x - axis

delta1  = 0.005;                  %half separation of wires at intermediate mass
delta2  = 0.005;                  %half separation of wires at test mass

%parameters in y - axis

eta0    = iy/2 + 0.003;           %half separation of wires at top plate
eta1u   = iy/2 + 0.003;           %half separation of wires at intermediate mass
eta1l   = iy/2 + 0.003;
eta2    = tr + 0.005;             %half separation of wires at test mass

```

```

%parameters in z - axis

t      = 0.003;          %height of upper wire at im (above cm)
s      = 0.000;          %height of lower wire at im (below cm)
h      = 0.001;          %height of wire at test mass (above cm)

%x-coupling factors

offV   = 0.001;          %vertical offset of spot on mirror (above cm)
offH   = 0.001;          %horizontal offset of spot on mirror
z2dn   = 1e-3;           %x-coupling from vertical to displacement noise

%*****
%local control damping parameters

xc      = 0.000;         %cross-coupling level in local control sensor/actuators

tdx     = 0.045;         %distance from vertical axis to tilt coil/magnet
tdz     = 0.000;         %vertical offset of tilt coil/magnet (above cm)
ldz     = 0.000;         %vertical offset of long coil/magnet (above cm)
sdx     = 0.045;         %distance from vertical plane to sideways coil/magnet
sdz     = 0.000;         %height of sideways coil/magnet (above cm)

%      x      y      z      tilt      rot      roll
lc = [ 1      xc      xc      ldz      xc      xc          %long
      xc      xc      1      tdx      xc      xc          %tilt & vert
      xc      xc      1      -tdx     xc      xc          %tilt & vert
      xc      1      xc      xc      sdx      sdz          %side & rot
      xc      -1     xc      xc      sdx      -sdz         %side & rot
      0      0      0      0      0      0      0      ]; %roll

lc_name = [ 3      7      7      7      7      7      -1 ]; %local_??

lc_gain = [ 0.5      0.0008 0.0008 0.063 0.063 0 ];
%normalised gain

return

```

A.6 dp_prot.m

Syntax

[] = dp_prot()

There are no inputs or outputs to this function.

Functions called by dp_prot.m:

- props.m

Purpose

This file sets parameters that describe the double pendulum designed by Euan Morrison (as detailed in [39]). These are set as global variables.

Source Code

```
function dp_prot
%list of parameter assignments for Euan's pendulum
%
%Stuart Killbourn (June 95)

fprintf(1,'Parameters for Glasgow Prototype Pendulum (Old) Assigned\n');

%*****
%global variables defined in this program

global modeld
global m1 I1x I1y I1z
global m2 I2x I2y I2z
global ix iy iz
global tx tr
global FibresU FibresL
global matU matL matI matT
global Qu Ql Yu Yl PRu PRl
global Ru Rl lu l2
global t s delta1 delta2 h
global eta0 eta1u eta1l eta2
global offV offH z2dn
global lc lc_name lc_gain

%*****
%Glasgow Prototype Pendulum
%With low frequency modes

modeld = 'Glasgow Prototype - Euan's Original';

ix      = 0.088;           %dimensions of intermediate mass
```

```

iy      = 0.080;
iz      = 0.025;

matI    = 'aluminium';

rhoI    = props(matI);

m1      = rhoI*ix*iy*iz;           %intermediate mass

I1x     = m1*(iy^2+iz^2)/12;      %moment of inertia (sideways tilt)
I1y     = m1*(iz^2+ix^2)/12;      %moment of inertia (longitudinal tilt)
I1z     = m1*(iy^2+ix^2)/12;      %moment of inertia (rotation)

tx      = 0.1016;                 %dimensions of test mass
tr      = 0.0635;

matT    = 'fused_silica';

rhoT    = props(matT);

m2      = rhoT*pi*tr^2*tx;        %calculation of mass and moment of inertia

I2x     = m2*(tr^2/2);            %moment of inertia (sideways tilt)
I2y     = m2*(tr^2/4+tx^2/12);    %moment of inertia (longitudinal tilt)
I2z     = m2*(tr^2/4+tx^2/12);    %moment of inertia (rotation)

FibresU = 2;                      %number of upper wires
FibresL = 4;                      %number of lower wires

matU    = 'steel';
matL    = '7thou';

[rho,Yu,Qu,PRu] = props(matU);
[rho,Yl,QL,PRl] = props(matL);

Ru      = 127e-6;                 %wire radii
Rl      = 89e-6;

lu      = 0.12;                   %upper wire length
l2      = 0.24;                   %lower wire lengths

%parameters in x - axis

delta1  = 0.025;                  %half separation of wires at intermediate mass
delta2  = 0.025;                  %half separation of wires at test mass

%parameters in y - axis

eta0    = iy/2;                   %half separation of wires at top plate
eta1u   = iy/2;                   %half separation of wires at intermediate mass
eta1l   = iy/2;
eta2    = tr;                      %half separation of wires at test mass

```

```

%parameters in z - axis

t      = 0.000;      %height of upper wire at im (above cm)
s      = 0.012;      %height of lower wire at im (below cm)
h      = 0.001;      %height of wire at test mass (above cm)

%x-coupling factors

offV   = 0.001;      %vertical offset of spot on mirror (above cm)
offH   = 0.001;      %horizontal offset of spot on mirror
z2dn   = 1e-3;       %x-coupling from vertical to displacement noise

%*****
%local control damping parameters

xc      = 0.001;      %cross-coupling level in local control sensor/actuators

tdx     = 0.030;      %distance from vertical axis to tilt coil/magnet
ldz     = 0.000;      %vertical offset of long coil/magnet (above cm)
ldy     = 0.030;      %horizontal offset of long coil/magnet
sdx     = 0.030;      %distance from vertical plane to sideways coil/magnet
sdz     = 0.000;      %height of sideways coil/magnet (above cm)

%      x      y      z      tilt      rot      roll

lc = [ 1      xc      xc      ldz      ldy      xc      %long
       xc      xc      1      tdx      xc      xc      %tilt & vert
       xc      xc      1      -tdx     xc      xc      %tilt & vert
       xc      1      xc      xc      sdx      sdz      %side & rot
       xc      -1     xc      xc      sdx      -sdz     %side & rot
       0      0      0      0      0      0      0      ]; %roll

lc_name = [ 6      6      6      6      6      6      -1 ]; %local_??

lc_gain = [ 0      0      0      0      0      0      0 ];
%normalised gain

return

```

A.7 dp_g6_mc.m

Syntax

[] = dp_g6_mc()

There are no inputs or outputs to this function.

Functions called by dp_g6_mc.m:

- props.m

Purpose

This file sets parameters that describe the double pendulum designed to suspend the modecleaner mirrors for the GEO 600 project (as detailed in Section 8.2). These are set as global variables.

Source Code

```
function dp_g6_mc
%list of parameter assignments for the GEO600 modecleaner suspension
%
%Stuart Killbourn (September 96)

fprintf(1,'Parameters for GEO600 Modecleaner Pendulum Assigned\n');

%*****
%global variables defined in this program

global modeld
global m1 I1x I1y I1z
global m2 I2x I2y I2z
global ix iy iz
global tx tr
global FibresU FibresL
global matU matL matI matT
global Qu Ql Yu Yl PRu PRl
global Ru Rl lu l2
global t s delta1 delta2 h
global eta0 eta1u eta1l eta2
global offV offH z2dn
global lc lc_name lc_gain

%*****
%GEO600 modecleaner and crude optics suspension

modeld = 'GEO600 Modecleaner Pendulum';

ix      = 0.070;           %dimensions of intermediate mass
```

```

iy      = 0.050;
iz      = 0.085;

matI    = 'aluminium';

rhoI    = props(matI);

m1      = rhoI*ix*iy*iz;          %intermediate mass

I1x     = m1*(iy^2+iz^2)/12;     %moment of inertia (sideways tilt)
I1y     = m1*(iz^2+ix^2)/12;     %moment of inertia (longitudinal tilt)
I1z     = m1*(iy^2+ix^2)/12;     %moment of inertia (rotation)

tx      = 0.050;                 %dimensions of test mass
tr      = 0.050;

matT    = 'fused_silica';

rhoT    = props(matT);

m2      = rhoT*pi*tr^2*tx;       %calculation of mass and moment of inertia

I2x     = m2*(tr^2/2);           %moment of inertia (sideways tilt)
I2y     = m2*(tr^2/4+tx^2/12);   %moment of inertia (longitudinal tilt)
I2z     = m2*(tr^2/4+tx^2/12);   %moment of inertia (rotation)

FibresU = 2;                     %number of upper wires
FibresL = 4;                     %number of lower wires

matU    = '5thou';
matL    = '5thou';

[rho,Yu,Qu,PRu] = props(matU);
[rho,Yl,Ql,PRl] = props(matL);

Ru      = 62e-6;                 %wire radii
Rl      = 50e-6;                 %4thou

lu      = 0.300;                 %upper wire length
l2      = 0.500;                 %lower wire lengths

%parameters in x - axis

delta1  = 0.002;                 %half separation of wires at intermediate mass
delta2  = 0.002;                 %half separation of wires at test mass

%parameters in y - axis

eta0    = iy/2 + 0.003;         %half separation of wires at top plate
eta1u   = iy/2 + 0.003;         %half separation of wires at intermediate mass
eta1l   = iy/2 + 0.003;
eta2    = tr + 0.002;           %half separation of wires at test mass

```

```

%parameters in z - axis

t      = 0.000;          %height of upper wire at im (above cm)
s      = 0.011;          %height of lower wire at im (below cm)
h      = 0.002;          %height of wire at test mass (above cm)

%x-coupling factors

offV   = 0.001;          %vertical offset of spot on mirror (above cm)
offH   = 0.001;          %horizontal offset of spot on mirror
z2dn   = 1e-3;           %x-coupling from vertical to displacement noise

%*****
%local control damping parameters

xc      = 0.001;         %cross-coupling level in local control sensor/actuators

tdz = 0.0375;           %vertical offset of tilt coil/magnet (above cm)
ldz = 0.000;           %vertical offset of long coil/magnet (above cm)
sdx = 0.030;           %distance from vertical plane to sideways coil/magnet
sdz = 0.000;           %height of sideways coil/magnet (above cm)

%      x      y      z      tilt      rot      roll
lc = [ 1      xc      xc      -tdz      xc      xc          %long
      1      xc      xc      tdz      xc      xc          %tilt & vert
      0      0      0      0      0      0          %tilt & vert
      xc      1      xc      xc      sdx      sdz          %side & rot
      xc      -1     xc      xc      sdx      -sdz         %side & rot
      0      0      0      0      0      0          ]; %roll

lc_name = [ 5      5      -1      5      5      -1 ]; %local_??

lc_gain = [ 0.05    0.06    0      0.063    0.063    0 ];
%normalised gain

return

```

A.8 fb_x1.m

Syntax

[a,b,c,d] = fb_x1()

There are no inputs to this function.

Outputs:

a	state-space matrix.
b	state-space matrix.
c	state-space matrix.
d	state-space matrix.

Functions called by fb_x1.m:

- assign
- constant.m
- dp_new.m
- dp2ss.m
- loss.m

Purpose

This function returns the state-space matrices which characterise the response of a double pendulum suspension to forces applied at the intermediate mass.

Algorithm

The state-space models for the pendulum (described in Section 5.3) and the transverse modes of the suspension wires are combined in a parallel path configuration. The pendulum model is obtained from the function **dp2ss.m**; the model for the transverse modes is found in Section 4.7. The Q factors of the transverse modes are determined by a structural damping term and a thermoelastic damping term. These are calculated from data defined in **props.m**. The Q factors are enhanced according to Equation 7.17 to account for the wire tension.

Source Code

```
function [a,b,c,d] = fb_x1
%model of transfer function of double pendulum
%force at intermediate mass to test mass displacement
%includes transverse modes of suspension wires

dp_name = 'dp_new';

%*****
%global variables defined in 'constant'

global g

constant;           %assign universal constants

%*****
%global variables defined in dp_name

global modeld
global m1 I1x I1y I1z
global m2 I2x I2y I2z
global FibresU FibresL
global matU matL matI matT
global Qu Ql Yu Yl PRu PRl
global Ru Rl lu l2
global t s delta1 delta2 h
global eta0 eta1u eta1l eta2
global offV offH z2dn
global lc lc_name lc_gain

assign(dp_name);

global fv

%*****
%transverse modes of the wires

mds      = 5;           %number of transverse modes included
n        = linspace(1,mds,mds);

[rho,Yl] = props(matL);

N2       = (eta2 - eta1l);
D2       = (delta2 - delta1);
U2       = sqrt(N2^2 + D2^2);
omega    = asin(U2/l2);

Tl       = m2*g/(FibresL*cos(omega)); %lower wire tension

Ix       = pi*Rl^4/4;           %moment of cross section
al       = sqrt(Tl/(Yl*Ix));    %bending length
```

```

lambda = rho*pi*Rl^2;
mwire  = lambda*l2;

fv      = (1/(2*l2))*sqrt(Tl/lambda).*n;
wv      = 2*pi*fv;

phi_w   = loss(dp_name, fv, 'lt');      %material loss
Q       = 1./(phi_w.*((2/(al*l2))*(1 + (n*pi).^2/(2*al*l2))));
%enhanced Q factor

kv      = (mwire/2)*wv.^2.*(1 + i./(Q.*wv));

m       = (mwire/2) * ones(1,mds);
M       = diag(m);

K       = -1 * diag(kv);

invMK   = inv(M) * K;

on      = ones(1,mds);
ze      = zeros(1,mds);

c1      = (mwire./(n*pi*m1));
c2      = -1 * (mwire./(n*pi*m2)) .* (-1).^n;

inputM  = [   on      1./m    ]';

av      = [   zeros(mds)    eye(mds)
            real(invMK)    imag(invMK) ];

bv      = inputM .* [   ze      c1      ]';

cv      = [   c2      ze      ];

dv      = [0];

%*****
%pendulum model (longitudinal)

[ff,iMKLT] = dp2ss(dp_name, '');

diMKLT   = 50000*diag(diag(imag(iMKLT(1:2,1:2))));

Fdamp    = 1;

ML       = [   1      1      1/m1    1/m2    ]';

AL       = [ zeros(2)                eye(2)
            real(iMKLT(1:2,1:2))    diMKLT/(2*pi*Fdamp)    ];

Bx1     = ML.*[ 0      0      1      0      ]';

```

```
Cx1    = [    0    1    0    0    ];
DL     = zeros(size(Cx1)*[1 0]',size(Bx1)*[0 1]');

%*****
%whole thing

[a,b,c,d] = parallel(AL,Bx1,Cx1,DL,av,bv,cv,dv);

return
```

A.9 fb_x2.m

Syntax

[a,b,c,d] = fb_x2()

There are no inputs or outputs to this function.

Outputs:

a	state-space matrix.
b	state-space matrix.
c	state-space matrix.
d	state-space matrix.

Functions called by fb_x2.m:

- assign.m
- constant
- dp_new.m
- dp2ss.m
- loss.m

Purpose

This function returns the state-space matrices which characterise the response of a double pendulum suspension to forces applied at the test mass. The internal modes are specific to the test masses used in the Glasgow prototype detector.

Algorithm

The state-space models for the pendulum (described in Section 5.3) and the internal modes of the test masses are combined in a parallel path configuration. (The transverse modes of the suspension wires can also be included – the model is as detailed for **fb_x1.m**.) The pendulum model is obtained from the function **dp2ss.m**. The model for the internal modes is described in Section 4.8 and the data refers to the test masses used in the Glasgow prototype.

Source Code

```
function [a,b,c,d] = fb_x2
%model of transfer function of pendulum with
%internal modes (and violin modes - optional)

dp_name = 'dp_new';

%*****
%global variables defined in 'constant'

global g

constant;          %assign universal constants

%*****
%global variables defined in dp_name

global modeld
global m1 I1x I1y I1z
global m2 I2x I2y I2z
global FibresU FibresL
global matU matL matI matT
global Qu Ql Yu Yl PRu PRl
global Ru Rl lu l2
global t s delta1 delta2 h
global eta0 eta1u eta1l eta2
global offV offH z2dn
global lc lc_name lc_gain

global f0 fv

%*****
%transverse modes of the wires

mds      = 5;
n        = linspace(1,mds,mds);

[rho,Yl] = props(matL);

N2       = (eta2 - eta1l);
D2       = (delta2 - delta1);
U2       = sqrt(N2^2 + D2^2);
omega    = asin(U2/l2);

Tl       = m2*g/(FibresL*cos(omega));   %lower wire tension

Ix       = pi*Rl^4/4;                   %moment of cross section
al       = sqrt(Tl/(Yl*Ix));           %bending length
lambda   = rho*pi*Rl^2;
mwire    = lambda*l2;
```

```

fv      = (1/(2*l2))*sqrt(Tl/lambda).*n;
wv      = 2*pi*f0;

phi_w   = loss(dp_name,fv,'lt');          %material loss
Q       = 1./(phi_w.*((2/(al*l2))*(1 + (n*pi).^2/(2*al*l2))));
%enhanced Q factor

kv      = (mwire/2)*wv.^2.*(1 + i./(Q.*wv));

m       = (mwire/2) * ones(1,mds);
M       = diag(m);

K       = -1 * diag(kv);

invMK   = inv(M) * K;

on      = ones(1,mds);
ze      = zeros(1,mds);

c1      = (mwire./(n*pi*m1));
c2      = -1 * (mwire./(n*pi*m2)) .* (-1).^n;

inputM  = [   on      1./m ]';

av      = [   zeros(mds)      eye(mds)
            real(invMK)      imag(invMK)   ];

bv      = inputM .* [   ze      c2      ]';

cv      = [   c2      ze      ];

dv      = [0];

%*****
%input parameters
%
%f0      resonant frequencies
%Q       Q factors (as measured)
%alpha   effective mass coefficient
%couple  coupling strength of magnet to internal mode

f0      = [ 23619  25509  28568  32000  36274  46812  47615  ];
Q       = [ 74000  220000  44000  50000  730  20000  13000  ];
alpha   = [ 0.55  0.36  0.72  2.5  0.19  0.32  0.055  ];
couple  = [ -0.044  0.635  -0.153  0.872  -0.106  0.448  -0.102  ];

f1      = [ 55840  57302  59585  64439  69195  74732  75670  79846];
Q1      = [ 9900  20000  17000  15000  9600  7700  19000  5000 ];
alpha1  = [ 0.192  0.489  0.046  0.708  0.112  0.080  0.077  0.034];
couple1 = [ -0.579  -0.313  -0.104  0.266  -0.112  -0.270  -0.094  0.049];
%some more modes that can be included

```

```

if 1

f0      = [    f0      f1      ];
Q       = [    Q       Q1      ];
alpha   = [    alpha  alpha1  ];
couple  = [    couple  couple1 ];

end

%*****
%pendulum model (longitudinal)

[ff,iMKLT] = dp2ss(dp_name,'');

diMKLT = 50000*diag(diag(imag(iMKLT(1:2,1:2))));

Fdamp   = 1;

ML      = [    1      1      1/m1  1/m2  ]';

AL      = [    zeros(2)          eye(2)
             real(iMKLT(1:2,1:2))  diMKLT/(2*pi*Fdamp)  ];

Bx2     = ML.*[ 0      0      0      1      ]';

Cx2     = [    0      1      0      0      ];

DL      = zeros(size(Cx2)*[1 0]',size(Bx2)*[0 1]');

%*****
%internal modes

m2      = 2.82;

m       = alpha*m2;
ki      = m.*(2*pi*f0).^2.*(1 + i./(Q*2*pi.*f0));
M       = diag(m);

K       = -1 * diag(ki);

invMK   = inv(M) * K;

on      = ones(1,size(K)*[1 0]');
ze      = zeros(1,size(K)*[1 0]');

inputM  = [ on 1./m ]';

ai      = [    zeros(size(K))  eye(size(K))
             real(invMK)      imag(invMK)      ];

bi      = inputM .* [ ze -couple ]';

```

```

ci      = [      on      ze      ];
di      = [0];

%*****
%whole thing

[a,b,c,d] = parallel(AL,Bx2,Cx2,DL,ai,bi,ci,di);

%[a,b,c,d] = parallel(a,b,c,d,av,bv,cv,dv);
%these are the violin modes - but really they make little
%difference to the transfer function of feedback to the
%test mass - I think it's okay to omit them - unless they
%really have a very high Q factor (fused silica?).

return

```

Appendix B

Derivation of Equation 4.8

A static solution is required for Equation 4.7, that is:

$$T \frac{\partial^2 x}{\partial z^2} - YI \frac{\partial^4 x}{\partial z^4} = 0 . \quad (\text{B.1})$$

This should give a valid description of the suspension wire dynamics at frequencies well below their transverse modes. A general solution for $x(z)$ is

$$x(z) = A + Bz + C e^{\frac{z}{\lambda}} + D e^{-\frac{z}{\lambda}} \quad (\text{B.2})$$

where A , B , C and D are determined by the boundary conditions and λ is the characteristic bending length of the wire (obtained by substitution of the general solution into Equation B.1):

$$\lambda = \sqrt{\frac{YI}{T}} . \quad (\text{B.3})$$

For wires tensioned close to their breaking stress, typically $\lambda \ll l$.

The elastic energy stored in the wire is given by [56]

$$E = \frac{1}{2} \int_0^l YI \left(\frac{\partial^2 x}{\partial z^2} \right)^2 dz \quad (\text{B.4})$$

where

$$\frac{\partial^2 x}{\partial z^2} = \frac{C}{\lambda^2} e^{\frac{z}{\lambda}} + \frac{D}{\lambda^2} e^{-\frac{z}{\lambda}} \quad (\text{B.5})$$

so the energy stored depends only on the parameters C and D in Equation B.2.

The boundary conditions at the wire ends are:

$$x(0) = x_1 \quad (\text{B.6})$$

$$x(-l) = x_2 \quad (\text{B.7})$$

$$x'(0) = -\alpha \quad (\text{B.8})$$

$$x'(-l) = -\beta \quad (\text{B.9})$$

where $z = 0$ is the top of the wire; $z = -l$ is the bottom, and x' is the first derivative of x with respect to z . Substitution of the boundary conditions into the general solution give

$$x_1 = A + C + D \quad (\text{B.10})$$

$$x_2 = A - Bl + C\epsilon^{-\frac{l}{\lambda}} + D\epsilon^{\frac{l}{\lambda}} \quad (\text{B.11})$$

$$-\alpha = B + \frac{C}{\lambda} - \frac{D}{\lambda} \quad (\text{B.12})$$

$$-\beta = B + \frac{C}{\lambda}\epsilon^{-\frac{l}{\lambda}} - \frac{D}{\lambda}\epsilon^{\frac{l}{\lambda}}. \quad (\text{B.13})$$

Equations B.10 and B.11 combine to eliminate A :

$$x_1 - x_2 = Bl + C \left(1 - \epsilon^{-\frac{l}{\lambda}}\right) + D \left(1 - \epsilon^{\frac{l}{\lambda}}\right). \quad (\text{B.14})$$

Using Equation B.12 to eliminate B in Equation B.14 gives

$$x_1 - x_2 + \alpha l = C \left(1 - \frac{l}{\lambda} - \epsilon^{-\frac{l}{\lambda}}\right) + D \left(1 + \frac{l}{\lambda} - \epsilon^{\frac{l}{\lambda}}\right). \quad (\text{B.15})$$

However, since $l/\lambda \gg 1$ then $\epsilon^{\frac{l}{\lambda}} \gg l/\lambda$ and certainly $\epsilon^{\frac{l}{\lambda}} \gg 1$. Also $\epsilon^{-\frac{l}{\lambda}} \ll 1$. Therefore, Equation B.15 simplifies to

$$x_1 - x_2 + \alpha l = C \left(1 - \frac{l}{\lambda}\right) - D\epsilon^{\frac{l}{\lambda}}. \quad (\text{B.16})$$

Combining Equations B.12 and B.13 to eliminate B gives

$$\alpha - \beta = \frac{D}{\lambda} \left(1 - \epsilon^{\frac{l}{\lambda}}\right) - \frac{C}{\lambda} \left(1 - \epsilon^{-\frac{l}{\lambda}}\right) \quad (\text{B.17})$$

which can also be simplified, giving

$$C = \lambda(\beta - \alpha) - D\epsilon^{\frac{l}{\lambda}}. \quad (\text{B.18})$$

Substitution of Equation B.18 into Equation B.16 leads to

$$D \left(\frac{l}{\lambda} - 2\right) \epsilon^{\frac{l}{\lambda}} = x_1 - x_2 + \alpha\lambda + \beta(l - \lambda) \quad (\text{B.19})$$

and since $l/\lambda \gg 2$, Equation B.19 becomes

$$D = \frac{\lambda}{l} [x_1 - x_2 + \alpha\lambda + \beta(l - \lambda)] e^{-\frac{l}{\lambda}}. \quad (\text{B.20})$$

Using Equation B.18 with Equation B.16 but this time to eliminate D gives (and again using $l/\lambda \gg 2$)

$$C = \frac{\lambda}{l} [x_2 - x_1 - \alpha(l - \lambda) - \beta\lambda]. \quad (\text{B.21})$$

Having obtained expressions for C and D in terms of the coordinates of the wire ends, the elastic energy stored in the wire is deduced from Equation B.4. First, the variables γ and δ defined as

$$\gamma = x_2 - x_1 - \alpha(l - \lambda) - \beta\lambda \quad (\text{B.22})$$

$$\delta = x_1 - x_2 + \alpha\lambda + \beta(l - \lambda) \quad (\text{B.23})$$

so that

$$\frac{\partial^2 x}{\partial z^2} = \frac{1}{\lambda l} \left[\gamma e^{\frac{z}{\lambda}} + \delta e^{-\frac{l}{\lambda}} e^{-\frac{z}{\lambda}} \right]. \quad (\text{B.24})$$

The square of Equation B.24 is

$$\left(\frac{\partial^2 x}{\partial z^2} \right)^2 = \frac{1}{\lambda^2 l^2} \left[\gamma^2 e^{\frac{2z}{\lambda}} + 2\gamma\delta e^{-\frac{l}{\lambda}} + \delta^2 e^{-\frac{2l}{\lambda}} e^{-\frac{2z}{\lambda}} \right] \quad (\text{B.25})$$

and the elastic energy expressed by (from Equation B.4)

$$E = \frac{1}{2} Y I \frac{1}{\lambda^2 l^2} \left[\gamma^2 \frac{\lambda}{2} e^{\frac{2z}{\lambda}} + 2\gamma\delta e^{-\frac{l}{\lambda}} z - \delta^2 e^{-\frac{2l}{\lambda}} \frac{\lambda}{2} e^{-\frac{2z}{\lambda}} \right]_{z=0}^{z=-l}. \quad (\text{B.26})$$

Keeping only the dominant terms (since $e^{-\frac{l}{\lambda}} \ll 1$), Equation B.26 becomes

$$E = \frac{b}{4} [\gamma^2 - \delta^2] \quad (\text{B.27})$$

where

$$b = \frac{\sqrt{Y I T}}{l^2}. \quad (\text{B.28})$$

Replacing γ and δ with their definitions; putting $X = x_2 - x_1$, and gathering like terms gives

$$E = \frac{b}{4} \left[2X^2 + (\alpha^2 + \beta^2) (2\lambda^2 - 2\lambda l + l^2) - 2lX(\alpha + \beta) + 4\alpha\beta\lambda(l - \lambda) \right] \quad (\text{B.29})$$

which is Equation 4.8 as presented in Chapter 4.

Bibliography

- [1] Einstein, A., *Preuss. Akad. Wiss. Berlin, Sitzungsberichte der Physikalisch-mathematischen Klasse*, 1916, pp. 688.
- [2] Thorne, K. S., to be published in '*Proceedings of the Snowmass 95 Summer Study on Particle and Nuclear Astrophysics and Cosmology*', edited by E. W. Kolb and R. Peccei, World Scientific.
- [3] Hough, J. *et al*, Design Study Report, '*A British Long Baseline Gravitational Wave Observatory*'. May 1986. GWD/RAL/86-001.
- [4] Lyne, A. G. and Lorimer, D. R., *Nature*, Vol. 369, 1994, pp. 127–129.
- [5] Schutz, B. F., presented at the *First Edoardo Amaldi Conference on Gravitational Wave Experiments*, 14 June 1994.
- [6] Schutz, B. F., Report AEI-003, *Max-Planck-Institut für Gravitationsphysik*, Feb 1996.
- [7] Wilson, J. R. and Mathews, G. J., *Physical Review Letters*, Vol. 75, No. 23, 4 Dec 1995, pp. 4161–4164.
- [8] Hawking, S. W. and Israel, W., '*300 Years of Gravitation*', Cambridge University Press, 1987.
- [9] Zimmermann, M., *Nature*, Vol 271, 9 February 1978, pp. 524.
- [10] Rawley, L. A., Taylor, J. H., Davis, M. M. and Allan, D. W., *Science*, Vol. 238, 1987, pp. 761.

- [11] Hough, J. *et al*, GEO 600, ‘*Proposal for a 600 m Laser-Interferometric Gravitational Wave Antenna*’, 20 September 1994, (submitted to PPARC).
- [12] Abramovici, A., Althouse, W. E., Drever, R. W. P., Gürsel, Y., Kawamura, S., Raab, F. J., Shoemaker, D., Sievers, L., Spero, R. E., Thorne, K. S., Vogt, R. E., Weiss, R., Whitcomb, S. and Zucker, M. E., *Science*, Vol. 156, 1992, pp. 325.
- [13] Bradaschia, C., Del Fabbro, R., Di Virgilio, A., Giazotto, A., Kautzkey, H., Montelatici, V., Passuello, D., Brilliet, A., Cregut, O., Hello, P., Man, C. N., Manh, P.T., Marraud, A., Shoemaker, D., Vinet, J.-Y., Barone, F., Di Fiore, L., Milano, L., Russo, G., Solimeno, S., Aguirregabiria, J. M., Bel. H., Duruisseau, J.-P., Le Denmat, G., Tourrenc, P., Capozzi, M., Longo, M., Lops, M., Pinto, I., Rotoli, G., Damour, T., Bonazzola, S., Marck, J. A., Gourghoulon, Y., Holloway, L. E., Fuligni, F., Iafolla, V. and Natale, G., *Nuclear Instruments and Methods Physics Research*, A289, 1990, pp. 518.
- [14] Weber, J., *Physical Review*, Vol. 117, 1960, pp. 306.
- [15] Morimoto, K. *et al*, ‘*Proceedings of the Fifth Marcel Grossmann Meeting on General Relativity*’, edited by D. G. Blair and M. J. Buckingham, World Scientific, 1989.
- [16] Astone, P. *et al*, *Physics Review D*, Vol. 47, No. 2, 15 Jan 1993, pp. 362–375.
- [17] J. A. Lobo, *Europhysics Letters*, Vol. 35, 1996, pp. 253.
- [18] Drever, R. W. P., ‘*Gravitational Radiation*’, edited by N. Deroulle and T. Piran, Proceedings of the Les Houches Summer Institute, June 1982.
- [19] Meers, B. J., *Physical Review D*, Vol. 38, No. 8, Oct 1988, pp. 2317–2326.
- [20] LISA, ‘*Laser Interferometer Space Antenna for the Detection and Observation of Gravitational Waves*’, ESA pre-phase A report, Dec 1995, (Report MPQ 208, *Max-Planck-Institut für Quantenoptik*).
- [21] Morrison, E., *Ph. D. Thesis*, University of Glasgow, 1993, pp. 41–43.

- [22] Saulson, P. R., *Physical Review D*, 3rd series, Vol. 42, No. 8, 15 Oct 1990.
- [23] Gillespie, A. D. and Rabb, F., *Physical Review D*, Vol. 52, July 1995, pp. 577.
- [24] Rowan, S., *Ph. D. Thesis*, University of Glasgow, 1995, pp. 71.
- [25] Robertson, N. A., Hoggan, S., Mangan, J. B. and Hough, J., *Applied Physics B*, Vol. 39, 1986, pp. 149–153.
- [26] Skeldon, K. D., Strain, K. A., Grant, A. I. and Hough, J., *Review of Scientific Instruments*, Vol. 67, No. 7, July 1996, pp. 2443–2448.
- [27] Skeldon, K. D. and Hough, J., *Review of Scientific Instruments*, Vol. 66, No. 4, April 1995, pp. 2760–2762.
- [28] Rüdiger, A., Schilling, R., Schnupp, L., Winkler, W., Billing, H. and Maischberger, K., *Optica Acta*, Vol. 28, 1981, pp. 641.
- [29] Mizuno, J., Report MPQ 203, *Max-Planck-Institut für Quantenoptik*, July 1995.
- [30] Robertson, D. I., Morrison, E., Hough, J., Killbourn, S. D., Meers, B. J., Newton, G. P., Robertson, N. A., Strain, K. A. and Ward, H., *Review of Scientific Instruments*, Vol. 66, No. 9, September 1995, pp. 4447–4452.
- [31] Jones, G. S., *University of Wales (College of Cardiff)*, Internal Report, 17 Dec 1996.
- [32] Morrison, E., *Ph. D. Thesis*, University of Glasgow, 1993, pp. 194–197.
- [33] Hough, J. *et al*, in *‘The Detection of Gravitational Waves’*, edited by D. Blair, Cambridge University Press, 1991.
- [34] M^cLaren, A. C., *Ph. D. Thesis*, University of Glasgow, 1996, pp. 207–223.
- [35] Morse, P. M., *‘Vibrations and Sound’*, McGraw-Hill, 1948, pp. 166.
- [36] Smith, B. T., Boyle, J. M., Dongarra, J. J., and Moler, C. B., *‘Matrix Eigen-system Routines - EISPACK Guide’*, Lecture Notes in Computer Science, Vol. 6, 2nd edition, Springer-Verlag, 1976.

- [37] Laub, A. J., *IEEE Transactions on Automatic Control*, Vol. AC-26, No. 2, April 1981, pp. 407-408.
- [38] Hutchinson, J. R. *Journal of Applied Mechanics*, Vol. 47, December 1980, pp 901-907.
- [39] Morrison, E., *Ph. D. Thesis*, University of Glasgow, 1993, pp. 154-191.
- [40] Fowles, G. R., '*Analytical Mechanics*', 3rd edition, Holt-Saunders. 1977, pp. 254.
- [41] Shoemaker, D., Schilling, R., Schnupp, L., Winkler, W., Maischberger, K. and Rüdiger, A., *Physical Review D*, Vol. 38, July 1988, pp. 423-432.
- [42] Mackenzie, N. L., *Ph. D. Thesis*, University of Glasgow, 1989, pp. 63-67.
- [43] Logan, J. E., *Ph. D. Thesis*, University of Glasgow, 1993, pp 182.
- [44] Drever, R. W. P., Hall, J. L., Kowalski, F. V., Hough, J., Ford, G. M., Munley, A. J. and Ward, H., *Applied Physics B*, Vol. 31, 1983, pp 97.
- [45] McLaren, A. C., *Ph. D. Thesis*, University of Glasgow, 1996, pp. 55-66.
- [46] Morrison, E., *Ph. D. Thesis*, University of Glasgow, 1993, pp. 118-130.
- [47] Camp, J., Sievers, L., Bork, R. and Heefner, J., *Optics Letters*, Vol. 20, No. 24, December 1995, pp. 2463-2465.
- [48] Strain, K. A., 'Electrostatic Drives for GEO 600', *GEO 600 Internal Report*.
- [49] Callen, H. B. and Welton, T. A., *Physical Review*, Vol. 83, No. 1, July 1951, pp. 34-40.
- [50] Kimball, A. L. and Lovell D. E., *Physical Review*, Vol. 30, December 1927, pp. 948-959.
- [51] Zener, C., *Physical Review*, Vol. 53, January 1938, pp. 90-99.
- [52] Kovalik, J., *Private communication*.

- [53] Saulson, P. R., *Private communication*.
- [54] Campbell, H., *Private communication with GEC Marconi*.
- [55] Gillespie, A. D., *Ph. D. Thesis*, California Institute of Technology, 1995, pp. 37.
- [56] Gonzalez, G. I. and Saulson, P. R., *Journal of the Acoustical Society of America*, Vol. 96, July 1994, pp. 207–212.
- [57] Fahy, F., *‘Sound and Structural Vibration’*, Academic Press, 1993, pp. 10, 14.
- [58] Wood, A. M., *Carnegie Summer Vacation Project Report*. University of Glasgow, November, 1992.
- [59] Gillespie, A. D., *Ph. D. Thesis*, California Institute of Technology, 1995. pp. 80–83.
- [60] Logan, J. E., Robertson, N. A. and Hough, J., *Physics Letters A*, Vol. 170, Nov 1992, pp. 352–358.
- [61] Gillespie, A. D., *Ph. D. Thesis*, California Institute of Technology, 1995, pp. 83–95.
- [62] Rowan, S., Twyford, S. M., Hutchins. R., Kovalik, J., Logan, J. E., McLaren, A. C., Robertson, N. A. and Hough, J., to be submitted to *Physics Letters A*.
- [63] Traeger, S., Willke, B. and Danzmann, K., *Physics Letters A*, Vol. 225, 27 Jan 1997, pp. 39–44.
- [64] Strain, K. A., *Ph. D. Thesis*, University of Glasgow, 1990, pp. 23–69.
- [65] Strain, K. A., *‘Longitudinal Control for GEO 600 - Revision 2.2’*, GEO 600 Internal Report, March 1996.
- [66] Schnupp, L., talk at a *European Collaboration Meeting on Interferometric Detection of Gravitational Waves*, Sorrento, 1988.

- [67] Takahashi, R., Mizuno, J., Miyoki, S. and Kawashima, N., *Physics Letters A*, Vol. 187, 1994, pp. 157.
- [68] Skeldon, K. D., *Private communication*.
- [69] Rowan, S., Twyford, S. M. and Hough, J., '*Analysis of Sapphire and Silicon as Suitable Materials for the Test Masses and Suspension Fibres in GEO 600*', GEO 600 Internal Report.
- [70] Braginsky, V. B., Mitrofanov, V. P. and Tokmakov, K. V., *Physics - Doklady*, Vol. 40, No. 11, 1995, pp 564-566. Translated from *Doklady Akademii Nauk*. Vol. 345, No. 3, 1995, pp. 324-326.
- [71] Schilling, R., *Private communication*.
- [72] Hough, J., Hutchins, R., Logan, J. E., M^cLaren, A. C., Plissi, M., Robertson, N. A., Rowan, S., Strain, K. and Twyford, S. M., '*Developments in Isolation, Suspension and Thermal Noise Issues for GEO 600*', GEO 600 Internal Report.

